NATURE OF LOW-SPIN EXCITATIONS AND SHAPE COEXISTENCE IN ^{64}NI

David Richard Little

A dissertation submitted to the faculty at the University of North Carolina at Chapel Hill in partial fulfillment of the requirements for the degree of Doctor of Philosophy in the Department of Physics.

Chapel Hill
2020

Approved by:

Robert V.F. Janssens

Arthur Champagne

Christian Iliadis

Reyco Henning

Fabian Heitsch

ABSTRACT

David Richard Little: Nature of Low-Spin Excitations and Shape Coexistence in ^{64}Ni
(Under the direction of Robert Janssens)

The structure of ^{64}Ni, the heaviest stable Ni isotope, has been investigated to search for shape coexistence, a phenomenon recently observed in neutron-rich ^{66}Ni and ^{70}Ni as well as in doubly-magic, $N = 40$, ^{68}Ni. In the latter case, the ground state is associated with a spherical shape, the 0_2^+ level was shown to be oblate, and the 0_3^+ one prolate. Such a prolate 0_2^+ level has also been reported in ^{70}Ni and, within the last two years, four 0^+ states have been established in ^{66}Ni, with the 0_1^+ and 0_3^+ levels being spherical, and the 0_2^+ and 0_4^+ ones oblate and prolate, respectively. The present search for evidence of these shapes in ^{64}Ni was stimulated by recent, state-of-the-art Monte Carlo shell-model calculations (MCSM), where the Hamiltonian includes effective interactions incorporating the monopole tensor force found to play an essential role in describing shell evolution in neutron-rich nuclei. In a first experiment, the wavefunctions of the low-spin excitations in ^{64}Ni were probed through reduced transition probabilities, B(E2), obtained from a high-statistics Coulomb excitation measurement. The structure of the nucleus at higher spin and excitation energy was also explored further through high-fold coincidence data collected following deep-inelastic reactions. From comparisons between the new results and MCSM and other shell-model calculations, a clearer picture of the structure of ^{64}Ni emerges. Specifically, most low-spin states are dominated by proton and neutron excitations within the *fp* shell, although a few involve the $g_{9/2}$ shape-driving neutron orbital. The agreement between data and MCSM results argues for a 0_2^+ level of small oblate deformation, and a spherical 0_3^+ state. The calculated lack of collective excitations along the yrast line has now been shown experimentally to persist in the spin 16-17 range up to 17.9 MeV excitation energy. Finally, the small upper limit deter-

mined for the B(E2) probability of a transition associated with the decay of a 3463-keV, 0_4^+ state discovered recently agrees with its proposed assignment to a prolate shape, herewith providing first evidence for triple shape coexistence in a stable Ni isotope.

ACKNOWLEDGEMENTS

This work is supported by the U.S. Department of Energy, Office of Science, Office of Nuclear Physics, under Grant Numbers DE-FG02-97ER41041 (UNC) and DEFG02-97ER41033 (TUNL).

I'm not sure that I'll ever have an opportunity to write something like this again. That being the case, I hope the reader will forgive my "thoroughness". I have no misgivings about the fact that I have not gotten to where I am on my own. Whether through their direct efforts, or simply by their presence in my life, I have so many people to whom I owe debts of gratitude, not only for their support in accomplishing this goal, but for shaping me as an individual. When I think about the person I was when I entered grad school nearly seven years ago, I'm continually surprised to see how I've grown as a person since then, and I'm exceedingly grateful for all those who've been by my side along the way. Realistically, ten years from now, there's a fair chance that I may, in fact, not remember all of the excited states in ^{64}Ni. I will, however, remember every single one of these people.

My advisor, Robert Janssens, is a man of excellent taste. I think he will appreciate that I'm leading with this. Whether it's music, food, or drinks, you can always trust his recommendations, and whatever his recommendation, he likely has a story to go along with it. He's a man who always has a story. Furthermore, in case you are unaware, he is also quite a talented physicist; you may have heard of him, as he is "**V**ery **F**amous" (R.**V.F.** Janssens). Although he was my advisor for the span of only two years, I learned an extraordinary amount in such a short time working with him. He was someone whom I truly did feel I was working with, and not simply working for. He genuinely made every possible effort to facilitate my success, and to promote my growth as a scientist. It was a sincere pleasure working, as well as celebrating, alongside him, and with all of the friends I've made through him, during my

time as his student. His steadfast commitment to this dissertation was also astonishing. Rarely do you find an advisor that will routinely read two full chapters of a dissertation in only two days, and return it to you covered in ink. And, indeed, I must stress the latter. He certainly drove me up a wall on more than one occasion throughout this process, though this is no news to him, but now that it's over, I can't help but chuckle about it. However, it was always clear to me that he had every desire to help make this dissertation the best it could possibly be, and something that I could be proud of. Now that it is finally done, I'm incredibly thankful that I have something I can look back on with fulfillment, knowing I gave it my absolute all. While I may no longer be working with Robert, I will always have many wonderful memories during my time in grad school. From our celebrations with the staff at Argonne after successfully completing an experiment, to our holiday dinners with our lab group, Robert truly showed me that being a scientist is about more than just the science. Every experiment with Robert was an adventure. With physicists from different universities, labs, and countries working alongside us, I truly felt like a part of a greater community, and that feeling is probably one of the things I'll miss the most. During experiments, we all rejoiced in our successes and agonized together over the difficulties, but whatever the case, we always felt like a team, and that was sincerely inspiring. It's nigh impossible to find someone who loves their work as much as Robert, but that's likely why I received the extraordinary experience that I did. It always tickled me that every experiment was like a party to him. You would receive an email stating, "Hey, we're running an experiment at Argonne! Come be a part of it!" People would travel from all over to participate, and after a long stressful week or two of running, the experience would culminate with a big dinner at a nearby restaurant, where I'd typically order a steak and a couple beers and subsequently try to avoid slipping into a food coma. Even conferences, which I used to dread, I started to view as opportunities to see all of my friends, and to share the exciting work I had been doing. It makes you significantly less nervous to give a talk when you see a third of the audience as your friends and colleagues rather than mere strangers. On a more personal note, it

really is a nice thing to have an advisor with good sense of humor, and this was something Robert possesses in spades. Whether it was dinner with him and his lovely wife, Claire, going out for drinks with the team, or just chatting in his office, there never was a want of joy and laughter. But likely the thing that struck me the most about Robert, is how much he cares. Every time we met in his office and every time we spoke on the phone, he would, without fail, ask me how I was doing. Not with some halfhearted formality that the cashier at your local fast food chain greets you with before prompting you for your order, but with sincerity, concern, and genuine interest in your life. Any trip I would take, he would always ask me to message him when I arrived at my destination to ensure that I got there safely. If you were having a difficult day, he wanted to know about it. And he always understood the importance of taking time for oneself to rest. As involved with my work as he was, he never made me feel like I was moving too slowly or not performing well enough. While positive feedback from advisors can sometimes be few and far between, Robert's was not, and his encouragement always made me feel like I was appreciated as his student. Outgoing, animated, colorful, understanding, and kind: these words describe him well, though the list is not comprehensive. It is no mystery to me why others gravitate to Robert. His positive nature attracts all the positive people around him. There's a "strong force" joke to be made here, but I'm not sure I have the energy. I can't express how fortunate I was to have had an advisor who showed me that grad school and physics are so much more than slaving away at a computer. It's about learning, passion, teamwork, community, and friendships. And I'm eternally grateful to call Robert my friend.

Before working with Robert, I had the pleasure of working with another exceptional physicist by the name of Arthur Champagne. As my friend likes to describe him, "Art Champagne: born cool, raised cool, grew up cool." And how could one not be with a name like Art Champagne? While a man of few words, he's quite adept at knowing just what to say and when to say it. It's also hard to meet a more understanding and even-tempered guy than Art. Also sharing an excellent music taste along with Robert, Art performed in

a Rolling Stones tribute band during my first few years of grad school. Walking into his office for the first time after I had joined the group, I noted a large skull on his computer monitor. I asked him about it and he informed me that he was, in fact, looking at a skull ring modeled after an actual skull, staying true to the Keith Richards motif. Committing a social faux pas, I asked him how much it cost. He responded, "more than I should be spending." Naturally, I would have been remiss not to attend one of his shows. It puts your advisor in a slightly different context when you see him on stage, shredding the guitar. The singer was even passing around the microphone and somehow I managed to sing the chorus to Jumpin' Jack Flash. My friend, Cody, who had also attended the show, decided it was only fitting that he utilize this as inspiration for one of his non-playable characters in Dungeons Dragons: enter, playboy and minstrel extraordinaire, Art Champagne. I relayed to Art that he had inspired a DD character, and he asked me to forward him the message my friend had sent me about it, stating in humble fashion, "maybe now my daughter will finally think I'm cool." More seriously though, during my time as his student, Art was always willing to answer any question I had, and he did so without ever making me feel embarrassed for asking. In fact, throughout my entire time as a grad student, Art has always been helpful, kind and encouraging. There are many examples, but one thing I'll always be appreciative of is the fact that he gave me a chance when it felt like others wouldn't. During my first year of grad school, I had been so excited to join a nuclear physics group, so I didn't waste any time asking around. However, no one I spoke to seemed to indicate that they had room for another graduate student. As my first year was nearing its end, I was still unable to find an advisor, yet some of the groups which had supposedly been full were recruiting other students from my class. I was becoming a bit disheartened until Art finally told me that they should be able to move some funds around so their lab could hire me, and that they'd make it work. I'm sure to him it probably wasn't a big deal, but at a difficult time in my life it seemed like someone was willing to give me a shot, and that's something that I was, and still am, very grateful for. It's no surprise to me that Art and Robert get along as well

as they do. They're both honest, authentic people who truly want what's best for their students. While for many students it may be considered a disadvantage or setback to have two different advisors during their time in grad school, for me it was very much a blessing.

Three other professors with whom I'd worked, Christian Iliadis, Tom Clegg, and Richard Longland were also incredibly positive influences as a graduate student. In all honesty, I don't believe I could have hoped for a more wonderful and supportive group of instructors. I'm not sure I've met anyone who genuinely seems to enjoy giving talks as much as Christian. Moreover, he's quite splendid at it. I had the good fortune of being able to take a nuclear astrophysics class taught by Christian, and he came in every day well-prepared and eager to teach. In many ways it was that class and my final project on ^{26}Al which taught me and motivated me in my nuclear astrophysics studies under Art, before my foray into nuclear structure. Christian was also kind and supportive in any endeavor I undertook, willing to help in any way possible. As for Tom Clegg, it's nearly impossible to find someone as energetic as him with such a zeal for science. When he took me on my first visit to TUNL during my prospective weekend, I was enthralled by Tom's excitement as he showcased the facility. I couldn't help but think of all the incredible work I could do there. He was also absolutely a proponent of getting your hands dirty, and always invited and encouraged me to participate in any of the hands-on work we did on the accelerators and beam line. Richard Longland, a professor at NC State who had previously worked in our lab as a UNC student, had the office just across the hall from mine. A relatively soft-spoken gentleman with a charming British accent, Richard always seemed to be in a pleasant mood. While I did not have the privilege of working with him directly, I did, on many occasions, darken his doorway in order to ask questions about GEANT4, nuclear astrophysics, or life in general. Naturally, as the kind person he is, he was always happy to oblige.

Regarding others who've guided me throughout this process, I must extend a sincere thank you to Professor Daniel Ayangeakaa from the U.S. Naval Academy for all that he has taught me about the world of nuclear structure, and, in particular, Coulomb excitation.

Not only was he involved in the process of running my Coulomb excitation experiment, but also, over the span of eighteen months, he taught me nearly everything I know about how to analyze nuclear structure data using software such as Radware and GOSIA. Moreover, he was incredibly patient as I bombarded him with dozens of questions about nuclear structure physics, and was always willing to help me understand anything I was struggling with. Beyond this, on more than one occasion when I had hit a brick wall, I was able to drive up to Annapolis, MD, and he took time out of his schedule to work with me to resolve whatever issues had been arresting me. There were times when I posted up in his office for two, or even three days, in order to ensure I was handling the analysis correctly. I feel perfectly comfortable saying that it was only with his help that this project could be completed in the timely manner it was. Daniel is overall just a charming person and a joy to interact with, and we look forward to him joining the team at UNC Chapel Hill in the near future.

It's thanks to a multitude of others that I was able to collect all of my data, and learn a great deal about nuclear structure, in such a short time. I briefly want to mention a few of them. I spent a significant of time working with Ching-Yen Wu, Shaofei Zhu, John Rohrer, Jack Henderson, Jing Li and Sanna Stolze setting up for the CHICO2 campaign at Argonne National Lab. We were horribly pressed for time and it was an exceedingly stressful two weeks, but somehow we managed to get everything up and running in time for the first experiment. Each one of us was ravenous by the time dinner rolled around. We'd break around 6 to scarf down a quick meal at one of the local Thai restaurants, just to come back to the lab and power through late into the evening. It was a true trial by fire, but it was the very sense of teamwork and camaraderie I mentioned previously that brought us all out the other side, with only minimal bumps and bruises. Throughout the rest of my visits to Argonne, dozens of others have assisted in carrying out experiments. I'm especially thankful for all the staff that made this work possible, including Michael Carpenter, John Greene, Dariusz Seweryniak. I have nothing but the highest praises for all of these scientists. Sitting around the dinner table with them as I cut into a medium-rare steak, listening to everyone

laugh at Robert's anecdotes and Partha Chowdhury's witty remarks as we celebrated an experiment well-done was consistently the highlight of my trips.

Throughout my time at UNC, I've also been blessed by the incredible quality and expertise of my labmates, from whom I've learned a great deal. My teammates at TUNL were some of the most impressive young scientists I've had benefit of knowing. Keegan Kelly, who taught me a great deal about GEANT4 (though it was not relevant to this dissertation) and HPGe detectors when I was just starting out, is an impressive scientist and one of the most patient individuals I've ever met. I'm not sure I could even name a time where I recall him being frustrated or upset. He also has one of the greatest abilities to persist that I've seen in an individual. Despite how many days he struggled against a problem, he never seemed to lose his determination or momentum. Always willing to help in any way possible, he was always a positive influence in the lab, and a good friend.

It's hard to say if anyone was more of a "jack of all trades" than Lori Downen. Lori had a wealth of experience in nearly everything our lab had to offer. If there was a problem with a piece of equipment that no one else was sure how to resolve, it was more than likely that Lori had dabbled in it. And much like I've said for many others, she was always willing to lend a helping hand (this is a continuing theme, so I hope the reader will forgive the redundancy). Not only was she glad to assist with lab-related issues, but she would always take the time to listen if you were ever having a rough day. On top of this, she is quite the talented baker, and on more than one occasion I ate myself sick with some of the treats she brought in for the rest of the lab.

Jack Dermigny became our expert on Bayesian statistics, created the GUI our lab uses for fraction fitting, and worked extremely hard to restore our SNICS source to working condition. In my opinion, he had quite a prolific tenure with our lab. One of the qualities I most appreciated about him though was his meticulousness. Whenever he worked, or whenever he was teaching you something, he took his time. He seemed to ensure that every action would produce the desired outcome and that everything was accounted for. When

he explained his methodologies, he took things step by step, making sure you could follow along with his thought process. It was incredibly refreshing, and I found him to be quite a good teacher.

I must give a considerable amount of praise to my labmate Sean Hunt, for having one of the most scientifically innovative minds I've ever encountered. Constantly coming up with new and interesting ideas, whenever one of his attempts failed, he would consistently find a way to attack the problem from an entirely different direction. Moreover, Sean's intuition was quite admirable as well. Whenever something would go awry, he was often adept at quickly diagnosing the issue, or narrowing down the possible culprits. Beyond this, I cannot thank Sean enough for how he would tutor my class weekly on qualifying exam problems during my first year of grad school, or for all the effort he put into training me on our JN Van de Graaff accelerator. Whenever I had a problem or a question about nuclear astrophysics, Sean was always one of the first people I went to, and he was always eager to assist. Sean also appreciates a good debate, and I thoroughly enjoyed the hours spent discussing the topics of religion, politics, and philosophy with him. Another friend I'm thankful for, and I'm glad we're still able to keep in touch.

Another colleague whom I have a great deal of respect for is a gentleman named Andrew Cooper. I'm not sure I've ever met another student who was as passionate about science as Andrew was. He would roll into the lab every day on his skateboard, often sporting his Apollo MA-1 flight jacket. It was probably apparent to most of us that Andrew was enthralled by the idea of space exploration, and, thus, being in a nuclear astrophysics group at the time likely suited him just fine. It was clear that Andrew made an intentional effort to learn as much as he possibly could, never taking shortcuts, and doing his best to get as far as he could manage before asking for help. I'd say it's very likely that he spent more time in the lab than any of us, often working late into the evening to rectify any problems that might be arising with our ECR ion source, for which he had designed a new acceleration column. Much like the rest of our group, Andrew was always willing to offer a helping hand,

and he would gladly walk you through any nuclear concepts that you might have difficulty grasping. He is also probably one of the most hilarious people I've ever met. I'm not sure whether it was his timing, his delivery, or the fact that he could do it all with a straight face, but he never failed to make me laugh.

A few other colleagues I would like to mention, though I didn't have the chance to work with them to the same extent. Michael Jones, our postdoc during my time working with Robert, worked with me on several experiments. We shared a lot of laughs together over dinner and drinks, and while often quiet, he was a pleasure to talk to once you got him going. Arthur Champagne's postdoc, Amber Lauer, excelled in the computational aspect of nuclear astrophysics. While I would offer to help with the more tactile components of her research, she was happy to assist me whenever my knowledge of computers was woefully lacking: a criterion that was routinely met. Moreover, her somewhat frenetic nature and interest in organizing social events made for several wonderfully entertaining luncheons and nights on the town. Lastly, I want to mention Caleb Marshall. A very bright student from NC State University, I was always impressed with his comprehension of the subject matter, and how quickly he became a skilled experimentalist. I have no doubt that he will make a fine scientist if he decides to go that route. Furthermore, a fellow with an excellent sense of humor, and even stronger sarcasm. It was a blast having drinks and playing trivia downtown with Caleb and Amber on the few occasions we were able.

Samantha, Clay, and Emily, it's been a pleasure working with all of you as you embark on your new journeys as graduate students. Each one of you shows the potential to be an exceptional scientist, and I look forward to seeing where this adventure takes you. Samantha, during my time working with you during your REU, you were amazingly driven and an incredibly hard worker. I have no doubt that you'll become a master at whatever research you take an interest in. Clay, you already know leagues more than I did when I became a graduate student. I'm sure you'll be the group's new GEANT4 expert in no time. Emily, you have a wonderful knack for assimilating new information. I can't wait to see what all

you'll learn.

My tenure as a UNC graduate student may have gone quite differently if it had not been for our Grants and Contracts Administrator, June Tirpak. Always a warm demeanor and a lively personality, June always made you feel welcome when you walked through the doorway, and she could easily strike up a conversation with you about anything. On a few occasions she even offered me her banana she had packed for lunch, noticing that it was getting late in the afternoon and I had not eaten yet. As a matter of course, I have to thank her for all of the work she did regarding our grants and contracts, as we would have been very much up a creek without that. However, I am especially grateful to her for going out of her way to make sure I had a place to park at TUNL. Despite having to travel to Duke from Chapel Hill for my research on a daily basis, there was, unfortunately, no place for graduate students to park aside from the parking deck, which charges twelve dollars a day. As this is not a price a graduate student can afford, the only other option is to take the bus from Chapel Hill, which can add an extra 1-2 hours to one's daily commute, and only runs during specific times of the day. June, however, happily provided me parking passes for my trips to TUNL during my last couple years of graduate school such that I was able to park just outside the lab. It felt like an immense amount of weight was lifted, and the difference in my state of mind was truly miraculous. Thank you again for all you do, June.

In terms of managing the more bureaucratic and logistical aspects of my graduate student career, I would like to extend an enormous "thank you" to our Graduate Affairs Coordinator, Maggie Jensen. If it weren't for her helpful reminders, I have no idea how many deadlines I, or my colleagues, would have missed regarding health insurance, funding, class enrollment, etc. I also must thank her for all of the insight and words of support she offered me as I applied for graduation and scheduled my defense, not to mention alleviating each and every one of my concerns about how one carries out a PhD defense during a pandemic. Being Robert's first graduate student at UNC, and this being my first (and likely only) PhD, Maggie was an immense help as we navigated this complex process. And no matter how

many times I walked into her office shamefaced because I had forgotten to fill out next semester's paperwork, I was always greeted with warmth and a smile.

I've been fortunate enough to have many close friends who have not only supported me through my adventure as a graduate student, but have also been by my side through the vicissitudes of the past seven years. As much I as I would love to mention them all by name, that would probably double the length of this document, so I'll have to settle for just a few. First, I want to thank all the members of my church and small group for their unrelenting love and support throughout this difficult process. Your prayers and kind words truly fortified my spirit. Two of my oldest and closest friends, however, I would like to mention by name: Cody Sutton and Ian Schock. Cody, another lover of science and nature, has been one of my best friends and "concert buddies" since sophomore year of high school. We've spent hours upon hours together talking, playing games, and writing asinine songs. I don't believe there has ever been anyone I've shared more laughs with. I have no desire to count how many times I bemoaned the difficulties of graduate school, and life in general, to him. But no matter what, he was always willing to listen. Ian Schock, whom I befriended my sophomore year of high school as well, has been alongside me throughout my Christian walk. An incredibly patient, wise, and intelligent gentleman, he has always been there to offer a word of comfort, even at my lowest points. I've been exceptionally blessed to have had him in my corner over the past seven years and throughout my life. Our discussions regarding faith and spirituality have cultivated my relationship with God more than I had ever anticipated. I am forever grateful for the love and kindness you've both shown me.

At last, I would be gravely remiss if I neglected to acknowledge the overwhelming love and support I've received from my parents, Rich and Diane Little. I've often found it easy to become so immersed in my work where I forget that, while I'm at the lab focused on carrying out an experiment, or at home laboring over this dissertation, my parents are thinking of me and praying for me every hour of the day. Despite being seven hours away, they make certain I know that I'm always on their minds. Their love and concern for me is unparalleled, and

they have done everything humanly possible to promote my health and happiness. I cannot describe how thankful I am to call them my parents. They have taught me such a great deal about life, and how to be the kind of person God desires me to be. Without these lessons, I'm certain I would not be where I am now. Mom and Dad, you have given me so much, I'm glad I can at least give you this. I love you both.

"Therefore do not be anxious about tomorrow, for tomorrow will be anxious for itself. Sufficient for the day is its own trouble."

Matthew 6:34

TABLE OF CONTENTS

LIST OF TABLES

LIST OF FIGURES

LIST OF ABBREVIATIONS AND SYMBOLS

ANL	Argonne National Laboratory
ATLAS	Argonne Tandem Linac Accelerator System
BGO	Bismuth Germanate
CHICO	Compact Heavy-Ion Counter
DAQ	Data Acquisition System
DCO	Directional Correlations
ED	Electric Dipole
FMA	Fragment Mass Analyzer
FOM	Figure-of-Merit
FRIB	Facility for Rare Isotope Beams
FWHM	Full Width at Half Maximum
GANIL	Grand Accélérateur National d'Ions Lourds
GRETA	γ-Ray Energy Tracking Array
GRETINA	γ-Ray Energy Tracking In-Beam Nuclear Array
HIγS	High Intensity γ-ray Source
HPGe	High-Purity Germanium
LBNL	Lawrence Berkeley National Laboratory
LNPS interaction	Lenzi-Nowacki-Poves-Sieja effective interaction

MCP	Microchannel Plate
MCSM	Monte Carlo Shell Model
MD	Magnetic Dipole
NRF	Nuclear Resonance Fluorescence
NSCL	National Superconducting Cyclotron Laboratory
PPAC	Parallel-Plate Avalanche Counter
R Process	Rapid Neutron Capture Process
RF	Radio Frequency
RIBF	Radioactive Isotope Beam Factory
RMS	Root Mean Square
SD	Superdeformed
SF_6	Sulfur Hexafluoride
TUNL	Triangle Universities Nuclear Laboratory

CHAPTER 1: Introduction

For more than a century, the nuclear structure community has been focused on unraveling the properties of the atomic nucleus. Situated at the center of the atom and at roughly a thousandth of the scale, the atomic nucleus is a densely-packed region composed of a mixture of protons and neutrons, all governed by the nuclear force. Acting only over a scale of a few nucleons, this nuclear force counteracts the electromagnetic repulsion between protons and allows for the existence of stable nuclei. These nuclei are situated along a line within the chart of nuclides, aptly referred to as the line of stability. At lower mass numbers, the line of stability follows a 45° inclination due to a preference for equal proton (Z) and neutron (N) numbers. However, as more protons are added, this line skews towards neutron-rich nuclei. This is because, for increasing proton numbers, neutron excesses are required in order to act as a sort of buffer and mitigate the growing repulsive force between protons, thus maintaining stability. When one strays too far from this line in terms of proton or neutron excesses, nuclei will undergo radioactive decay. On the neutron-rich side, nuclei will undergo β^- decay, converting a neutron into proton and a β^- particle in order to re-establish stability and conserve charge. Proton-rich nuclei on the other hand, will β^+ decay or proceed through electron capture, converting a proton into a neutron. Additionally, some heavy nuclei may even decay via the emission of an α particle, fission, p-decay, or other exotic processes. These decay modes carve out a region of bound nuclei, terminating at the proton and neutron drip lines.

The vast majority of nuclear knowledge obtained thus far has come from isotopes near the line of stability, and this information serves as the foundation for many nuclear models. However, these nuclei only account for a small fraction of the total number, making our understanding limited. Unfortunately, unstable nuclei can be challenging to study due to

the difficulty of reproducing them in the laboratory, and so information on their properties is at present quite limited in many instances. One of the main questions in nuclear structure today is how well nuclear models predict nuclei far from stability. In recent decades, advances in radiation detection technology as well as particle acceleration techniques have allowed nuclear scientists to push outwards from the line of stability towards even more exotic nuclei. Modern facilities are now capable of creating exotic isotope beams at intensities sufficient to carry out detailed experiments, and the information obtained from these sheds light on new phenomena, alter existing nuclear models, and even change the way we think about fundamental nuclear interactions [1].

The structure of the lowest-lying energy levels in a nucleus, as well as many of its inherent properties, depend heavily on the number protons and neutrons it possesses. These states are representative of at least two different excitation modes: single-particle excitations and collective ones. As the name implies, single-particle states arise from the excitation of individual nucleons, while collective states are brought about by the interplay of many nucleons operating together in a group. Many nuclear models have been developed in order to comprehend these modes of excitation. In theory, starting from nucleons and their basic interactions, one should be able to fully describe the structure and properties of any nucleus under a single unifying model. However, due to our nascent understanding of the nuclear force, as well as to the computational scale of the problem, this has not yet come to fruition except for the lightest systems ($A \leq 12$). Instead, theorists use data obtained from nuclear structure experiments to further improve their models, making use of certain simplifying assumptions in order to reduce the model space and render calculations possible. One of the most prominent models in nuclear structure, the nuclear shell model, utilizes experimentally observed energy gaps associated with specific proton and neutron numbers to manage the breadth of their calculations. These gaps, occurring at N=Z= 2, 8, 20, 28, 50, 82 and 126 (for neutrons only, as Z=126 has not yet been observed), correspond to nucleon "shell closures", and the numbers are referred to as magic numbers. Nuclei with one or both of

these numbers exhibit unique properties as compared to their surrounding neighbors. The shell model treats these nucleon numbers as useful to define inert "cores" for the sake of calculations where, to first order, they do not interact with the nucleons outside of them. The remaining nucleons outside this core or "shell" are considered to be valence nucleons. It is then predominantly these valence nucleons that describe and influence the nuclear states, either by individual excitations, or by their interactions with one another, or by both.

The nuclear shell model is effective at describing the structure and properties of nuclei near magic numbers, but has a difficult time describing more collective motions like rotations and vibrations, often exhibited by nuclei further from magicity. For these more collective nuclei, the so-called Bohr-Mottelson model and others derived from it are typically more applicable. These models describe the collective interplay of all nucleons in order to predict the structure of the nucleus [2]. Most nuclei exhibit properties characteristic of both single-particle and collective excitations, and the interaction between the two modes is being studied. As a result, a combination of these two models is necessary to provide a complete description of the nucleus. For this reason, experimental studies probing the overlap and interaction between these two fundamental modes are essential if a comprehensive understanding of nucleon-nucleon interactions is to be achieved. Despite being one of the four fundamental forces, and quite literally the mechanism that holds the universe together, the strong nuclear force is still not well understood. How it evolves as a function of neutron-to-proton ratio, and the specifics of how nucleon-nucleon interactions affect more global properties such as the degree of collectivity and the nuclear shape, are still being thoroughly investigated [3]. The studies of exotic and neutron-rich nuclei seek to elucidate these issues by examining the effects of neutron excess on the aforementioned nuclear properties.

One of these global properties, the nuclear shape, is particularly interesting in that some nuclei may manifest different shapes all at relatively low excitation energies, due to the collective motion of the nucleons. For example, while a nucleus may have a spherical ground state, some low-lying excitations may cause it to exhibit shapes similar to that of an amer-

ican football or a frisbee. These deformed nuclear shapes are referred to as prolate and oblate, respectively, and are brought about by the quadrupole nature of the nucleus' charge distribution. When more than one of these shapes is displayed by a nucleus at low energies, the associated phenomenon is known as shape coexistence. An intriguing and fairly rare property, shape coexistence is present throughout all regions of the nuclear chart, but, in recent years, interest has focused on the emergence of this phenomenon in regions far from stability. An improved understanding of shape coexistence and nuclear structure in these regions can add much to our knowledge of nucleon-nucleon interactions and fundamental nuclear forces.

The first instance of shape coexistence in a nucleus was suggested by Morinaga in 1956 [4], with regard to the observation of a 0^+ excited state in ^{16}O located at 6.06 MeV. At this point, it had already been established that shape deformation was prevalent in heavy nuclei, especially those far from a closed shell, where the collective motion of many valence nucleons drives the nucleus away from sphericity. However, ^{16}O, a doubly-magic nucleus, was expected to be rigidly spherical, and in no way was it anticipated to exhibit characteristics of a deformed nucleus at low energies. Despite its obviously spherical ground state, a low-lying 0^+ excited state indicated the possibility of a rotational band (to be discussed in the following Theory chapter). It was asserted that, while the ground state is associated with a closed shell, excited states are conversely not in closed-shell configurations, opening up the possibility of shape coexistence. If this was indeed the case, then a 2^+ rotational state should be located not far above the 6.06-MeV, 0^+ excitation. In fact, that is precisely what was seen with a 2^+ state located at 6.91 MeV, only 850 keV higher than the 0^+ level. Later on, 4^+ and 6^+ states were also found lying atop the aforementioned 2^+ at energies suggestive of a rotational band, further solidifying the argument for shape coexistence [5, 6].

The next instance of shape coexistence did not arise until 1964, when G. Brown proposed the idea of potential shape coexistence in the doubly-magic ^{40}Ca, based on theoretical models. This was confirmed much later, in 2001, to in fact be associated with a so-called

superdeformed (SD) band (i.e., a band associated with a very large deformed prolate shape) via experiments carried out by Ideguchi et al and Chiara et al [7, 8]. Again, building upon an excited 0^+ state, an SD rotational band was observed the entire way to a spin of 16^+ and predicted to be associated with an eight-particle-eight-hole (8p-8h) excitation, meaning eight particle-hole pairs were created by exciting nucleons out of their respective orbitals (to be discussed further in the following chapter). Several more examples of shape coexistence were unearthed over the years, but arguably the most striking was found in the lead nuclei, specifically ^{186}Pb [9]. With a closed proton shell at Z=82 and the neutron number sitting halfway between the N=82 and N=126 shells at N=104, this semi-magic nucleus provided a unique opportunity to investigate the competition between shape excitations, collective motion and intrinsic excitations. In addition, the two lowest-lying excited states had already been identified as both having spin and parity 0^+, making them excellent candidates for so-called deformed bandheads. A calculation of the potential energy surface of ^{186}Pb, displayed in Figure 1.1, also predicts the coexistence of oblate and prolate minima around 1 MeV, alongside a spherical ground state. In the calculations, the former is associated with a 2p-2h configuration, while the latter is related to a 4p-4h excitation. All three 0^+ states were populated via α-decay from the ground state of ^{190}Po, and their reduced α-decay widths were measured. It was known, a priori, that the ground state of ^{190}Po is likely associated with a 4p-2h configuration and, thus, the speed of different decay modes could provide insight into the structure of the three 0^+ levels. It was observed that the decay from ^{190}Po to the ground state of ^{186}Pb proceeded much more slowly than that to the first excited state, indicating that it is likely that the first excited 0^+ state in ^{186}Pb is of multiparticle-multihole character. Then, using the reduced α-widths and extrapolating from known higher-spin states in ^{186}Pb, it was possible to associate the third 0^+ level, at 650 keV, with the prolate bandhead, and the second 0^+ state at 532 keV with an oblate shape. This provided a truly singular "laboratory" for the study of collectivity, and a nearly unparalleled view on triple shape coexistence [9].

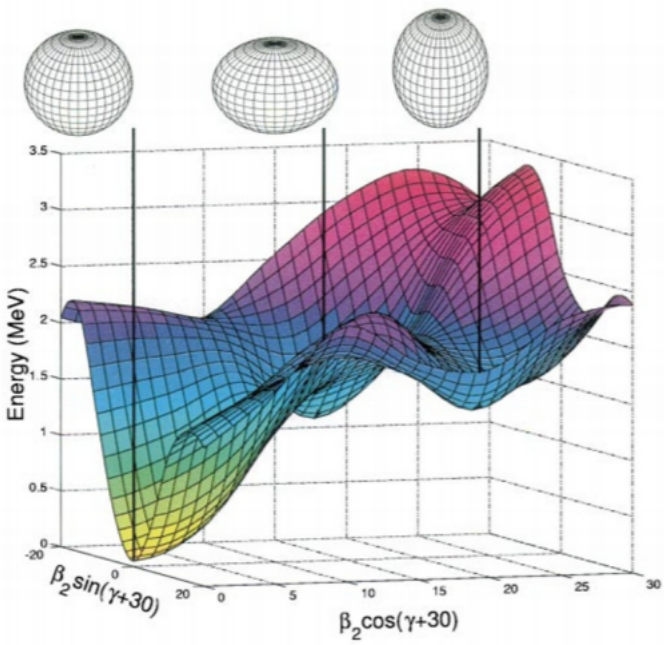

Figure 1.1: The potential energy surface calculated for ^{186}Pb. Here, β represents the elongation the nucleus and γ refers to its axial symmetry. It can be seen from these calculations that the first, second, and third 0^+ levels in this nucleus are proposed as spherical, oblate, and prolate minima, respectively [9].

Around the N=20 region of the nuclear chart, peculiar phenomena were also coming to light. For example, the N=20 shell gap seemed to disappear in neutron-rich neon, sodium, and magnesium isotopes. Specifically, it was anticipated that $^{32}Mg_{20}$ would be semi-magic and would be well-described via the shell model. However, the first excited, 2^+, state is at the low excitation energy of 885 keV, suggesting the onset of nuclear deformation in this nucleus and its neighbors, pointing to the breakdown of the N=20 magic number. Following thorough investigation and calculations performed by Caurier et al [10], it was discerned that low-lying "intruder" states were responsible for driving these deformations and that, by including them in the valence space of the calculations, these unique effects could be reproduced. These intruder levels are brought about when spin-orbit coupling causes states situated in one shell to drop down into the lower-lying shell. This region became known as the "island of inversion" or "island of deformation", due to the prevalence of these shape-driving intruder orbitals and the "inversion" of normal and intruder configurations. Besides

these unexpected configurations, new shell gaps were also observed in neutron-rich nuclei around N=32 and 34 [11]. These phenomena are both brought about through an interaction known as the tensor force, which will be discussed at length in the following chapter. These findings added invaluable knowledge to our understanding of nuclear structure [12].

This sets the stage for the study of one of the most intriguing families of isotopes. The nickel isotopic chain has been an important area of interest where knowledge of structure properties extends from the proton drip line at ^{48}Ni [13] to the neutron-rich ^{78}Ni isotope [14]. The proton shell closure at Z=28 allows us to probe the extent of the magicity of these nuclei, and to thoroughly document the evolution of nuclear structure as a function of neutron excess. This, of course, includes spanning the magic neutron numbers of N=20, 28, and 50, as well as a subshell closure located at N=40, which exists due to a large gap between the orbitals $\nu p_{1/2}$ and $\nu g_{9/2}$, where ν specifies neutron orbitals (Figure 1.2). The first nucleus to catalyze this pursuit was the "doubly-magic" ^{68}Ni. The existence of a 1605-keV, 0^+ first-excited state in this nucleus piqued the interest of many, and provided evidence for the possibility of a subshell closure at N=40 [15]. Comparisons with Monte Carlo shell-model (MCSM) calculations (to be defined later in this dissertation) reinforced the idea that ^{68}Ni may likely possess a spherical ground state alongside an oblate first-excited 0^+ level brought about by neutron excitations. Furthermore, these calculations have also suggested that a previously-observed 0^+ state at 2511 keV could be associated with a prolate deformation arising predominantly from 2p-2h proton excitations [16]. Thus, the calculations strongly support the idea of shape coexistence in this nucleus. However, many experiments have suggested that the N=40 subshell gap may not be as wide as initially anticipated, and that deformed structures become energetically favorable as protons are removed. Such is the case for certain neutron-rich isotopes of Cr, Mn, Fe and Co where level structures are dominated by deformed configurations [17]. Shape coexistence in this region can be understood via Type-II Shell Evolution, as a consequence of the proton-neutron tensor force between the $\pi f_{5/2,7/2}$ and $\nu g_{9/2}$ orbitals, to be explained further in the following Theory chapter. More

simply put, multi particle-hole interactions induce changes in the effective single-particle energies and result in level sequences associated with different shapes.

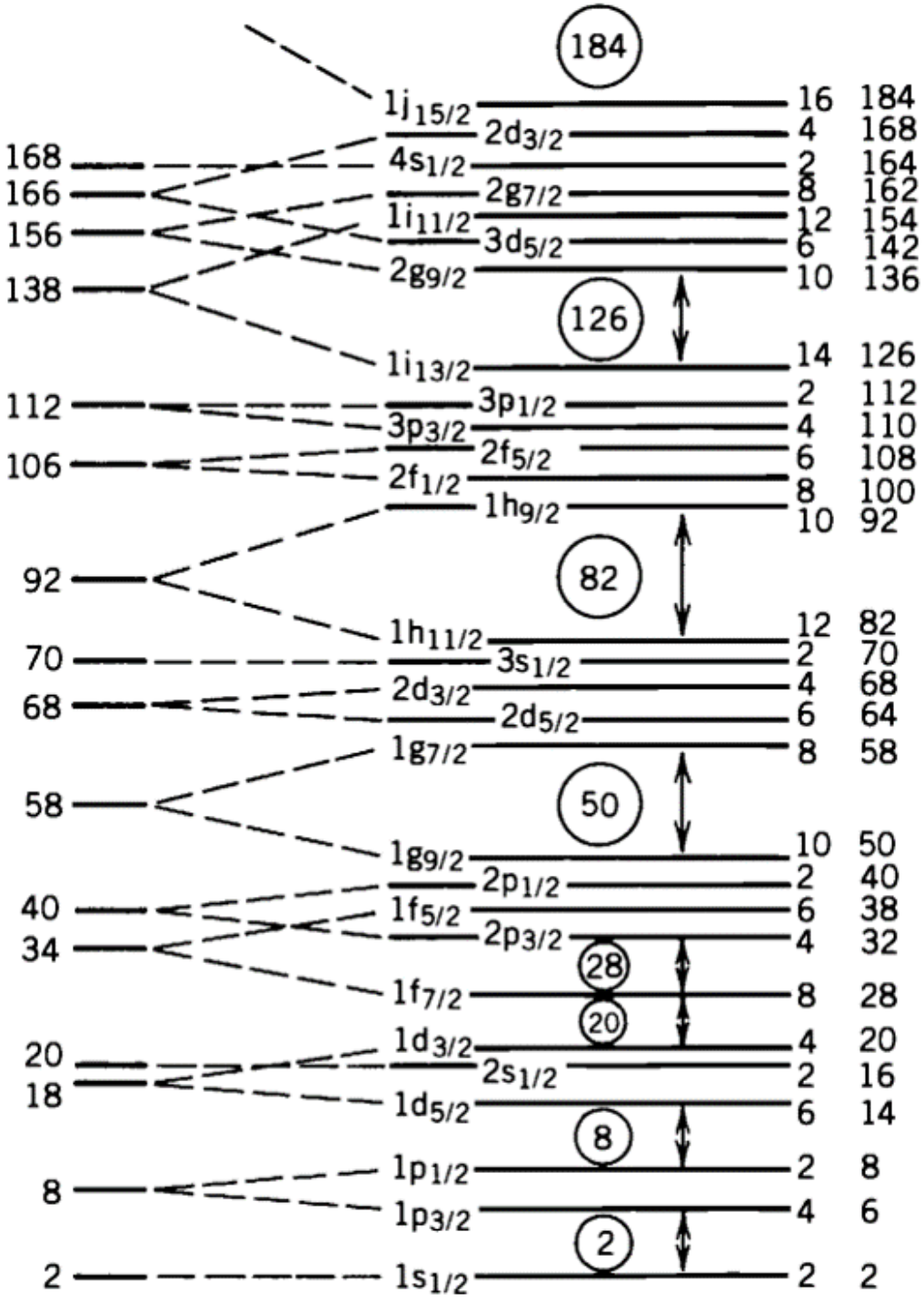

Figure 1.2: A classical depiction of spin-orbit splitting and the shell gaps located at magic numbers.

Following the investigation of ^{68}Ni, other isotopes of Ni in this mass region were studied with a focus on shape coexistence. First, an examination of the ^{70}Ni nucleus was performed using multinucleon-transfer and secondary fragmentation reactions [18]. When comparing with MCSM calculations, the observed second 2^+ and (4^+) excited states could only be accurately reproduced if there was an additional allowance for excitations of protons across the Z=28 shell gap. These calculations indicated that these two states were likely part of a prolate-deformed intruder sequence, a clear parallel to the situation in ^{68}Ni (however, the work of Elman et al has since questioned this interpretation [19]). Naturally, the next step was to search for the 0^+ bandhead of this proposed prolate-deformed sequence. Using β-delayed, γ-ray spectroscopy following the decay of ^{70}Co, a (0_2^+) state was observed at an energy of 1567 keV and has been proposed as being associated with prolate deformation. With the addition of two neutrons, the notable drop of the prolate-deformed 0^+ state between ^{68}Ni and ^{70}Ni aligned nicely with MCSM predictions and placed even further emphasis on the importance of the monopole tensor interaction when describing neutron-rich nuclei [20]. Following this discovery, the search for shape coexistence continued down the Ni isotopic chain, going from ^{70}Ni, possessing an additional two neutrons with respect to the doubly-magic ^{68}Ni, down to ^{66}Ni, a comparable analogue where instead two neutrons are removed (also viewed as a two-neutron hole nucleus with respect to the closed shell ^{68}Ni). Additionally, three excited 0^+ states have been observed in this nucleus, making it another excellent candidate for shape coexistence. While the precise interpretation of the data is still a matter of debate, calculations performed using the Lenzi-Nowacki-Poves-Sieja (LNPS) interaction, which is based on a ^{48}Ca core and allows p-h excitations to $\nu g_{9/2}$ and $\nu d_{5/2}$ orbitals [21, 22], assert that while the third 0^+ state located at 2.671 MeV takes on a spherical nature, the second and fourth 0^+ levels at 2.443 and 2.965 MeV are likely associated with weak oblate and strong prolate deformations, respectively [23]. MCSM calculations and lifetime measurements carried out by Ref. [24] have reinforced this interpretation. Figure 1.3 presents the MCSM calculation of a potential energy surface for ^{66}Ni, where the locations of each

of the four 0^+ states are labeled. The axes indicate the value of the electric quadrupole moment (to be discussed in the following chapter), where a large Q moment is indicative of a well-deformed nucleus. The 60° and 0° lines are associated with oblate and prolate deformations, respectively. One can see from the figure that the first and third 0^+ levels fall within a spherical minimum, while the second and fourth lie within oblate and prolate minima, respectively. Moreover, not only do the excited states in ^{66}Ni make a case for shape coexistence, but properties such as the observed lifetimes and branching ratios also support this hypothesis. Notably, in every observed instance of shape coexistence within the Ni isotopic chain, all prolate structures are interpreted as arising from sizable proton excitations from the $\pi f_{7/2}$ subshell to the $\pi f_{5/2}$ and $\pi p_{3/2,1/2}$ ones, as well as excitations of neutrons from the $\nu f_{5/2}$ and $\nu p_{3/2,1/2}$ orbitals to the $\nu g_{9/2}$ and $\nu d_{5/2}$ states. MCSM calculations predict this pattern to continue in lighter Ni isotopes as well, down to ^{62}Ni. So the mounting evidence for shape coexistence in the Ni isotopic chain motivates exploring the possibility that this phenomenon manifests itself in the most neutron-rich, stable isotope of Ni, ^{64}Ni.

Many experiments have already been carried out in order to illuminate some of the characteristics of the level structure in ^{64}Ni. In one of the most comprehensive experiments on this nucleus, a large data set was obtained for quasi-elastic and deep-inelastic reactions of a 430-MeV ^{64}Ni beam on a thick ^{238}U target. This resulted in the extensive level scheme of Figure 1.4, which was published in Ref. [25].

As can be seen in Figure 1.4, two 0^+ excited states have already been observed in ^{64}Ni at respective energies of 2867 and 3026 keV, both of which decay to the first excited 2_1^+ level via γ rays of 1521 and 1680 keV. However, more information on the collectivity of these states is required if one is to make a determination on the potential for shape coexistence. A model-independent method for probing the collectivity of a nucleus is via the process of Coulomb excitation, in which a target nucleus is bombarded by a projectile at energies below the Coulomb barrier, causing both nuclei to be excited purely through their electromagnetic

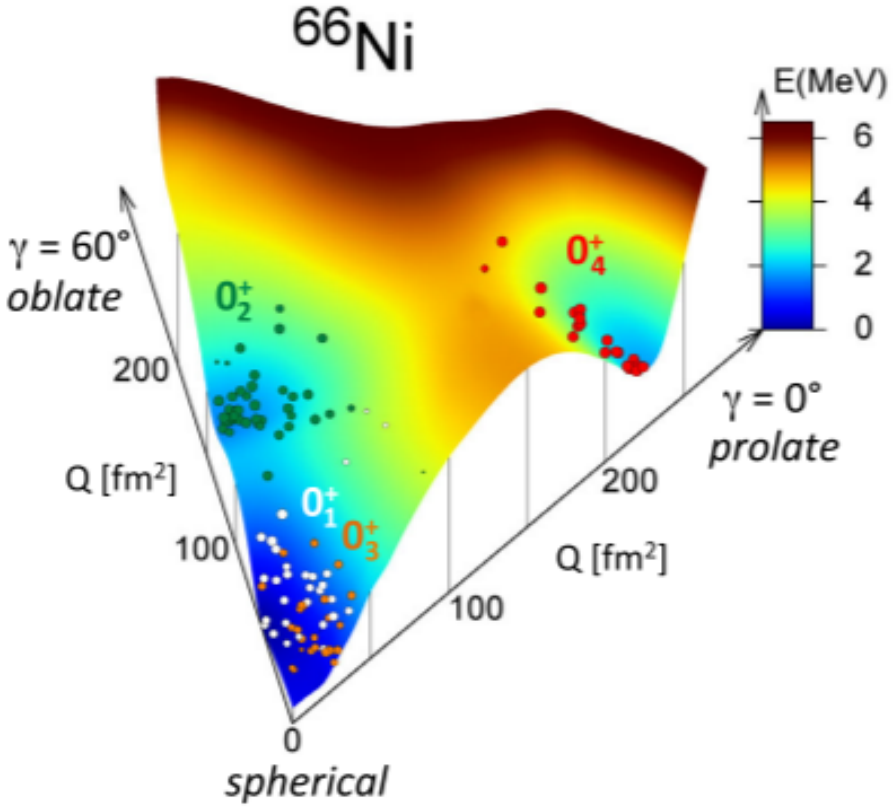

Figure 1.3: A potential energy surface calculated within the MCSM framework for ^{66}Ni. Axes are defined by the electric quadrupole moment, Q, and the axial symmetry parameter of the nucleus, γ. Calculations predict the first and third 0^+ states to lie in a spherical minimum, while the second and fourth are associated with oblate and prolate minima, respectively [24].

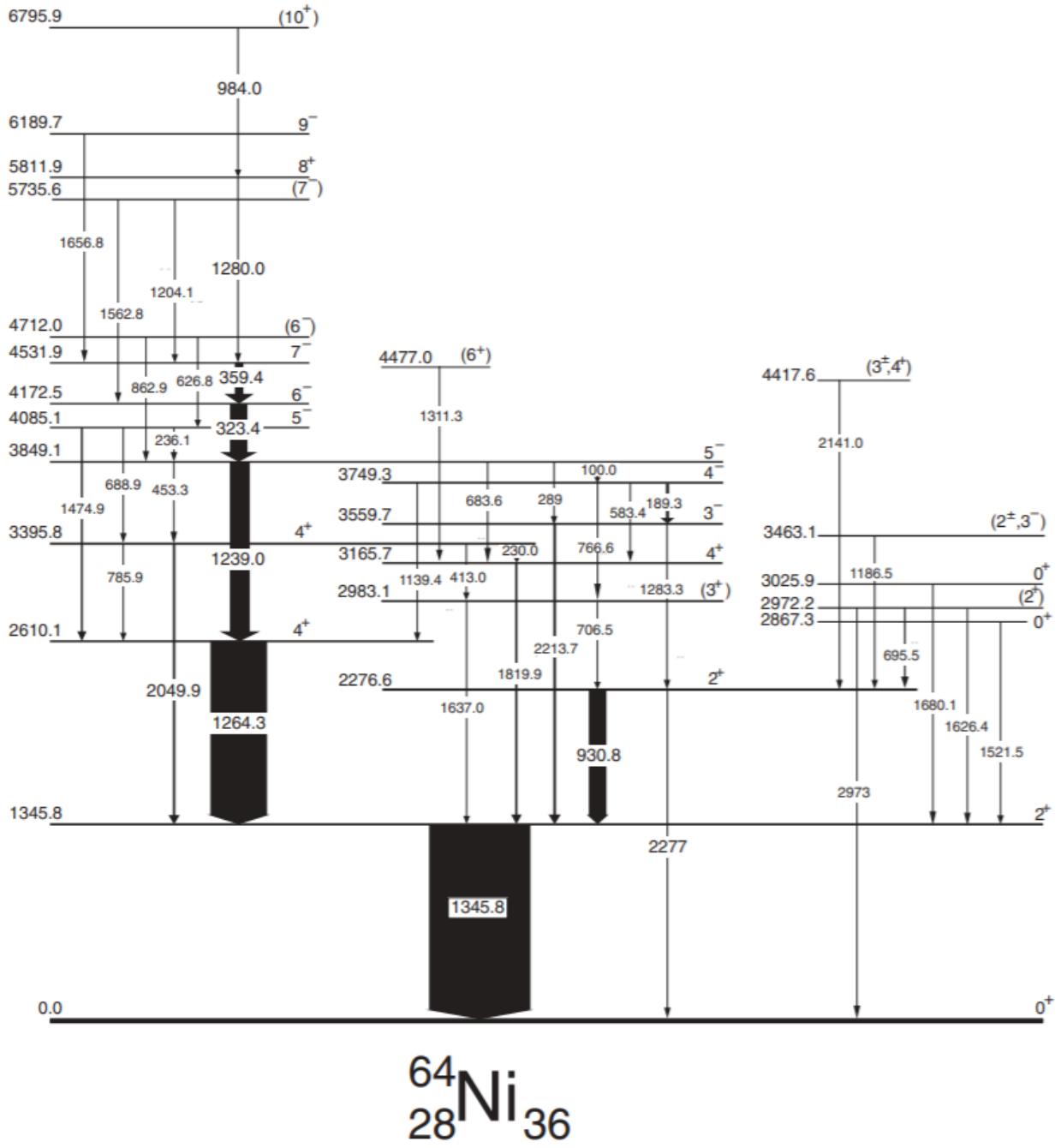

Figure 1.4: Level scheme for ^{64}Ni obtained from deep-inelastic reactions between ^{64}Ni and ^{238}U. As is typical for complex reactions, the states extend to moderately high spin and high energy, and a variety of decay paths are observed, including those associated with the two 0^+ excited states located at energies of 2867 and 3026 keV [25].

interaction. This enables the projectile nucleus to populate many low-lying energy levels, regardless of whether or not they are the lowest-energy states available for a given spin, otherwise known as yrast. This is, of course, especially important for the population of the two previously observed excited 0^+ states in ^{64}Ni, as well as for observation of any possible sequence of states that might be built upon them. Additionally, since these states are populated via a purely electric interaction, their decay proceeds naturally through electric and magnetic multipole transitions. In even-even nuclei, E2 transitions are highly favored, the analysis of which is an indicator of the quadruopole nature and collectivity of the associated states, as discussed later in this dissertation. By studying the quadrupole moments and reduced transition strengths, B(E2), resulting from the decay of these states, we are able to gauge the extent of collectivity and shape deformation in ^{64}Ni. Yet, the extent of existing Coulomb excitation data on ^{64}Ni is severely limited, including only the B(E2) values from the de-excitations of the 2^+ and 4+ yrast states, corresponding to 7.7(3) and 6.6 (1) single-particle units (to be defined in the following theory section), respectively [26]. Clearly, a thorough and comprehensive investigation on the Coulomb excitation of ^{64}Ni must be performed and, thus, an experiment of this type was carried out using the ATLAS facility at Argonne National Laboratory.

In addition to this Coulomb excitation experiment, a supplemental analysis of ^{64}Ni was carried out on a data set obtained from a separate ATLAS measurement, involving the deep-inelastic reaction of ^{48}Ca on ^{26}Mg. In this experiment, a thin ^{26}Mg target was bombarded by a ^{48}Ca beam at energies of 275, 290, and 320 MeV, creating a diverse population of high-spin, high-energy, product nuclei. The prompt γ rays emitted by the de-excitation of these nuclei were detected using the Gammasphere HPGe detector array, while the product nuclei themselves were, subsequently, separated and observed using a high-resolution mass spectrometer device known as the Fragment Mass Analyzer (FMA). These devices are described in a forthcoming chapter. From this experiment, extensive structure information on collectivity in ^{61}Co and ^{62,63}Ni has already been published [27–29]. However, with the FMA,

it was possible to also isolate ^{64}Ni as the species of interest, and produce clean γ-ray spectra for analysis. All observed γ rays were placed in a level scheme, tabulated, and intensities were extracted for each peak in the nucleus of interest. Lastly, a (γ, γ') experiment has also been performed at the HIγS facility at the Triangle Universities Nuclear Laboratory (TUNL) in order to directly populate some of the higher-lying, low-spin states in ^{64}Ni. Analysis of this data set is presently ongoing, and thus it will not be discussed in this dissertation.

The two experiments forming the foundation of this dissertation, Coulomb excitation and deep-inelastic scattering, serve as exceptional complements to one another for the following reasons. Firstly, because "safe" (below Coulomb barrier) Coulomb excitation seeks to avoid nuclear interactions, beam energies must be sufficiently below the Coulomb barrier. This means the states that are populated are often of low-spin and low excitation energy. This approach is necessary when pursuing non-yrast states, such as excited 0^+ levels, which can be difficult to populate with high statistics by other means. Additionally, the inherent nature of Coulomb excitation provides insight into the collectivity and shape of the nucleus through the exploitation of its quadrupole charge distribution and transition strengths. However, this in itself does not provide a comprehensive picture of the nucleus of interest. Deep-inelastic scattering, on the other hand, imparts large amounts of energy and angular momentum to the reaction products, populating a variety of moderately high-spin, high-energy states, which often funnel strength into the ground state via yrast transitions. This provides an extensive view of the level structure of the nucleus, and by examining the variation in peak intensity with respect to angle, the multipole nature of many different transitions can be discerned, allowing one to assign spins to multiple levels. These two experiments offer different views into the nuclear structure of ^{64}Ni, and the combination of them provides a level of insight into this nucleus that has not been achieved previously.

The next chapter discusses the basic nuclear theory underlying this dissertation, followed by an overview of the methodology and tools employed in both experiments. Then the results will be presented and subsequently discussed. Lastly, conclusions are drawn from this work

and the future outlook is addressed.

CHAPTER 2: Theory

In the discipline of nuclear physics, one should theoretically be able to describe the underlying structure of a nucleus based solely upon the nucleons involved and our understanding of the basic nuclear interaction. However, due to the complex nature of the nuclear force, as well as to limitations in computing power, this goal has yet to be realized. Thus, a wide array of nuclear models is employed in order to predict the varying characteristics and structure of all known nuclei. In addition, one would ultimately hope to describe also the exotic nuclei involved in nucleosynthesis processes, such as the rapid neutron capture process (r process). These are located very far from the valley of stability with little or no hope of ever being observed in the laboratory.

Section 2.1: The Nuclear Shell Model

One model of particular importance and efficacy is known as the Nuclear Shell Model. This model, first proposed by Dmitry Ivanenko (together with E. Gapon) in 1932, serves as a good descriptor of nuclei near the line of stability. The underlying assumptions for this model are as follows: individual nucleons move in orbits independent of one another, and operate under the influence of an average potential that represents the interactions of all other nucleons on an individual one. To first order, these assumptions are quite reasonable. One of the main supporting arguments for shell structure within nuclei comes from experimentally determined "magic numbers". These magic numbers, corresponding to N=Z=2, 8, 20, 28, 50, 82, and 126 for neutrons only, represent closed "shells" in a nucleus, and can be obtained through the application of a phenomenological model such as a harmonic oscillator or Woods-Saxon potential.

According to Ref. [30], when deriving the nuclear shell model, we can begin our approach by employing one of the simplest and most commonly used potentials: the harmonic oscillator. The potential for a simple harmonic oscillator is given by

$$U(r) = \frac{1}{2}m\omega^2 r^2 \tag{2.1}$$

where m is the mass of the nucleon and ω is the oscillator frequency. The Schrodinger equation for this potential can be easily solved as the eigenvalues are known analytically [31]. This give a series of regularly-spaced energy eigenvalues,

$$E_n = \bar{h}\omega\left[2(n+1) + l + \frac{3}{2}\right] = \bar{h}\omega\left(N + \frac{3}{2}\right) \tag{2.2}$$

where N is the major oscillator quantum number. These levels are illustrated in Figure 2.1 (a).

An unsuitable aspect of the harmonic-oscillator potential, however, is that it unrealistically approaches infinity at large values of r. This is contradictory to the short-range nature of the nuclear force. A more accurate potential that resolves the problem of an infinite well is known as the Woods-Saxon potential, which is given by

$$V(r) = \frac{-V_0}{1 + exp\frac{(r-R)}{a}} \tag{2.3}$$

where V_0 is the depth of the well, R is the nuclear radius and a is a parameter describing the diffuseness of the surface. This form is chosen for its similarity to the distribution of nucleons due to the short range of the nuclear force. The use of the Woods-Saxon potential lifts the l degeneracy of the harmonic-oscillator states, as depicted in Figure 2.1 (b). Note that states with higher l are shifted lower in energy.

Although the Woods-Saxon potential is more accurate than the harmonic oscillator, the eigenfunctions are not known analytically. For this reason, a harmonic-oscillator potential is often preferred, applying necessary corrections to lift the degeneracy of states with different

l values. This partially mitigates the undesired asymptotic behavior of the potential. This modification is typically made by subtracting a term proportional to l^2, so the potential becomes

$$U(r) = \frac{1}{2}m\omega^2 r^2 - Dl^2 \tag{2.4}$$

The use of either the Woods-Saxon, or the modified harmonic-oscillator potential, results in irregular level spacing where large energy gaps in the sequence correspond to "major shell closures", and the number of nucleons required to fill up to such a gap is referred to as a "magic number". The magic numbers determined by the Woods-Saxon and harmonic-oscillator potential do not agree with those obtained empirically. However, these experimentally-determined magic numbers can be reproduced by adding an *ad-hoc* spin-orbit term to the nuclear Hamiltonian [32, 33]. The spin-orbit term arises from the coupling of the intrinsic and orbital angular momentum vectors "**l**" and "**s**", and is written as

$$\hat{H}_{s.o.} = V_{s.o.}\boldsymbol{l} \cdot \boldsymbol{s} \tag{2.5}$$

where $V_{s.o.}$ is a function related to the potential $U(r)$, often given by

$$V_{s.o.} = -V_{is}\frac{1}{r}\frac{\partial U(r)}{\partial r} \tag{2.6}$$

in which V_{is} is an empirical parameter, usually fitted to known single-particle energies in the mass-region of interest, and is of order $41A^{-1/3}$ MeV. Within the nucleus, each nucleon is subject to equal forces in every direction as a result of having neighboring nucleons on all sides, whereas particles at the surface only experience force from one side. Thus, typical potentials only have a large gradient near the surface, implying this is the only region where the spin-orbit term is significant. This term further lifts the degeneracy of the states, shifting those with higher-j values down and those with lower-j values up, as given by

$$\langle\phi_{nlj}|\hat{H}_{s.o.}(r)|\phi_{nlj}\rangle = \begin{cases} -\frac{1}{2}(l+1)\langle V_{s.o.}\rangle_{nl}, & j_< = l - \frac{1}{2} \\ \frac{1}{2}l\langle V_{s.o.}\rangle_{nl}, & j_> = l + \frac{1}{2} \end{cases}$$

where $\langle V_{s.o.}\rangle_{nl} = \int_0^\infty R_{nl}(r)^2 V_{s.o.} r^2 dr$. The result of applying spin-orbit coupling to a simple nuclear potential is shown in Figure 2.1 (c). Here, the magic numbers agree with those observed experimentally. However, it should be noted that the ordering of orbitals within major shells may have some mass dependence, and may also change under the influence of other nucleon-nucleon interactions, such as those described later in this chapter.

Due to the fact that any mean-field potential is only an approximation of the real system, differences arise between predicted energy levels and those observed experimentally. These differences are known as "residual interactions", and they are expressed as a perturbation to the basic Hamiltonian given in 2.5. A two-body interaction results in a single-particle Hamiltonian of the form

$$\hat{h} = t_i + \sum_{\substack{j=1 \\ j\neq i}}^{A} \omega(\boldsymbol{r}_{ij}) \tag{2.7}$$

where t_i is the kinetic energy of the ith particle and $\omega(\boldsymbol{r}_{ij})$ represents the two-body interaction between nucleons i and j. Therefore the full Hamiltonian is

$$\hat{H} = \sum_{i=1}^{A} t_i + \frac{1}{2}\sum_{i=1}^{A}\sum_{\substack{j=1 \\ j\neq i}}^{A} \omega(\boldsymbol{r}_{ij}) \tag{2.8}$$

where the factor of $\frac{1}{2}$ is necessary to avoid double counting. If the mean central potential is invoked, then the Hamiltonian becomes

$$\hat{H} = \underbrace{\sum_{i=1}^{A}\{t_i + U(r_i)\}}_{\hat{H}_0} + \underbrace{\frac{1}{2}\sum_{i=1}^{A}\sum_{\substack{j=1 \\ j\neq i}}^{A}\omega(\boldsymbol{r}_{ij}) - \sum_{i=1}^{A} U(r_i)}_{\hat{H}'} \tag{2.9}$$

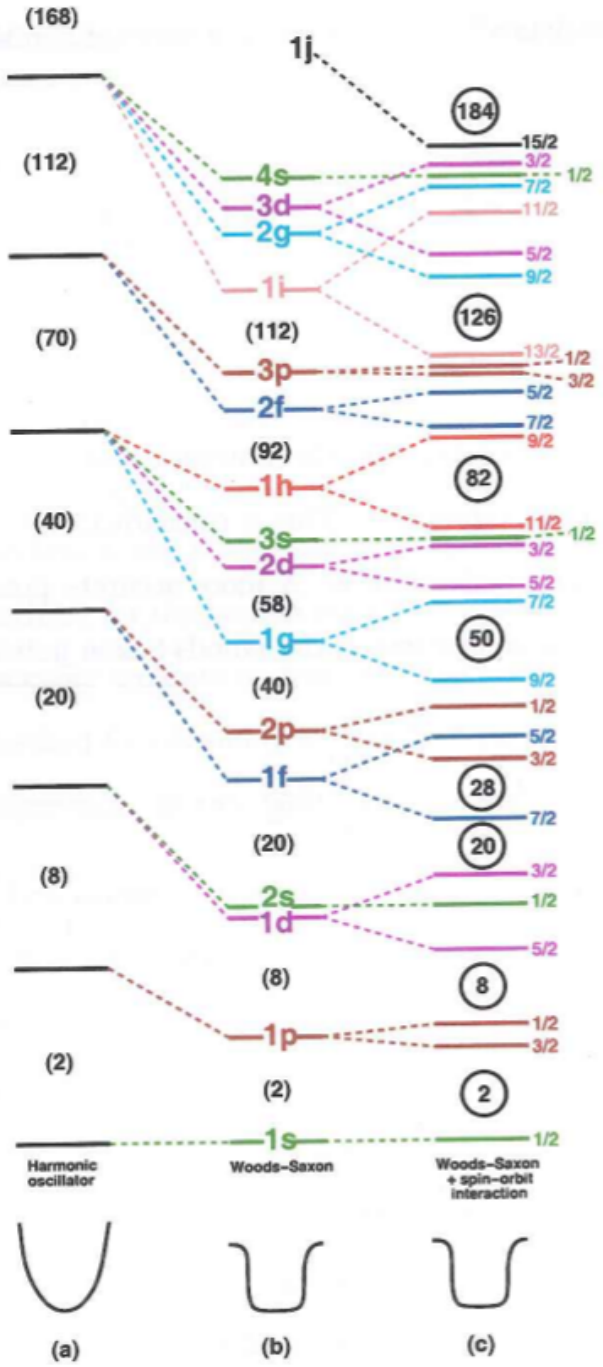

Figure 2.1: [Color] Schematic ordering of single-particle orbitals and "magic" shell gaps reproduced by (a) a harmonic oscillator potential (b) the Woods-Saxon potential and (c) the Woods-Saxon (or modified harmonic oscillator) potential with spin-orbit coupling [34]. Orbitals are color coded according to their l value. Numbers in parentheses indicate magic numbers predicted by the respective potentials, and the circled values coincide with experimentally determined magic numbers along the line of stability. Numbers on the far right-hand side refer to the j of each state after spin-orbit splitting. Each of these orbitals can accommodate $2j + 1$ nucleons of each isospin [30].

Here, $\hat{H}_0$ is the nuclear Hamiltonian for an independent particle, and $\hat{H}'$ is the residual interaction — the difference between the real potential the nucleon actually experiences and the average potential used in the mean-field approximation. In order to accurately reproduce the shell model, these residual interactions are often modified by fitting their matrix elements to experimental levels in nuclei. The resulting interactions are then referred to as "effective" interactions.

Two prominent effective interactions often used for dealing with the *fp*-shell nuclei of interest in the work are discussed here. They are referred to as the GXPF1A interaction, and the jj44pna interaction. The first of these, GXPF1A, is a modified version of the GXPF1 interaction [35], which is based on several methods provided in Refs. [36] and [37]. This interaction employs the entire *fp* model space, which is bounded by proton number Z=20-28, and neutron number N=28-40. Empirical corrections were made in the development of GXPF1(A), consisting of 699 data of binding and excitation energies from 87 nuclei, being $^{47-51}$Ca, $^{47-52}$Sc, $^{47-52}$Ti, $^{47-53,55}$V, $^{48-56}$Cr, $^{50-58}$Mn, $^{52-60}$Fe, $^{54-61}$Co, $^{56-66}$Ni, $^{58-63}$Cu, $^{60-64}$Zn, ^{62,64,65}Ga, ^{64,65}Ge. Meanwhile, the jj44pna effective interaction focuses heavily on the region around $^{68-78}$Ni. This interaction employs the jj44 valence space $(f_{5/2}, p_{3/2,1/2}, g_{9/2})$, taking advantage of the fact that, for nuclei in this region, the spin-orbit interaction pushes the $g_{9/2}$ and $f_{7/2}$ orbitals down, relative to the lower-l orbits. Additionally, the jj44 model space was derived from a fit to experimental data using specifically Ni isotopes from A=*57* to *78*, as well as N=50 isotones from ^{79}Cu to ^{100}Sn, for neutrons and protons, respectively [38]. In other words, one could say that the jj44pna effective interaction specializes in the Ni isotopic chain, particularly with regard to neutron excitations. This makes it an important interaction to consider for ^{64}Ni.

Besides performing shell-model calculations with truncated valence spaces using effective interactions, another method used for reproducing the matrix elements, level energies, and parities is known is the "auxiliary-field quantum Monte Carlo technique", otherwise known as the Monte Carlo shell model (MCSM) technique. This method is unique in that the matrix

elements are determined for the entire model space. Subsequently, Monte Carlo sampling is used to select a small number (30-40) of many-body basis states from the matrix, sufficiently reducing its size. This selection is based upon the coherence of the states, or in other words, the overlap of their wavefunctions. Coherent states, i.e., those with large matrix elements, have been known to give a good approximation, in particular, for low-lying states. Thus, using these coherent states as bases, diagonalization of the nuclear matrix can be performed, providing a good approximation for the space covered by these states [39–41].

In the shell model, all of the aforementioned effective interactions or techniques take advantage of the fact that a magic nucleus, one that possesses proton and/or neutron numbers equal to the magic numbers, can be depicted as a closed shell or core, beyond which one must supply a large amount of energy (several MeV) to generate an excited state. The first excited state found in a magic nucleus is, then, typically associated with the excitation of an individual nucleon across this energy/shell gap. This type of excitation is referred to as a single-particle excitation, and a simple example of this is illustrated in Figure 2.2.

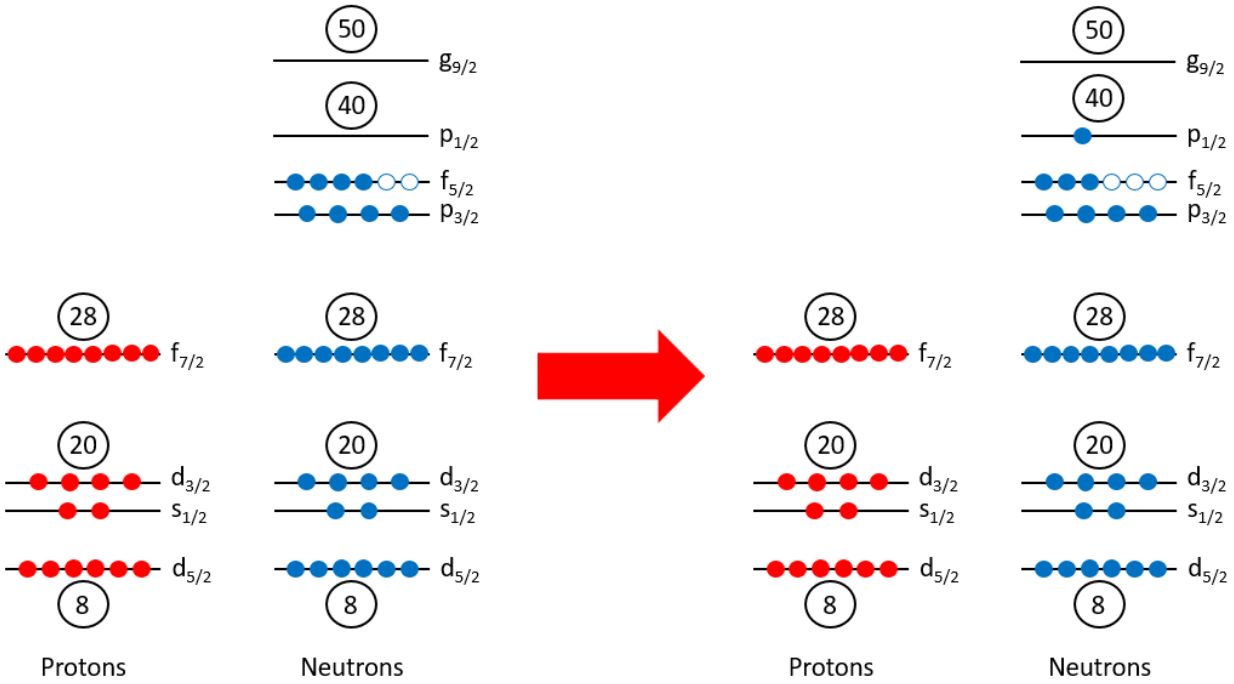

Figure 2.2: An example of a single-particle excitation in a ^{64}Ni nucleus, where a neutron has been promoted to the $\nu p_{1/2}$ orbital, here with creating a hole in the $\nu f_{5/2}$ one.

In the nuclear shell model, nuclei are composed of two separate regions: an inert core of nucleons corresponding to some magic number, and the remaining valence nucleons. This core exerts some average potential upon the valence nucleons, but only the latter particles are treated as being capable of excitation. This means that, in the shell model, every excited state of the nucleus in question is described by the individual (single-particle) and collective excitations of these valence nucleons. For example, shell model calculations of ^{64}Ni (Z=28, N=36) may utilize a $^{56}_{28}\mathrm{Ni}_{28}$ inert core along with 8 valence neutrons populating the $f_{5/2}$ and $p_{3/2,1/2}$ subshells. However, for nuclei like ^{64}Ni, where the N/Z ratio is rather unbalanced, the situation quickly becomes a bit more complex, and the shell structure begins to evolve away from the "simple" one.

Section 2.2: Shell Evolution

The evolution of shell structure as nuclei move away from stability is brought about by the monopole component of a general two-body interaction. Let us begin our explanation of this phenomenon by considering an individual nucleon, characterized by angular momentum j, on top of a doubly-closed shell or core. This nucleon has a single-particle energy denoted as ϵ_j. According to Ref. [42], for the case of a single nucleon and core system, if this nucleon is in the orbit j, the ϵ_j energy then consists of the kinetic energy and the additional contribution from the effects of nuclear forces from all nucleons in the core. This scenario is well-described by the shell model, but as the N/Z ratio becomes more unbalanced, ϵ_j begins to change. Specifically, as extra neutrons are added, ϵ_j develops a slight dependence on the mass number "A" of the nucleus. While this has a mild or even negligible effect on the kinetic energy contribution to ϵ_j, the single-particle energy can still undergo notable changes due to differences in the nuclear interactions as Z or N are altered.

To assess this change, as previously mentioned, we will focus on the monopole component

of a general two-body interaction, $\hat{\nu}$. The monopole matrix element is defined by

$$\nu_m(j,j') = \frac{\sum_{\mu,\mu'}\langle j,\mu,j',\mu'|\hat{\nu}|j,\mu,j',\mu'\rangle}{\sum_{\mu,\mu'}1} \tag{2.10}$$

where j and j' are shorthand notations for the (n, l, j) quantum numbers of the orbit, μ and μ' being the magnetic substates, respectively, and $\langle ...|\hat{\nu}|...\rangle$ standing for the two-body matrix element. The denominator in equation 2.10 is the number of two-particle states. The monopole matrix element is then obtained, for a given pair of orbits j and j', as the average over all possible orientations of the two states $\mu \bigotimes \mu'$. The denominator is then the number of such two-particle states. This reduces the equation to

$$\nu_m(j,j') = \frac{\sum_J (2J+1)\langle j,j';J|\hat{\nu}|j,j';J\rangle}{\sum_J (2J+1)} \tag{2.11}$$

where J is the sum total angular momentum of the two orbits, $\vec{J} = \vec{j} + \vec{j'}$, and $(2J+1)$ is the degeneracy of the two-particle states possessing the same value of J. Using the monopole matrix element from Equation 2.11, one can then derive the monopole component, $\hat{\nu}_m$, of the interaction $\hat{\nu}$. This is referred to as the monopole interaction.

The monopole interaction we discuss here refers predominantly to the interaction between a proton and neutron, and, thus, is given by

$$\hat{\nu}_m = \sum_{jj'} \nu_m(j,j')\hat{n}_j\hat{n}_{j'} \tag{2.12}$$

where orbit j refers to that of a proton and j' is that of a neutron, or vice versa. The total monopole interaction containing this contribution as well as those from neutron-neutron and proton-proton interactions is a significant component of the complete two-body interaction $\hat{\nu}$. The remaining piece is referred to as the multipole interaction, $\hat{\nu}_M$, however it will not be discussed at length here, as the monopole component is far more influential on nuclear shell structure and, specifically, on the phenomenon of shape coexistence.

The most important aspect of the monopole interaction in this context is the effect it

has on the single-particle energy of orbit j due to the occupancy of the orbit j'. When one calculates the expectation value of the operator $\hat{n_{j'}}$, the occupation number of orbital j', with respect to a many-body reference state, one gets

$$\Delta\epsilon_j = \nu_m(j, j')n_{j'} \tag{2.13}$$

where $n_{j'}$ represents the expectation value $n_{j'} = \langle\hat{n_{j'}}\rangle$. This implies that the single-particle energy of the orbit j is altered in proportion to $n_{j'}$ [42, 43]. In other words, the single-particle energy of a proton is affected by the occupation of neutron orbitals and vice versa. This interaction behaves in a similar manner with regard to proton-proton and neutron-neutron cases as well. For a more in-depth explanation of all of the monopole interaction components, refer to Ref. [43]. Combining all of these, the complete expression for the monopole interaction is

$$\hat{\nu}_{mono} = \hat{\nu}_{pp,mono} + \hat{\nu}_{nn,mono} + \hat{\nu}_{pn,mono} \tag{2.14}$$

The direct effect of this interaction, simply put, is that the occupation of orbital j' has the capability of "drawing down" or "pushing up" orbital j. This effect serves as the foundation for shell evolution. Two main types of shell evolution have been identified, aptly referred to as Type I and Type II, with the latter playing a pivotal role in the phenomenon of shape coexistence. We will briefly introduce both of these concepts.

One can see the effects of the monopole interaction by examining a chain of isotopes. By adding more neutrons or protons to an orbit j', the occupation number $n_{j'}$ increases. This results in an effect known as Type-I shell evolution. Above, we discussed the monopole interaction in the context of some general two-body interaction. However, in reality, it is a specific interaction known as the tensor force that drives this phenomenon of attraction and repulsion between occupied orbitals, and it is the monopole component of this force to which we are referring. The predominant origin of the tensor force is the one-pion exchange

process between nucleons, and it can be written as follows

$$V_T = (\vec{\tau}_1 \cdot \vec{\tau}_2)([\vec{s_1}\vec{s_2}]^{(2)} \cdot Y^{(2)})f(r) \tag{2.15}$$

where $\vec{\tau}_{1,2}(\vec{s}_{1,2})$ is the isospin (spin) of nucleons 1 and 2, $[...]^{(K)}$ means the coupling of two operators in the brackets to an angular momentum (or rank) K, Y denotes the spherical harmonics for the Euler angles of the relative coordinate, and the symbol $(\cdot)$ means a scalar product [44]. In addition, $f(r)$ is a function of the relative distance, r. With this we can rewrite the general interaction from Equation 2.11 as one specific to the tensor force

$$V^T_{j,j'} = \frac{\sum_J (2J+1)\langle j, j'|V|j, j'\rangle_{JT}}{\sum_J (2J+1)} \tag{2.16}$$

where $n_{j'} = \langle j, j'|V|j, j'\rangle_{JT}$ stands for the (diagonal) matrix element of a state where two nucleons are coupled to an angular momentum J and an isospin T. We will begin our explanation with an illustration of the basic properties of the monopole interaction through the tensor force, as illustrated in Figure 2.3.

Figure 2.3(a), displays proton orbits and a neutron orbit. Here, the proton states depicted are spin-orbit partners, i.e, they represent different spin states of the same orbit. They are represented by

$$j_> = l + \frac{1}{2}, \qquad j_< = l - \frac{1}{2} \tag{2.17}$$

where l is the orbital angular momentum and $\frac{1}{2}$ is the spin of the proton. The coupling between nucleons of different spin states, $j_<$ and $j'_>$, is attractive for the tensor force, as exemplified in Figure 2.4.

However, the coupling between two nucleons of the same spin state, $j_<$ and $j'_<$, or $j_>$ and $j'_>$, is repulsive. A more elaborate explanation is provided in Ref. [45]. Figure 2.3(b) shows how this force operates with two neutrons situated above the core, occupying the same $j'_>$ orbit. These two neutrons exert an attractive force on the proton of opposite spin (blue

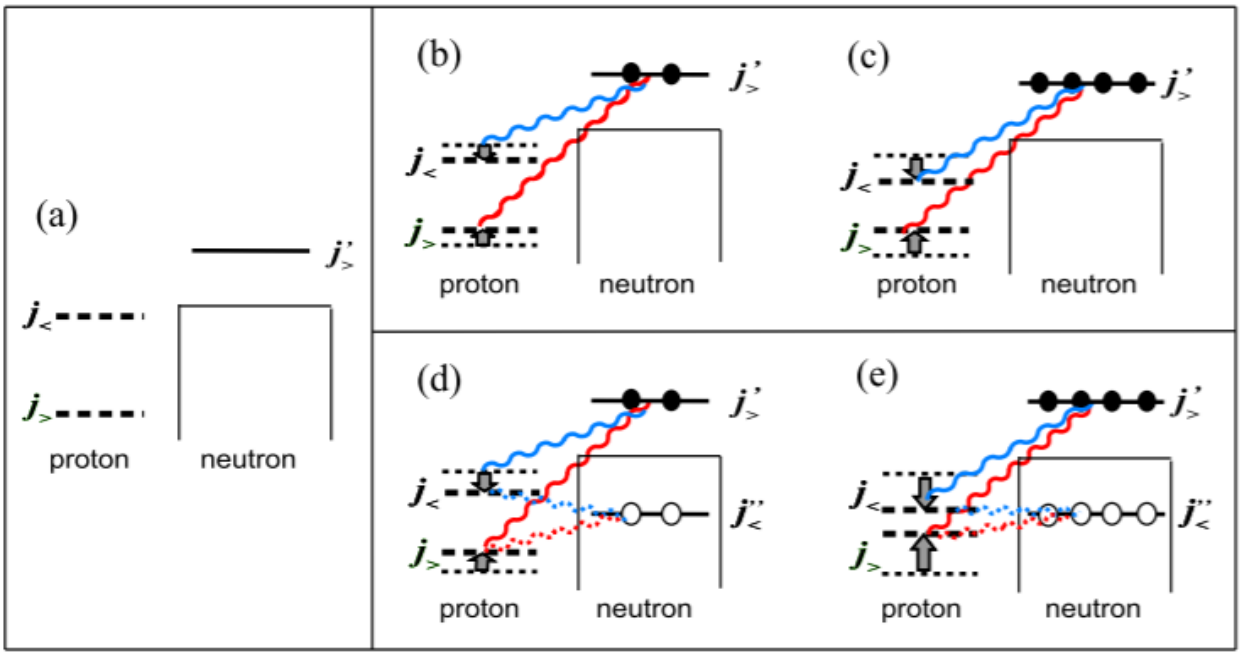

Figure 2.3: Illustration of type I and II shell evolutions, where j and j' represent proton orbits and a neutron orbit, respectively. Blue (red) wavy lines indicate an attractive (repulsive) tensor force. Closed (open) circles denote neutron particle (holes). Short dashed lines depict the initial level of the proton orbital and long dashes indicate the final level. For simplicity, these images focus solely on the effect neutron orbitals have on the spin-orbit splitting of proton orbitals, however, in reality, the reverse mechanism also occurs [42].

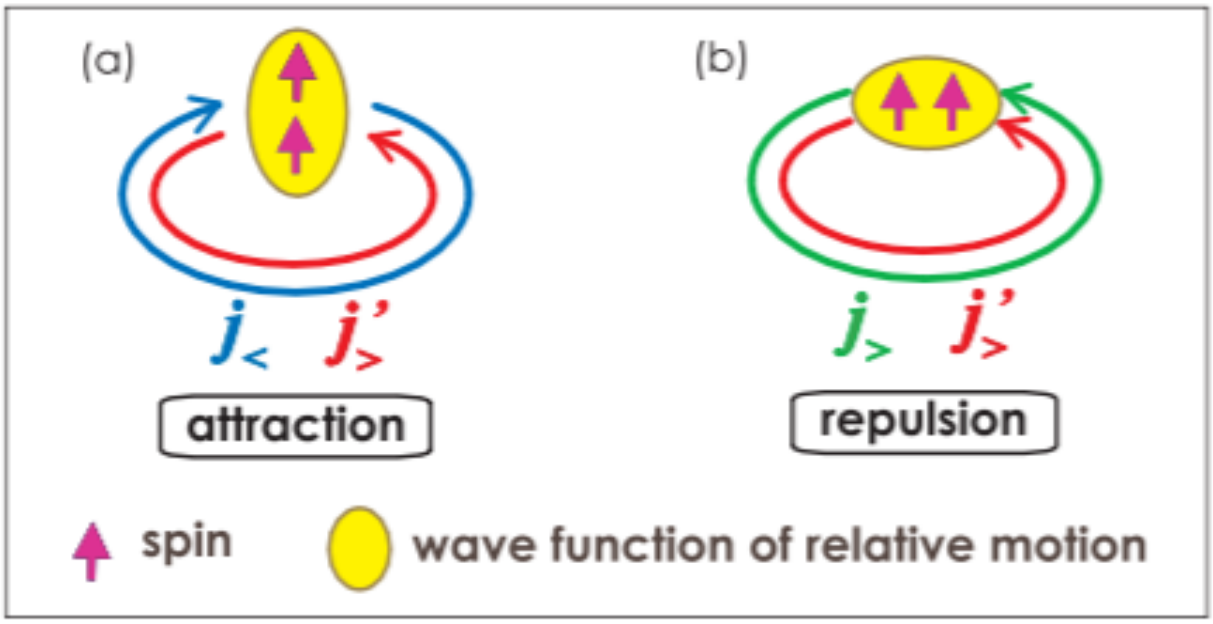

Figure 2.4: The tensor force acting between two nucleons in orbits j and j'. Orbits of the same spin state experience a repulsive force between one another, whereas those of opposite spin states are attracted [44].

wavy line), lowering the single-particle energy of the $j_<$ orbit. Conversely, the single-particle energy of the $j_>$ orbit is raised due the repulsive tensor force (red wavy line). Together, these interactions reduce the effect of spin-orbit splitting. Additionally, since the monopole effect is linear, doubling the neutrons in orbit $j'_>$ doubles the effect expressed in Figure 2.3(b). So as greater numbers of neutrons occupy orbit $j'_>$, the spin-orbit splitting becomes less and less. This is what is known as Type-I shell evolution. It is evident that the main impact of the tensor force is an altering of shell structure that may result in the weakening or even the disappearance of some shell gaps and the appearance of others. Hence, magic numbers are no longer as immutable as once thought.

While we have discussed the effects of the monopole tensor force in reference to valence neutrons and protons, it can also be applied in the context of holes. Just like particles, holes can also exert attractive and repulsive forces upon other nucleons, and it is this interaction that gives rise to Type-II shell evolution. This is depicted in Figure 2.3(d) and (e), where particle-hole pairs are created by exciting neutrons from orbit $j''_<$ to orbit $j'_>$. Identical to

Figure 2.3(b), the neutrons in orbit $j'_>$ act to reduce the spin-orbit splitting. However, the consideration of neutron holes now produces a new phenomenon in that these holes reduce the effect of the tensor force monopole interaction from the fully occupied $j''_<$ orbit. This changes Equation 2.13 to

$$\Delta\epsilon_j = \nu_m(j, j')n_{j'}^{hole} \tag{2.18}$$

where $n_{j'}^{hole}$ stands for the number of holes in orbit $j'_>$. This means that, in Figure 2.3(d), the neutron hole in orbit $j''_<$ lowers the proton $j_<$ state. Conversely, the proton $j_>$ orbit is raised by the neutron particle in orbit $j'_>$ and the neutron holes in orbit $j''_<$. With the addition of these two effects, the reduction in spin-orbit splitting is even starker than in Figure 2.3(b). Thus, the effects of Type-II shell evolution are even more pronounced than those of Type-I, sometimes leading to even more significant changes in nuclear structure. A large spin-orbit splitting tends to make nuclei more spherical, and mitigate deformation [Otsuka 2016]. Thus, a reduction in this splitting, particularly through Type-II shell evolution, catalyzes unique phenomena, among which figures shape coexistence.

Section 2.3: Reduced Transition Probability

Previously, we discussed the idea that excited states in nuclei arise from either single-particle or collective excitations. Type-II shell evolution and shape coexistence can be viewed as collective phenomena brought about by all the nucleons involved, so, if our goal is to identify such phenomena, it is important to our discussion that we make known some signatures of collectivity within nuclei. There are three main indicators of collectivity relative to this work. These signatures are: reduced transition probabilities, quadrupole moments, and band structure. In short, reduced transition probabilities refer to the strength of a transition, quadrupole moments quantify the deformation of a nucleus, and, specific level spacings in band structures can provide a "smoking gun" for deformation and the associated rotation,

or vibration. Each of these will be expounded on in this and the following sections.

One of the most explicit indicators of collectivity is referred to the reduced transition probability, or transition strength, B($\pi\lambda$). Here, π refers to the electric or magnetic nature of a transition and λ indicates its multipolarity. The reduced transition probability is one of the primary characteristics determined from Coulomb excitation experiments. As one might expect, it refers to the strength or readiness of a transition, and is directly related to the lifetime of the de-exciting state. Since many low-lying excited states in even-even nuclei decay via E2 transitions, the quality most often quoted is the B(E2) strength. For single-particle transitions, these B(E2) values are relatively low, corresponding to states with longer lifetimes. On the other hand, the B(E2) strengths associated with the decays of collective states tend to be larger and the lifetimes of these states are correspondingly shorter. A simple way to think about these concepts is the fact that a so-called single-particle excited state, consisting of one particle and one hole, has only one mode of de-excitation available. However, sometimes angular momentum selection rules do not favor this transition, so it may be hindered, preventing the state from decaying quickly. Collective states, on the other hand, arise from multiple particle-hole pairs, and, consequently, numerous possible de-excitation modes may be possible. Nucleons have more freedom to re-organize themselves in an energetically favorable manner to allow for decay, and, thus, these states tend to have shorter lifetimes and higher transition probabilities. Now that we have introduced the concept of the reduced transition probability, let us briefly discuss how this value is obtained from experiments like Coulomb excitation.

Reduced transition probabilities can be derived from a value known as the reduced matrix element, which is often calculated by Coulomb excitation analysis codes such as GOSIA [46] used in this experiment. In simple terms, the reduced matrix element, $\langle\Psi_f||\pi\lambda||\Psi_i\rangle$, indicates the extent of "overlap" between the wavefunctions of an initial and final state. A stronger overlap implies the wavefunctions of the two states are similar, and so the transition between them is more likely. It is referred to as the "reduced" matrix element because it contains

no dependence on the angular momentum substate, m. Coulomb excitation analysis codes perform χ-squared optimizations to calculate these values based on gamma-ray yields, lifetimes, branching and mixing ratios, and other known matrix elements. The reduced matrix element is directly related to the reduced transition probability through

$$B(\pi\lambda)_{\downarrow} = \frac{1}{2J_i + 1}\langle \Psi_f || \pi\lambda || \Psi_i \rangle^2 \tag{2.19}$$

where J_i refers to the initial state before the decay. It is important to note that here we refer to the $B(\pi\lambda)$ "down" strength. Reduced transition probabilities may be calculated in either a "downward" or "upward" direction depending upon which state is considered "initial" and which is "final". For the sake of cross-literature comparison, one may instead be interested in calculating the $B(\pi\lambda)_{\uparrow}$ value. It is possible to convert from $B(\pi\lambda)_{\downarrow}$ to $B(\pi\lambda)_{\uparrow}$ by using the following equation

$$B(\pi\lambda)_{\uparrow} = \frac{2J_i + 1}{2J_f + 1}\, B(\pi\lambda)_{\downarrow} \tag{2.20}$$

where J_i and J_f are defined as the spins of the higher- and lower-lying states, respectively. By default, GOSIA supplies $B(\pi\lambda)_{\downarrow}$ values, as these may be directly converted to an intuitive quantity known as the single-particle (Weisskopf) strengths. Single-particle or Weisskopf strengths are useful in that they provide a rough estimate of how many nucleons are contributing to the radiation emitted by the nucleus, thus allowing one to get an idea of the degree of collectivity of the state. A single Weisskopf transition probability is normalized to the radiation contribution from a single nucleon for a given nucleus. As a result, these estimates are often referred to in terms of Weisskopf "units" or as "single-particle" units. More simply put, one single-particle unit is roughly equivalent to the radiation produced by the transition of a single nucleon from an excited state to the ground state. A single-particle

strength for electric and magnetic multipole transitions, respectively, may be calculated by

$$B(E\lambda; J_i \rightarrow J_{gs}) = \frac{(1.2)^{2\lambda}}{4\pi}(\frac{3}{\lambda+3})^2 A^{2\lambda/3} \;\; e^2(fm)^{2\lambda} \tag{2.21}$$

and

$$B(M\lambda; J_i \rightarrow J_{gs}) = \frac{10}{\pi}(1.2)^{2\lambda-2}(\frac{3}{\lambda+3})^2 A^{(2\lambda-2)/3} \;\; \mu_N^2(fm)^{2\lambda-2} \tag{2.22}$$

where A is the mass number and λ is the multipolarity of the transition. This reduces to the following expressions for the first few values of λ.

$$B(E1; J_i \rightarrow J_{gs}) = 6.446\ 10^{-4}\ A^{(2/3)} \;\; e^2(barn) \tag{2.23}$$

$$B(E2; J_i \rightarrow J_{gs}) = 5.940\ 10^{-6}\ A^{(4/3)} \;\; e^2(barn)^2 \tag{2.24}$$

$$B(E3; J_i \rightarrow J_{gs}) = 5.940\ 10^{-8}\ A^2 \;\; e^2(barn)^3 \tag{2.25}$$

$$B(E4; J_i \rightarrow J_{gs}) = 6.285\ 10^{-10}\ A^{(8/3)} \;\; e^2(barn)^4 \tag{2.26}$$

$$B(M1; J_i \rightarrow J_{gs}) = 1.790\ (\frac{e\hbar}{2Ac})^2 \tag{2.27}$$

By dividing all experimental reduced transition strengths, $B(\pi\lambda)_{\downarrow}$, by the appropriate value for a single-particle estimate, one obtains an intuitive measure of the collectivity of that particular transition in Weisskopf units. These units are useful for gauging collectivity due to the fact that, by definition, single-particle excitations are often no more than a few Weisskopf units. Thus, at a glance, one can get a feel for the collectivity of a nucleus and easily compare across different isotopes. Reduced transition probabilities are one of the few

ways to explicitly probe the collectivity of a nucleus, making them very valuable for tracking down instances of shape coexistence. However, one cannot draw an accurate conclusion with regard to shape coexistence based solely on reduced transition probabilities.

Section 2.4: Electric Quadrupole Moments

The second signature of collectivity in a nucleus comes from a quantity known as the nuclear electric quadrupole moment. Like it sounds, the electric quadrupole moment value quantifies the shape of the quadrupole component of the electric field produced by the nucleus. By obtaining these values, it is possible for one to explicitly determine the extent of deformation within a nucleus. Just like the reduced transition probabilities, the electric quadrupole moments may be calculated directly from the nuclear matrix elements, but the nomenclature surrounding quadrupole moments can be somewhat complicated, so it is important that a few terms be defined first. There are typically four types of electric quadrupole moments that are referred to in literature; these are transition and static, and spectroscopic and intrinsic. Let us begin by defining "transition" and "static" quadrupole moments. Looking at a table of nuclear matrix elements, there are off-diagonal elements that correspond to transitions between two different states, and then there are diagonal elements, that represent transitions between m-substates of a single level. The quadrupole moments calculated from these off-diagonal matrix elements are aptly referred to as "transition" quadrupole moments. The transition quadrupole moment is related to the B(E2) through

$$Q_t(J) = \left(\frac{16\pi}{5} \times \frac{B(E2)_{\downarrow}}{\langle J2(J-2)|K0K\rangle} \right)^{1/2} \tag{2.28}$$

where $\langle J2(J-2)|K0K\rangle$ represents the Clebsch-Gordon coefficient associated with the appropriate angular momentum coupling, and J refers to the higher spin state. Using Equation

2.19, this can be rewritten in terms of the matrix element as

$$Q_t(J) = \sqrt{\frac{16\pi}{5}} \frac{1}{\sqrt{2J+1}} \frac{\langle \Psi_f || E2 || \Psi_i \rangle}{\sqrt{\langle J2(J-2)|K0K\rangle}} \tag{2.29}$$

where Ψ_i and Ψ_f refer to the wavefunctions of the initial and final states, respectively. It is worth mentioning that the transition quadrupole moment, Q_t, is not often utilized, likely due to the more convenient nature of the B(E2) strength itself. However, reduced transition probabilities do not exist for diagonal matrix elements, and thus, the quadrupole moments associated with these quantities are especially useful. The quadrupole moments calculated from diagonal matrix elements are often called "static" quadrupole moments because they do not refer to a transition between different nuclear levels, but only to substates of the same level. This phenomenon of change in the population of m substates is known as the "reorientation effect". Both of these quantities, transition and static quadrupole moments, may be considered either spectroscopic or intrinsic, but from this point forward we will refer solely to static quadrupole moments for simplicity. Whether a quadrupole moment is spectroscopic or intrinsic simply depends upon the reference frame in which it is calculated. The "spectroscopic" quadrupole moment is the quantity typically measured experimentally, and describes the overall deformation of the nucleus as measured in the laboratory reference frame. For a transition between substates, i.e, a static moment, equation 2.29 reduces to the following

$$Q = \sqrt{\frac{J(2J-1)}{(J+1)(2J+3)(2J+1)}} \sqrt{\frac{16\pi}{5}} \langle \Psi_f || E2 || \Psi_i \rangle \tag{2.30}$$

where Q is the spectroscopic quadrupole moment. It is important to note that the above expression may differ by a factor of $\sqrt{2I+1}$ depending upon different conventions related to the Wigner-Eckhart theorem. One final quantity of particular significance is known as the intrinsic quadrupole moment, Q_0, that is simply the quadrupole moment as measured in the rest frame of the nucleus, i.e., rotating with the axis of symmetry. This quantity is

especially useful for comparisons due to the fact that it is not dependent upon the spin of the state. The static intrinsic quadrupole moment is related to the matrix element via

$$eQ_0 = \sqrt{\frac{16\pi}{5}} \frac{1}{\sqrt{2J+1}} \frac{\langle \Psi_f || \pi\lambda || \Psi_i \rangle}{\langle JK20|JK \rangle} \tag{2.31}$$

in which $\langle JK20|JK \rangle$ represents the Clebsch-Gordon coefficient associated with an E2 transition between different substates of the same state (i.e., the reorientation effect). This may be approximated by

$$eQ_0 = \sqrt{\frac{16\pi}{5}} \langle \Psi_f || \pi\lambda || \Psi_i \rangle \tag{2.32}$$

Furthermore, a positive intrinsic quadrupole moment is indicative of a prolate deformed nucleus, while a negative one is associated with an oblate shape. It is important to assert another distinct difference between spectroscopic and intrinsic quadrupole moments at this juncture. That is, if one rotates an intrinsically prolate nucleus about an axis perpendicular to its axis of symmetry, one obtains a time-averaged distribution that is oblate. In other words, a prolate (oblate) nucleus is associated with a positive (negative) intrinsic quadrupole moment, but a negative (positive) spectroscopic quadrupole moment. More simply put, $Q_0 > 0$ implies $Q < 0$, and vice versa. This is illustrated in Figure 2.5. Intrinsic quadrupole moment values greater than one or two are typically associated with a deformed nuclear shape and positive values indicate a prolate deformation while negative ones imply an oblate shape. Table 2.6 from [47] gives an indication of what sorts of intrinsic quadrupole moments are expected for spherical versus deformed nuclei. Ref. [47] states that most spherical nuclei have intrinsic quadrupole moments that fall within the 0.06-0.5 eb range. Beyond 0.5 eb, nuclei tend to be more deformed, with a typical deformed nucleus possessing an intrinsic quadrupole moment value of over 1 or 2 eb. Thus, by examining the quadrupole moment of a nucleus, one can readily gauge the nuclear deformation, an important indicator of collectivity.

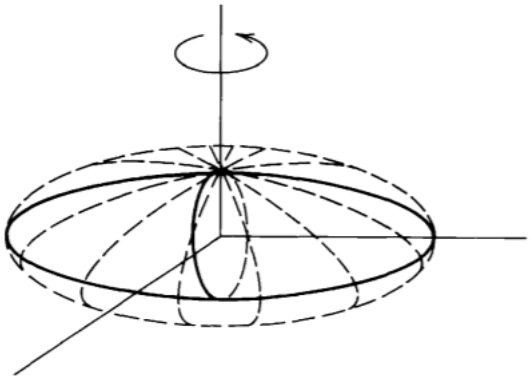

Figure 2.5: An illustration of how the time-averaged distribution of an intrinsically prolate nucleus appears oblate [47].

Nuclide	Q (b)
^{2}H (D)	+0.00288
^{17}O	−0.02578
^{59}Co	+0.40
^{63}Cu	−0.209
^{133}Cs	−0.003
^{161}Dy	+2.4
^{176}Lu	+8.0
^{209}Bi	−0.37

Figure 2.6: Typical expected values for intrinsic quadrupole moments, Q_0 (labeled Q(b) above). The values associated with ^{161}Dy and ^{176}Lu are indicative of deformed and superdeformed nuclei, respectively [47].

Section 2.5: Band Structures

The final hallmark of collectivity only applies to deformed nuclei (and collective motion), and has to do with the nuclear level structure itself. Energy levels within a nucleus are often organized into γ-ray cascade sequences. This roughly means that the γ rays that are emitted in series with one another are typically grouped together, and these sequences are usually characterized by descending spin and are associated with similar wavefunctions (shapes). One of these sequences is naturally associated with the ground state of the nucleus. For even-even nuclei, it's normal to expect a ground state with spin and parity 0^+ because of the pairing force coupling nucleons two-by-two to $I^\pi = 0^+$. In a sequence that is associated with a spherical shape, such as the one beginning with the ground state in a typical even-even nucleus, the spacings between these states, as well as the spins associated with them, are often irregular and difficult to predict. Additionally, spherical sequences often exhibit a variety of multipole transitions, such as E1, M1 and E2, as well as both states with "-" and "+" parities. Lastly, as previously stated, the transitions within these non-collective sequences have typical reduced transition probabilities of only a few Weisskopf units. A prime example of a single-particle nucleus is illustrated with ^{146}Gd in Figure 2.7.

When a nucleus is excited, however, it can manifest a variety of sequences. There exist several different types of structures besides spherical sequences that possess very unique characteristics. When a deformed nucleus is excited via rotational modes, rotational symmetry is broken, and the nucleus will exhibit distinct level structures. These unique, deformed sequences are referred to as rotational "bands", and they stand in stark contrast to spherical sequences for a few reasons. Firstly, as opposed to spherical sequences, rotational bands exhibit a very distinct spacing between energy levels. This is because the energies of the states in a rotational band are all characterized by the equation

$$E = \frac{\bar{h}^2}{2I} J(J+1) \tag{2.33}$$

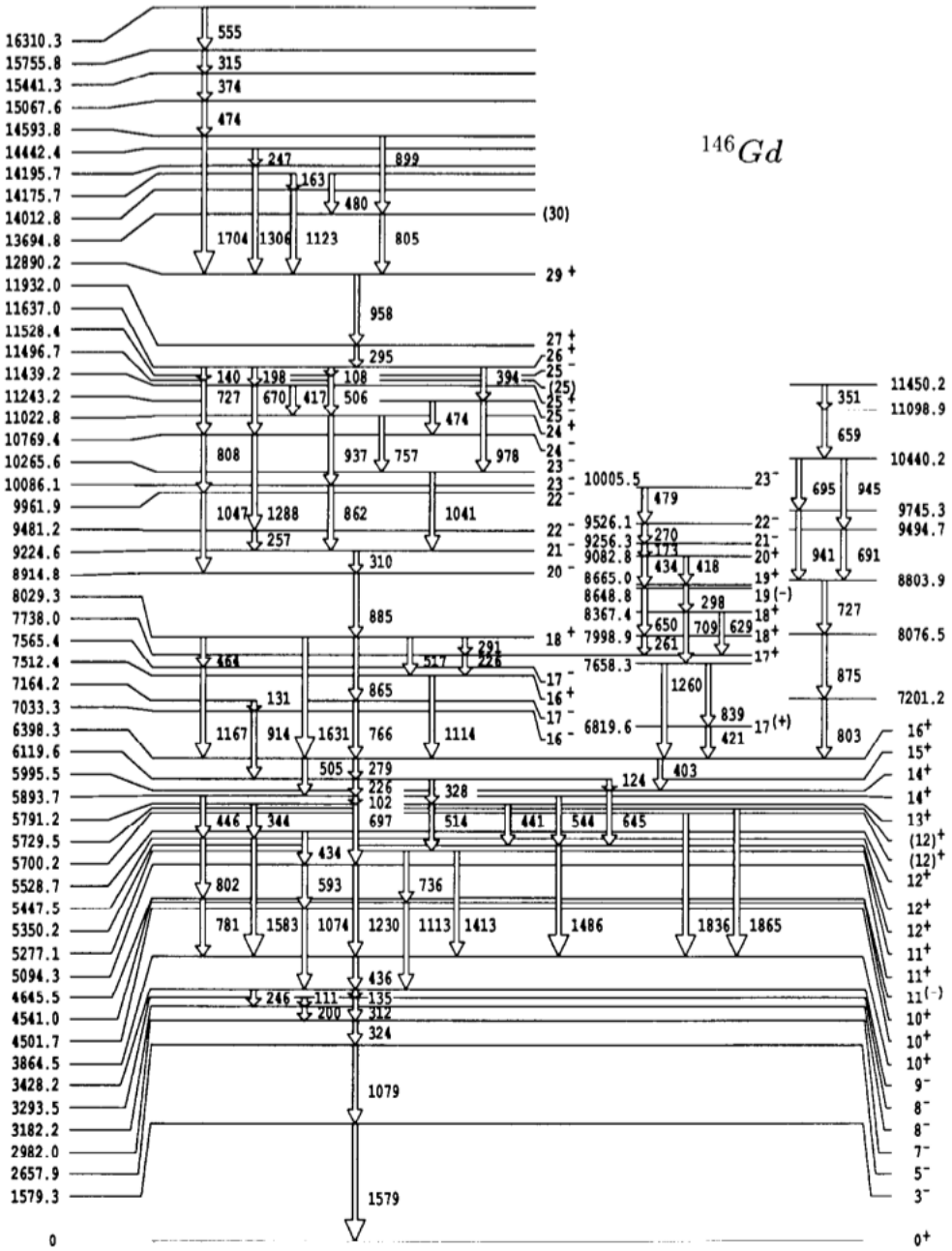

Figure 2.7: An example of a typical single-particle, spherical nucleus. Note the irregularity of the energies, spins, and parities associated with each level [48].

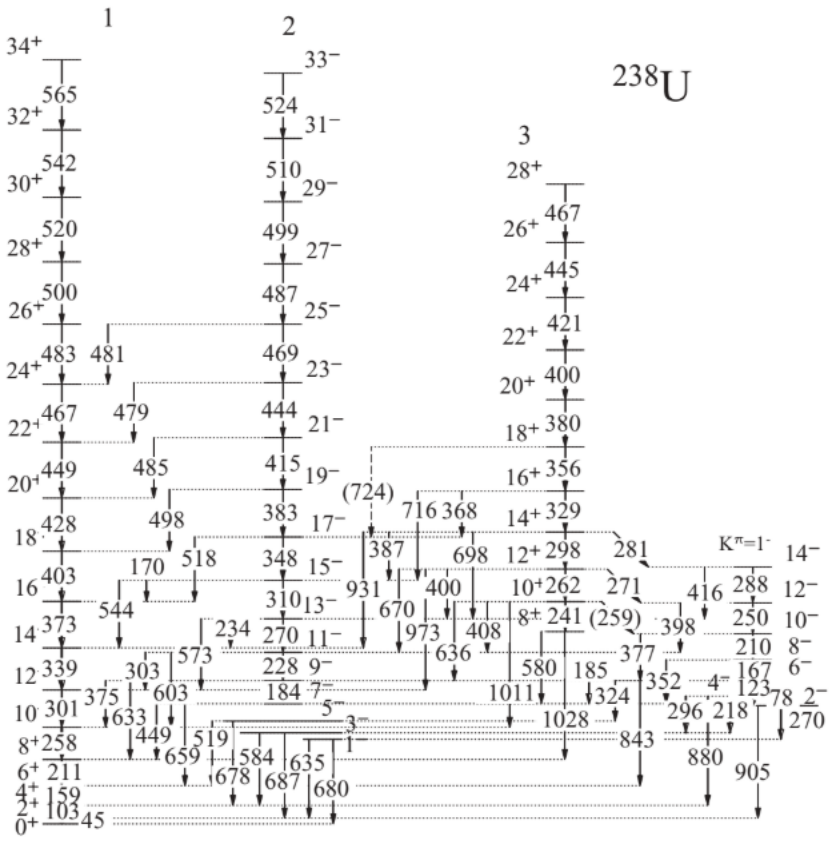

Figure 2.8: Illustration of rotationally deformed bands in ^{238}U [49].

where I is the moment of inertia and J is the spin of the level. This produces an easily recognizable γ-ray spectrum with a "picket fence"-like appearance. Examples of a spectrum and level scheme associated with typical rotational deformation are illustrated by a ^{238}U nucleus in Figures 2.8 and 2.9, respectively, while a superdeformed nucleus, ^{152}Dy and its associated spectrum are depicted in Figures 2.10 and 2.11. Secondly, rotational bands stand apart from spherical sequences because they are dominated specifically by E2 transitions with large reduced transition strengths, indicative of collectivity.

These easily distinguishable rotational structures, when observed, are "smoking guns" for nuclear collective motions and, thus, also serve as good indicators for shape coexistence.

Another somewhat common collective excitation available to nuclei is known as a vibrational excitation mode. Vibrational bands can often be more difficult to recognize and extract from amongst other structures due to being more complex than rotational ones, however,

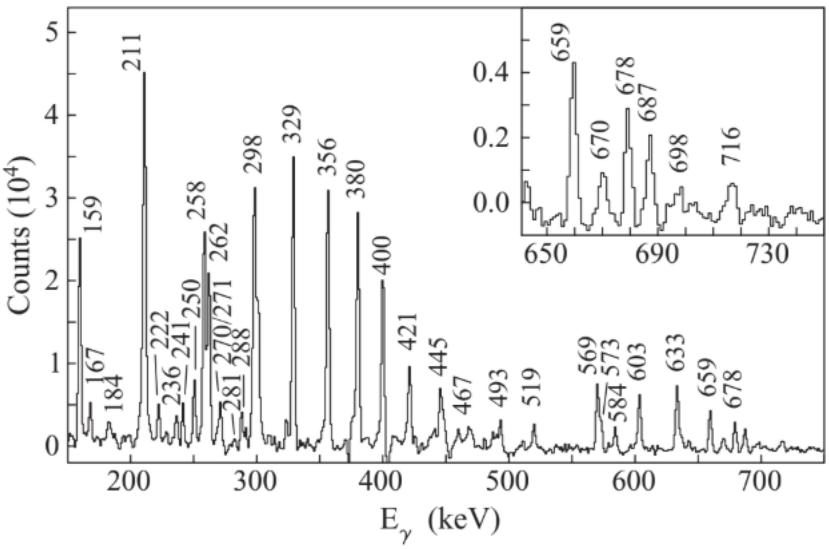

Figure 2.9: Picket-fence spectrum observed in ^{238}U [49].

vibrational symmetry breaking also has its own interesting signature. These modes arise from phonon excitations within the nucleus and manifest themselves differently depending upon the type of vibration. Quadrupole vibrational bands typically exhibit a 0^+ bandhead with a 2^+ state lying some energy E above it. This 2^+ level arises from a single phonon excitation. The next states in the band are brought about by two-phonon excitations. Here, level splitting results in states of spin 0^+, 2^+ and 4^+, depending on the spin orbit coupling, all lying at an excitation energy of roughly $2E$. A three-phonon excitation is then located higher, at an energy of roughly $3E$, with states exhibiting spin values from 0^+ to 6^+ in increments of 2, and so on. Additionally, a separate type of vibrational mode known as an octopole vibration possesses a 3^- spin state as the one-phonon excitation, and is expected to have a quartet of states (0^+, 2^+, 4^+, and 6^+) associated with its two-phonon excitation. One well-known example of such a vibration is found in ^{208}Pb, although only one level associated with the two-phonon excitation has so far been observed in this nucleus [52]. However, in this case the one-phonon 3^- level is actually the first excited state.

The observation of 0^+ excited states in nuclei, such as those seen in ^{64}Ni, suggests the possibility that these states may form the head of some collective band. This is why excited 0^+ levels are considered hallmarks of shape coexistence. In order to determine this, however,

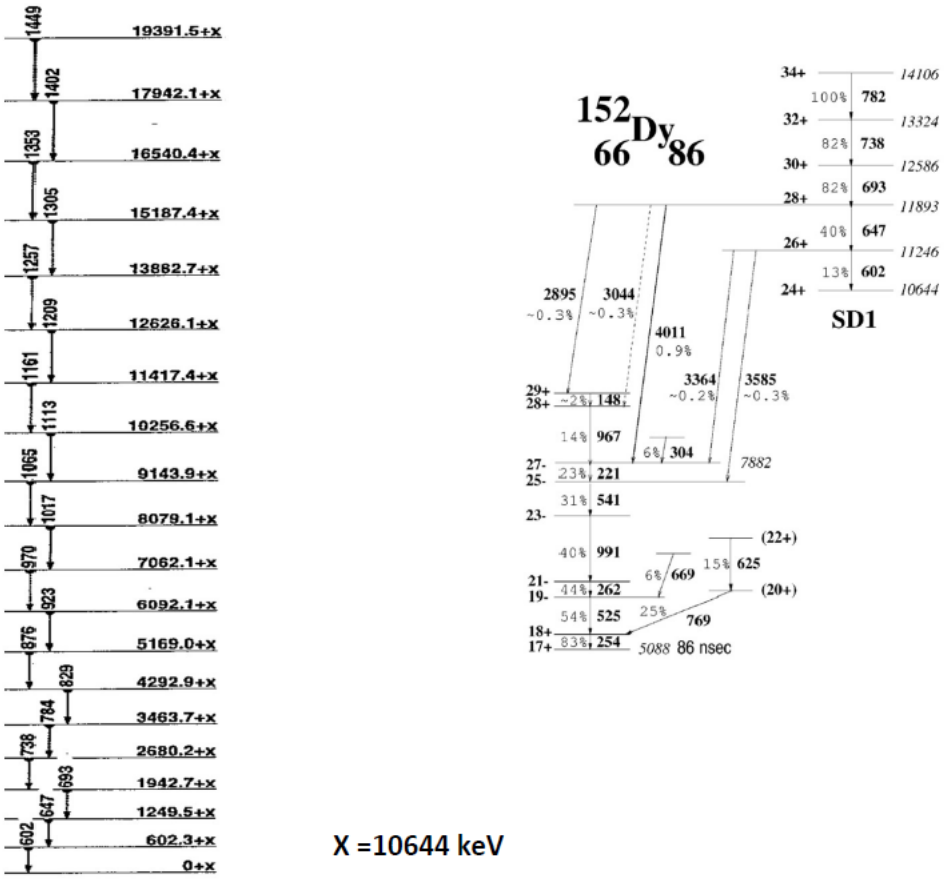

Figure 2.10: (Left) Depiction of a superdeformed rotational band in ^{152}Dy. (Right) The same superdeformed band de-excites into a sequence of irregularly spaced states associated with single-particle excitations [50].

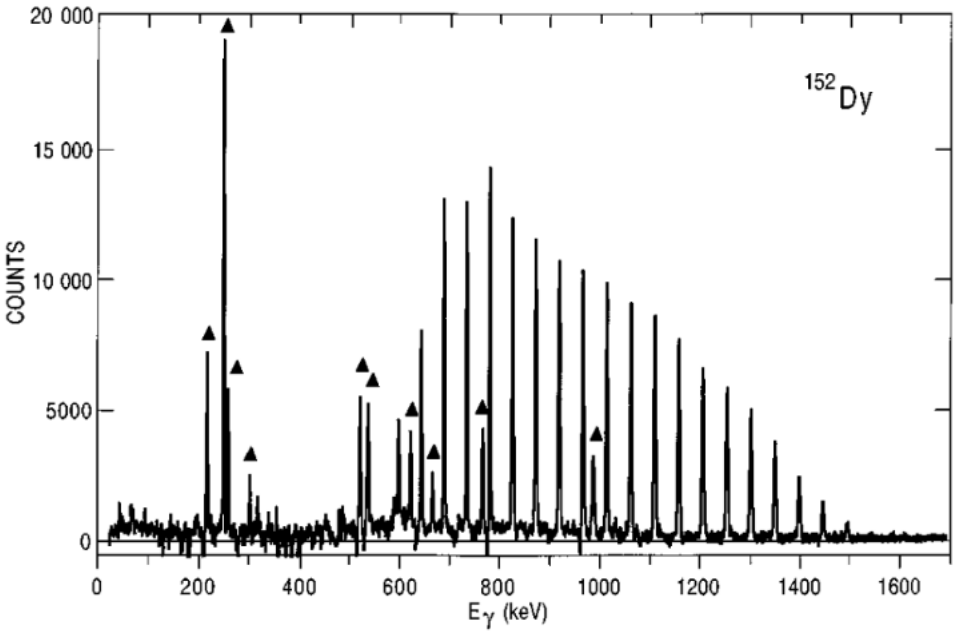

Figure 2.11: Picket-fence spectrum produced by a superdeformed rotational band in ^{152}Dy. Peaks marked with triangles correspond to transitions that are not members of the rotational band [51].

one must probe further above those states in order to examine the higher-spin structure. The pursuit of this higher-lying collective structure is one of the main investigative priorities behind the experiments discussed in this work, along with ascertaining the aforementioned reduced transition probabilities and quadrupole moments. In theory, all three of these quantities can be observed through the process of Coulomb excitation, but as an extra measure, using data from the deep-inelastic experiment allows one to penetrate higher into the ^{64}Ni level scheme, which is useful when attempting to map out collective bands. The following chapter discusses the methodology of both experiments, as well as the specifics of the techniques and tools used in both.

CHAPTER 3: Methods

In this chapter, the methodology of both experiments, the Coulomb excitation measurement and the study following a deep-inelastic reaction, will be discussed. Multi-step Coulomb excitation of ^{64}Ni was performed at the ATLAS facility at Argonne National Laboratory (ANL), where a 0.5 mg/cm^2, isotopically-enriched ^{208}Pb target, with a 6 μg/cm^2 Al front layer and a 40 μg/cm^2 C backing, was bombarded by a ^{64}Ni beam at an energy of 272 MeV, a value 14% below the Coulomb barrier. The ^{64}Ni beam was provided by the Argonne Tandem Linear Accelerator System (ATLAS) and delivered to the target with a charge state of Q=13$^+$ and an intensity of around 26 electrical nanoAmps (enA) or 2 particle nA (pnA). The RF pulse of the accelerator occurred once every 82 ns, a number corresponding to the fundamental acceleration frequency of ATLAS. The choice of ^{208}Pb as a target is significant in this, as well as in other Coulomb excitation experiments, for multiple reasons. Firstly, the high-Z value of Pb provides a strong electric field, allowing for greater excitation probability of the projectile nucleus. Next, the lowest-lying energy level in ^{208}Pb is a 3$^-$ state, which has a relatively small B(E3) value associated with it, making it more difficult to excite; i.e., the corresponding cross section is relatively small when compared to that for states in ^{64}Ni. Third, this state is located at a comparatively high energy of 2614 keV, meaning that the γ rays emitted by the excitation of this 3$^-$ state will not significantly "contaminate" the total γ-ray spectrum. Lastly, due its large mass, ^{208}Pb achieves a recoil velocity starkly different from that of ^{64}Ni in the inelastic scattering process and this is useful for particle identification. A thin target was essential for this experiment in order to enable both target and projectile nuclei to escape and, subsequently, be detected and used for particle identification. Additionally, it is important to choose a projectile energy well below the Coulomb barrier such that nuclear effects can be ignored and the interaction can be postulated to

be purely electromagnetic. This is known as the "safe Coulex" technique, as opposed to "unsafe" or "relativistic" Coulomb excitation, which is performed at above-barrier energies [53–55]. The γ rays of interest were detected using the GRETINA tracking array [56] operated in coincidence with the two reaction partners observed by the CHICO2 compact heavy-ion counter [57]. At the time of the experiment, 12 GRETINA modules or so-called "quads" were available, providing a total of 48 highly-segmented coaxial HPGe detectors (see below for further description). These detectors were first calibrated in energy using a ^{88}Y γ-ray source and efficiency calibrations were carried out using ^{152}Eu, ^{56}Co, and ^{243}Am sources. The CHICO2 avalanche counter is composed of two hemispheres, each containing 10 position-sensitive, parallel-plate avalanche counters (PPACs) arranged symmetrically around the beam axis. However, during this experiment, 2 of the 20 avalanche counters were inoperable, leading to a reduction in efficiency. These two problematic detectors were placed at forward angles. Due to the fact that the statistics collected in forward detectors already dwarfs that observed in the rear ones, and because rear angles are associated with a wider variety of excitation modes, due to a greater degree of interaction between the target and projectile nuclei, this deficiency was not considered to be a significant issue.

In this experiment, an event is defined by the coincidence of both reaction partners, ^{64}Ni and ^{208}Pb, detected in CHICO2, alongside at least one γ ray observed in GRETINA. Naturally, the γ rays produced by the reaction are always detected prior to the ions, but the signals from these interactions are significantly delayed as they are required to pass through GRETINA's complex electronics. Thus, the particle energy and timing information must also be delayed such that it arrives at the data acquisition system (DAQ) contemporaneously with the signals produced by the γ rays. Then, by operating GRETINA as a "slave" to CHICO2, all γ rays not in coincidence with the ions of interest are ignored, significantly reducing the background and the random coincidence events. The trigger rate for GRETINA during this measurement was around 1500 events per second. Since all γ rays observed in coincidence with both reaction partners were recorded, in order to obtain a clean ^{64}Ni spectrum, it was

necessary to isolate those originating from the nucleus of interest. In order to achieve this, a time-of-flight spectrum for the reaction partners was generated using CHICO2. By delaying the signal from the RF pulse of the accelerator, this could be used as a timing gate for the ions of interest. Then, the time-of-flight (ΔT_{tof}) of each reaction product could be measured with respect to the delayed RF pulse, making it possible to discriminate between ^{64}Ni and ^{208}Pb ion species. In this experiment, a timing resolution (FWHM) of roughly 1.7 ns was achieved for CHICO2. This is ascertained from Ref. [57] in which a similar experiment was performed with ^{72,76}Ge beams on a ^{208}Pb target. A time-of-flight spectrum depicting the FWHM of recoiling ^{208}Pb from a ^{72}Ge beam is provided by Figure 3.1. The present limitation on timing and position resolution is mainly due to the target thickness, as well as to the intrinsic resolution of CHICO2. In addition, an average timing resolution of 9 ns (FWHM) was achieved for GRETINA in this experiment. This resolution was determined in Ref. [56], by measuring the time difference between crystal-crystal pairs in a module, using the two coincident γ rays, of 1173 and 1333 keV, from a ^{60}Co source. Lastly, the mass of each reaction partner may be calculated with the assumption of two-body kinematics using the equation

$$m_1 = \frac{\Delta_{TOF_{1,2}} + (d_2/P_2)M_{tot}}{(d_1/P_1) + (d_2/P_2)} \tag{3.1}$$

where $\Delta_{TOF_{1,2}}$ is the time-of-flight difference for the two nuclei, d_1 and d_2 are the two flight paths, and P_1 and P_2 are the reaction partners' momenta. Using a calculated mass spectrum, the FWHM for the mass of the incident particles can be ascertained. Examples of such spectra are illustrated in Figure 3.2. It can be seen that the angular and time resolution of CHICO2 result in a mass resolution, $\Delta m/m$, of roughly 5%, which is sufficient to resolve nuclei of similar masses, such as the ^{238}U and ^{208}Pb nuclei shown in this example. Further specifics on GRETINA, the CHICO2 particle detector, and the data analysis techniques are documented in the following sections.

In addition to the Coulomb excitation experiment, a study of complex reactions was also

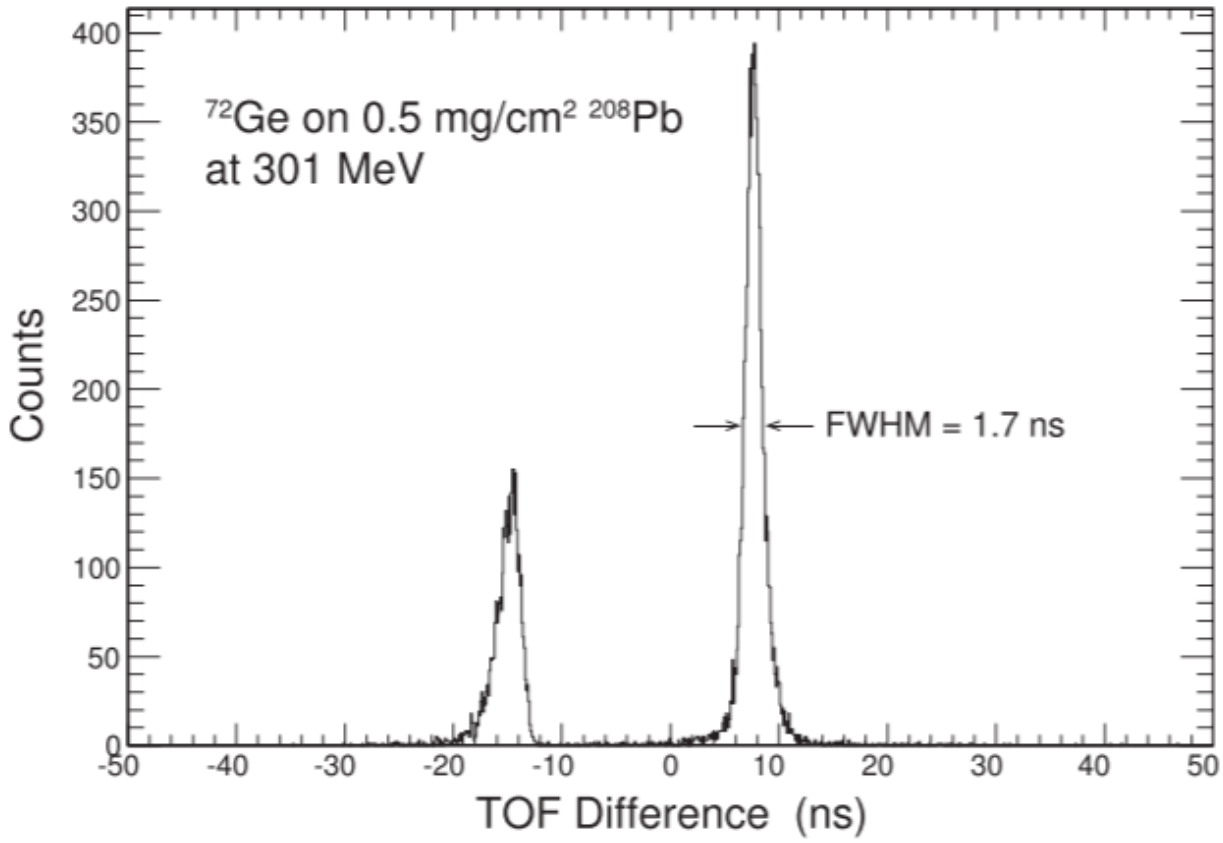

Figure 3.1: Spectrum of projected time-of-flight difference for the CHICO2 parallel-plate avalanche counters (PPACs). The peak on the right is associated with ^{72}Ge, while the one on the left corresponds to ^{208}Pb. A time resolution (FWHM) of 1.7 ns was achieved for our experiment as well, due to the similar masses of ^{72}Ge and ^{64}Ni [57].

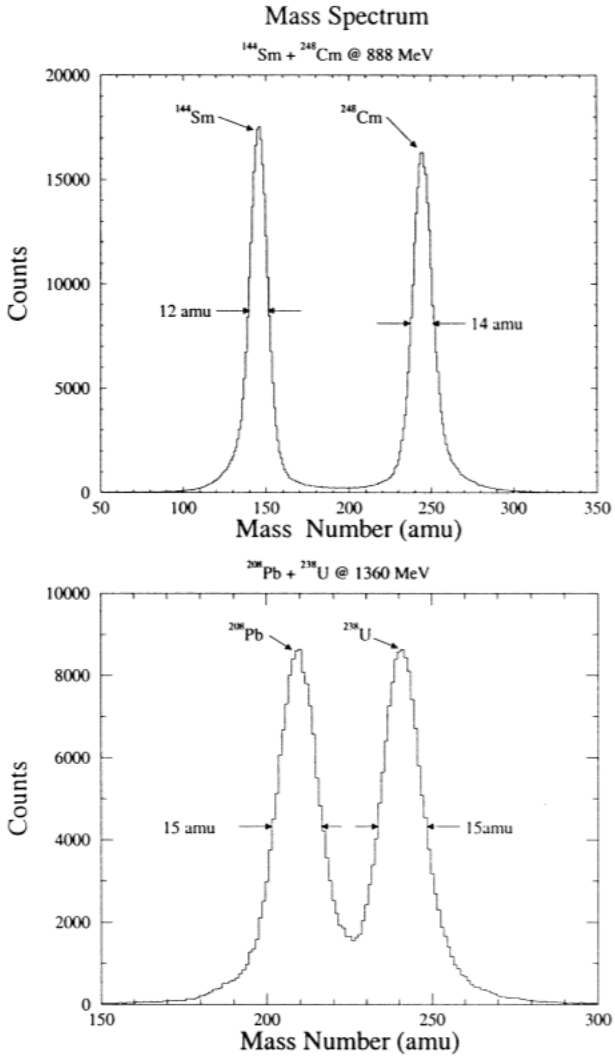

Figure 3.2: Examples illustrating the capabilities of CHICO2; calculated mass spectrum from the reaction ^{114}Sm + ^{248}Cm at 888 MeV (upper) and ^{238}U + ^{208}Pb at 1360 MeV (lower). The mass resolutions (FWHM) are indicated. [57].

performed. In this experiment, a beam of ^{48}Ca, provided by the ATLAS facility, was striking a self-supporting ^{26}Mg target isotopically enriched to 98%, and of thickness 0.974 mg/cm^2, at energies roughly 200% above the Coulomb barrier, resulting in so-called deep-inelastic scattering reactions. From these reactions, a wide variety of nuclei were produced at high excitation energies and angular momenta. Several species of product nuclei were created, including those of Ni, Co, Cu, Zn, Fe, and Ga. However, for this analysis, our main interest pertained to ^{64}Ni. The experiment was run for 6 days at beam energies of 275, 290, and 320 MeV in order to facilitate multi-nucleon transfer processes in inverse kinematics. Energy and efficiency calibrations were performed using ^{56}Co, ^{152}Eu, ^{182}Ta, and ^{243}Am sources. During the experiment, the ^{26}Mg target was placed in a target holder at the center of the Gammasphere HPGe detector array that was located directly in front of the ANL Fragment Mass Analyzer (FMA). Prompt γ rays emitted from the product nuclei were detected by Gammasphere, and were later corrected for the Doppler-shift, based upon the kinematics of their respective nuclei. In order to determine the appropriate Doppler shift correction, the FMA was used to pair each individual γ ray with the nucleus it was emitted from.

After the product nuclei exit Gammasphere, they immediately enter the FMA, a recoil mass separator that uses a series of dipoles and quadrupoles to disperse the ions along the focal plane based upon their mass-to-charge ratio (A/q). It is important to note that during this particular experiment, a titanium foil (0.7 mg/cm^2) was placed in front of the FMA entrance in order to attenuate the energies of the reaction products [29]. This attenuation was necessary to slow down the ions to the point where they could be suitably bent by the electric and magnetic fields. These ions were then observed by a microchannel plate (MCP) detector that provided the position information from which the A/q ratio could be determined. For additional Z identification, a three-fold segmented ionization chamber operated at 25 Torr was placed 50 cm behind the focal plane. The first two segments, each of 5 cm in length, were used to determine the energy loss of the ions before they came to rest in the 20 cm long third segment. The trigger logic required a γ-ray detection multiplicity of

≥ 2 (i.e., at least two γ rays properly Compton-suppressed) in coincidence with a particle detection in the MCP detector, thus significantly reducing background contributions due to beam scattering. Once again, both signals were required to be coincident within a timing gate set by the RF pulse of the accelerator [29]. An A/q resolution of 10 mm/% relative to the central value was achieved for this experiment, along with a timing resolution of $10 - 15$ ns. Specific information on the techniques and tools employed, including Gammasphere and the FMA, as well as a detailed explanation of the data analysis is provided in later sections.

Section 3.1: Coulomb Excitation

Coulomb excitation is a process of inelastic scattering that allows the exchange of energy between a projectile and a target through the electromagnetic field. Arguably, the most useful quality of safe Coulomb excitation is the fact that it is "model-independent". One will recall that a variety of different nuclear models exist that are used to predict nuclear properties, but due to the disagreement between these models, as well as our limited understanding of the strong nuclear force, interpreting results can sometimes prove difficult or ambiguous. The value in safe Coulomb excitation is that it circumvents some of these problems by minimizing the potential for nuclear interaction. This is done by utilizing beam energies that fall well below the Coulomb barrier. In doing so, the target and projectile nuclei interact and excite solely through the repulsion of their electric fields, at distances far enough apart that nuclear effects may be entirely neglected. In the semi-classical approximation of Coulomb excitation, the nuclei are considered to obey the Rutherford scattering formula and, therefore, follow hyperbolic trajectories. An example of this is illustrated in Figure 3.3. The equation for calculating the maximum "safe" bombarding energy for a head-on collision is as follows:

$$E_{max}(MeV) = 1.44\frac{A_1 + A_2}{A_2} \cdot \frac{Z_1 Z_2}{1.25(A_1^{1/3} + A_2^{1/3}) + 5} \tag{3.2}$$

where index "1" denotes the projectile and "2" is used for the target [46]. This equation corresponds to a minimum separation distance of 5 fm between the nuclear surfaces, ensuring that nuclear effects on the excitation cross sections are less than 0.1%. Any closer and these effects can lead to significant changes in the static moments of low-lying excited states [1]. In contrast to the nuclear force, the electromagnetic interaction is thoroughly understood, and it is thus possible to glean important information from the nuclei excited through this process. Namely, one can deduce the electromagnetic matrix elements from γ-ray spectra, which can then be used to compare directly with the predictions from nuclear models. As addressed in the previous chapter, these matrix elements are necessary for deriving important information on collectivity such as reduced transition probabilities and quadrupole moments.

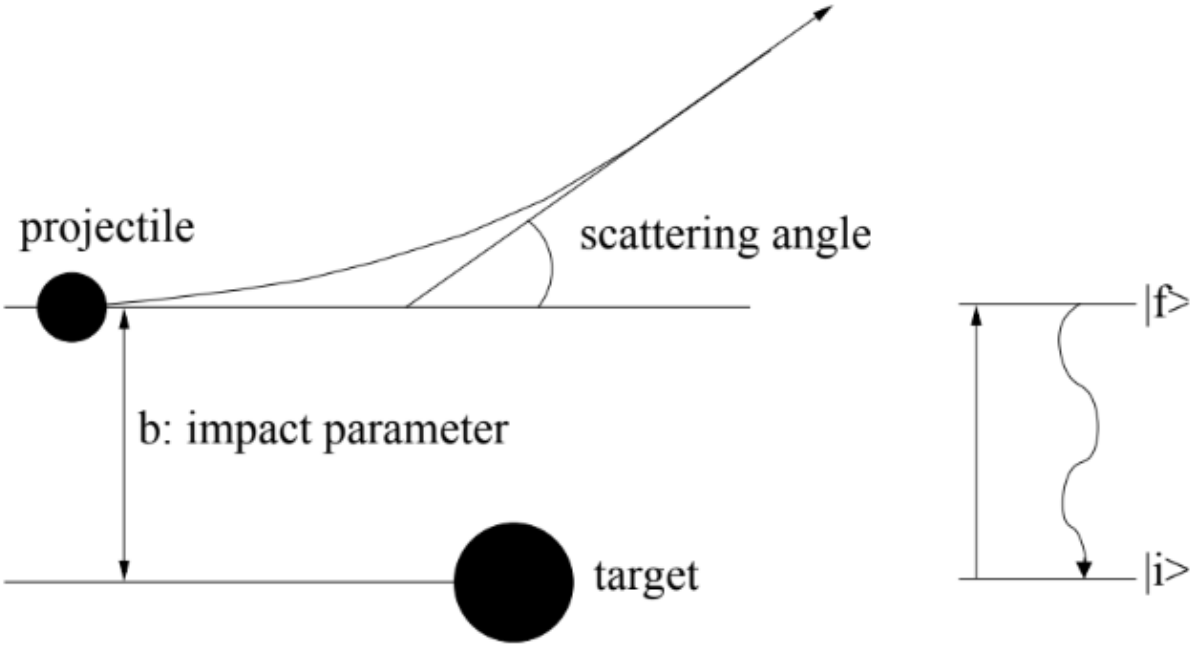

Figure 3.3: The semi-classical framework of Coulomb excitation. While for the semi-classical approximation of Coulomb excitation, nuclei are assumed to obey the Rutherford scattering formula, the transitions between nuclear states are treated quantum mechanically [1].

One might then anticipate that one of the most telling transitions regarding the quadrupole moment of the nucleus is the E2, or electric quadrupole transition. Another advantage provided by Coulomb excitation is that it heavily favors these specific transitions. This is

because the Coulomb excitation cross section is defined by

$$\sigma_\gamma = \sum_{\pi\lambda} \sigma_\gamma^{\pi\lambda}(\epsilon) \tag{3.3}$$

where, for a given multipolarity $\pi\lambda$,

$$\sigma_\gamma^{\pi\lambda}(\epsilon) = \frac{(2\pi)^3(\lambda+1)}{\lambda[(2\lambda+1)!!]^2} \sum_f \rho_f(\epsilon)\kappa^{2\lambda-1} B(\pi\lambda, I_i \rightarrow I_f) \tag{3.4}$$

Here, κ is defined as the wave number, and $B(\pi\lambda, I_i \rightarrow I_f)$ is again the reduced transition probability [58]. Upon inspection, it is possible to discern that the cross section favors low-multipole transitions. One may expect that this implies that Coulomb excitation would be dominated by E1 transitions. However, for the majority of even-even nuclei, E1 transitions are less available in the low excitation energy regime, which is typically the region probed by Coulomb excitation. So, many of the states populated tend to be associated with E2 excitation (and de-excitation) instead, this being the next-lowest multipolarity. This abundance of E2 transitions is especially favorable when attempting to gauge the quadrupole moment of the nucleus.

Another significant benefit of Coulomb excitation is that it may be used to determine γ-ray multipolarities based on their angular dependencies. This is because each multipolarity has a unique angular signature that can be observed experimentally, based upon the nucleus of interest. Such a phenomenon is depicted in Figure 3.4. These determinations are often made by measuring the intensities of γ rays as a function of angle and using complex Coulomb excitation codes, such as GOSIA, to discern the nature of the observed transitions. According to [58], the angular distribution of the γ rays emitted into a solid angle Ω_γ, as a function of the scattering angle of the projectile θ, is given by

$$W(\theta_\gamma) = 1 + \sum_{k=2,4,\ldots} b_k^{\pi L}(\theta) P_k(cos\theta_\gamma) \tag{3.5}$$

where $P_k(cos\theta_\gamma)$ are the Legendre polynomials, and the coefficients, $b_k^{\pi L}(\theta)$ are related to the Coulomb excitation amplitudes and the reduced transition probabilities. Thus, by determining the interaction points of the product ions and the emitted γ rays, multipolarites can be assigned to the observed transitions.

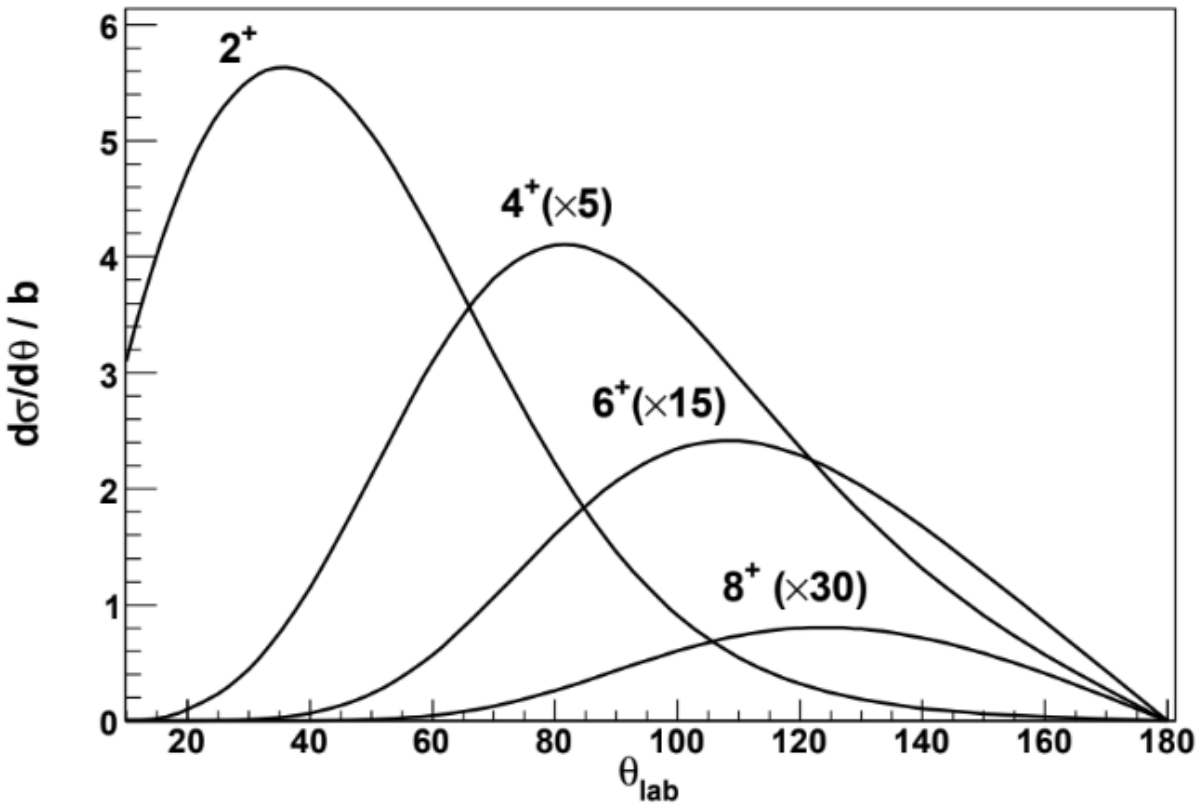

Figure 3.4: GOSIA calculated excitation cross sections for a typical rotational nucleus as a function of angle. Note that the excitation of the highest-spin state occurs at larger angles. The process involves multiple excitation steps, and this requires larger interaction times. This in turn implies larger scattering angles.

Lastly, to reiterate, due to the tendency of Coulomb excitation to populate states of low energy and spin, it is capable of reaching states that are not easily reached via more "invasive" reactions such as deep-inelastic scattering or fusion evaporation. Whereas methods like deep-inelastic scattering will populate high-energy, high-spin states in the hope that some low-spin, non-yrast [1] states may be observed in the subsequent decay, Coulomb excitation can directly

[1]yrast — a state of a nucleus with a minimum of energy for a given angular momentum

populate these low-lying levels from the ground state up. This is due to the fact that in complex reactions which populate high-energy states, these levels tend to decay towards the lowest-lying states possible, herewith removing as much energy as possible, often missing weaker de-excitation paths. Coulomb excitation, on the other hand, simply populates any (predominantly) low-spin level it can reach, so there is rarely any preference for funneling towards the yrast sequence. This makes Coulomb excitation exceptional for examining low-spin, non-yrast states, which is especially relevant with regard to the pursuit of a study of 0^+ excited states, a main focus of this work. This method can truly illuminate many questions regarding collectivity and shape-coexistence within nuclei by probing some of the most essential quantities. However, its greatest advantage is also its biggest limitation, in that it can only probe relatively low excitation energies. In the search for shape coexistence, it is necessary to examine the levels located above these 0^+ excited states and de-exciting toward them in order to find evidence for band structures. The latter tend to lie out of reach of the Coulomb excitation process, and this is where deep-inelastic reactions form a complementary approach.

Section 3.2: Deep-Inelastic Reactions

A "deep-inelastic transfer reaction", or "deep-inelastic reaction" in short, is a complex process in which a nucleus traveling at high energy and momentum is directed upon a target, causing the two nuclei to momentarily "stick" together and "torque" before separating. During the sticking time, projectile and target exchange particles, angular momentum and energy. The process is usually characterized by N/Z equilibration; i.e., the partner with the largest number of neutrons will transfer a number of these to the other nucleus involved. The process is stochastic in nature and rather complex. In addition to the exchange of nucleons, the transfer in energy is often such that particle evaporation will also occur. This reaction mechanism(s) is (are) discussed hereafter.

These reactions produce a large number of products at once, all resulting in a significant

number of γ rays that make up a complex total γ-ray spectrum. When a thin target is used, the products are typically segregated based on their mass-to-charge ratio as they pass through an ion separator, and the γ rays can subsequently be linked to their nucleus of origin through selective coincidence gating. These types of experiments have started playing an important role in the study of neutron-rich nuclei because they provide a means to reach and investigate, at moderate spins, species that cannot be produced with fusion-evaporation reactions. It is important to note that, until fairly recently, deep-inelastic reactions could rarely be utilized, due to the nature and characteristics of older detector systems. It was only with the advent of Compton-suppression techniques and multi-detector HPGe arrays such as Gammasphere, that data from such reactions could finally be adequately analyzed. This is because, with such a wide variety of reaction products and complex γ-ray spectra, Compton-suppression is essential to sufficiently lower the background and optimize the peak-to-total ratio necessary to analyze the required coincidence relationships. Furthermore, a large number of detectors is necessary so that high-statistics γ-γ coincidence matricies (to be discussed later) can be constructed. It is only by employing these coincidence relationships from spectra with good peak-to-background ratios that one can ensure that individual γ rays are associated with a specific nucleus of interest.

The first true exploitation of deep-inelastic reactions for γ-ray spectroscopy was performed by Broda et al. [59], in an experiment with a 255-MeV beam of ^{60}Ni ions bombarding a ^{92}Mo target, resulting in an extensive γ-ray spectrum. This study indicated that deep-inelastic processes are capable of facilitating a variety of transfer reactions with useful cross sections, making it a versatile tool. Subsequently, an experiment was performed by Krolas et al. [60], who studied in detail the potential for spectroscopy of this reaction mechanism. In this instance, two sets of collisions were studied: ^{130}Te + 275-MeV ^{64}Ni, and ^{208}Pb + 345-MeV ^{58}Ni. From their work, Krolas discerned that deep-inelastic scattering reactions seek to achieve N/Z equilibration through the transfer of nucleons. These two studies did highlight some of the most fundamental characteristics of deep-inelastic reactions.

According to [61], deep-inelastic reactions combine characteristics of at least two nuclear processes: direct reactions and compound nucleus decay. Similar to direct reactions, deep-inelastic ones are characterized by a strong coupling between entrance and exit reaction channels. This is to say that the products do not entirely "forget" the direction of motion of the initial nuclei, nor their atomic and mass numbers, although those will change significantly. Light reaction products are typically emitted at small angles and the mass and charge distributions of the products exhibit a maximum in the vicinity of the A and Z of the original nuclei, but with significant cross sections for processes involving the exchange of a large number of nucleons; i.e., the distributions in A and Z around the projectile and target are broad. On the other hand, much like compound nucleus decay, much energy is imparted to the products as the reactions are "damped"; i.e., the kinetic energy in the entrance channel is transferred to the partners in the form of both kinetic and intrinsic excitation energy. Additionally, the cross sections for the productions of individual isotopes by deep-inelastic reactions exhibit only a small degree of statistical equilibrium, nevertheless sufficient to induce particle evaporation. The manifestation of these different phenomena make deep-inelastic reactions a particularly unique area of study and a tool for nuclear spectroscopy.

The peculiar characteristics brought about by deep-inelastic reactions are a consequence of the two-nucleus composite system formed during the collision. This system results from high nuclear viscosity and the low compressibility of nuclear matter. It manifests itself as a large overlap between nuclear surfaces. In other words, upon collision, there is a significant amount of surface contact between the two nuclei as they stick together and rotate. However, the two nuclei, being quite dense, are not highly-compressed when coming into contact with one another. It is for this reason that nucleon transfer in deep-inelastic reactions predominantly involves the nucleons located at the surfaces of the partners, leading each reaction product towards N/Z equilibrium. The high viscosity results in an extreme dissipation of kinetic energy that is transferred to the excitation of the two systems, and the low compressibility prevents the large penetration of the nuclei into one another. These two factors result

in a dumbbell-shaped system exhibited by the two nuclei. The nuclear shell structure is also important in this composite system. As these two nuclei interact by exchanging nucleons and energy, the tightly-bound nucleons of the lower shells (i.e. the cores), to some extent, preserve the individuality of the original nuclei [61]. A depiction of the two-nucleon system is given in Figure 3.5.

Figure 3.5: Creation and decay of the two-nuclei system in deep-inelastic transfer reactions. Nuclei 1 and 2 momentarily stick and rotate together while nucleons are transferred before separating again into the reaction products 3 and 4 [61].

One of the most important advantages of deep-inelastic transfer reactions is their ability to produce nuclei that cannot be reached by other means. In particular, they can reach nuclei that cannot be obtained through fusion evaporation. They also serve as an excellent complement to Coulomb excitation due to their ability to populate a diverse array of states, including those of high-energy and moderately high-spin values (10-20$\hbar$). By generating product nuclei through complex, high-energy, high-angular-momentum reactions, one gains access to excited states, that then decay towards the yrast sequence through a variety of decay paths. Of course, product nuclei can be created at various different excitation energies and spins, so the level structure of a nucleus can be thoroughly examined from high-spin levels all the way down to the ground state. While these types of reactions do not provide information on collectivity through B(E2) or quadrupole moment values, as is the case with Coulomb excitation, they are beneficial when searching for higher-up rotational or vibrational band structures indicative of deformation. So, the combination of these two experiments, Coulomb excitation and deep-inelastic scattering, should provide an opportunity to probe

each important aspect of nuclear collectivity.

Section 3.3: GRETINA

The 2π γ-ray Energy Tracking In-beam Nuclear Array (GRETINA), the first step towards the full 4π γ-ray Energy Tracking Array (GRETA), is a state-of-the-art spherical γ-ray tracking array designed for the purpose of providing large detection efficiency with the resolution of HPGe detectors. Comprising 48 highly-segmented, hexagonal HPGe crystals packed into 12 "quads" (4 crystals per quad), it also seeks to improve upon the resolution for γ rays emitted in-flight through accurate Doppler reconstruction. Both of these goals are accomplished by utilizing the manifold segmentation offered by each detector in the array. For this reason, it is important that we understand how segmentation and tracking are employed by GRETINA before going further, so let us briefly introduce both of these concepts.

Arguably, GRETINA's most important attribute, and its main advantage over its predecessors, is its ability to completely reconstruct a photon through its various interactions in the crystal, such as Compton scattering or pair production. This can be done by using its high degree of segmentation in combination with complex algorithms applied to determine precise interaction points based off real and image charges. Each GRETINA crystal is electrically segmented into six slices radially as well as along the length of the crystal, leading to 36 total segments (Figure 3.6 (a)). When a γ ray interacts at some point in a GRETINA detector, the 36 separate segments along with the core (central contact) produce a total of 37 signals. The segment in which the interaction occurs measures a real or "net" charge, while the surrounding ones measure image charges. The shape and amplitude of the image-charge signals in the neighboring segments contains information on the depth and polar angle of the interaction point. Using the real charge along with the image ones, one can apply a signal-decomposition algorithm to obtain the information about the original interaction point. It is worth noting that this decomposition algorithm is the result of extensive studies carried out with collimated sources irradiating the crystal at various locations. Once the position of the

interaction points is determined, another algorithm reconstructs the full photon. It is based on the well-understood Compton scattering formula, and it allows one to achieve an interaction position resolution of sub 0.5 mm and, in doing so, enables γ-ray tracking capabilities. This also means that when a γ-ray interacts in one detector and scatters into an adjacent one, where it is completely absorbed, the total energy of the photon can be reconstructed from the interactions across both detectors, thus contributing to the peak counts rather than the Compton background. This provides a major advantage over previous generations of HPGe detector arrays by greatly improving the signal-to-background ratio and increasing the efficiency. Additionally, due to the advent of electrical segmentation and γ-ray tracking, Compton suppression shields, such as those used in previous detector arrays to suppress events with partial energy collection, are no longer necessary. This means that while a large amount of the solid angle in earlier detector arrays was dedicated to Compton suppression shields, with GRETINA/GRETA the entire solid angle coverage may be composed of HPGe detectors, significantly increasing the efficiency. Lastly, despite GRETINA's ability to be operated in tracking mode, for this particular experiment, complete reconstruction of all γ rays was not employed. Rather, in our case, the interaction that deposited the largest amount of energy in the crystal was assumed to correspond to the first interaction point. This was due to the fact that, when used in conjunction with CHICO2, background could be greatly reduced, making tracking inessential [56].

The four-crystal detector modules used in GRETINA were manufactured by the Canberra France-Lingolsheim facility based on the design and requirements specified by Lawrence Berkeley National Laboratory(LBNL). Each crystal is of the n-type coaxial geometry. It is tapered to a hexagonal shape at the front face such that four of these can be optimally packed closely, and 30 of these "quads" can be assembled into a spherical shell. As referenced previously, GRETINA covers nearly 2π of the total solid angle, but when completed, the full 4π GRETA apparatus will consist of 120 hexagons of two different shapes (60 of each), as well as 12 pentagonal openings through which signal cables may be passed for auxiliary

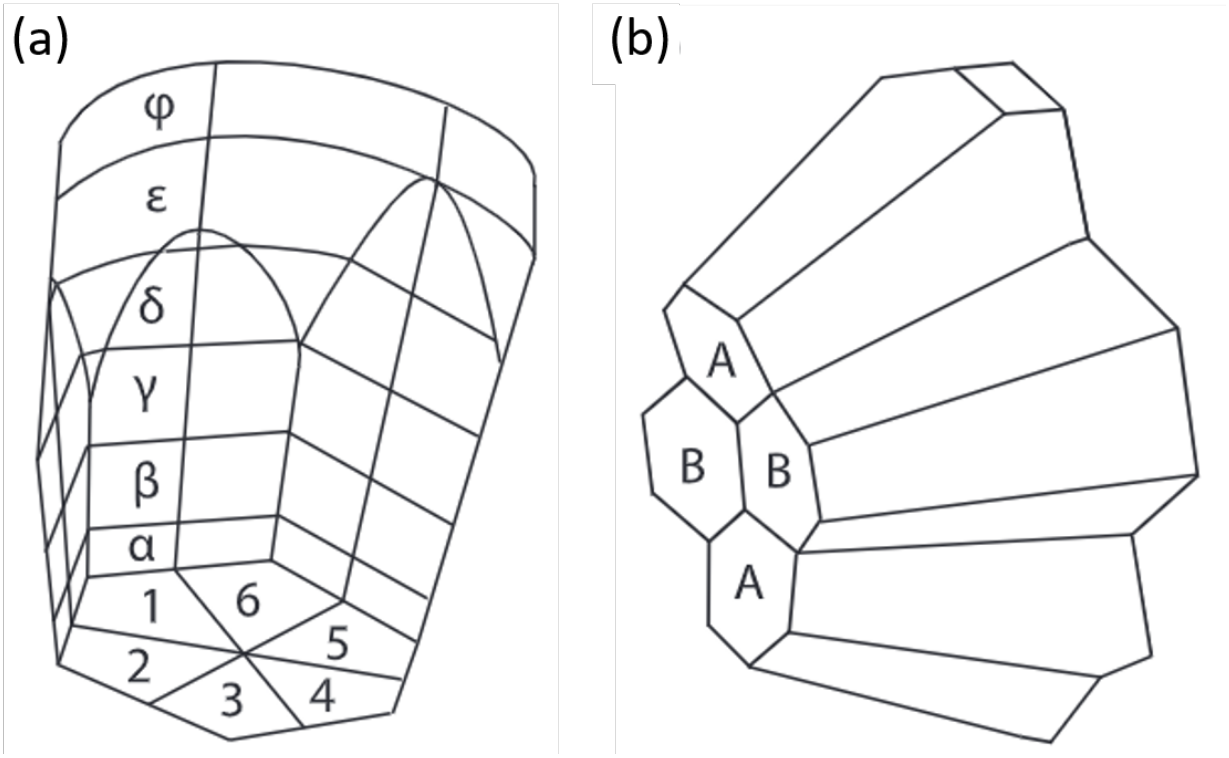

Figure 3.6: (a) Illustration of axial and longitudinal segmentation in GRETINA crystals. (b) Basic schematic of a GRETINA quad utilizing two different hexagonal crystal shapes [56].

detectors. A basic example of the two hexagonal shapes situated in each quad is given in Figure 3.6(b). When GRETINA was originally constructed (phase I), it consisted of 7 quads covering 1π of solid angle, and possessed a "calorimetric" efficiency of 6.3% at 1.3 MeV. This number corresponds to the arrays' maximum singles efficiency when tracking is not applied. However, by applying a figure-of-merit (FOM) cut to the fit of the Compton track of the γ ray, one can significantly improve the peak-to-total ratio at the cost of the overall efficiency. By defining a 25% FOM cut, one obtains a tracked efficiency of 4.7% (6.3%*0.75), but a peak-to-total of 49% [62]. While the precise efficiency of GRETINA when comprising 48 detectors is not explicitly stated in the literature, a plot of the efficiency versus energy for an 8-module (32-detector) GRETINA is provided in Figure 3.7 [63].

Using the 120-hexagon geometry, the distance from the front face of the detector caps to the center of the array is 18 cm. Examples of the arrangement of GRETINA detector quads are shown in Figures 3.8 and 3.9. Each HPGe detector is about 90 mm long and 80 mm in diameter with a 10 millimeter diameter bore that extends 15 mm from the crystal face. The four crystals contained in each quad all share a single cryostat and dewar (illustrated in Figure 3.10) and each quad always consists of two different types of hexagons. Each individual detector is encapsulated in its own aluminum canister of 0.8 mm thickness and there is a 0.5 mm distance between the aluminum wall and the crystal surface. The total crystal-to-crystal distance for crystals within the same quad is less than 2.7 mm, and for crystals in different quads the corresponding distance is 9.2 mm. This closely-packed geometry makes GRETINA proficient at high-efficiency γ-ray detection, while maintaining the superior resolution of HPGe detectors. This properly combined with its photon reconstruction capability, is what makes GRETINA one of the leading next-generation detector arrays. In fact, it has at present only one competitor on the world scene, the European AGATA array. A comparison between the properties and performance of GRETINA and AGATA can be found in Ref. [64].

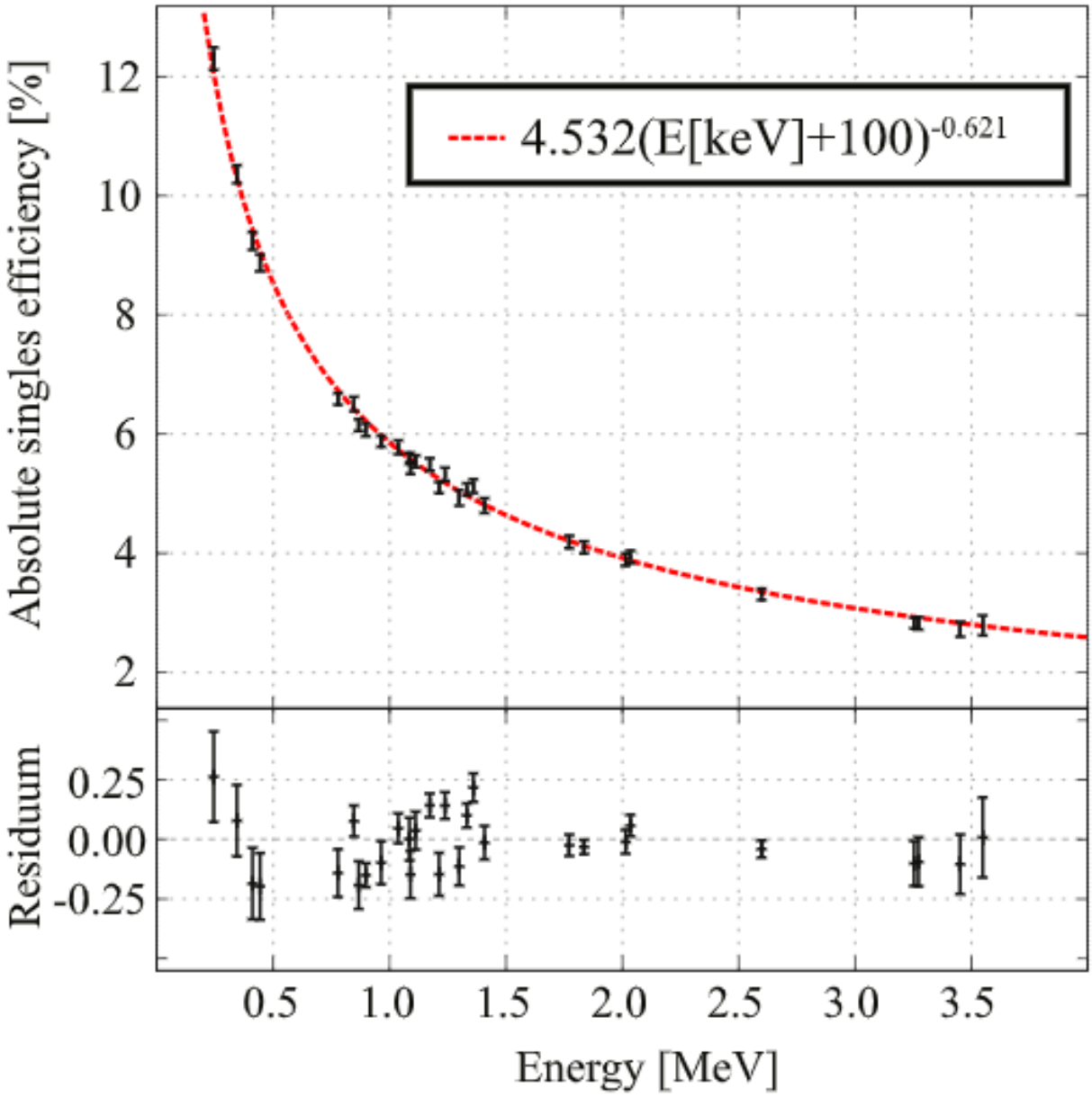

Figure 3.7: Singles efficiency for an 8-module (32-detector) GRETINA. The red dashed line indicates the calculated efficiency curve using the data points given in black. The residuum displays the difference between the data points and the curve [63].

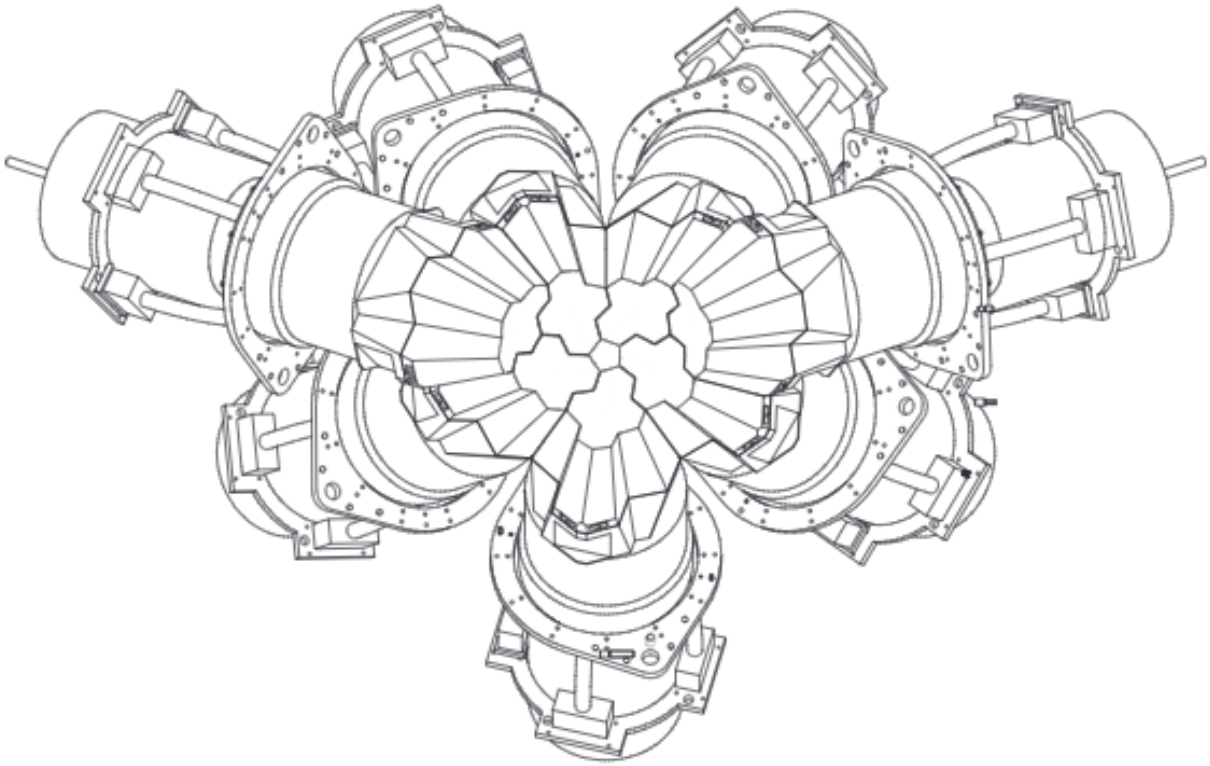

Figure 3.8: Schematic of a partially completed GRETA. Note the pentagonal opening at the center through which cables can be passed for auxiliary detectors [56].

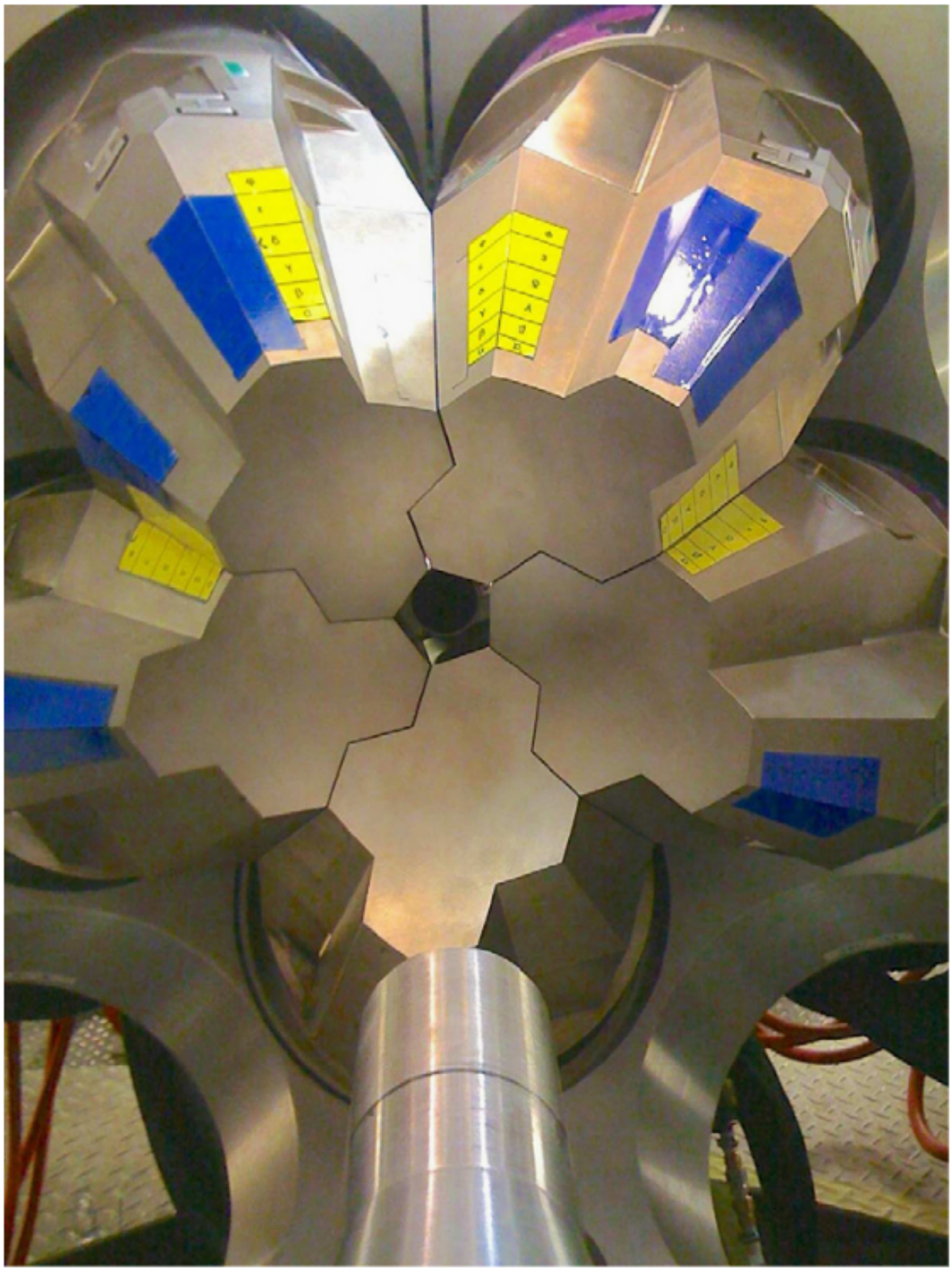

Figure 3.9: Image of five adjacent GRETINA quads with the characteristic pentagonal opening at the center [56].

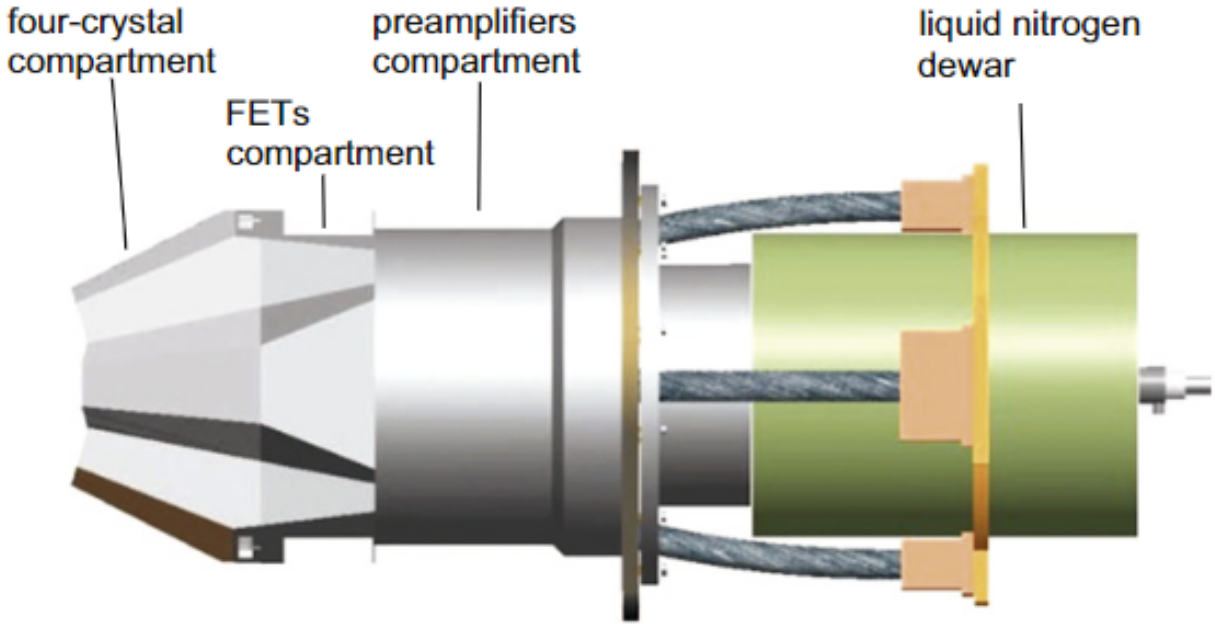

Figure 3.10: Basic schematic of a GRETINA quad along with cryostat and liquid nitrogen dewar [56].

Section 3.4: CHICO2

The Compact Heavy Ion Counter (CHICO), developed by the University of Rochester and Lawrence Livermore National Laboratory, is a highly-segmented, position-sensitive parallel-plate avalanche counter (PPAC) with large solid-angle coverage for charged-particle detection [65]. Originally designed as an auxiliary detector for Gammasphere, an upgrade of the device to CHICO2, was necessary in order to make it compatible with the new GRETINA tracking array. As a unique particle detection device, CHICO(2) has been used for a variety of experiments ranging from Coulomb excitation and few-nucleon transfer, to deep-inelastic reactions and fission.

CHICO consists of two identical hemispheres, each containing 10 PPACs, covering 69% of the solid angle; the azimuthal angular ranges are defined by $12^\circ < \theta < 85^\circ$ and $95^\circ < \theta < 168^\circ$, and the polar angle, ϕ, covers 280°. Each PPAC comprises a thin-film anode and a cathode circuit board. The cathode consists of three layers. When CHICO was originally designed, the first layer, where the particles are detected, was segmented into 1°-

wide traces of constant polar angle θ. This was later improved in the upgraded CHICO2, where ϕ pixelation was added alongside the already existing θ one in order to accommodate GRETINA's superior precision. This upgrade will be addressed later in this section. Each trace is connected to one tap of a delay line that is mounted on the bottom (third) layer of the cathode board, where the delay line has a delay of 1 ns per tap. These two layers (layers 1 and 3) are separated by a grounding plane that makes up the second layer of the cathode. This plane serves to decouple the traces of the first and third layers and, thus, significantly improves the performance of the delay line.

The anode is made of approximately 100 $\mu g/cm^2$-thick stretched polypropylene with an approximately 20 $\mu g/cm^2$ evaporated aluminum coating. In the first version of CHICO, the aluminum coating of each anode was segmented into two electrically-isolated sections in order to provide azimuthal angle segmentation, where one section had a width of 9.3° and the other a width of 18.6°. However, after the upgrade to CHICO2 and the addition of the ϕ pixelation on the cathode, anode segmentation became unnecessary. Lastly, the anode and the cathode are separated from one another by a 3.2 mm spacer. Schematics and examples of the original anode and cathode design, as well as the upgraded cathode for CHICO2, are displayed in Figures 3.11, 3.12, and 3.13, respectively.

Two aluminum hemispheres, of 1.58-mm thickness and 14-inch diameter, each house 10 anodes and 10 cathodes. A conical aluminum frame covered with a sheet of 0.9 μm-thick Mylar acts to sequester the detector gas, used for the PPACs, from the high-vacuum target chamber. The detector space is slowly filled with isobutane gas and kept at a pressure of 4 Torr. Note that all ten detectors in each hemisphere share the same gas volume. The gas circulation and pressure in each hemisphere is controlled by two separate gas-handling systems. A conical tungsten collimator, with a 6.4 mm diameter entrance and 5.1 mm diameter exit hole, can also be mounted in the target chamber, and was included for this experiment. This collimator is necessary in order to ensure that the beam does not directly come in contact with the PPACs, thereby damaging them. For experiments with radioactive

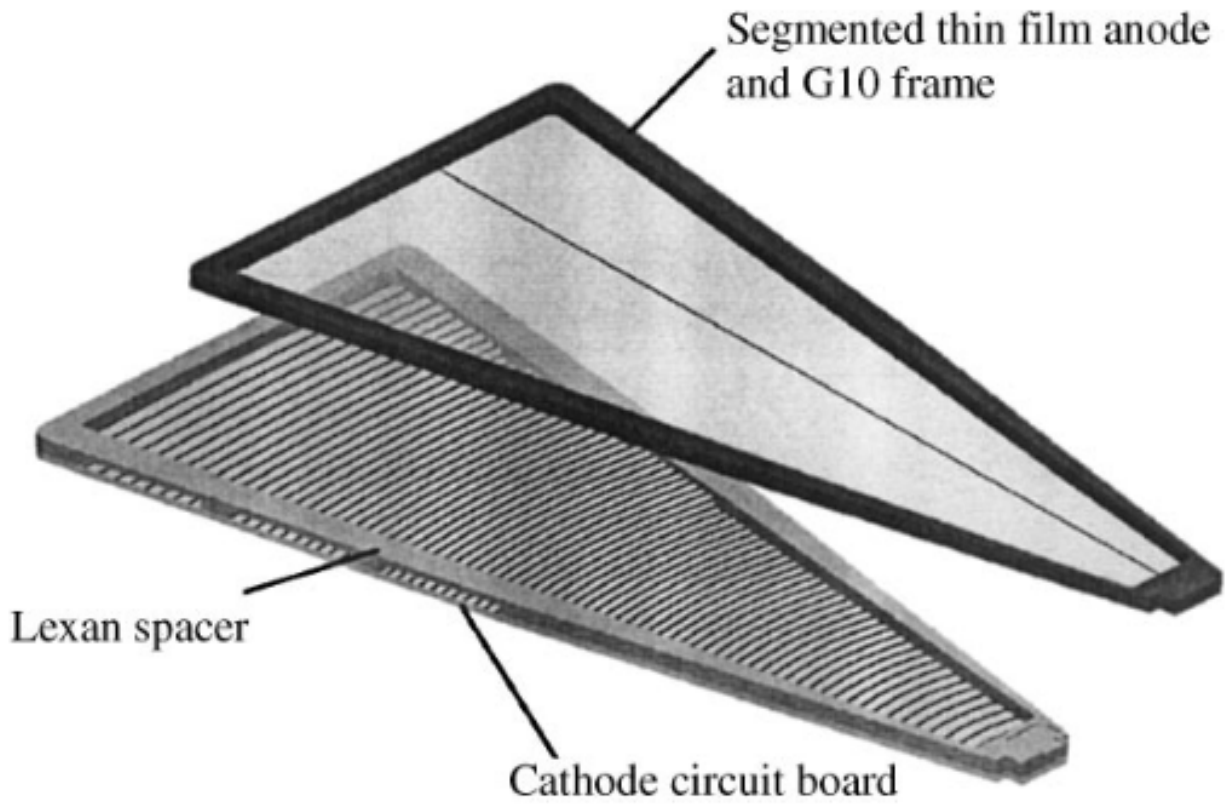

Figure 3.11: PPAC assembly displaying the anode and cathode design for the original CHICO [65].

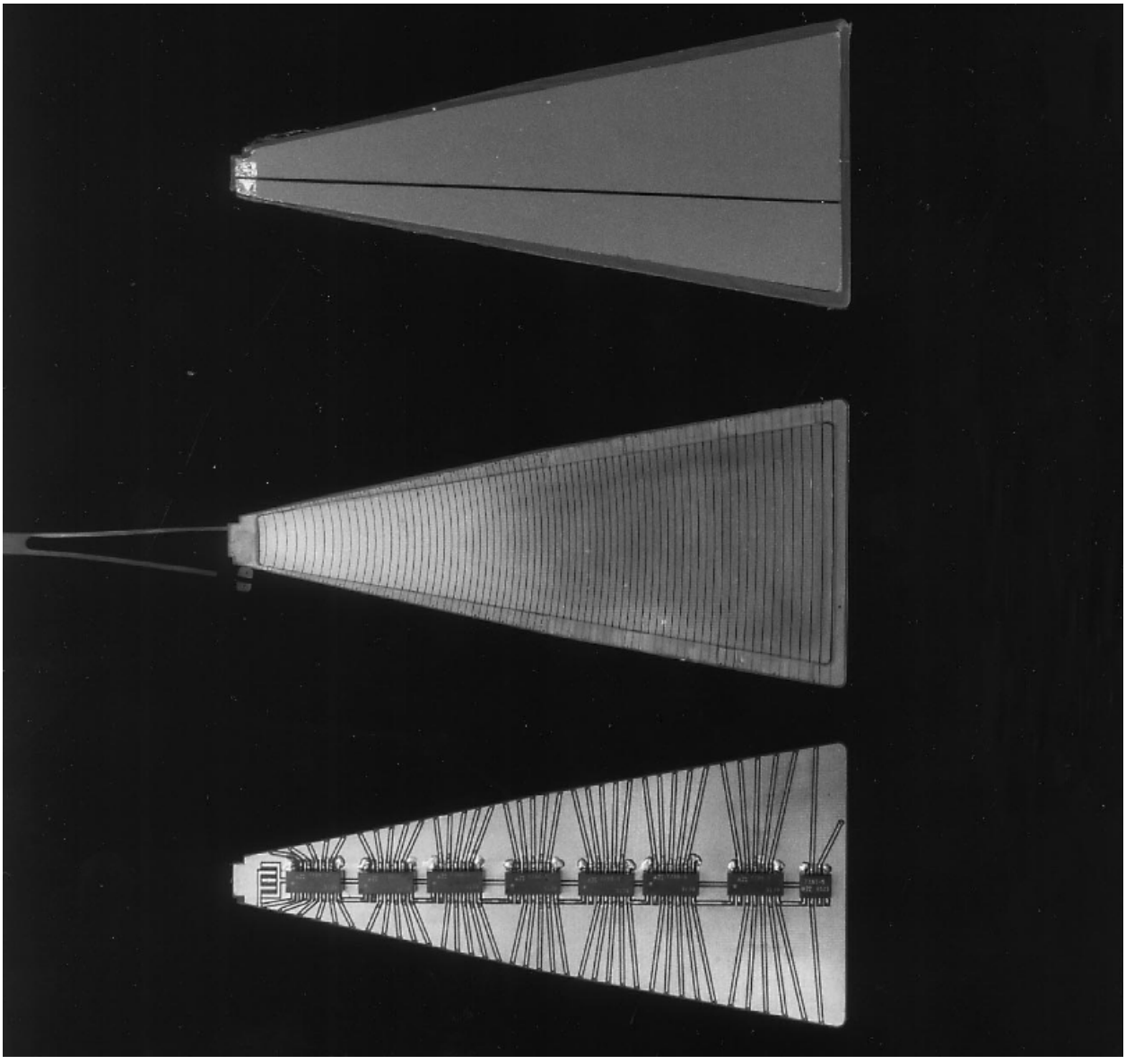

Figure 3.12: Photograph (from top down) of the CHICO anode, active side of a cathode board with attached transmission line, and the back of the cathode board displaying the delay line [65].

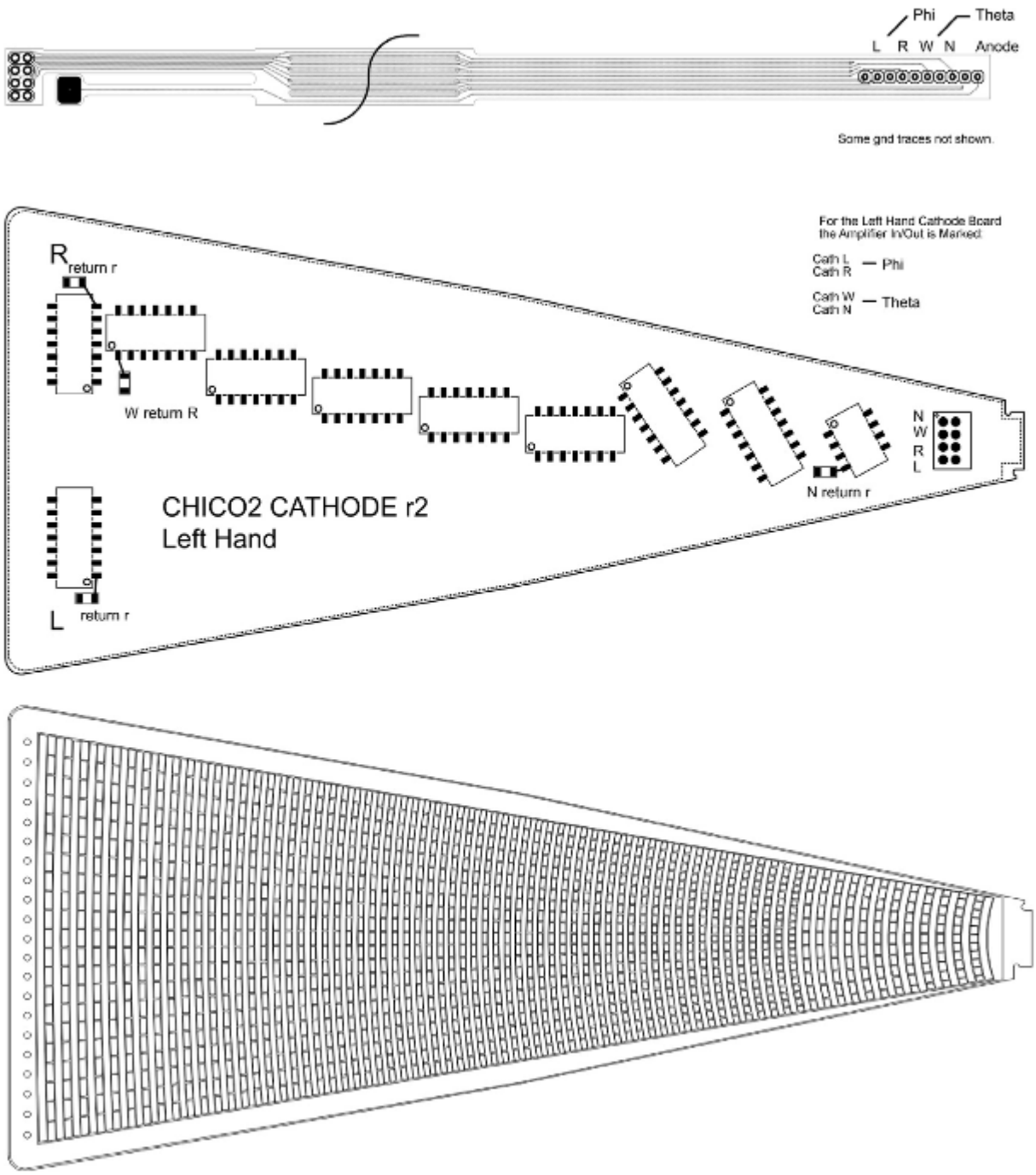

Figure 3.13: Schematic view of the pixelated cathode board and transmission line for CHICO2. Note the increased pixelation in comparison to Figures 3.11 and 3.12 [57].

beams, generally of small intensity (1 pico-Amp or less), the collimator is often removed. Finally, a target ladder is mounted on a thick aluminum ring with O-rings seated on both sides. The two hemispheres of CHICO are pressed firmly against the O-rings and the target chamber is pumped out such that it may be kept sealed under high vacuum. Images of a single CHICO2 hemisphere and the full CHICO2 array seated inside GRETINA are portrayed in Figures 3.14 and 3.15, respectively.

In the updated CHICO2 array, each cathode board possesses 1478 pixels in total, giving each pixel a θ dimension of 0.5°, corresponding to a 1-2 mm position resolution, and a ϕ dimension of 1.4°, corresponding to 2-4 mm one. When a particle is incident on a pixel, its specific location is determined by the time difference between the two ends of the delay line for both x and y coordinates. The basic idea of the pixel readout is illustrated in Figure 3.16. A valid signal requires that both θ and ϕ pixels are read out for every interaction.

Due to its high degree of pixelation, CHICO2 possesses an angular resolution of better than 1° in both the θ and ϕ coordinates. Additionally, for binary reactions, target- and projectile-like nuclei can be identified with a $\Delta m/m$ mass resolution of about 5%, as discussed previously. Using the measured masses, recoil velocities, and angles of incidence, an appropriate Doppler-shift correction can be applied to all γ rays emitted by the ion of interest, once the angle of incidence of the photons is determined from the information provided by GRETINA. This results in a pristine spectrum that heavily emphasizes the relevant γ rays. Further information on CHICO and CHICO2 can be found in Refs. [65] and [57].

Section 3.5: Gammasphere HPGe Detector Array

Gammasphere is a closely-packed, spherical array consisting of coaxial HPGe detectors arranged in a "honeycomb-like" shape utilized for high-efficiency γ-ray detection. The array is capable of employing up to 110 HPGe detectors at once, 70 of which are electrically segmented longitudinally to produce two "D-shaped" halves, effectively creating a total of 180 detectors [66]. This longitudinal segmentation is especially beneficial with regard to

Figure 3.14: Photograph of a single hemisphere of CHICO2 including mylar window and collimator.

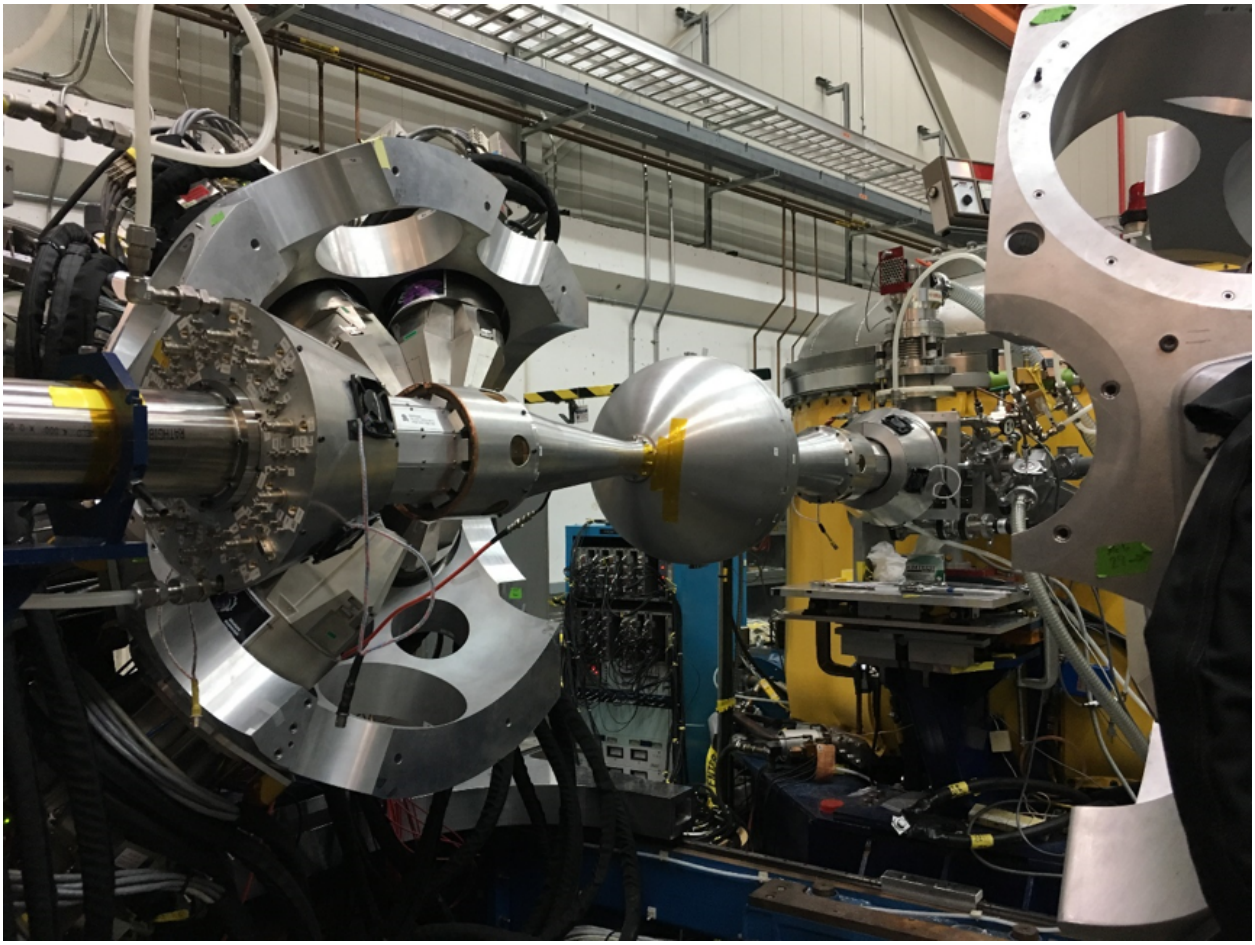

Figure 3.15: Photograph of the CHICO2 assembly situated inside an open GRETINA array.

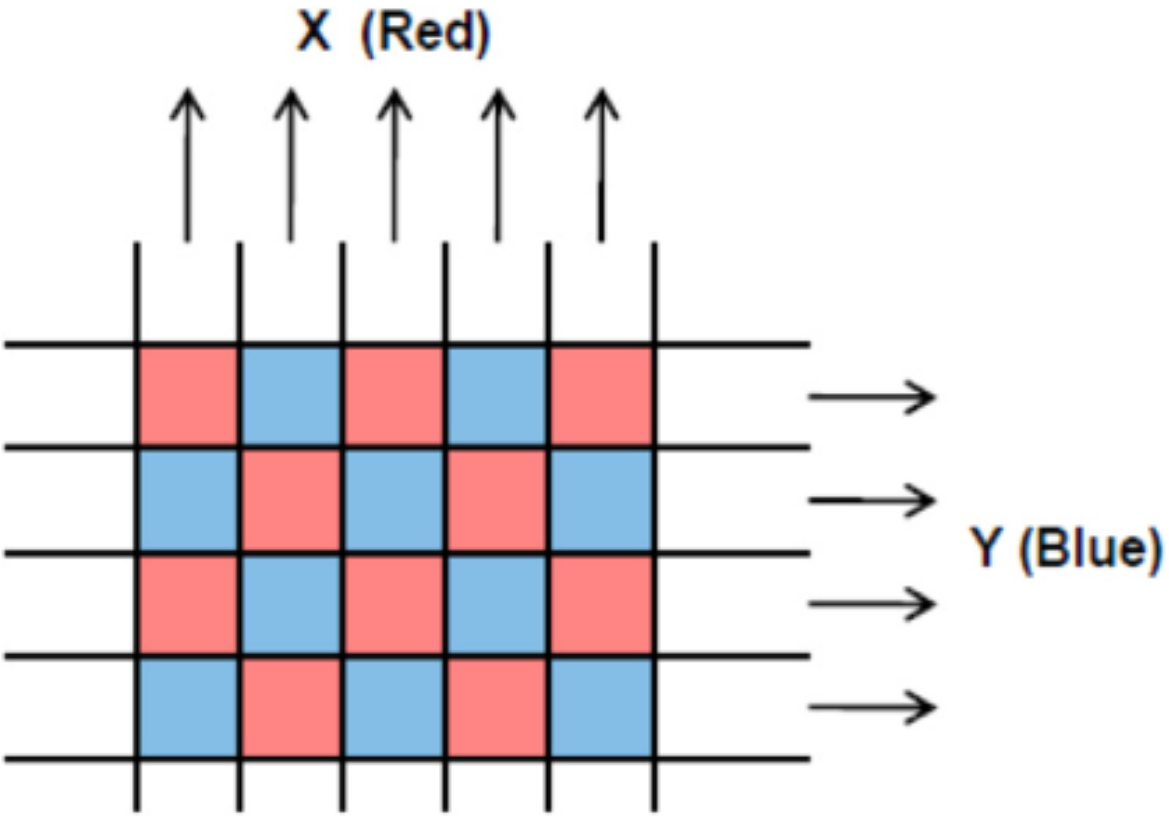

Figure 3.16: Depiction of how both X and Y positions are read off of the CHICO2 cathode using the improved pixelation. Arrows point in the direction of the delay lines [57].

mitigating the Doppler shift of the detected γ rays emitted from target nuclei. However, during this particular experiment, only 101 out of the possible 110 detectors were utilized, in part to enable the transmission of the reaction products into the FMA (see below).

On average, each HPGe crystal has a diameter of 7.1 cm and a depth of 8 cm, and is contained within an aluminum cap. Every individual HPGe detector is then surrounded by six slabs of Bismuth Germanate (BGO), each with a complex geometry and a depth of 18.8 cm, forming the aforementioned hexagonal, "honeycomb-like" pattern (Figure 3.17). Additionally, a BGO plug with the same diameter of the HPGe crystal is positioned behind the crystal in order to completely encapsulate it [67]. A cutaway view of a Gammasphere detector is given in Figure 3.18.

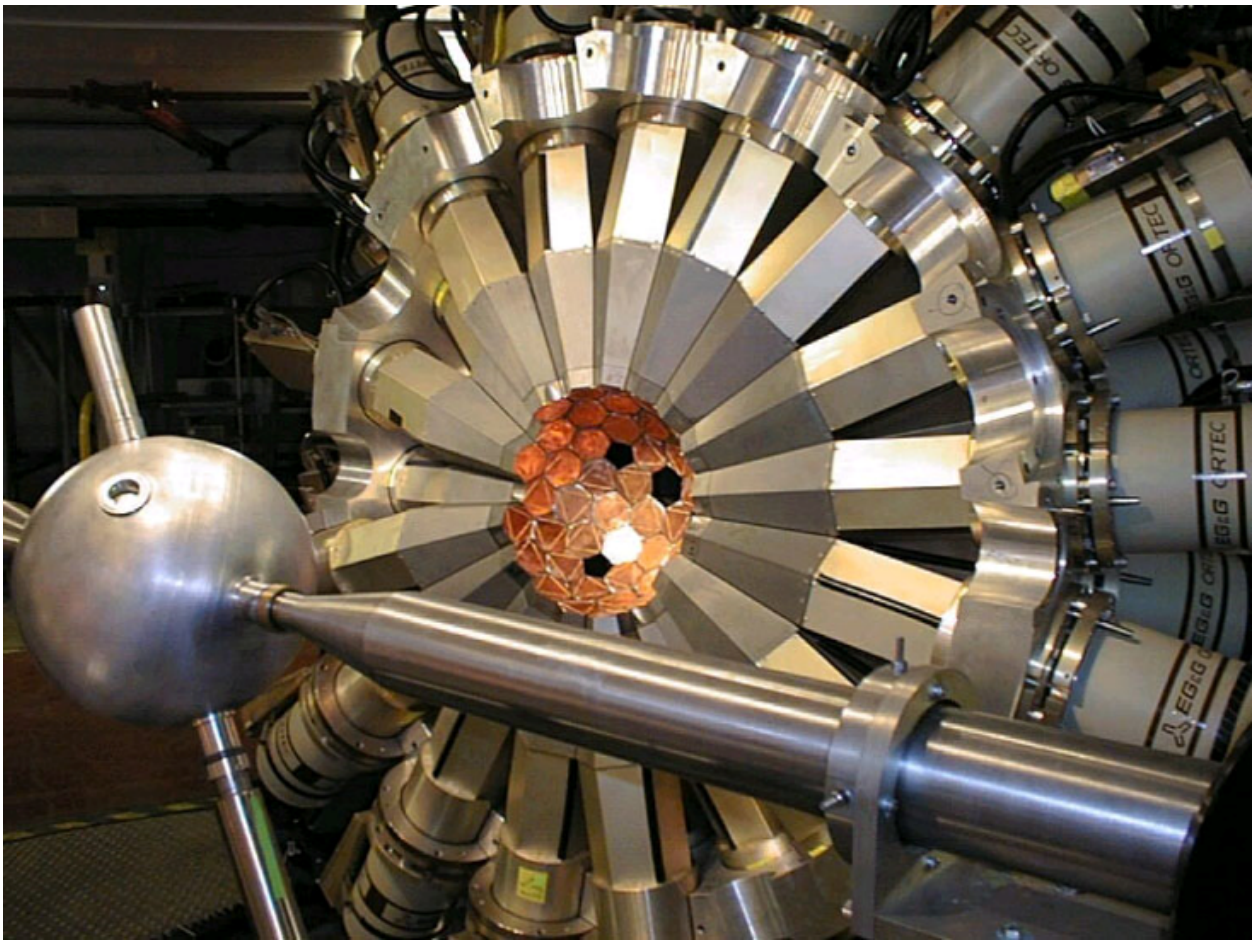

Figure 3.17: Image of one hemisphere of Gammasphere showing crystals, cryostats and dewars, along with the dedicated target chamber.

Figure 3.18: Schematic of a Gammasphere detector and cryostat components. The BGO scintillators are in grey, and the HPGe crystals are in green. The orange pieces in front of the BGO detectors represent the heavymet absorbers shielding these scintillators from the γ rays emitted at the target.

The use of highly-efficient BGO scintillators in Gammasphere offers significant background reduction via a mechanism known as Compton suppression. Simply put, whenever a signal is detected within any of the BGO scintillators surrounding an individual HPGe crystal, any coincident event detected in that HPGe crystal will be vetoed and discarded. This allows for greatly improved peak-to-total ratios in γ-ray spectra because the majority of Compton-scattered γ rays no longer contribute to the background. Instead, the majority of "accepted" signals result from total energy deposition of a γ ray into an individual HPGe crystal. For comparison, the peak-to-total ratio for an unsuppressed Gammasphere HPGe detector is about 0.25, however with BGO Compton suppression this ratio rises to 0.60 [66]. An example of a Compton-suppressed spectrum is displayed in Figure 3.19.

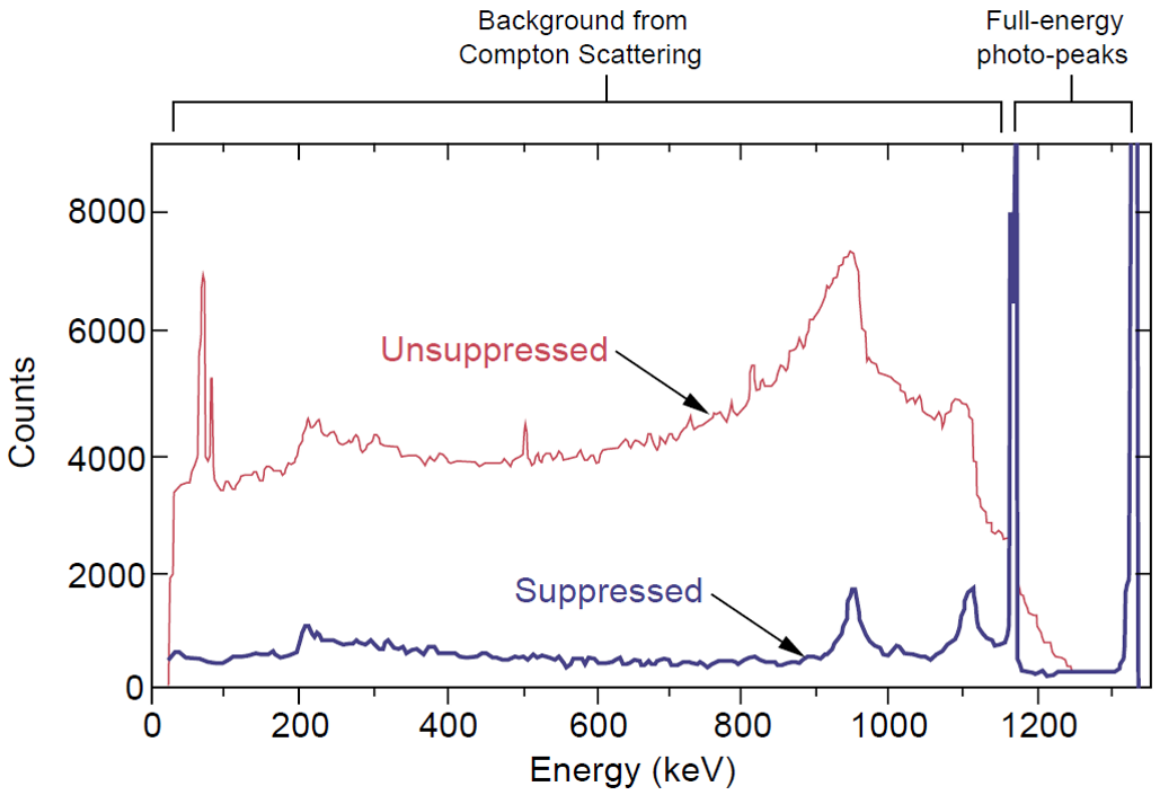

Figure 3.19: The effect of Compton suppression on a ^{60}Co spectrum obtained with Gammasphere. Note that the two photopeaks vastly exceed the vertical scale. The two spectra are scaled such that the photopeaks in the suppressed spectrum have the same height as those in the unsuppressed spectrum [67].

Naturally, it is then also extremely important to sufficiently shield the BGO scintillators

from all γ rays emitted by the source, as this would otherwise result in a severe decrease in efficiency. This is done by placing 3-cm thick absorbers composed of heavy metals directly in front of the BGO scintillators. These absorbers, aptly referred to as "heavymets", are made of a tungsten alloy (90% W, 6% Ni, 4%Cu), and are employed in the majority of experiments carried out with Gammasphere. At lower energies, the addition of the heavymet absorbers can lead to a slight drop in efficiency, as illustrated in Figure 3.20. However, beyond about 1 MeV, the effect on the efficiency is negligible. Lastly, hexagonal absorbing plates are also placed on the front of each detector in order to mitigate background from low-energy X rays emitted from the target when hit by the beam. These X rays, often generated through atomic processes; i.e., electrons hit by the beam, can sum together with the γ rays of interest to produce undesired background. The absorbers typically comprise 3 separate plates of Ta, Cd, and Cu arranged with Ta closest to the source and Cu directly in front of the detector. The type, number and thickness of the plates used depend on the experiment and are chosen based upon the energy of the potential X rays. When used, all three plates are organized in this manner such that X rays from the source are absorbed by the Ta plate, and the subsequent X rays then produced by the Ta are of an energy that may then be absorbed by Cd. In the same way, Cd produces X rays that may be absorbed by Cu, while the majority of Cu X rays are attenuated by the Al cap before ever reaching the HPGe crystal. This also leads to an efficiency loss at lower energies, but above 200 keV, there remains around a 90% transmission rate, as depicted in Figure 3.21.

For these HPGe detectors, the intrinsic peak efficiency for γ rays of 1.33 MeV is about 21%. When placed in the array, the faces of the detectors are 25 cm away from from the source or target location, and for a complete sphere of 110 detectors, the HPGe detectors themselves cover 43.6% of the solid angle, while the combination of HPGe and BGO covers 48.0% [66, 70]. This leads to an absolute efficiency of 9.9% for γ rays of 1.33 MeV emitted at the center of the sphere. The impressive efficiency, solid-angle coverage, resolution, and background suppression of Gammasphere make it an indispensable tool for γ-ray spectroscopy,

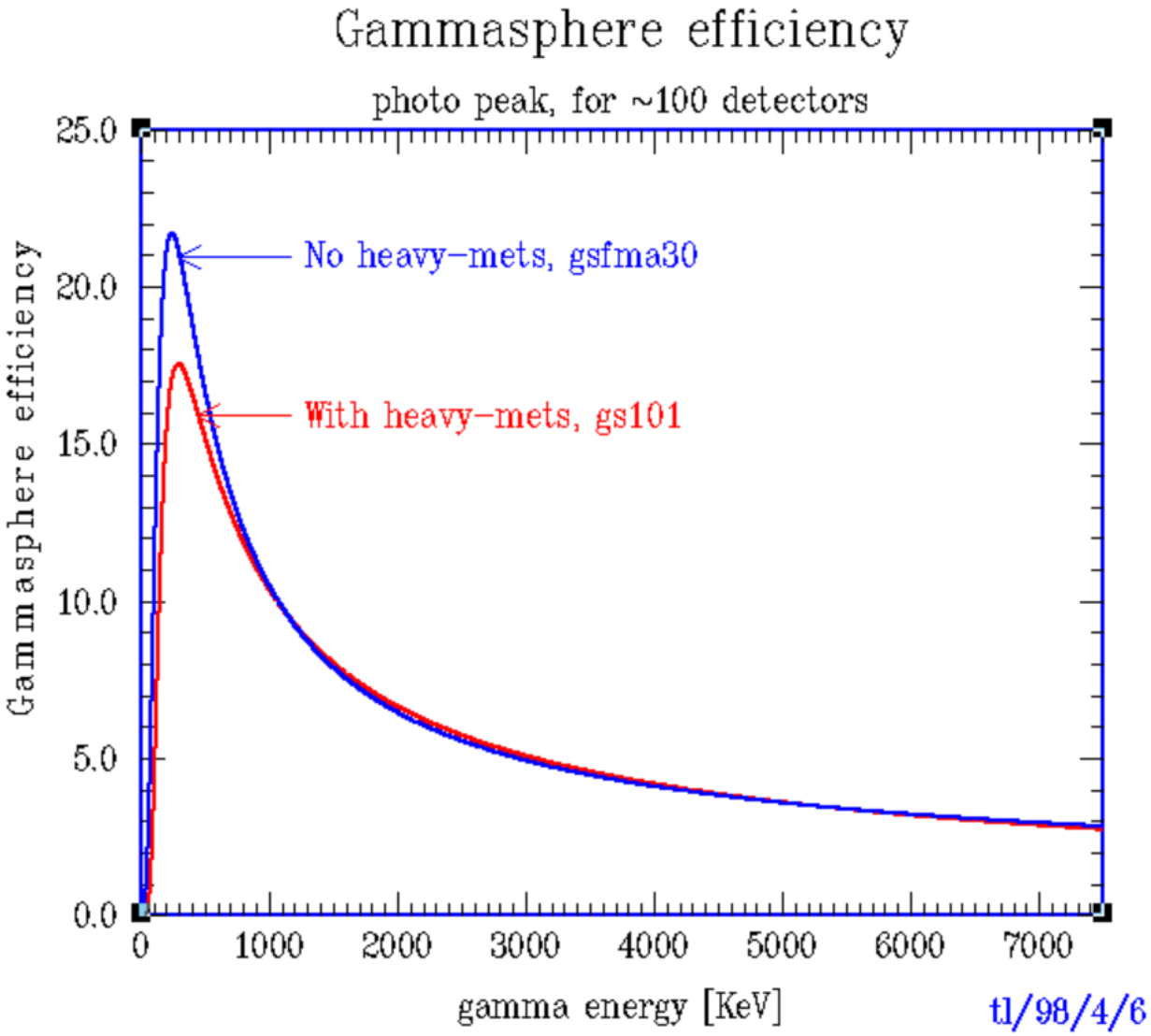

Figure 3.20: Efficiency curves for Gammasphere utilizing 100 detectors, with and without heavymets [68].

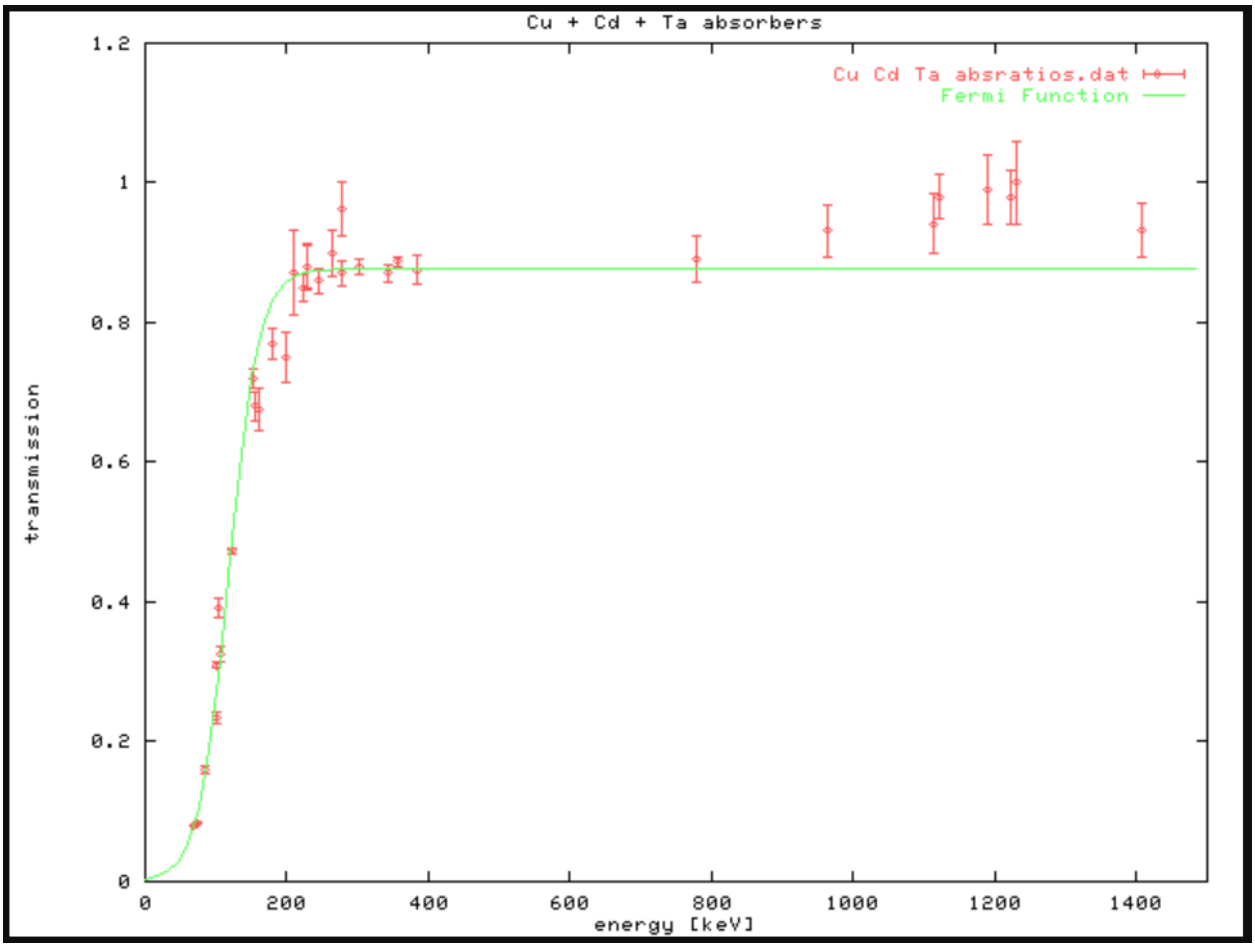

Figure 3.21: Transmission efficiency through Gammasphere absorbers as a function of energy [69].

in particular for events with high γ-ray multiplicity.

Section 3.6: Fragment Mass Analyzer

Another integral detection component for this experiment is a high-resolution mass spectrometry device located at ATLAS referred to as the Fragment Mass Analyzer (FMA). The FMA is an 8 meter-long recoil mass spectrometer, capable of separating ions, produced predominantly by fusion-evaporation with heavy-ion beams, based on their mass-to-charge ratio (A/q). As shown in Figure 3.22, the FMA is composed of two electric dipoles (ED), one magnetic dipole (MD), and two magnetic quadrupole doublets. A very basic explanation would state that the quadrupole doublets serve as focusing elements for the reaction products, and the centralized sequence of one magnetic and two electric dipoles removes unreacted beam while also spreading out the various reaction products according to their A/Z ratio. The residual ion species are then dispersed further and focused on the focal plane using the final quadrupole doublet. The diameters of the entrance and exit quadrupole apertures are 10 and 15 cm, respectively; the larger diameter aperture of the exit quads is to accommodate the dispersion of the ion species. In addition, several slits are located along the path of ions through the FMA that are used to clean up the spectra and suppress unreacted beam. The space optics of the FMA calculated by the general ion optics code GIOS are given in Figure 3.23 and further specifics of the optical components are provided in Refs. [71] and [72].

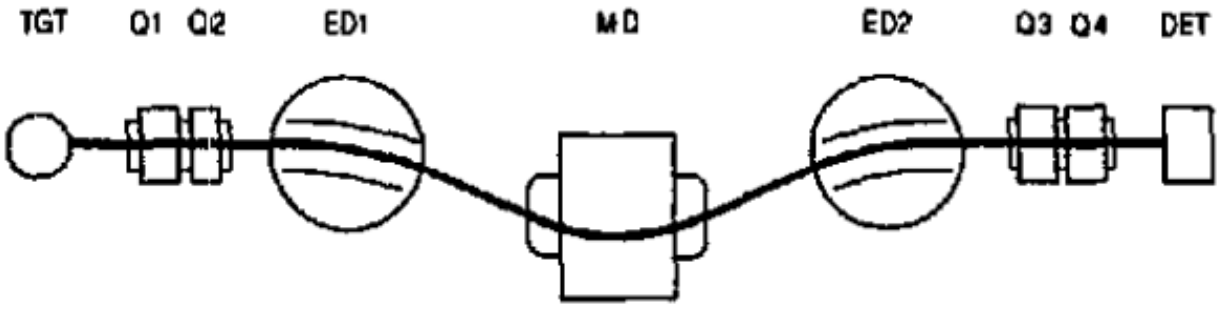

Figure 3.22: Basic schematic of the Argonne Fragment Mass Analyzer where "ED" and "MD" refer to electric and magnetic dipoles, "Q" indicates a quadrupole magnet, and TGT and DET specify target and detector, respectively [72].

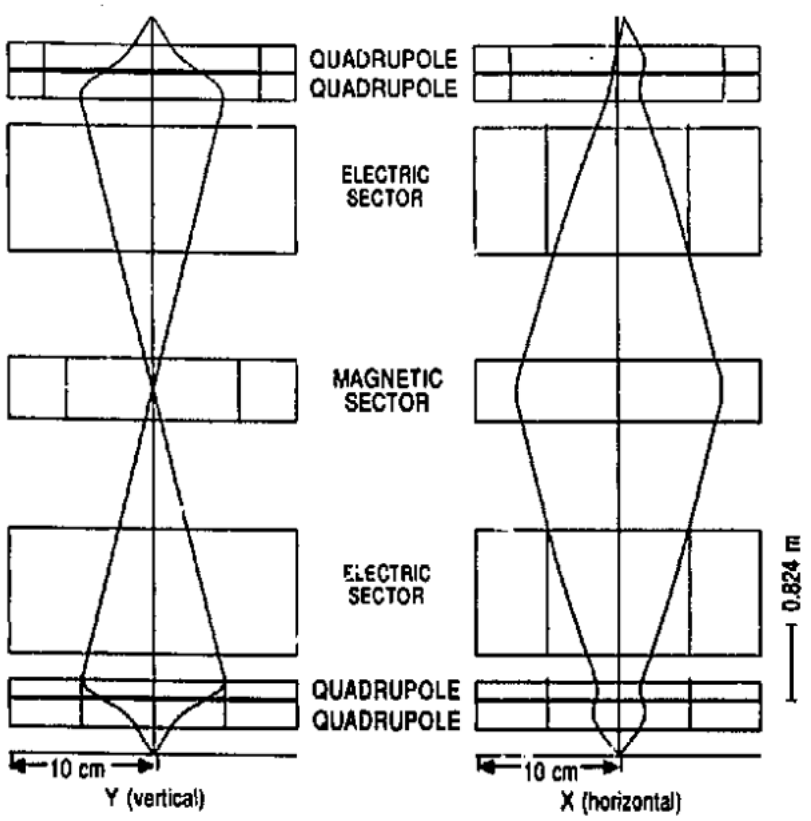

Figure 3.23: Diagram of the space optics of the FMA. Beam moves from bottom to top [72].

One of the strongest attributes of the FMA is its high acceptance capacity. The FMA has an energy acceptance of ±20% around the central energy and ±7% around the central mass-to-charge state. Another valuable characteristic of this instrument is its impressive resolving power. The A/q resolving power typical of the FMA amounts to roughly 10 mm/% relative to the central value. This means that for ions with mass A=100, the A/q peaks will be separated by about 10 mm [71]. The combination of these two attributes allows for a tool that is capable of examining a wide range of ion species at once, while simultaneously possessing a high degree of resolving power between each of these individual species. These properties were especially significant for this analysis because the central A/q chosen for this experiment was, in fact, not ^{64}Ni. The fact that this entire analysis, as well as several others, could be performed on an peripheral ion species is a testament to the strength of the FMA.

The more complex components of the FMA comprise the sequence of two electric dipoles

and one magnetic dipole located towards the center of the 8 meter track. The magnetic dipole, located between the two electric dipoles, is used primarily as an analyzing magnet for bending ion species of interest. It provides a uniform field with a maximum deflection angle of 40° and pole rotation angles of +7° at both the entrance and exit. The field strength has a maximum value of 1.1 T and is monitored by an NMR probe placed in a pocket within the magnet. Both electric dipoles are separated from the magnetic dipole by a distance of 1.2 m, in order to negate the first-order effects of the energy dispersion. It is also important to note that, as mentioned above, for this particular experiment, titanium attenuators had to be placed in front of the entrance to the FMA such that the reaction products could be suitably bent.

The electric dipoles used in the FMA have a unique and novel design as shown in Figure 3.24. Again used for bending of the reaction products and for removal of undesired species and scattered beam, the electric dipoles essentially consist of two titanium electrodes 26 mm thick, housed inside large cylindrical vacuum vessels. These electrodes are brought up to high voltage via Cockroft-Walton multiplier stacks, which are isolated from the vacuum chamber by a ceramic housing in order to prevent electrical breakdown. In order to further mitigate the possibility of breakdown, the ceramic housing is flooded with sulfur hexafluoride gas (SF_6), a gas commonly used as an electrical insulator. An important note is that the majority of the primary beam is stopped on the anode of the first electric dipole. However, because the excess current provided by the beam is a small fraction of that supplied by the multiplier stack, there are typically no adverse effects on the electrode. The majority of the primary beam is then removed ($\geq$99%) and the remaining ion species proceed through the rest of the FMA [72].

The FMA allows for 60 cm of variation in its radial position in order to accommodate large detector arrays. It also has the useful capability of rotating from $-5°$ to $+45°$ around the target, making it a useful tool for reaction mechanism studies, where the specific angular distribution of reaction products plays a major role. Additional types of experiments that

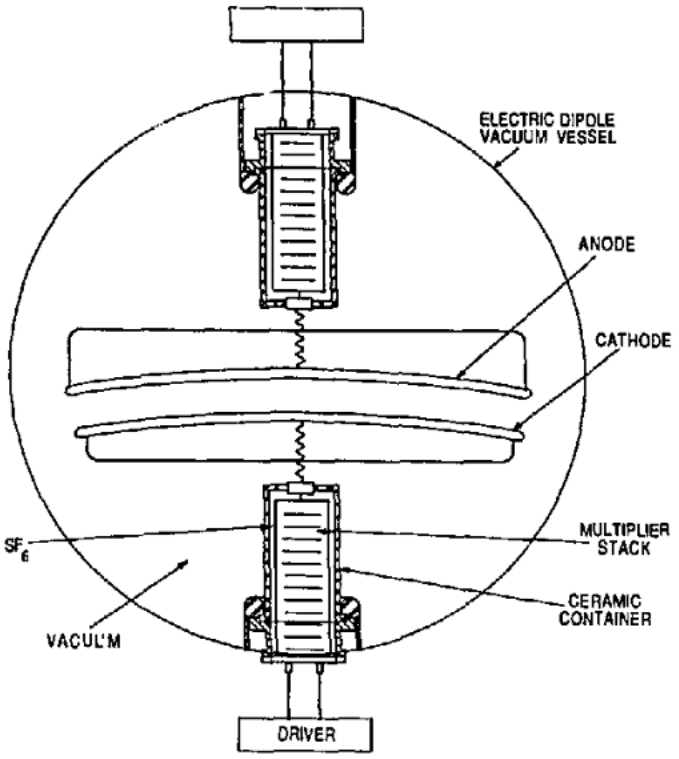

Figure 3.24: Schematic top view of an electric dipole, depicting the high-voltage power supplies and electrodes. Many details, including a number of high-voltage shields have been omitted for clarity [72].

utilize the FMA include Beta-NMR and nuclear moment measurements as well as recoil-isomer tagging [72, 73].

Section 3.7: Data Acquisition and Analysis

For the Coulomb excitation experiment, GRETINA and CHICO2 were utilized to collect γ-ray and particle data, respectively. Using GRETINA, the precise interaction position of the γ rays, including which and how many detectors fired, as well as the energy and timing information, was collected. The same was done with CHICO2 regarding the reaction products; i.e. the positions of the ions were obtained alongside their energy and timing information. As previously referenced, by obtaining the timing and position information from the product ions, it was possible to create a time-of-flight spectrum where ΔT, the time difference between the particle detection and the delayed RF pulse, was plotted as a function of the azimuthal angle. Such a spectrum is displayed in Figure 3.25. The spectrum of the forward hemisphere was separated into two, 90° halves, due to the sheer number of statistics, whereas the spectrum of the rear hemisphere encompassed the entire 180 degrees. Additionally, a slight aberration is noted in the figure around the 58° line that arises from the interference of the aluminum truss used to affix the mylar window, which can also be seen in Figure 3.14.

Due to the ample mass difference between Ni and Pb, there is a clear delineation between the two species in the time-of-flight spectrum. As one might expect, the lighter ^{64}Ni ions have a negative ΔT since they're detected just before the RF pulse, whereas ^{208}Pb is observed slightly afterwards, giving it a positive ΔT. In addition, the ^{64}Ni ions have a wider angular spread than that of ^{208}Pb. This makes it possible to gate specifically on the ions of interest, in this case ^{64}Ni, and obtain clean γ-ray spectra for analysis. Then, using CHICO2, the trajectories of the reaction partners could be determined on an event-by-event basis. Due to the utilization of a thin target, the γ rays emitted by the product nuclei were Doppler-shifted, so this information makes it possible to apply precise Doppler-shift corrections on γ

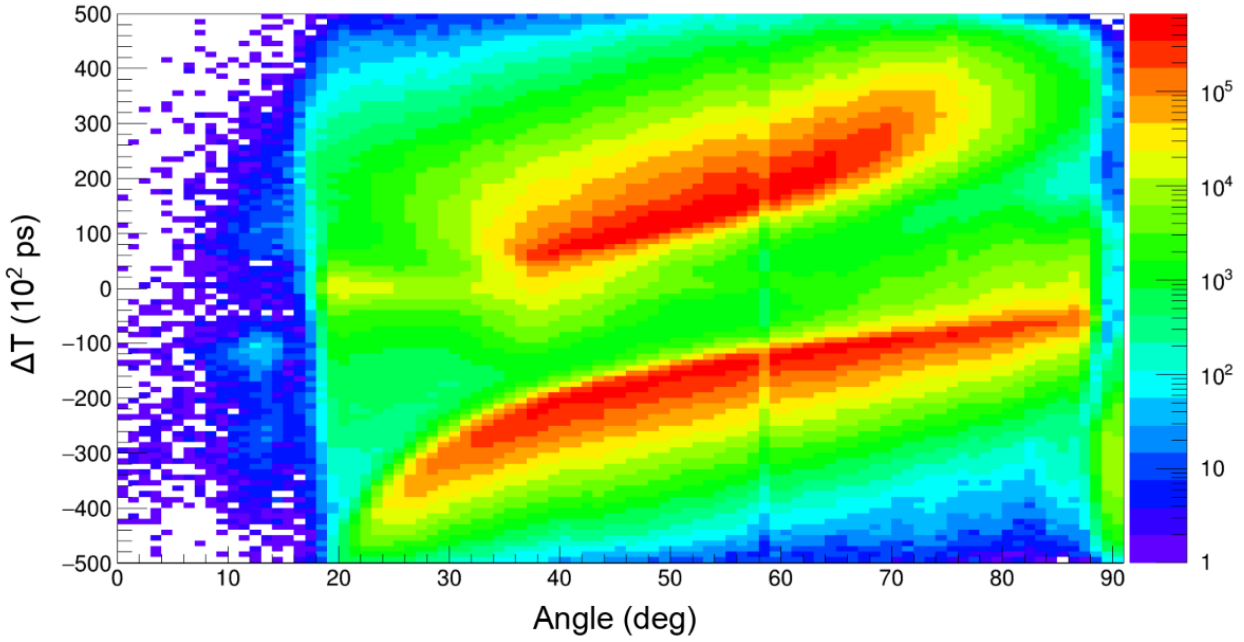

Figure 3.25: Time-of-flight spectrum as function of azimuthal angle produced by CHICO2 for the Coulomb excitation of ^{64}Ni on ^{208}Pb. The time-of-flight, ΔT, is measured with respect to the signal generated by the RF pulse of the accelerator. Here it is apparent that the two ion species, ^{208}Pb (top) and ^{64}Ni (bottom), can be easily separated from one another using the CHICO2 particle detector.

rays of interest observed with GRETINA.

For the data analysis, spectra were separated into seven angular ranges based upon the ^{64}Ni scattering angle: 30°-40°, 40°-50°, 50°-60°, 60°-70°, 70°-80°, 96°-130°, and 130°-166°, in order to study the dependence of the Coulomb excitation cross section probabilities on the scattering angle. Each of these seven γ-ray spectra were examined using Radware's "gf3" program [74], and all transitions known to be associated with ^{64}Ni were fit and their intensities determined. Examples of three different peak-fitting techniques using gf3 are shown in Figures 3.26, 3.27, and 3.28.

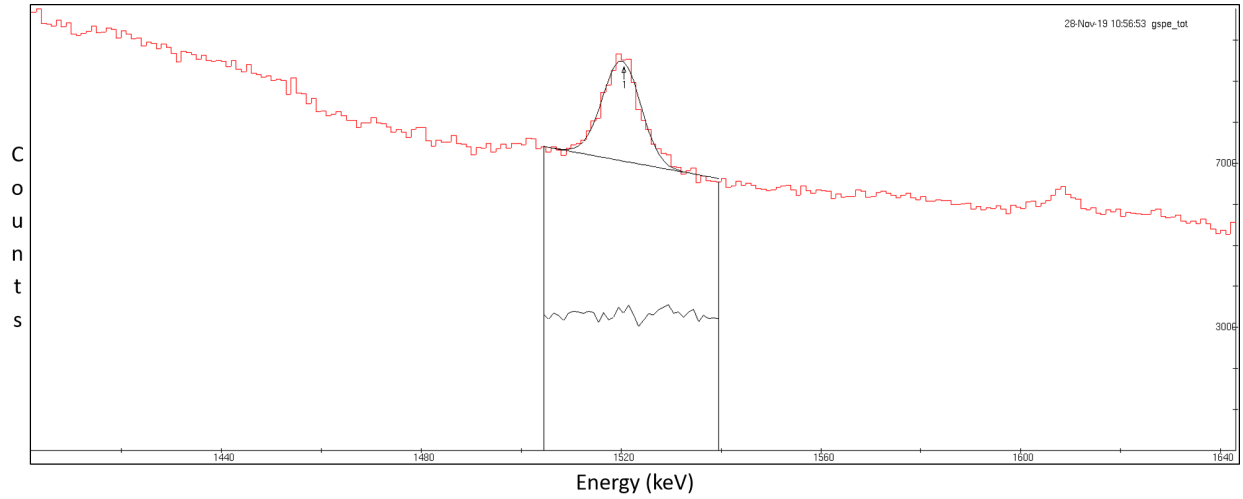

Figure 3.26: Peak fitting using the "New Fit" (nf) command in Radware's gf3 fitting program. By establishing the limits for the fit and identifying the number of peaks to be fit within that region, gf3 fits each specified peak with a Gaussian distribution based on several adjustable parameters. The peak area and errors are then extracted. Here, the peak area comprises everything underneath the calculated Gaussian fit but above the black background line. The jagged black line underneath the fit indicates the discrepancy between the calculated fit and the data, where a flat line would signify a perfect fit [74].

Subsequently, each of these intensity values were corrected for detector efficiency. As addressed previously, this was done using efficiency calibration sources, ^{152}Eu, ^{56}Co, and ^{243}Am, to generate a polynomial efficiency curve that determines efficiency as a function of energy. The resulting yields were then analyzed with the semi-classical Coulomb excitation code, GOSIA [46], a coupled-channel, least-squares fit code that derives matrix elements from a standard χ^2 analysis by comparing experimental yields to calculated ones. The precise

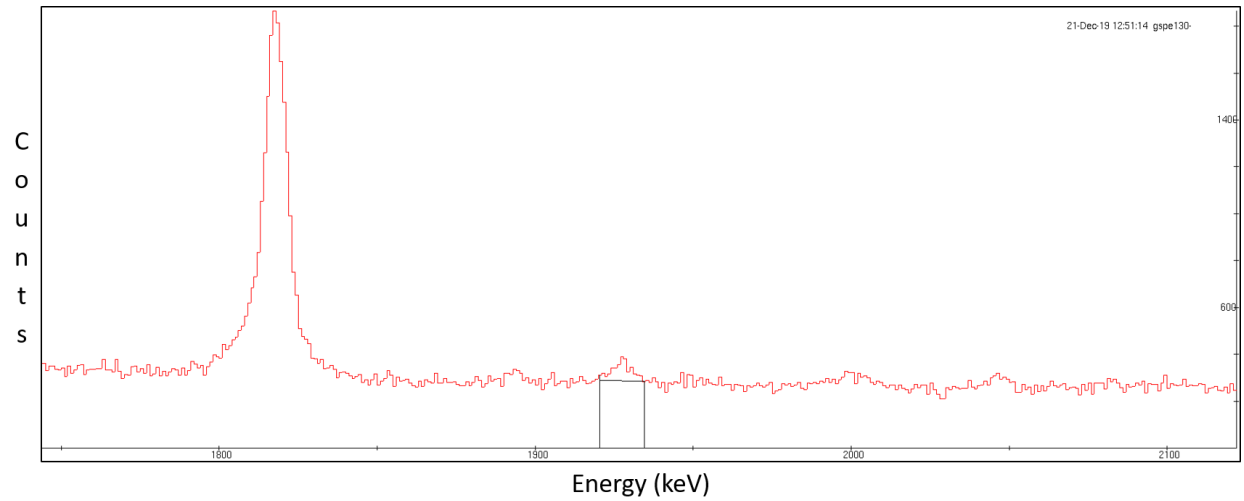

Figure 3.27: Peak fitting using the "Sum with Background subtraction" (sb) command in Radware's gf3 fitting program. By selecting a precise x and y position just above background on both sides of a peak, gf3 will draw a line directly between these two points. The peak area and errors are extracted. In this instance, the peak area consists of everything above the black background line, which is why it is important to ensure that the chosen limits are both at or above background. As one might discern, this is typically used as a rough method for estimating the area of a weak peak. It is for this reason that "sb" is often employed only as a last resort in order to extract peak areas that may not be attainable otherwise, or to provide an upper limit on the intensity of a very weak transition [74].

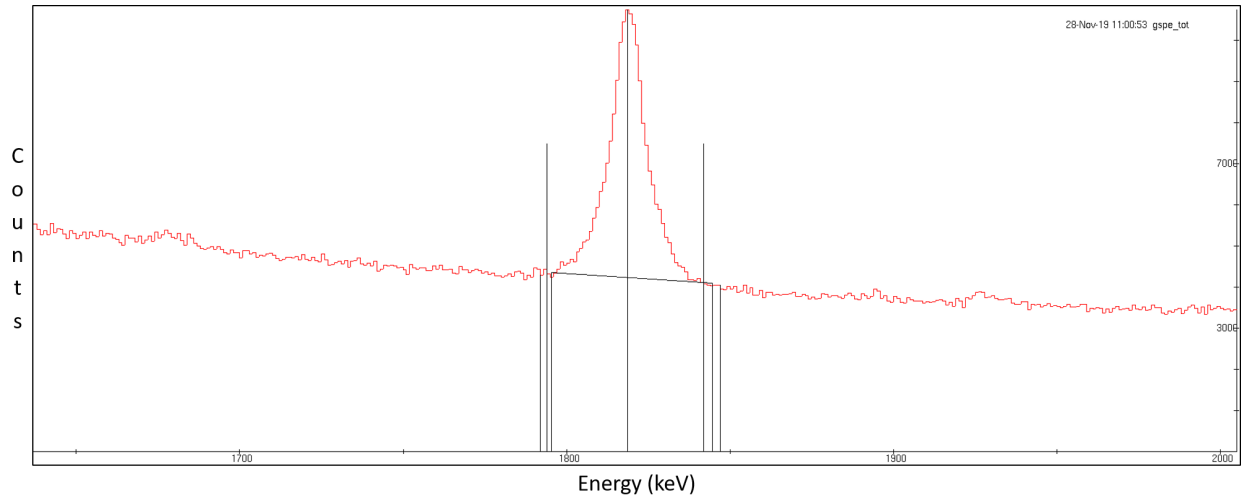

Figure 3.28: Peak fitting using the "PeaK" (pk) command in Radware's gf3 fitting program. By selecting the centroid of an individual peak, gf3 automatically determines the background below the peak, and the optimum peak integration limits. Then the peak area and errors are extracted. In this case, the peak area comprises everything above the black background line that lies within the fit limits. It is important to note that this command is not as successful with weak peaks. In those instances, the nf and sb commands are often more reliable [74].

experimental setup was incorporated into GOSIA, including the two dysfunctional forward detectors in CHICO2 (see above), in order to appropriately correct for the geometrical efficiency. Preliminary electromagnetic matrix elements were supplied to GOSIA as starting parameters for the χ^2 analysis. Using these parameters, as well as lifetimes, branching and mixing ratios, GOSIA compares the measured γ-ray yields to the calculated ones. At the onset, known matrix element values, lifetimes, branching and mixing ratios were included as constraints of the relevant parameters. Due to the lack of information available regarding ^{64}Ni, the only matrix element from the literature applied at the outset was that of the first-excited to ground-state transition ($2_1^+ \rightarrow 0^+$) corresponding to 0.268(5) eb determined in Ref. [75]. This value was fixed initially, but was then allowed to become a free parameter upon establishing the global minimum in order to gauge the reliability of the fit. Additionally, throughout the minimization process, literature lifetimes, branching and mixing ratios were added in order to perform a more informed and accurate fit. The literature values provided for this fit are expounded upon in the following chapter.

With regard to the deep-inelastic scattering experiment, the Gammasphere array and the FMA were employed to obtain γ-ray and particle data, respectively. Due to the fact that Gammasphere lacks the sophisticated segmentation and tracking algorithms of GRETINA, position information for each γ ray was determined based upon the HPGe detector in which it was observed. Energy and timing information for each γ ray was also collected using Gammasphere. The FMA was used to obtain the position, energy and timing information from each of the reaction products. By utilizing this information, it was possible to develop a series of particle spectra that could then be used to isolate the species of interest, this being ^{64}Ni in our case. The typical particle identification plots are shown in Figure 3.29. By plotting the energy deposition in the first two segments of the ionization chamber with respect to the total energy of the products, it was possible to separate the ion species by their proton number (Figure 3.29 (a)). The cut made to specifically isolate the nickel ions is shown in the figure as well. Then, using the position information gleaned by the MCP

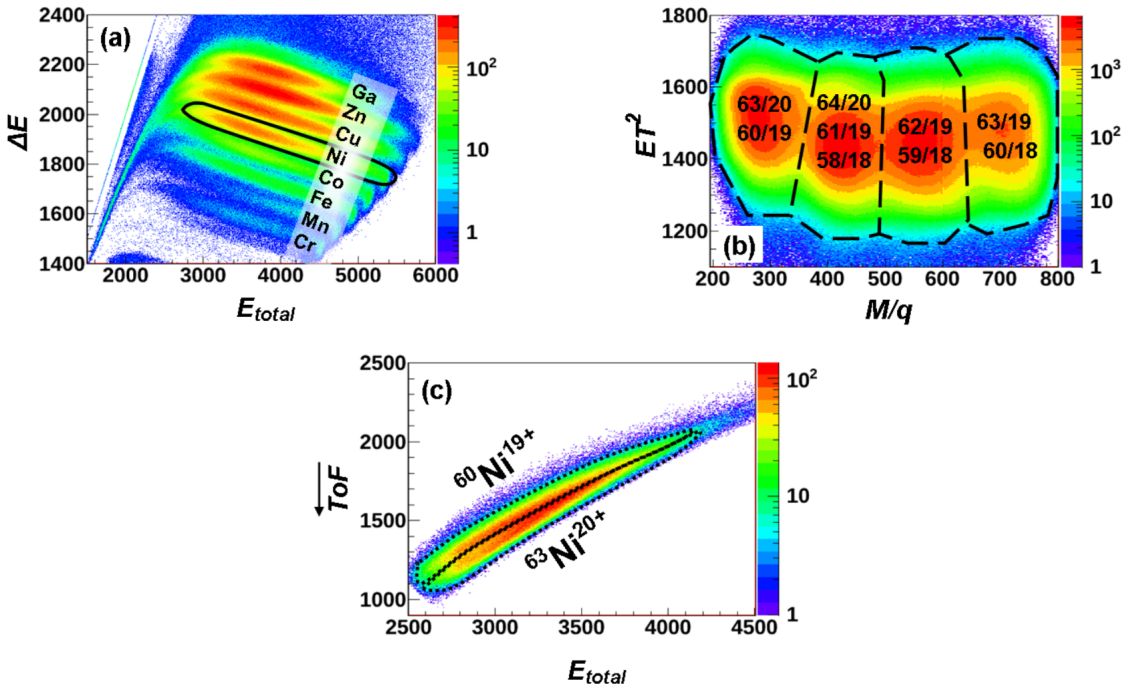

Figure 3.29: Example spectra depicting how the FMA is used to isolate ion species; (a) Energy deposited in the first two segments of the FMA ionization chamber, ΔE, as a function of the total energy of the ions, E_{total}. As the energy loss, ΔE, of the reaction products in the detector gas is Z-dependent, the various isotopic chains can be cleanly identified and separated. (b) After the ions are dispersed across the focal plane based on their mass to charge ratio, A/q, their position information is collected by the MCP and specific charge states can be isolated. Note the A/q ambiguities shown in this plot. (c) If ambiguities still exist after the first two gates, an additional gate can be employed by examining the time-of-flight as a function of the total energy. This helps alleviate the A/q ambiguities shown in (b). See Ref. [29] for further details.

detector, the Ni ions could be separated based on their A/q values (Figure 3.29 (b)). Often these two cuts may prove sufficient, but in this case it is evident in Figure 3.29 (b) that ambiguities remain in the A/q values, such that it was necessary to employ an additional coincidence gate. By gating on the time-of-flight with respect to the total energy of the ions, it was possible to achieve additional separation between the ambiguous A/q states (Figure 3.29 (c)). Finally, once the ion species of interest were isolated, γ-γ coincidence matrices were constructed containing all γ rays detected by Gammasphere in coincidence with these ions. Then, projecting these matrices along one axis results in pure "^{64}Ni" γ-ray spectra, which can subsequently be used for analysis.

After the ^{64}Ni spectrum from Gammasphere was obtained, Radware's "escl8r" program was used to place gates on different γ-ray transitions, allowing one to identify sequences and construct a level scheme of ^{64}Ni up to high-spin states based on the observed coincidence relationships. The total projection of the ^{64}Ni matrix as well the same spectrum gated on the 1346-keV transition are depicted in Figure 3.30. Despite the excellent resolution of the FMA, however, the ^{64}Ni spectrum produced by the γ-γ coincidence matrix still contained traces of what was identified as transitions assigned to ^{64}Cu (Figure 3.31).

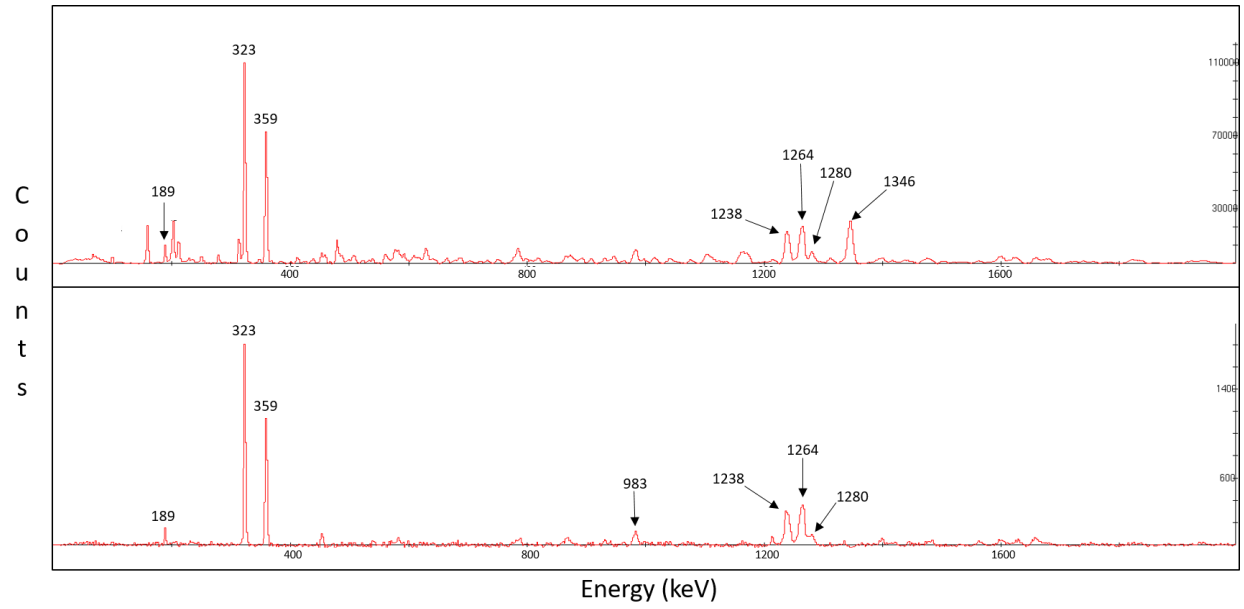

Figure 3.30: (Top) Total projection of the ^{64}Ni matrix obtained by employing the gates illustrated in Figure 3.29. (Bottom) ^{64}Ni matrix gated on the 1346-keV, $2_1^+ \rightarrow 0^+$ transition. Here, all γ rays associated with the yrast sequence identified in Ref. [25] can be seen.

Owing to the contamination and the low statistics of the resulting gated ^{64}Ni spectrum, it was important to employ the entire γ-ray matrix of all ions in conjunction with the ^{64}Ni gated matrix in order to obtain information on some of the less intense peaks. This was done using Radware's "4dg8r" package, which allows one to gate on up to 3 γ rays simultaneously, as opposed to "escl8r" which only enables a single coincidence gate. By using the full coincidence matrix and then triple- or quad-coincidence gating on the characteristic 1346-keV peak produced by the decay of the first excited state in ^{64}Ni, as well as one or

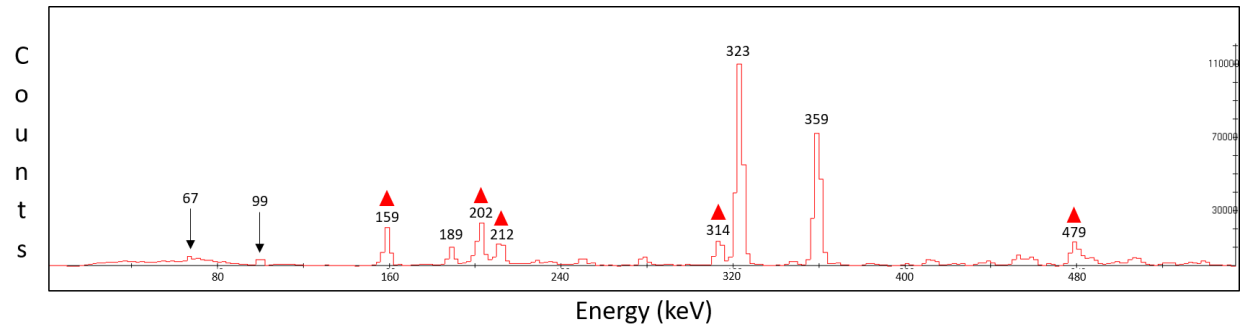

Figure 3.31: Low-energy region of the total projection of the ^{64}Ni matrix obtained by employing the gates illustrated in Figure 3.29. Transitions marked by red triangles are those known to be associated with the contaminant ^{64}Cu.

two other strong yrast transitions, it was possible to obtain a variety of very pure (i.e. contaminant-free) gated coincidence spectra from which new transitions could be identified and characterized. An example of the total spectrum comprising the γ rays of all ions, as well as the same spectrum with a quadruple-coincidence gate applied using only known transitions from ^{64}Ni, are displayed in Figure 3.32.

Finally, the data were re-sorted by separating Gammasphere detectors by angles into a series of 10 rings along the beam axis, specified by azimuthal angles of 31.7°, 37.4°, 79.2°, 80.7°, 90.0°, 99.3°, 100.8°, 142.6°, 148.3°, and 162.7°. From this, two histograms were created: one combined the γ-ray spectra measured at the forward- and rear-most angles. That is to say that the spectra for angles below 79.2° and above 142.6° were summed together into a single histogram designated as "0°". A second, "90°", histogram was created by summing the spectra of all the central Gammasphere detectors between 79.2° and 142.6°. The intensities of each identified ^{64}Ni peak in both the 0° and 90° spectra were again extracted using Radware's gf3 [74] peak-fitting package and, subsequently, corrected for detector efficiency using a polynomial efficiency curve obtained from the ^{56}Co, ^{152}Eu source measurements. In the process of extracting the intensities of each peak for both of the angular assignments, a coincidence gate was placed on the 1346-keV $2_1^+ \rightarrow 0^+$ transition to obtain a pure ^{64}Ni spectrum. Thus, the intensities of all transitions measured at 0° and 90° were extracted from a spectrum gated on this transition, aside from the 1346-keV γ ray itself, whose intensity

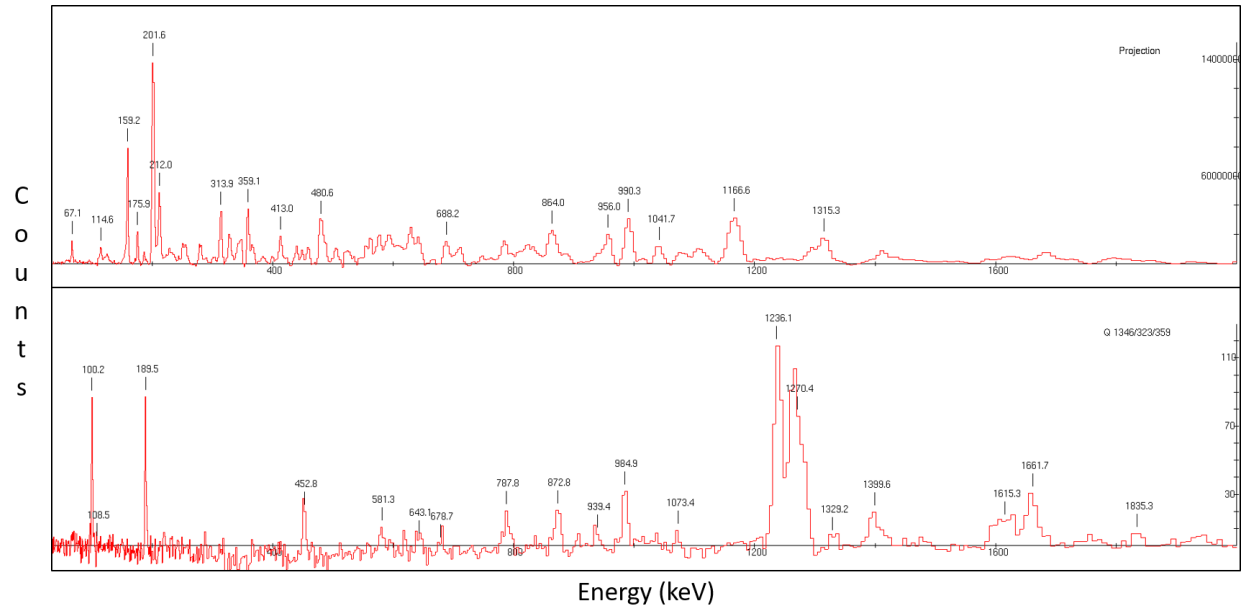

Figure 3.32: (Top) Total projection of the complete γ-γ matrix obtained by Gammasphere, containing γ rays from every reaction product. Note that only the intense 359-keV transition from ^{64}Ni is readily apparent, potentially because it may be contaminated by other ion species as well. (Bottom) A quad-coincidence spectrum gated on the three most intense transitions from ^{64}Ni, identified as 1346, 323, and 359 keV. This produces a clean ^{64}Ni spectrum from which new transitions could be extracted. Combinations of gates employing these three, as well as other transitions, can be used to examine different regions of the ^{64}Ni level scheme. The spectrum is expanded for clarity.

was obtained by gating on the most intense ^{64}Ni transition observed, corresponding to the 323-keV decay. It was then possible to take a ratio of each peak intensity at 0° and 90°. This ratio, often referred to as the directional correlations (DCO) ratio, is indicative of the multipolarity of the associated γ ray [76]. Simply put, if the intensity of a particular γ ray is higher at 0° than it is at 90°, the DCO ratio will be larger than 1, indicating that the transition is likely of E2 character. Conversely, if the DCO ratio is less than 1, the γ ray most likely possesses either E1 or M1 multipolarity. Using the calculated DCO ratios, it was then possible to propose spins and sometimes parity to the newly discovered, higher-lying states. Relative intensities were also obtained with respect to the 323-keV γ ray, which was chosen specifically due to it having the largest intensity of all transitions in the spectrum. The results of both experiments will be addressed in the following chapter.

CHAPTER 4: Results

Section 4.1: Coulomb Excitation

Beginning with the results obtained from Coulomb excitation, an example of a spectrum obtained in coincidence with ^{64}Ni projectiles is presented in Figure 4.1. This spectrum assumes the kinematics adequate for the projectile rather than the target; i.e., the Doppler-shift correction has been applied assuming an energy and trajectory corresponding to ^{64}Ni. The γ rays labeled in the spectrum of Figure 4.1 can be associated with known transitions in ^{64}Ni [25], with the exception of the Doppler-broadened peak centered at 2614 keV that arises from the decay of the first excited state in ^{208}Pb ($3^- \rightarrow 0^+$), for which the applied Doppler-shift correction is inappropriate. The level diagram comprising the thirteen ^{64}Ni transitions observed in this experiment is given in Figure 4.2, and the intensities for each of these γ rays were extracted for every angular segment in which they were observed. In addition to these transitions, several other weak peaks were also identified within the spectrum. However, these could not be positively associated with ^{64}Ni. In order to determine whether or not a peak originated from a transition in ^{64}Ni, it was tracked across each of the seven angular segments in order to examine its behavior. If the intensity of the peak fluctuated inconsistently, or if the centroid shifted more than 2-3 keV from angle to angle, this implied an inappropriate Doppler-shift correction, indicating that the γ ray was most likely a contaminant and, thus, was not considered in the extraction of relevant yields. The correction for detector efficiency varied based upon the energy of the observed γ ray and was applied using the calculated efficiency curve for GRETINA illustrated in Figure 4.3. Our method of assessing the background was briefly discussed in the methods chapter, but here we will elaborate further on how the background was determined specifically for certain peak

shapes observed in the Coulomb excitation spectra. Initially, spectral regions on both sides of a peak were examined and, if the rate of change of these two regions appeared constant, a straight background line could be drawn directly from one region to the other, above which, all the counts were integrated and considered as part of the peak intensity. However, if the background regions adjacent to the peak of interest appeared to exhibit some curvature (a changing slope), the background was fit differently depending upon the fitting command used in the gf3 code. Using the fitting command "sb", the user specifies the location of two points in the spectrum, between which a straight background line is drawn, and all counts above this line are integrated into the peak. The command "pk" works similarly in the sense that a straight background line is drawn from one edge of the automatically-fitted region to the other, above which, all counts are incorporated. Lastly, the "nf" command fits more complex backgrounds through the combination of a step function and a smoothing function, the weights of which may be altered individually in order to obtain a fit that more accurately contours the background region. The latter of these three methods is naturally the most complex, but often proves to be the most versatile when fitting non-linear background shapes. The appropriateness of a fit can be judged from the χ^2 value obtained.

Spectra depicting the variations in peak intensity from $50^\circ - 166^\circ$ are provided in Figures 4.4 and 4.5. For convenience, these spectra are focused on the energy region containing the transitions from the two excited 0^+ states of interest, corresponding to γ rays of energies 1522 ($0_2^+ \rightarrow 2_1^+$) and 1680 ($0_3^+ \rightarrow 2_1^+$) keV. The 1606-, $4_4^+ \rightarrow 4_1^+$, and 1626-keV, $2_3^+ \rightarrow 2_1^+$, transitions are also visible in this range. Furthermore, this series of spectra serves to reinforce the importance of the contributions by ions detected at backward angles, as it is apparent how quickly the intensities of these weaker peaks are overwhelmed by the Compton background as one moves toward small scattering angles. In fact, angles less than 50° were not included in the aforementioned figures precisely due to the absence of any and all peaks in the specified region. Indeed, at these most forward angles, Compton background — mostly from the 2614-keV transition ^{208}Pb transition — dominates the spectra as expected for a one-step

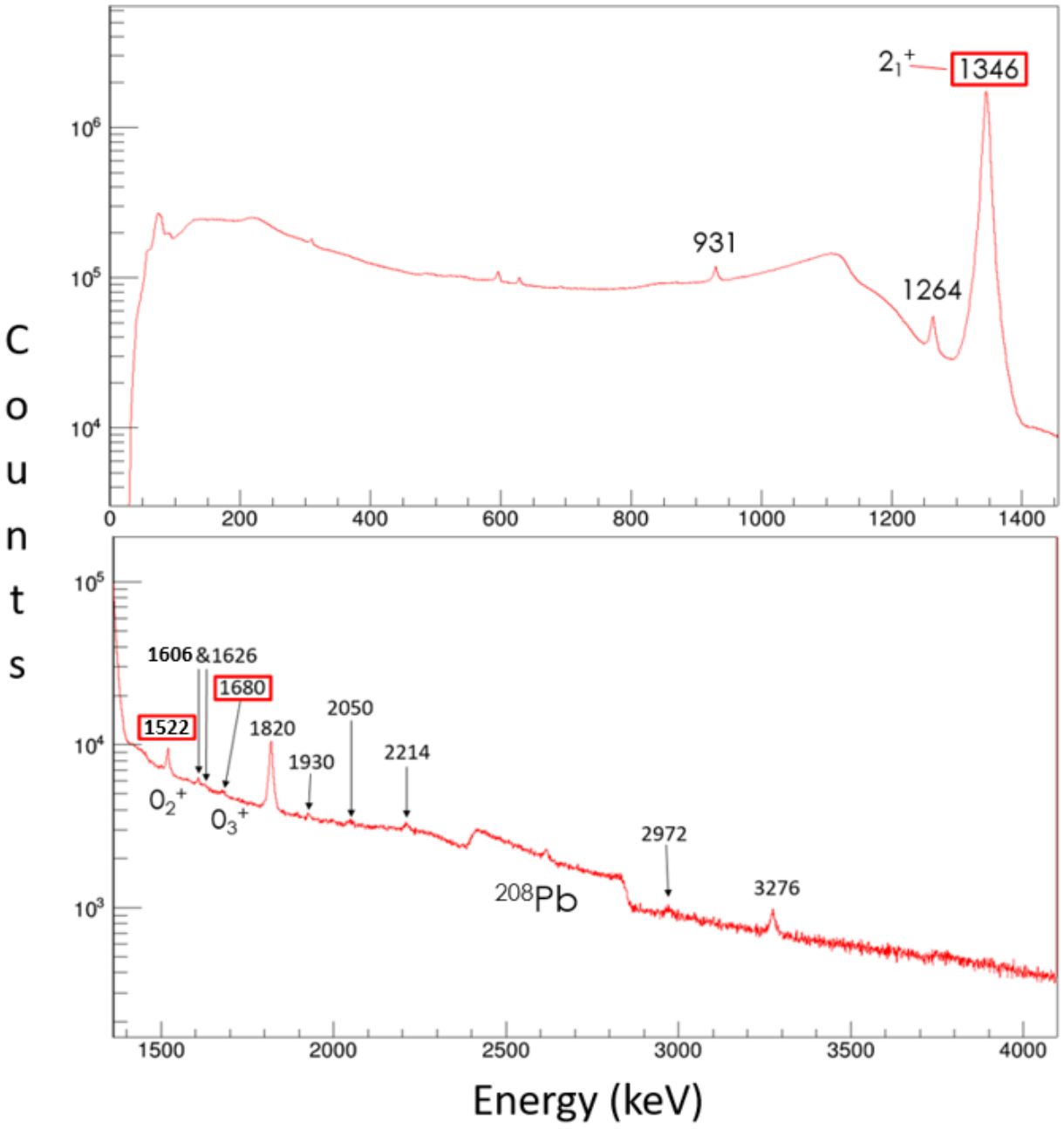

Figure 4.1: Total γ-ray spectrum obtained from Coulomb excitation, encompassing the full azimuthal range for CHICO2. The spectrum has been corrected for the Doppler shift assuming a ^{64}Ni kinematics. All labeled γ rays are associated with transitions in ^{64}Ni. The three most significant transitions are placed in boxes, and correspond to the $2_1^+ \rightarrow 0_1^+$, $0_2^+ \rightarrow 2_1^+$, and $0_3^+ \rightarrow 2_1^+$ transitions, respectively.

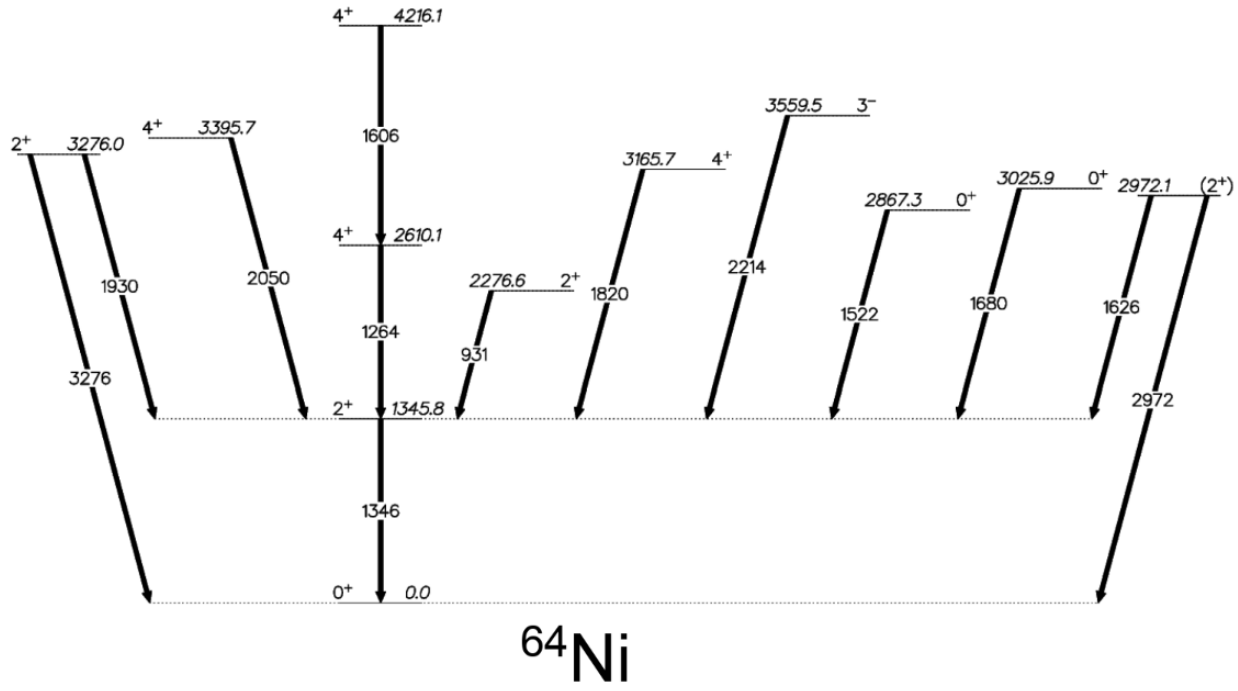

Figure 4.2: Level scheme depicting all thirteen known ^{64}Ni transitions observed in this Coulomb excitation experiment. Parentheses indicate tentative spin-parity assignments.

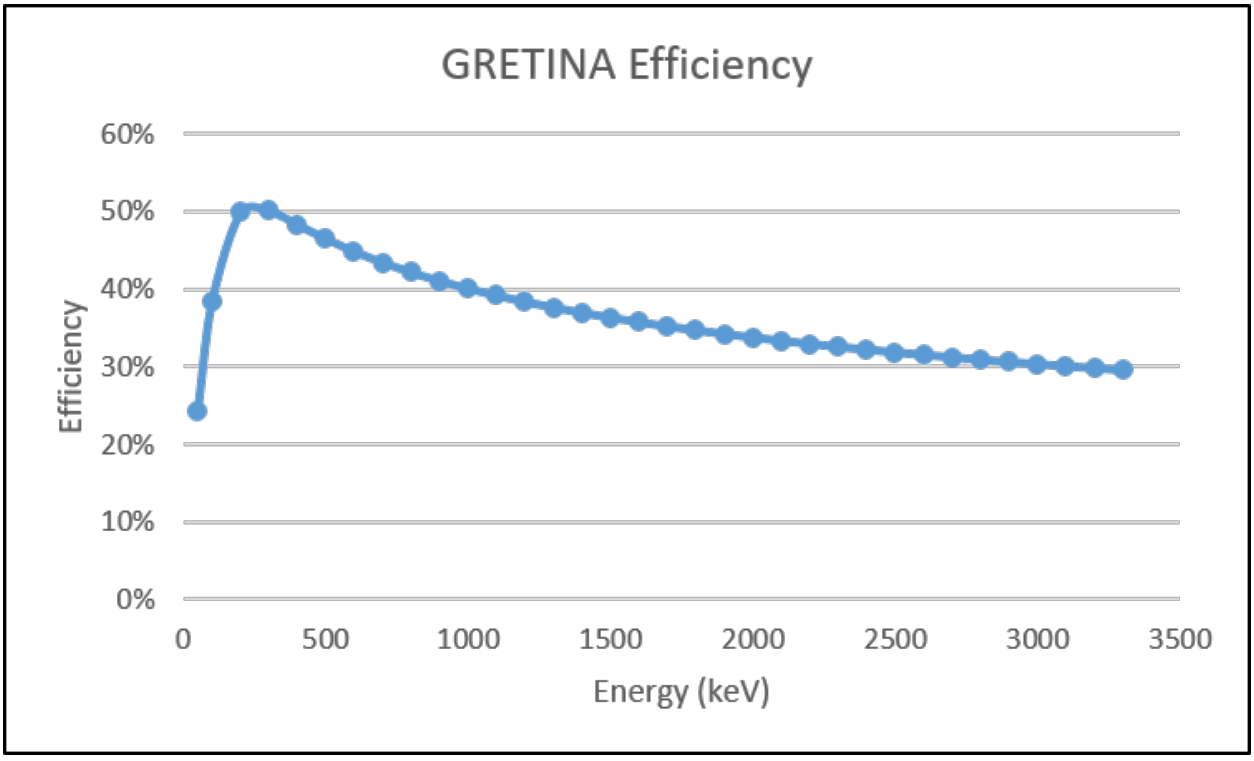

Figure 4.3: Detector efficiency curve for GRETINA deduced from γ-ray measurements with ^{152}Eu, ^{56}Co, and ^{243}Am sources. This curve was used to correct γ-ray yields obtained from spectra for detector efficiency.

process.

Six low-energy peaks were observed at energies of 308, 484, 545, 583, 595, 627, and 691 keV, none of which were utilized for GOSIA calculations for various reasons explained below. Two of the peaks, those at 545 and 583 keV, grew from about 30°-85° and then were not present at backwards angles, which is contrary to what would be expected when examining transitions from the ion of interest. It is true that a 583-keV γ ray is known to be associated with ^{64}Ni as a de-excitation of the 3749-keV, 4_1^- state. However, the shifting of the centroid of this peak from angle to angle, in combination with the fact that it is very unlikely to feed a 4_1^--spin state via Coulomb excitation, led us to determine that this peak was most likely a contaminant, and, thus, it was excluded from the fit. The peaks located at 308 and 484 keV could not be identified and have never before been reported in any ^{64}Ni study [77]. Without γ-γ coincidence data, the origins of these peaks could not be verified, and, consequently, they were not included in the fit. Both the 626- and 691-keV transitions have, in fact, been observed in this nucleus previously, but were not supplied to GOSIA for different reasons. The 627-keV γ ray appears in a cascade with, and just above, a 236-keV one, and lies in series with the yrast 1238-keV transition (Figure 1.4), but neither of the latter two transitions were observed. The 627-keV transition also lies in a sequence with the observed 2050-keV ($4_3^+ \rightarrow 2_1^+$) one, however none of the γ rays linking these two (such as the 236- or 453-keV ones identified in Figure 1.4) were seen either. Beyond this, the peak centroid appeared to shift inconsistently with respect to the angle, indicating that it may, in fact, be a contaminant that simply lies at the same energy as the known transition for specific angular ranges. For this reason, the transition was not included. The 691-keV γ ray could unfortunately not be used because it sits atop a known neutron-induced peak in ^{72}Ge, making it impossible to obtain an accurate yield. Attempts were initially made to utilize this yield for the GOSIA fit, but it was clear that the intensity of the peak fluctuated inconsistently from angle to angle and, thus, the decision was made to exclude it. Lastly, the 595-keV peak was identified with another neutron-induced peak in ^{74}Ge, and so this one was

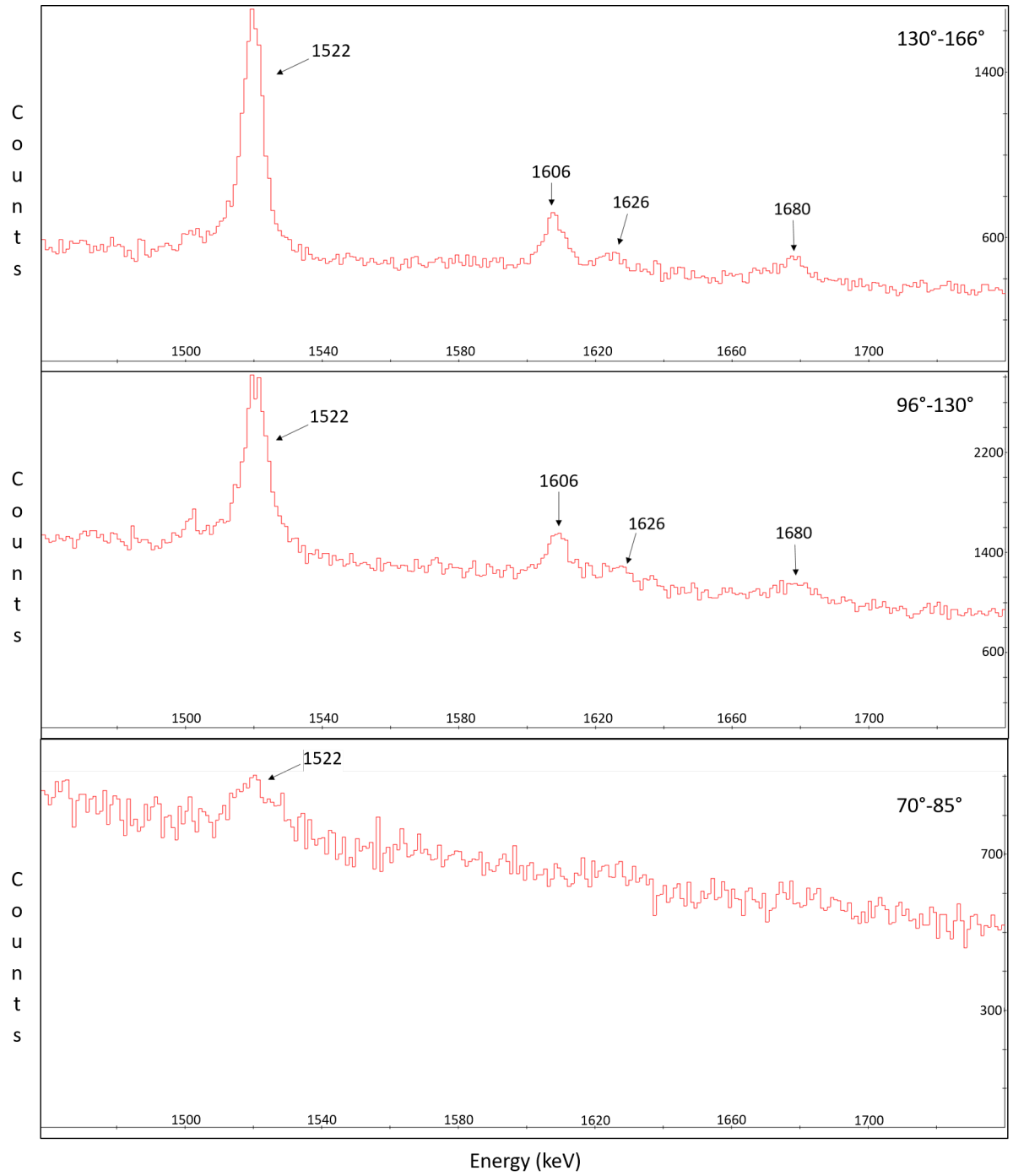

Figure 4.4: Spectra corresponding to the three rearmost angular segments: $130° - 166°$ (top), $96° - 130°$ (middle), $70° - 85°$ (bottom). Spectra are expanded to focus on the region pertaining to the 1522- and 1680-keV transitions from the 0_2^+ and 0_3^+ excited states, respectively. Note the significant decrease in peak intensity while moving toward forward angles. This, as well as Figure 4.5, serves to illustrate the importance of γ-ray detection at backward angles.

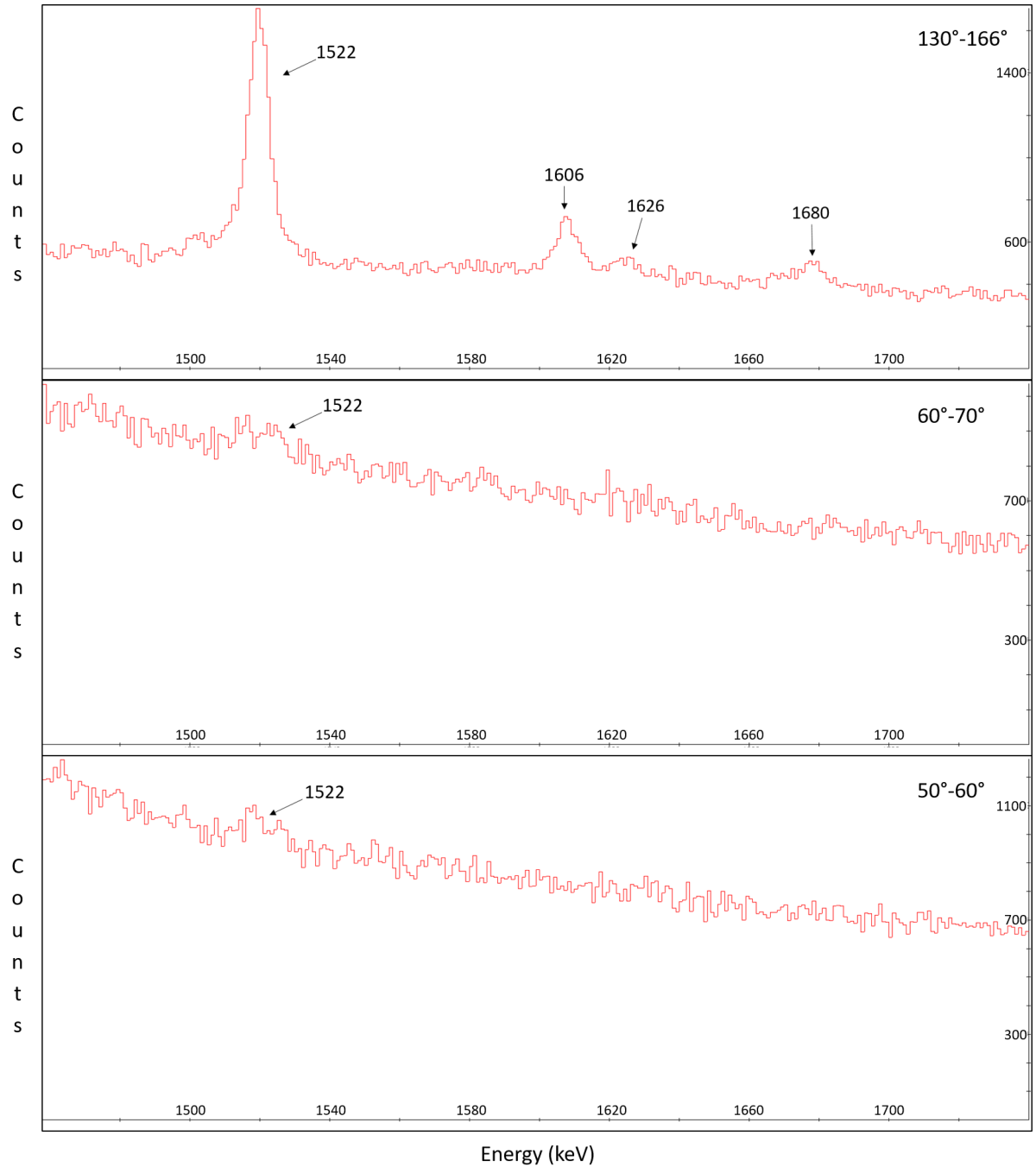

Figure 4.5: Spectra associated with the rearmost angular segment ($130° - 166°$) (top), and two front segments corresponding to ranges of $60° - 70°$ (middle), $50° - 60°$ (bottom). Spectra are expanded to focus on the region pertaining to the 1522- and 1680-keV transitions from the 0_2^+ and 0_3^+ excited states, respectively. Here, the difference between rear and forward angles is even more pronounced than in Figure 4.4. The two forward-most angular segments were not included in these figures due to the complete absence of the peaks of interest in this energy range. It is clear from these figures that γ-ray detection at backward scattering angles is integral to multi-step Coulomb excitation experiments. See text for further details.

avoided as well. A list of known neutron-induced background lines in germanium detectors is provided in Ref. [78].

As stated above, the level scheme depicted in Figure 4.2 displays the thirteen ^{64}Ni transitions that were observed in this experiment. Ten of these γ rays were previously observed in Ref. [25], the most recent work on ^{64}Ni, where excited states were populated via quasi-elastic and deep-inelastic reactions of a 430-MeV ^{64}Ni beam on a thick ^{238}U target. The remaining three γ rays placed in the figure include a 1606-keV transition from a tentative 4^+ state at 4216 keV, and two transitions of 1930 and 3276 keV connecting an excited 2_4^+, 3276-keV level with the first-excited and ground states, respectively. These three transitions had also been observed previously [79]. Of the observed γ rays, the two most significant ones for the present work are the 1522- and 1680-keV transitions linking the two known 0^+ excited states of 2867 and 3026 keV, with the 2_1^+ state at 1346 keV. This is because these two levels could possibly be associated with different ^{64}Ni minima along the potential energy surface, and, thus, they possess a potential for nuclear deformation and shape coexistence. It is also important to note the difference in the general feeding pattern between this work and the deep-inelastic experiment performed in Ref. [25]. As previously mentioned, while deep-inelastic reactions tend to populate a number of high-spin, yrast states, Coulomb excitation populates a wide range of low-spin levels showing less preference for feeding along the yrast line. The observation of both excited 0^+ states as well as the three γ rays not observed in Ref. [25] are indicative of this difference in feeding. While these 0^+ excited states were still observed in deep-inelastic scattering, it was at nowhere near the intensity provided by Coulomb excitation.

As discussed in the previous chapter, once the γ-ray yields were extracted from the spectra and corrected for detector efficiency, they were utilized by the Coulomb excitation analysis code GOSIA to perform a χ^2 minimization from which the matrix elements could be determined. However, in order to carry out an accurate minimization, known matrix element values, lifetimes, branching and mixing ratios were also supplied to GOSIA to be

used as constraints of the relevant parameters. Literature branching ratios included three decay modes from the 2972-keV (2_3^+) state leading to the ground, first-excited, and second 2^+ (2_2^+, 2277 keV) levels, as well as a branching ratio for the de-excitation of the 2_4^+ state at 3276 keV, i.e. the intensity ratio between the 3276- and 1930-keV transitions. All branching ratios are imposed as the ratio of a single decay mode relative to another, so the applied branching ratio between the 695-keV and 1626-keV transitions from the 2972-keV state was 0.8(3), while that between the 2972-keV and 1626-keV γ rays was 0.6(2) [80]. The branching ratio used for the de-excitation of the 3276-keV level to the ground versus the first-excited state was 0.33(10) [81]. The measured lifetime for the first excited state of 1.47(7) ps [82] was included along with a single mixing ratio of 0.75(20) for the 931-keV, $2_2^+ \rightarrow 2_1^+$ transition [83]. Lastly, it is important to note that GOSIA only considers relative yields and, consequently, all yields were normalized to the 1346-keV, $2_1^+ \rightarrow 0_1^+$ transition. All our reported reduced matrix elements were determined from the χ^2 minimization process.

Once all the desired literature values, detector setup, and experimental yields were supplied to GOSIA, it was possible to begin a χ^2 minimization. During the fit, GOSIA uses the supplied values for matrix elements, lifetimes, etc. to calculate yields for each observed transition. These yields are then compared to those determined experimentally and a χ^2 value is calculated, quantifying the difference between these two sets of values. Then, GOSIA adjusts the matrix elements within their allowed uncertainties and attempts another fit. This iterative process continues until a minimum is reached. At this point, one may choose to "fix" certain matrix elements while others remain free parameters. For example, one may choose to fix all matrix elements involving a specific level while freeing the rest, or vice versa. By changing which matrix elements are fixed and which are allowed to vary, and then proceeding with further minimizations, it is possible to avoid trapping into local minima and improve chances to move the fit towards the actual global minimum. However, if this method does not succeed in bypassing a local minimum, or if there remains a doubt on the issue, it may be necessary to manually alter one or more of the matrix elements in order to proceed with

the minimization. By examining the agreement between the calculated and experimental γ-ray yields, it is sometimes obvious which matrix elements should be adjusted in order to improve the fit. For instance, if one reaches a local minimum where the calculated yield for the 931-keV, $2_2^+ \rightarrow 2_1^+$ transition varies significantly from the experimental one, it likely makes sense to manually adjust the matrix element for that transition, or to allow variations of all matrix elements involving those two states while fixing most, if not all of the others. Additionally, if a matrix element starts to become unusually large ($\geq$ 1.5 eb), this may also be an indication that it should be adjusted manually. It is also important to note that, once the fit has been released from a local minimum, after a few iterations, any manually adjusted or otherwise fixed matrix elements should once again be freed in order to perform an appropriate minimization. These two approaches, fixing/loosening and manual adjustment, are applied as needed throughout the minimization process. The global minimum is achieved once the χ^2 value for the fit is at or near 1, and cannot be further reduced through application of the aforementioned approaches. All in all the process is time-consuming and requires constant attention, but reaching results in which one has confidence comes at this cost. After the global minimum is reached, the matrix elements, reduced transition probabilities, and the errors associated with these quantities can be extracted. These quantities, including transition strengths given in both e^2fm^4 and Weisskopf (single-particle) units, are provided in Table 4.1.

When carrying out the GOSIA analysis, it is entirely at the user's discretion which matrix elements should be considered. If one desires, it is possible to include matrix elements for every possible pairing of states; however, this often leads to the system being overly constrained, making minimization challenging, if not impossible. For this reason, many matrix elements are excluded from the fit, predominantly those corresponding to forbidden transitions. This also means that some matrix elements are included in the procedure that may, in fact, not correspond to directly observed transitions. Matrix elements listed in Table 4.1 without an associated γ ray were those calculated by GOSIA without an experimental

$E(keV)$	$I_i^\pi \to I_f^\pi$	$Mult(\pi\lambda)$	$E_\gamma(keV)$	$< i\|M(E2)\|f >^*$	$B(\pi\lambda_\downarrow; i \to f)^*$	$B(\pi\lambda; i \to f)W.u.$
1345.8	$2_1^+ \to 0_1^+$	E2	1346	0.268(16)	140(20)	9(1)
2276.6	$2_2^+ \to 0_1^+$	E2		$0.005^{+0.002}_{-0.001}$	$0.05^{+0.05}_{-0.02}$	$0.003^{+0.003}_{-0.001}$
2276.6	$2_2^+ \to 2_1^+$	E2	931	$0.149^{+0.007}_{-0.004}$	44^{+4}_{-2}	$2.9^{+0.3}_{-0.2}$
2276.6	$2_2^+ \to 2_1^+$	M1	931	1^{+1}_{-3}	$0.1^{+0.6}_{-0.1}$	$0.07^{+0.32}_{-0.07}$
2610.1	$4_1^+ \to 2_1^+$	E2	1264	$0.244^{+0.013}_{-0.008}$	66^{+7}_{-4}	$4.4^{+0.5}_{-0.3}$
2610.1	$4_1^+ \to 2_2^+$	E2		$0.42^{+0.05}_{-0.03}$	200^{+50}_{-30}	13^{+3}_{-2}
2867.3	$0_2^+ \to 2_1^+$	E2	1522	0.070(2)	48(3)	3.2(2)
2867.3	$0_2^+ \to 2_2^+$	E2		0.27(4)	700(200)	50(10)
2972.1	$2_3^+ \to 0_1^+$	E2	2972	0.009(1)	0.15(5)	0.010(3)
2972.1	$2_3^+ \to 2_1^+$	E2	1626	0.05(2)	5^{+5}_{-3}	$0.3^{+0.3}_{-0.2}$
2972.1	$2_3^+ \to 2_1^+$	M1	1626	$-0.003^{+0.041}_{-0.033}$	$0.000002^{+0.000378}_{-0.000002}$	$0.000001^{+0.000211}_{-0.000001}$
2972.1	$2_3^+ \to 2_2^+$	E2		$0.03^{+0.08}_{-0.07}$	2^{+20}_{-2}	$0.1^{+1.5}_{-0.1}$
2972.1	$2_3^+ \to 2_2^+$	M1		$-0.19^{+0.04}_{-0.08}$	$0.007^{+0.003}_{-0.005}$	$0.004^{+0.002}_{-0.003}$
2972.1	$2_3^+ \to 4_1^+$	E2		0.26(5)	130(50)	9^{+4}_{-3}
3025.9	$0_3^+ \to 2_1^+$	E2	1680	0.030(2)	10(1)	0.65(7)
3025.9	$0_3^+ \to 2_2^+$	E2		$0.25^{+0.05}_{-0.07}$	600(300)	40(20)
3165.7	$4_2^+ \to 2_1^+$	E2	1820	0.249(4)	69(2)	4.5(2)
3276.0	$2_4^+ \to 0_1^+$	E2	3276	0.030(2)	$1.80^{+0.03}_{-0.02}$	$0.12^{+0.02}_{-0.01}$
3276.0	$2_4^+ \to 2_1^+$	E2	1930	$-0.069(5)$	9(1)	$0.62^{+0.09}_{-0.08}$
3276.0	$2_4^+ \to 2_1^+$	M1	1930	$0.02^{+0.03}_{-0.05}$	$0.00006^{+0.00031}_{-0.00006}$	$0.00003^{+0.00017}_{-0.00003}$
3395.7	$4_3^+ \to 2_1^+$	E2	2050	0.047(5)	2.5(5)	$0.16^{+0.03}_{-0.04}$
3559.5	$3_1^- \to 2_1^+$	E1	2214	0.035(6)	$0.017^{+0.007}_{-0.005}$	$0.016^{+0.007}_{-0.005}$
4216.1	$4_4^+ \to 2_1^+$	E2		0.101(7)	$11.4^{+1.6}_{-1.5}$	0.7(1)
4216.1	$4_4^+ \to 4_1^+$	E2	1606	$-0.9^{+0.7}_{-0.1}$	900^{+2000}_{-200}	60^{+130}_{-10}
4216.1	$4_4^+ \to 4_1^+$	M1	1606	$1.3^{+0.5}_{-3}$	0.2(2)	0.1(1)

Table 4.1: Table of matrix elements and transition strengths for the Coulomb excitation of ^{64}Ni as calculated by the analysis code GOSIA.
*Eλ matrix elements are given in units of $e \cdot barns^{\lambda/2}$, and M$\lambda$ ones are given in units of $\mu_n barns^{(\lambda-1)/2}$, where λ is the multipolarity of the transition. Units for reduced transition strengths are μ_n^2, e^2fm^2, and e^2fm^4 for M1, E1, and E2 transitions, respectively.

observation of the specific transition involved.

As previously noted, at the outset of the minimization process, the matrix element for the first excited-to-ground state transition was kept fixed at the value reported by Allmond et al. [75] following single-step Coulomb excitation of the ^{64}Ni + ^{12}C system. Once a global minimum was achieved, this value was then released and another series of minimizations was carried out. Again, a global minimum was reached, this time with the matrix element for the $2_1^+ \rightarrow 0_1^+$ transition acting as a free parameter. As displayed in Table 4.1, at the end of the minimization process, a final value of $< i|M(E2)|f >$=0.268(16) eb was obtained for this transition. This compares favorably with the previous experimental value of 0.268(5) eb reported in [75], thus providing confidence in the validity of the analysis and the accuracy of our results. No Coulomb excitation data was available for other ^{64}Ni states prior to this work. However, a B(E2; $4_1^+ \rightarrow 2_1^+$) transition probability of 6.6 (1.0) W.u. was extracted from a lifetime measurement carried out alongside a g-factor determination in Ref. [26]. Our value of 4.4(+5/-3) W.u., reported in Table 4.1 compares favorably with the reported one, while offering an increased level of precision, further reinforcing confidence in the reliability of our data.

The majority of the B(E2) reduced transition probabilities (Table 4.1) correspond to values on the order of a few single-particle units (1-10 Weisskopf units). This is suggestive of non-collective excitations. This character is relatively consistent, regardless of excitation energy or spin. For example, the 1346-keV ($2_1^+ \rightarrow 0^+$) transition from the first-excited state to the ground state corresponds to 9 W.u., and the 2050-keV, $4_3^+ \rightarrow 2_1^+$ transition from the excited state at 3395 keV possesses a strength of only 0.16 W.u., which is particularly non-collective. Moreover, looking at the 2214-keV γ ray from the 3_1^- state ($3^- \rightarrow 2_1^+$), it is found to be associated with an even smaller transition strength of 0.016 W.u., though this is not unusual for an E1 transition as noted, for example, by E.S. Paul [84] and as discussed further below.

Only three values of Table 4.1 are considerably larger than 10 W.u., suggesting possibly

that one is dealing with more collective excitations. Two of these values correspond to matrix elements connecting the two known 0^+ excited states with the 2_2^+ level. It is important to acknowledge that the $0_2^+ \rightarrow 2_2^+$ and $0_3^+ \rightarrow 2_2^+$ transitions, associated with W.u. values of 50(10) and 40(20) respectively, were not directly observed in this work. Efforts were made to search for peaks at the nominal transition energies that would be associated with these de-excitation modes (590 and 749 keV, respectively); however, none were found in the spectra. This task required some care as the 590-keV energy is close to that of one of the Ge(n,n') peaks [78] for which the applied Doppler correction is inappropriate. The other transition at 749 keV is close to a contaminant from neutron scattering on tungsten, a component of the GRETINA cryostat. As a result, upper limits of 3 and 2 W.u. were determined from the spectra for these two transitions. These values are notably smaller than those reported in Table 4.1. The large errors reported in the GOSIA fits following the χ^2 minimization process, on the one hand, indicate that the available experimental constraints are insufficient for an accurate determination and, on the other, that the actual transition strengths are likely smaller than those calculated. A large number of checks were made to ensure that these strengths do not impact the strengths for other de-excitation paths out of these two states.

The third reduced transition strength greatly exceeding 10 W.u. is associated with the observed $4_4^+ \rightarrow 4_1^+$ transition, corresponding to a γ-ray of energy 1606 keV de-exciting the 4216-keV (4_4^+) state. The transition strength of 60^{130}_{-10} W.u. for the E2 component of the 1606-keV transition, while indicative of a more collective excitation, cannot be precisely determined due to the large uncertainty on the value. Attempts were made to gauge the effect of potential improper M1/E2 mixing on this transition strength; however, even after imposing a mixing ratio of $1^{+0.2}_{-0.2}$, the change in the transition strength was negligible. For this quantity, one can at most ascertain a lower limit of 50 W.u., again suggesting the possibility of a significant degree of collectivity.

Let us now examine the strengths provided by the analysis for the observed transitions of the 0_2^+ and 0_3^+ levels to the first-excited, 2_1^+ state. These correspond to single-particle values

of 3.2 and 0.65 W.u., respectively. Neither of these strengths, in and of themselves, imply a high degree of collectivity within the nucleus. However, what can be said at first glance is that the 0_2^+ level likely has a larger wavefunction overlap with the 2_1^+ state than the 0_3^+ level does. Further theoretical study is necessary in order to validate such claims, which will also be revisited momentarily with the insight provided by the quadrupole moment values.

It is important to also examine the strengths of some of the other transitions. For example, the strengths of the transitions from the 4_1^+ and 4_2^+ levels to the first-excited 2_1^+ state, corresponding to γ rays of 1264 and 1820 keV, respectively, are both very similar in magnitude. The $4_1^+ \rightarrow 2_1^+$ transition has an associated strength of $4.4^{+0.5}_{-0.3}$ W.u. while the $4_2^+ \rightarrow 2_1^+$ one possesses a strength of 4.5(2) W.u., which may indicate that both of these excited 4^+ states are characterized by wavefunctions with a similar degree of overlap with the wavefunction of the first-excited state. However, both of these values are about half the strength of the $2_1^+ \rightarrow 0_1^+$ transition, so it is possible that the wavefunctions of the ground and first-excited 2_1^+ state possess a stronger overlap than either of the aforementioned 4^+ levels do with the first-excited state. This will also be revisited below in light of the quadrupole moment values. Looking also at the 931-keV, $2_2^+ \rightarrow 2_1^+$ E2 transition, a strength of 2.9 W.u. was calculated, with an M1 component of only 0.07 W.u. This too could imply a weaker overlap between these two states in addition to the transition likely being of a single-particle nature. Additionally, the 2972-keV level is presently marked by a tentative spin-parity of 2^+, and by comparing the transition strengths for the γ rays from this state to the de-excitation modes from other 2^+ levels, one can gain a better understanding of whether or not this spin assignment is valid. Comparing the strength of the 2972-keV, $2_3^+ \rightarrow 0_1^+$ transition to that of the 3276-keV $2_4^+ \rightarrow 0_1^+$ one, i.e. 0.01 versus 0.12 W.u., indicates that both of these transitions are of a single-particle nature. Examining, then, the 1626-keV, $2_3^+ \rightarrow 2_1^+$ decay path with respect to the comparable 1930-keV, $2_4^+ \rightarrow 2_1^+$ one, respective strengths of 0.3 and 0.62 W.u. are extracted from this data. These values are quite similar and, once again, imply a single-particle character in both instances. Thus, the comparisons between these

Nucleus	$I_i^\pi \rightarrow I_f^\pi$	$B(E1)W.u.$
^{58}Ni	$3_1^- \rightarrow 2_1^+$	0.00060(22)
^{58}Ni	$3_1^- \rightarrow 2_2^+$	0.0008(4)
^{60}Ni	$3_1^- \rightarrow 2_1^+$	0.0006(3)
^{60}Ni	$3_1^- \rightarrow 2_2^+$	0.0010(5)
^{62}Ni	$3_1^- \rightarrow 2_1^+$	$0.000087^{+0.000016}_{-0.000022}$
^{62}Ni	$3_1^- \rightarrow 2_2^+$	$0.00045^{+0.00009}_{-0.00012}$
^{72}Ge	$3_1^- \rightarrow 2_2^+$	0.000024
^{72}Ge	$3_1^- \rightarrow 4_1^+$	0.000026
^{76}Ge	$3_1^- \rightarrow 2_1^+$	0.0080

Table 4.2: Typical B(E1) strengths for nuclei similar to ^{64}Ni.

$E\ level(keV)$	$I_i^\pi \rightarrow I_f^\pi$	$Mult(E\lambda)$	$< i\|M(E2)\|f > (eb)$	$Q(eb)$	$Q_0(eb)$
1345.8	$2_1^+ \rightarrow 2_1^+$	$E2$	0.11(3)	0.09(2)	0.3(1)
2276.6	$2_2^+ \rightarrow 2_2^+$	$E2$	$0.30^{+0.03}_{-0.05}$	$0.23^{+0.03}_{-0.04}$	$1.0^{+0.1}_{-0.2}$
2610.1	$4_1^+ \rightarrow 4_1^+$	$E2$	$-0.4^{+0.1}_{-0.3}$	$-0.3^{+0.1}_{-0.2}$	$-1.3^{+0.3}_{-1.0}$
3165.7	$4_2^+ \rightarrow 4_2^+$	$E2$	$0.1^{+0.1}_{-0.3}$	$0.07^{+0.08}_{-0.23}$	$0.3^{+0.3}_{-1.0}$

Table 4.3: Table of spectroscopic (Q) and intrinsic (Q_0) quadrupole moments for states in ^{64}Ni. While the spectroscopic and the intrinsic moment for a given state will share the same sign, it is important to understand how these values should be interpreted. A positive (negative) spectroscopic quadrupole moment indicates an oblate (prolate) nature as observed in the laboratory reference frame. Consequently, this equates to a prolate (oblate) nature with respect to the intrinsic reference frame of the nucleus. This is because a time-averaged oblate charge distribution appears prolate, and vice versa. Intrinsic quadrupole moment values in the 0.06-0.5 eb range are typical of spherical charge distributions.

two pairs of decay modes point to their similar transition strengths, a finding that reinforces the tentative 2^+ assignment for the 2972-keV level. One last point worth explicitly noting relates to the decay from the 3^- state. Firstly, this is the only negative-parity state that was observed in Coulomb excitation, and the fact that it lies at a relatively low excitation energy is noteworthy. The decay from this state to the 2_1^+ state is marked by a transition strength of only 0.016 W.u., strongly implying single-particle character. As this γ ray is associated with an E1 multipolarity, such a small transition probability is fitting, due to the usual lack of collectivity of such transitions. Table 4.2 provides a list of typical B(E1) strengths for nuclei similar to ^{64}Ni [85, 86]; they are all at the mW.u. level or below.

The spectroscopic and intrinsic quadrupole moments were also obtained from diagonal matrix elements in the GOSIA analysis. These are provided in Table 4.3.

As discussed in Chapter 2 of this dissertation, intrinsic quadrupole moment values greater

than one or two are typically associated with a deformed nuclear shape and positive values indicate a prolate deformation, while negative ones imply an oblate shape. As seen Table 4.3, two of the calculated intrinsic moments, those associated with the 2_1^+ and 4_2^+ levels, fall well within the 0.06-0.5 eb range suggested for spherical nuclei by Ref. [47]. The other two moments, associated with the 2_2^+ and 4_1^+ states at 2277 and 2610 keV, respectively, are slightly outside of the range of what is typically considered spherical, with the former exhibiting a marginally prolate nature and the latter a slightly oblate one. That being said, neither of these states should be considered significantly deformed, especially in comparison with the values found in deformed nuclei; see for example Ref. [47]. This assessment also agrees well with the B($\pi\lambda$) values gathered from Table 4.1.

Hereafter, we examine the quadrupole moments and how they and the transition strengths may be interpreted in light of one another, however, we will revisit these points in the Discussion chapter by utilizing comparisons with theory as well as by examining the wavefunctions of each state. It is clear that the first-excited and ground states share a similar shape, which is predicted to be spherical, and that the transition between these two states, while not collective, is still relatively strong for a transition of a single-particle nature. Thus, it is expected that the intrinsic quadrupole moment for the 1346-keV state would indicate a spherical nucleus, which it indeed does. It can also been seen that the 2277- (2_2^+) and 2610-keV (4_1^+) states, both possessing intrinsic quadrupole moments of around 1 eb, link to the spherical 2_1^+ state in ^{64}Ni via E2 transitions of 2.9 and 4.4 W.u., respectively. Again, such transition strengths are not indicative of a high degree of collectivity. However, one might speculate, upon comparing these strengths with that of the $2_1^+ \rightarrow 0_1^+$ transition, that the overlap of the wavefunctions of these states with the first-excited level is less than that between the first-excited and ground states. One possibility is that, while significant collectivity is not attributed to either the 2277- (2_2^+) or the 2610-keV (4_1^+) levels, they could be of a slightly more collective nature than the 2_1^+ or 0_1^+ states, but these transition strengths could also be the result of differing components of the wavefunction (to be examined in

the Discussion chapter). This suggestion is supported by the intrinsic quadrupole moment values. Moreover, it is worth noting that the strength calculated for the transition between the 2610- (4_1^+) and 2277-keV (2_2^+) levels themselves is sufficiently higher (13 W.u.), further suggesting that these two levels possess similar wavefunctions, both associated perhaps with minor deformation. Lastly, the quadrupole moment value corresponding the 3165-keV (4_2^+) state indicates a charge distribution very similar to that of the first-excited state. This is bolstered by the B(E2) strength provided in Table 4.1. Despite the fact that both 4_2^+ and 2_1^+ levels are predicted to be spherical and non-collective, the strength of the transition between them (4.5 W.u.) is larger than that between either the 2277- (2_2^+), or 2610-keV (4_1^+) levels, and the 2_1^+ state. This points to similarities in the wavefunctions of the 4_2^+ and 2_1^+ levels, with both states exhibiting spherical shapes. One again, we will elaborate on these points further in the Discussion chapter.

Let us now revisit the 0^+ excited states in the context of the quadrupole moments of Table 4.3. As previously mentioned, the data lead to only three transition strengths significantly exceeding 10 W.u. (Table 4.1). One of these strengths, associated with the $4_4^+ \rightarrow 4_1^+$ transition, has a very large related uncertainty. The other two correspond to transitions between both 0^+ excited states and the 2277-keV, 2_2^+ level. As noted above, both transitions present challenges of their own because of the transition energies involved. Nevertheless, for the present discussion, the values extracted from the GOSIA analysis reported in Table 4.1 are being considered. Thus, while neither of the γ rays involved were clearly observed in this experiment, GOSIA-calculated strengths for the purported $0_2^+ \rightarrow 2_2^+$ and $0_3^+ \rightarrow 2_2^+$ transitions of 50(10) and 40(20) W.u., respectively, are considered here. Based on the calculated intrinsic quadrupole moment for the 2_2^+ state, as well as on its weak overlap with the first-excited level, one could assert that this state diverges slightly from sphericity. If this is the case, then it is intriguing that both 0^+ excited states may exhibit larger transition strengths, and, thereby, greater wavefunction overlaps, with the 2_2^+ level than with the 2_1^+, first-excited state. Additionally, we recall that the matrix element connecting the 2_2^+ level

and a state possessing a similar quadrupole moment value, namely, the 2610-keV, 4_1^+ level, corresponds to a transition strength of around 13 W.u. These facts together could possibly indicate that both 0^+ excited states possess aspherical charge distributions and degrees of collectivity comparable to, or perhaps greater than that of the 2_2^+ level. The difficulty with such a statement is that neither a $0_2^+ \rightarrow 2_2^+$ nor a $0_3^+ \rightarrow 2_2^+$ transition has been explicitly observed, making this discussion rather speculative at present. Such a hypothesis could be evaluated with more confidence if one were to observe the level structure lying above these 0^+ excited states. Indeed, the observation of a rotational or vibrational band would provide evidence for shape coexistence. Unfortunately, no higher-lying states could be determined using Coulomb excitation. Nevertheless, for good measure, upper limits were determined for potential transitions with energies below 400 keV, in order to address the possibility that, in the future, any of the small "bumps" seen in the spectra would be found to be associated with the de-excitation from a higher-lying state. Three different upper limits were calculated at energies of 241, 260 and 380 keV. The upper limit obtained for the small "bump" at 241 keV was calculated to be $\leq 3 \cdot 10^{-2}$ W.u., but it is important to note that this protrusion could possibly be associated with the 236-keV γ ray de-exciting the 4085-keV level observed by Broda et al. [25]. The upper limits determined for the 260- and 380-keV "possible" transitions were established to be $6 \cdot 10^{-3}$ and $3 \cdot 10^{-3}$ W.u., respectively. Lastly, as previously mentioned, a small peak was observed around 308-310 keV that was assumed to be a contaminant based on the behavior of its intensity from angle to angle. If this corresponded instead to a new transition in ^{64}Ni, it would have a strength of around $5(1) \cdot 10^{-2}$ W.u. The small values of these limits rule out any sign of collectivity. The complementary deep-inelastic scattering experiment was analyzed, in part, to probe further for states above the 0^+ excitation and assess the possible presence of collectivity.

Section 4.2: ^{64}Ni Levels from Deep-Inelastic Reactions

The level diagram obtained from the analysis of the deep-inelastic scattering experiment comprising all observed ^{64}Ni transitions is illustrated in Figure 4.6. Here, dashed horizontal lines indicate a tentative ordering of transitions, and parentheses denote tentative spin and parity (when available) assignments. Transitions were considered to be tentative only if their placement relative to other γ rays in the level scheme was uncertain. Spins and parities were regarded as tentative if the value for the spin and/or parity of a level could not be determined based on the relevant DCO ratio(s) for the transitions populating, and de-exciting from, that level. Furthermore, because DCO ratios are a useful indicator of γ-ray multipolarity, but not an absolute metric, the spins and parities of all newly discovered states established on the basis of such ratios were also considered to be tentative, with the most likely value(s) indicated on the figure. The DCO ratio as well as the relative intensity of each γ ray is provided in Table 4.4. Thirteen new transitions were observed in this experiment, all lying atop previously identified sequences [25].

As noted previously, the multipolarities of the newly identified transitions were determined based upon the measurement of their DCO ratios. As a confidence check, the DCO ratios of known transitions were used to compare the proposed γ-ray multipolarities with those found in the literature. For all but two previously observed γ rays, the multipolarity suggested by the measured DCO ratio was found to be in agreement with the literature value. For example, a DCO ratio of 1.11(4) was obtained for the well-known 1346-keV, $2_1^+ \rightarrow 0_1^+$ transition; a result in agreement with the established E2 character of this γ ray as it is larger than 1 (see previous Chapter for a detailed presentation of the relationship between the value of a DCO ratio and the associated multipolarity). Conversely, ratios of 0.78(4) and 0.87(5) were determined for the strong 359- and 323-keV M1 γ rays de-exciting the 4532- and 4173-keV levels, respectively, herewith again validating our metric. Moreover, the multipolarities assigned for every transition within the previously observed yrast sequence by Broda et al. [25] agree with what was deduced using our DCO ratios, further

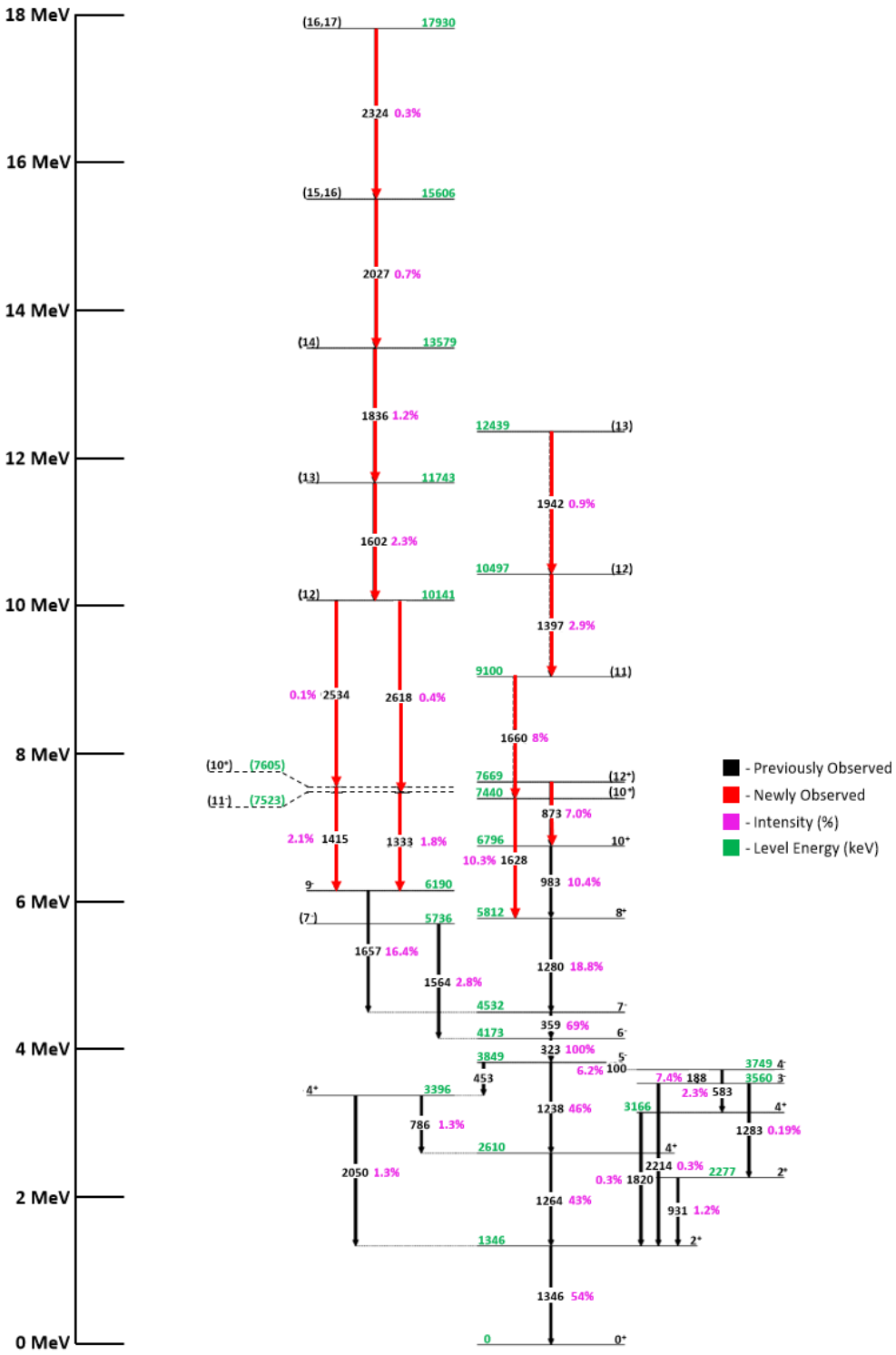

Figure 4.6: ^{64}Ni level scheme obtained from this deep-inelastic experiment. Dashed lines and parentheses indicate tentative levels and spin assignments, respectively.

strengthening our confidence in the accuracy of this method. The only two transitions for which an agreement was not found are the 1820-keV γ ray associated with the decay of the 4_2^+ state at 3166 keV to the 2_1^+ level, and the 1283-keV line connecting the first 3^- and 2_2^+ states. For the 1820-keV transition, the peak in the various spectra appeared to be located close to a contaminant not originating from ^{64}Ni, making a correct extraction of the intensity as a function of angle doubtful (Figure 4.7). Moreover, the statistics for this peak in the 0° and 90° spectra were quite low, further making it difficult to determine with confidence a suitable value for the DCO ratio. Regarding the 1283-keV peak, an accurate estimate of the peak intensity could not be extracted from either the forward or rear detectors in Gamma-sphere, due to the fact that it is close in energy to the strong, 1280-keV ($8_1^+ \rightarrow 7_1^-$) yrast transition. It was, however, possible to extract with large uncertainty a relative intensity for this peak from the total spectrum, due to the increased statistics available in this case. These two transitions will be revisited later in this chapter. Barring these two instances, good agreement between the multipolarites deduced on the basis of the DCO ratios and those reported in the literature was found. Hence, the ratios appear to be a suitable metric for a proposed multipolarity assignment to each newly-discovered transition.

Using the DCO ratios of Table 4.4, γ-ray multipolarities were proposed for all but 2 of the 13 new transitions, and spins could be proposed for 8 of the 12 newly identified states. Most of these transitions were placed unambiguously in the level scheme of Figure 4.6, but we will examine each of them and expound on the evidence for their location. Let us begin our analysis by examining the yrast sequence observed in this study, and then proceed upward from the ground state. The very same yrast sequence depicted in Ref. [25] was observed in this work. This includes the 1346-, 1264-, 1238-, 323-, 359-, 1280-, and 983-keV transitions, leading from the spin-0^+ ground state all the way up to a spin 10^+ level at an excitation energy of 6796 keV. In addition, an 873-keV γ ray originating from a 7669-keV level was added on top of the previously established yrast sequence. Based on the measured DCO ratio of $1.1^{+0.5}_{-0.4}$ measured for this transition, it is proposed to be of E2 character, and the

$E_\gamma(keV)$	I_γ	$E_i(keV)$	$DCO\ ratio$	$I_i^\pi \rightarrow I_f^\pi$	$Mult(\pi\lambda)$
100	$6.2^{+0.9}_{-0.8}$	3849	$0.2^{+0.2}_{-0.1}$	$5_1^- \rightarrow 4_1^-$	$E1$
188	7.4(5)	3749	0.7(2)	$4_1^- \rightarrow 3_1^-$	$M1$
323	100(2)	4173	0.78(4)	$6_1^- \rightarrow 5_1^-$	$M1$
359	69(3)	4532	0.87(5)	$7_1^- \rightarrow 6_1^-$	$M1$
453	3.7(3)	3849	$0.8^{+0.2}_{-0.1}$	$5_1^- \rightarrow 4_3^+$	$E1$
583	2.3(3)	3749	$1.3^{+0.5}_{-0.3}$	$4_1^- \rightarrow 4_2^+$	
786	$1.3^{+0.6}_{-0.5}$	3396	$0.4^{+0.2}_{-0.1}$	$4_3^+ \rightarrow 4_1^+$	$M1$
873	7.0(5)	7669	$1.1^{+0.5}_{-0.4}$	$(12_1)^+ \rightarrow 10_1^+$	$E2$
931	1.2(4)	2277	3^{+3}_{-1}	$2_2^+ \rightarrow 2_1^+$	$E2$
983	$10.4^{+0.6}_{-0.5}$	6796	1.5(3)	$10_1^+ \rightarrow 8_1^+$	$E2$
1238	46(1)	3849	$0.74^{+0.08}_{-0.07}$	$5_1^- \rightarrow 4_1^+$	$E1$
1264	43(1)	2610	1.08(8)	$4_1^+ \rightarrow 2_1^+$	$E2$
1280	18.8(8)	5812	0.7(1)	$8_1^+ \rightarrow 7_1^-$	$E1$
1283	0.19(9)	3560		$3_1^- \rightarrow 2_2^+$	$E1$
1333	1.8(8)	7523	3^{+5}_{-2}	$X \rightarrow 9_1^-$	$E2$
1346	54(2)	1346	1.11(4)	$2_1^+ \rightarrow 0_1^+$	$E2$
1397	2.9(8)	10487	$0.8^{+0.9}_{-0.5}$	$(12) \rightarrow (11)$	$E1/M1$
1415	2.1(6)	7605	$0.7^{+0.5}_{-0.3}$	$X \rightarrow 9_1^-$	$E1/M1$
1564	2.8(5)	5736	$0.9^{+4.4}_{-0.7}$	$(7_2)^- \rightarrow 6_1^-$	$M1$
1602	2.3(6)	11743	$1.0^{+0.7}_{-0.4}$	$(13_1) \rightarrow (12)$	$E1/M1$
1628	10.3(6)	7440	$1.4^{+1.2}_{-0.7}$	$(10_2)^+ \rightarrow 8_1^+$	$E2$
1657	16.4(8)	6190	$2.5^{+1.4}_{-0.9}$	$9_1^- \rightarrow 7_1^-$	$E2$
1660	8^{+4}_{-3}	9100	$0.8^{+0.9}_{-0.3}$	$(11) \rightarrow (12_1)$	$E1/M1$
1820	$0.3^{+0.2}_{-0.1}$	3166	$0.8^{+0.4}_{-0.3}$	$4_2^+ \rightarrow 2_1^+$	$E2$
1836	1.2(2)	13579	$0.8^{+1.3}_{-0.5}$	$(14) \rightarrow (13)$	$E1/M1$
1942	0.9(3)	12439	$0.6^{+0.8}_{-0.4}$	$(13_2) \rightarrow (12)$	$E1/M1$
2027	0.7(2)	15606	$1.0^{+0.9}_{-0.5}$	$X \rightarrow (14)$	
2050	1.3(2)	3396	2^{+6}_{-1}	$4_3^+ \rightarrow 2_1^+$	$E2$
2214	0.2(1)	3560	$0.8^{+1.1}_{-0.5}$	$3_1^- \rightarrow 2_1^+$	$E1$
2324	0.3(1)	17930	≥ 1		$E2$
2534	0.1(1)	10141	$1.1^{+1.6}_{-0.7}$	$(12) \rightarrow X$	$E2$
2618	0.4(2)	10141	$1.0^{+3.3}_{-0.8}$	$(12) \rightarrow X$	$E1/M1$

Table 4.4: Table of DCO ratios and intensities determined for each observed transition in the deep-inelastic spectra. The level and γ-ray energies listed are accurate to within 2 keV. Here, X is used as a placeholder for an unidentified spin value associated with a state.

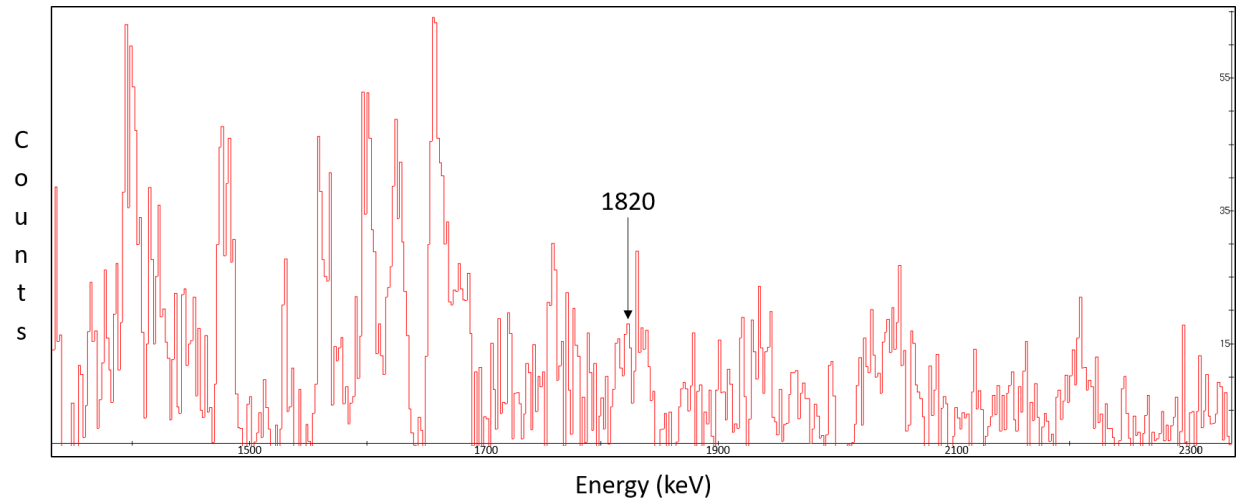

Figure 4.7: Coincidence spectrum gated on the 1346-keV $2_1^+ \rightarrow 0_1^+$ transition depicting the 1820-keV γ ray identified in this and previous work on ^{64}Ni. It can be seen that it lies closely alongside contaminant peaks, i.e. transitions from another nucleus, making it difficult to extract an accurate DCO ratio. Note the limited energy range displayed here.

7669-keV state was assigned a tentative spin and parity of 12^+ as a result. A ^{64}Ni coincidence spectrum, gated on the 1346-keV yrast transition, is displayed in Figure 4.8, and every yrast transition up to, and including, the newly identified 873-keV transition can be seen.

Proceeding from the ground state upwards, let us examine the levels and transitions identified in this experiment. It is sufficient to state that every transition lying below the 6796-keV yrast state has been observed previously by Broda et al [25]. As noted above, the multipolarities determined from the DCO ratios of all of these transitions, and, consequently,

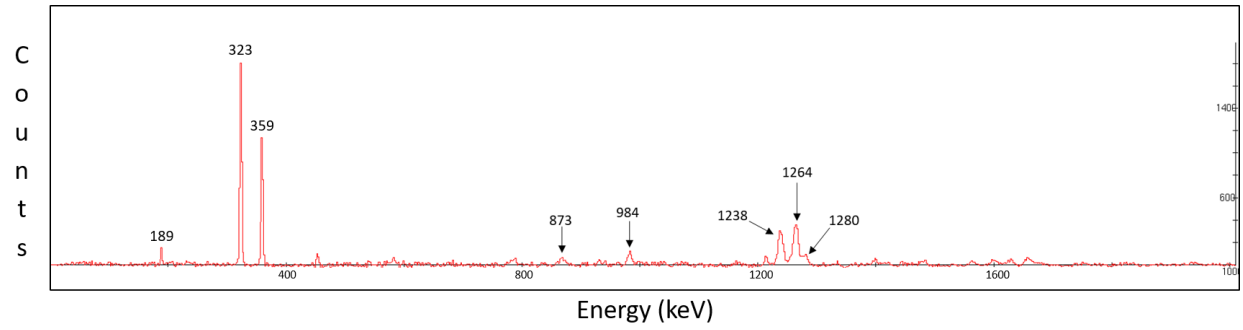

Figure 4.8: ^{64}Ni coincidence spectrum gated on the 1346-keV, $2_1^+ \rightarrow 0_1^+$ transition. The transitions that are part of the yrast sequence up to the newly discovered 873-keV line are labeled.

the spins and parities of the associated states, agree with literature values. Two transitions in this known excitation region below 6793 keV did, however, present some difficulty. Firstly, as addressed earlier, the peak shape of the 1820-keV, $4_2^+ \rightarrow 2_1^+$ γ ray appeared to be too broad, likely indicating that it was contaminated by another γ ray. So while it was possible to extract an estimate for the intensity of this peak, the associated error is relatively large. Additionally, the contamination led to spurious coincidence relationships, when gating on this 1820-keV peak, but since coincidence data with a gate on this γ ray were not required in order to recover any of the other observed transitions, this was not considered to be an issue. A DCO ratio of $0.8^{+0.4}_{-0.3}$ was derived, likely impacted by the contaminant peak, as it indicates a dipole transition. However, this is known not to be the case from earlier studies, so the previously established E2 multipolarity was adopted instead. The second transition in this region of the level scheme with some ambiguity is associated with the 1283-keV, $3_1^- \rightarrow 2_2^+$ transition. Due to the fact that this γ ray is seated directly on top of the yrast 1280-keV, $8_1^+ \rightarrow 7_1^-$ transition, it was not possible to extract yields reliably from the 0° and 90° spectra. Hence, no DCO ratio could be calculated and an E1 multipolarity was adopted for this γ ray, based on the previous literature value [25]. However, it was still possible to confirm the coincidence relationships for this 1283-keV γ ray by extracting a triple-gate from the coincidence data using the 1346-, 323-, and 1564-keV transitions. Due to the fact that the 1564-keV transition lies in parallel with the yrast 1280-keV γ ray, this triple coincidence gate removes the 1280-keV peak, leaving a trace of the weaker 1283-keV one untouched, as depicted in Figure 4.9.

Moving upward from the yrast sequence, a 1628-keV γ ray was observed for the first time in parallel with the 983-keV transition, the latter being the highest-observed line in the previous work [25]. It was possible to confirm the coincidence relationships for this new transition as well as to determine its placement through the application of triple-coincidence gates. First, a triple-gated coincidence spectrum was produced by using the 323-, 359- and 1280-keV yrast transitions, indicating that the 1628-keV γ ray belongs in the same sequence

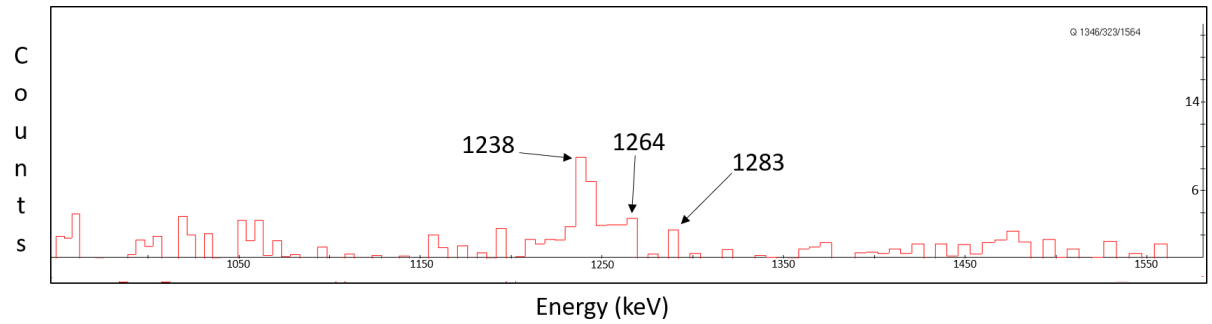

Figure 4.9: A triple-gated coincidence spectrum using the 1346-, 323-, and 1564-keV γ rays. Since the 1564-keV transition lies in parallel with the 1280-keV one, this set of gates provides weak evidence for the 1283-keV line, which is normally obscured by the stronger 1280-keV γ ray.

as the 983-keV one. However, when subsequently triple-gating on the 323-, 359-, and 983-keV transitions, the 1628-keV line disappears, showing it to, indeed, be in parallel with the 983-keV γ ray. Figure 4.10 provides the relevant coincidence spectra supporting this conclusion. For the 1628-keV γ ray, a DCO ratio of 1.4 was measured indicating that it is likely of E2 character and connects the 5812-keV, 8^+ state with a tentative 10^+ state located at 7440 keV. Above this transition lie two γ rays of 1397 and 1660 keV placed in series with one another. Based on their measured DCO ratios, both of these transitions were determined to be of dipole character, but it was initially difficult to determine their relative ordering based on their intensities in the coincidence spectrum gated on the 359-keV transition. It was necessary, in this case, to gate on the 1280-keV γ ray rather than on the 359-keV one, in order to obtain a better perspective of the relative intensities involved. This is due in part to the fact that the 1280-keV line is located in the same sequence as the 1397- and 1660-keV transitions, only slightly lower in the level scheme. It is, thus, not coincident with the γ rays from adjacent sequences and, as a result, provides a clearer picture of the intensities of the 1397- and 1660-keV γ rays with respect to one another. Consequently, it was possible to determine that the 1660-keV transition lies below the 1397-keV one. Lastly, directly above the 1397-keV transition, a 1942-keV one was observed and associated with an E1 or M1 multipolarity based on a measured DCO ratio of $0.6^{+0.8}_{-0.4}$. Tentative spins for

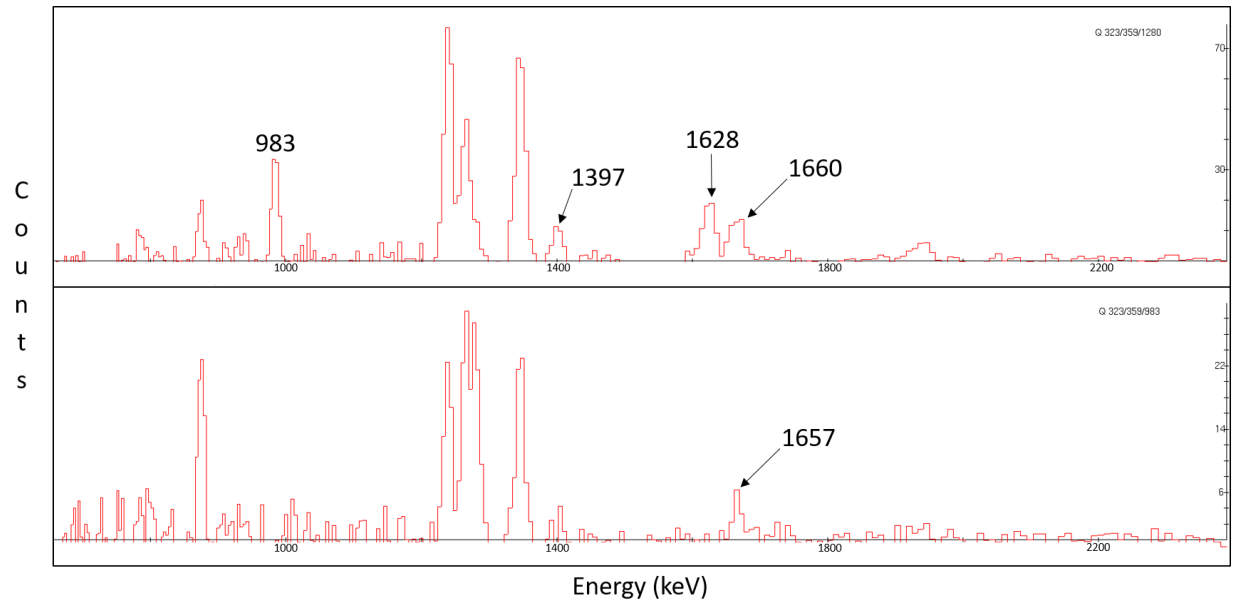

Figure 4.10: Two triple-gated coincidence spectra used to discern the placement of the 1628-keV transition. (Top) Spectrum gated on the 323-, 359- and 1280-keV γ rays. All labeled peaks lie in sequence with these three transitions, as noted by their appearance in the spectrum. (Bottom) When the spectrum is now gated on the 323-, 359-, and 983-keV γ rays, the 1628-, 1660- and 1397-keV lines vanish, indicating that these lie in a sequence parallel to the 983-keV one. The remaining peak is associated with the 1657-keV line which also lies parallel to the 983-keV one, but is more intense than the 1660-keV transition and, thus, persisted due to coincidence ambiguities (improper background subtraction).

the associated levels were proposed based on the deduced multipolarity of each transition assuming, in addition, that the spin values increase along the cascades.

Examining the other sequence lying above the previously observed 1657-keV transition indicates that eight new γ rays were observed. Directly above this transition, two parallel cascades were identified. Each of these cascades comprises two γ rays, one in a 1415- 2534-keV sequence, and another with 1333- and 2618-keV transitions. For both cascades, we were unable to discern the exact ordering of the transitions; e.g., it is possible that the ordering is reversed from that shown in Figure 4.6. For this reason, it is necessary to indicate that the two intermediate states at 7605 and 7523 keV are only tentative as the sequences could be reversed. Furthermore, the DCO ratios associated with the 2534- and 2618-keV γ rays are both very close to one with large errors (Table 4.4), making it difficult

to ascertain their respective multipolarity. However, it can be stated, based on the observed coincidence relationships, that these two cascades likely branch from the same 10141-keV state. Moreover, while the aforementioned DCO ratios for the 2534- and 2618-keV transitions are ambiguous, those of the 1415- and 1333-keV ones are not and, in fact, suggest they are of respective dipole and quadrupole character. Thus, knowing the multipolarity of one γ ray in each cascade, in addition to the fact that both cascades begin and end in the same states, leads to the conjecture that the 2534- and 2618-keV transitions are likely of quadrupole and dipole character, respectively. Realizing that each of these cascades is associated with three units of angular momentum, one can conclude that they connect the 9^-, 6190-keV level with a most likely spin 12 level at 10141 keV. Insufficient information is available to propose a parity for this level. Directly above this 10141-keV state, 1602- and 1836-keV γ rays were identified, both of dipole character. Lastly, two transitions of energies 2027- and 2324-keV were placed atop the 1836-keV γ ray. Unfortunately, due to the lack of statistics in the peaks at 2027 and 2324 keV, the calculated intensities were difficult to extract, and the resulting errors are quite large. Hence, no assignment could be proposed, based on the DCO values and spins for the associated levels could be determined only within 1-2 $\hbar$.

In addition to the observation of new γ rays and the proposed assignments of spins and parities, relative intensities were also determined for each of the observed transitions. As mentioned in the previous chapter, all γ-ray intensities were measured relative to that of the 323-keV transition, as this was the most intense in the total spectrum. It is likely that the 1346-keV, $2_1^+ \rightarrow 0_1^+$ transition appeared weaker than the 323-keV one even after efficiency corrections because of the presence of rather long-lived states in the cascade between the 323-keV γ ray and the decay from the first excited state. Keeping in mind that the product nuclei recoil out of the target, any such longer-lived state(s) below the 323-keV transition would cause the 1346-keV γ ray to be somewhat delayed, so that its decay in flight would occur partially outside the view of the Gammasphere detectors, resulting in the decrease of its observed intensity relative to that of the 323-keV γ ray. By combining the spectra of

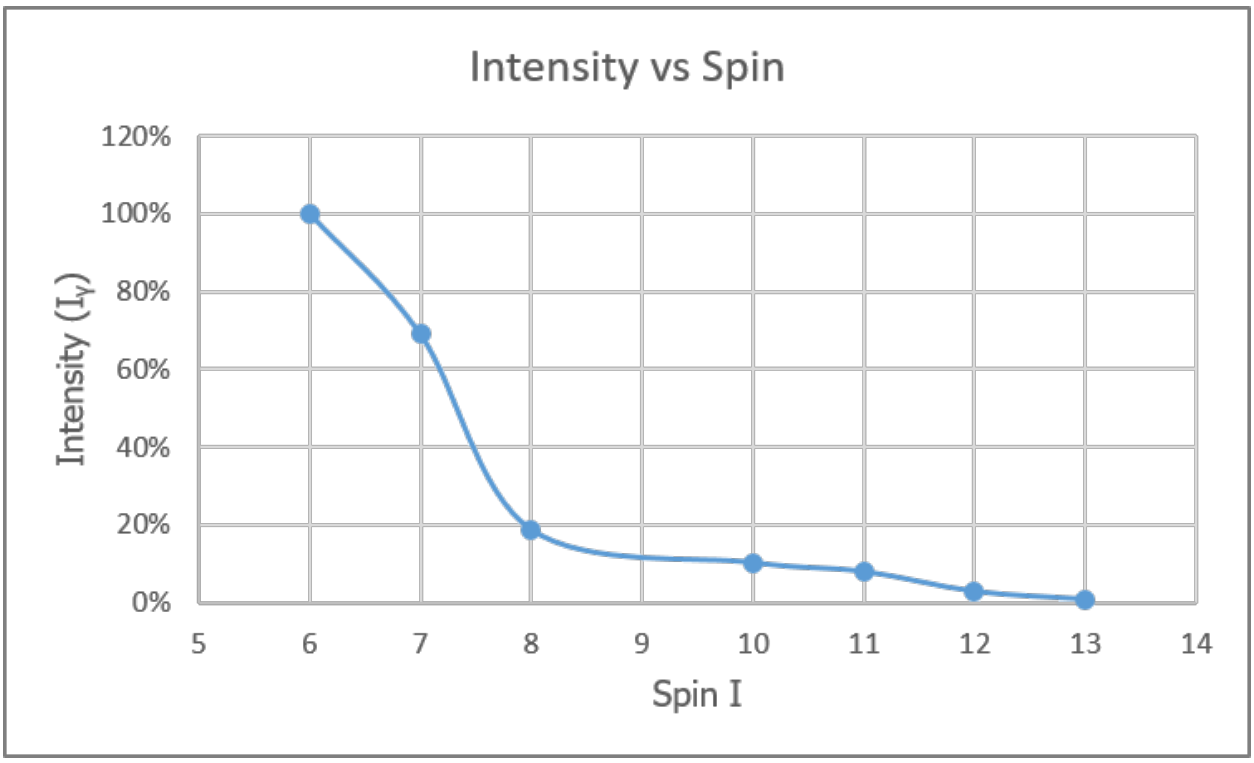

Figure 4.11: An illustration of how, as the spins of the states increase, the relative intensities of the γ rays de-exciting the levels involved decrease. This plot begins with the most intense transition, corresponding to a 323-keV γ ray, de-exciting a 6^- state and moves upwards, following the 359-keV branch and then the 1628-keV one, up to the 1942-keV transition de-exciting a tentative spin-13 state at 12439 keV (see the level scheme of Figure 4.6). Values on the X-axis indicate the spin of the initial state from which the γ ray was emitted.

every angular range together and gating on one of three γ rays of 1346-, 359-, or 1280-keV, it was possible to determine the intensity of each transition relative to the 323-keV one. The 1346- and 359-keV gates were chosen as these transitions are the most intense aside from the 323-keV one, and, in addition, produced the cleanest coincidence spectra. As discussed above, the 1280-keV coincidence gate was used solely to determine the intensity of the 1660-keV γ ray in order to accurately place it within the level scheme of Figure 4.6. The relative intensity of each γ ray is listed in Table 4.4. If we examine the sequence from the most intense line (323-keV) upward, following the 1628-keV branch, we see that as the spin of the states increases, the intensities of the γ rays de-exciting the levels involved decreases. Figure 4.11 clearly illustrates this trend.

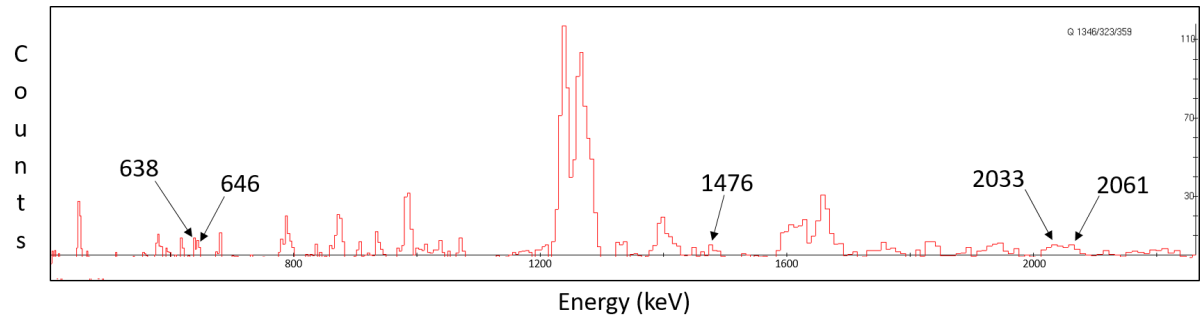

Figure 4.12: ^{64}Ni spectrum with a triple-coincidence gate on the 1346-, 323-, and 359-keV transitions. Labeled peaks were those observed in the deep-inelastic experiment that could not be placed due either to ambiguities in the coincidence relationships, the presence of contaminants, or weak intensity.

Several transitions observed in this reaction could not be placed in the ^{64}Ni level scheme, either due to ambiguities in the coincidence relationships, the presence of contaminants, or weak intensity. A few of these are worth mentioning here. These include, two low-energy γ rays of 638 and 646 keV, one at 1476 keV, and two higher-energy peaks at 2033 and 2061 keV. All of these can be seen in Figure 4.12, which is an expanded version of the 1346-, 323-, 359-keV triple-gated spectrum provided in the bottom half of Figure 3.32. The two transitions of 638 and 646 keV, as well as the 1476-keV line could not be positively assigned to ^{64}Ni, due to the contamination of the spectra by contributions from other nuclei. When double or triple-gating with any one of these three individual γ rays together with one or two known ^{64}Ni transitions, a number of peaks was observed, some of which could be identified as belonging to ^{64}Ni, while others were most likely contaminants, predominantly from ^{64}Cu. The fact that all three of these peaks appeared in the spectrum provided in Figure 4.12 may suggest that some coincidence relationships might be ambiguous with doublets belonging to both nuclei, making it impossible to place the transitions in the ^{64}Ni level scheme with any certainty. Additionally, the two high-energy peaks at 2033 and 2061 keV could not be placed due to their weak intensity, as well as to their close vicinity to one another and to the known 2050-keV transition in ^{64}Ni.

As a final note, while multiple new transitions and states have been identified via these

deep-inelastic reactions, no trace of the desired 1522- or 1680-keV γ rays associated with the de-excitation from the 0^+ excited states was observed. Again, this is likely due to the tendency for deep-inelastic reactions to funnel the γ-ray yield towards the yrast sequence, missing sequences of similar spins, but higher excitation energies. Unfortunately, this means that there was no opportunity to probe the level structure located above such states and search for collective bands, as was hoped for. Thus, no direct evidence for shape coexistence based on rotational sequences in ^{64}Ni has been found at this point. This is noteworthy as the deep-inelastic reactions producing ^{62}Ni and ^{63}Ni in the same experiment resulted in the direct observations of 3 collective sequences in the odd isotope and 2 rotational bands in the even one [28, 29]. A comparison of these results to shell-model and MCSM calculations will be addressed in the following chapter.

CHAPTER 5: Discussion

Section 5.1: Comparisons with Adjacent Even-Even Ni Isotopes

At the onset of this chapter, a comparison with the known properties of states in the neighboring even-even Ni isotopes is worthwhile, be it only to highlight similarities and differences. The comparisons focus on the level structures at low excitation energy; e.g., those reached by Coulomb excitation in the case of ^{64}Ni. Beginning with ^{62}Ni, one notes that the first excited state (2_1^+) is located at 1173 keV, has a spectroscopic quadrupole moment of 0.05(12) eb and a transition strength for the decay to the ground state of 179(6) e^2fm^4 [87]. This does not stray far from the observations of the first-excited state in ^{64}Ni, which is the 2_1^+ state located at slightly higher excitation energy (1346 keV), with a spectroscopic quadrupole moment and a transition strength of 0.09(2) eb and 140(20) e^2fm^4, respectively. Hence, the first excited states in the two nuclei appear to be of similar character. Moving onto the two known excited 0^+ states in ^{62}Ni, which are located at energies of 2049 and 2891 keV, one may note, unfortunately, that the associated transition strengths and quadrupole moments are unknown thus far. The 0^+ excited states in ^{64}Ni, on the other hand, are located slightly higher in energy, at 2867 and 3026 keV, and are considerably closer to one another than the 0_2^+ and 0_3^+ levels in ^{62}Ni. Additionally, little is known about the 2_2^+ state in ^{62}Ni other than its excitation energy of 2302 keV, a value that is quite close to that of the analogue in ^{64}Ni: 2277 keV. A similar statement applies to the excited 4^+ states in ^{62}Ni that are located at 2337 and 3177 keV, again lying at energies similar to those of the 2610-keV 4_1^+ and 3066-keV 4_2^+ states in ^{64}Ni. While much information regarding the degree of collectivity of ^{62}Ni remains unknown, it is clear that, in terms of level energies, transition strengths, and quadrupole moments the similarity with ^{64}Ni is notable.

Moving onto the heavier neighbor, ^{66}Ni, the first-excited 2^+ state is located at 1425 keV, again, close to the 1346-keV, first-excited state in ^{64}Ni. The reduced transition strength for the decay of this state, as determined by Ref. [88], is reported as 120(20) e^2fm^4, which, once again, is comparable to the 140(20) e^2fm^4 value observed in ^{64}Ni. No quadrupole moment was reported as the work of Ref. [82] is based solely on a lifetime measurement. Two 0^+ excited states were observed in this nucleus at 2445 and 2965 keV, as well as an additional, tentative 0^+ level at 2664 keV [89]. The energies of these excitations aren't particularly far off from the 0_2^+ and 0_3^+ ^{64}Ni levels positioned at 2867 and 3026 keV, respectively. Moreover, as described in Chapter 1 above, LNPS shell-model calculations performed in Ref. [23] assert that, while the 0_3^+ state is predominantly spherical, the 0_2^+ and 0_4^+ ones are likely associated with weak oblate and strong prolate deformations, respectively. This interpretation was reinforced further by the MCSM calculations and lifetime measurements carried out in Ref. [24]. Such a notable case of shape coexistence for a Ni isotope possessing a midshell neutron number is worth emphasizing once more when examining ^{64}Ni, which also possesses a neutron number around midshell. Regarding the 2_2^+ and 2_3^+ states, the only information available is their respective excitation energies of 2907 and 3229 keV [25]. These two levels are, thus, located considerably higher in energy than the analogous states in ^{64}Ni at 2277 and 2972 keV. Three 4^+ states have been established with certainty at excitation energies of 3185, 3614 and 3792 keV, which differ by a few hundred keV from the energies of states with the same spin-parity in ^{64}Ni. On the other hand, a 3^- level has been observed in ^{66}Ni at an energy of 3371 keV, not far from the 3^- state in ^{64}Ni at 3560 keV. For a low-lying, 3^- level in an even-even nucleus, this similarity is worth noting.

Stepping 4 neutrons away from ^{64}Ni leads to the stable ^{60}Ni and the N=40 ^{68}Ni isotopes. Beginning with ^{60}Ni, the 2_1^+ state is located at an energy of 1333 keV, very close to that of the 2_1^+ level in ^{64}Ni. A transition strength has been reported for the decay of this state by Ref. [90]. It corresponds to a value of 175(14) e^2fm^4, which compares favorably to the 140(20) e^2fm^4 value in ^{64}Ni. For this level, a spectroscopic quadrupole moment of -0.104(18)

eb was determined by Ref. [91] via an electron scattering technique. When comparing with the ^{64}Ni value of 0.09(2) eb, a difference in sign is noted, signifying that the 2_1^+ state in ^{60}Ni has a slightly prolate shape while the same level in ^{64}Ni is marginally oblate, however, both values are small and the states remain essentially spherical with nearly the same, small degree of deformation. The first two excited 0^+ states in ^{60}Ni are located at energies of 2285 and 3318 keV, again comparable to those in ^{64}Ni. Comparatively, the separation between these two excitations is larger than that seen in the nucleus of interest. Relevant transition strengths and quadrupole moments are not known for these states in ^{60}Ni, nor for the 4_1^+ and 4_2^+ excited states. A B(E4) transition strength is available for the 4_1^+ state from inelastic electron scattering. However, such a transition was not observed in the present experiment, nor was the strength of the analogous transition calculated by GOSIA. Nevertheless, it is worth pointing out that these two excited 4^+ states are located at energies of 2506 and 3120 keV, each only about 100 keV different from those of the states with the same quantum numbers in ^{64}Ni. Lastly, examining the 2_2^+ level in ^{60}Ni at 2159 keV, it is noted that it lies at an excitation energy comparable to that of 2277 keV in ^{64}Ni. Additionally, a transition strength of 3(1) e^2fm^4 for the decay of this state to the ground state was derived in Ref. [92]. While this is a couple orders of magnitude larger than the $0.05^{+0.05}_{-0.02}$ e^2fm^4 value for ^{64}Ni, both consistently indicate a single-particle character for the transition involved.

Now turning to the doubly-magic ^{68}Ni nucleus, the situation becomes a little more involved. As one may recall from the introductory chapter, the first excited state no longer is a 2^+ level, but, rather, a 0_2^+ state located at an energy of 1770 keV. The 2_1^+ state is then situated at 2034 keV, considerably higher in energy than the 1346-keV, 2_1^+ level in ^{64}Ni. This is to be expected for a doubly-magic nucleus (Z=28, N=40). The $2_1^+ \rightarrow 0_1^+$, B(E2) transition strength was established individually by Refs. [88], [93], and [94], corresponding to consistent values of 51(12), 56^{+24}_{-20}, and 52.5(84) e^2fm^4, respectively. These strengths are less than half that of the $2_1^+ \rightarrow 0_1^+$ decay for ^{64}Ni, indicating that there is potentially less collectivity for this level in ^{68}Ni, or perhaps that the wavefunctions of the 2_1^+ and ground

states overlap more completely in the lighter case. Small transition strength in this case is not unusual, however, as one is dealing with a doubly-magic nucleus, which is expected to be rigidly spherical. Quadrupole moments for both the 0_2^+ and 2_1^+ excited states have not been determined. Naturally, the 0_2^+ level lies much lower in ^{68}Ni than in ^{64}Ni. The highest-known 0^+ assignment in the former is associated with a 0_3^+ level at an excitation energy of 2511 keV, a value which is still lower in energy than that for both of the known excited 0^+ states in ^{64}Ni, located at 2867 and 3026 keV. In addition, it is worth recalling from Chapter 1 that, according to MCSM calculations, the 0_2^+ level is most likely associated with an oblate deformation [95], while the 0_3^+ one is thought to be of prolate character, arising predominantly from 2p-2h proton excitations [16]. A B(E2) strength of 39.0(34) e^2fm^4 for the $0_3^+ \rightarrow 2_1^+$ transition was also measured by Crider, et al. [94], which is significantly larger than the 10(1) e^2fm^4 strength of the same decay mode in ^{64}Ni, as determined by this experiment. This stands to reason for the prolate-deformed 0_3^+ state in ^{68}Ni, however, the same level in ^{64}Ni is likely close to spherical, as discussed further below. Regarding the 2_2^+ level located at 2743 keV, no quadrupole moment or transition strength from the decay of this state has yet been measured. Furthermore, no higher-lying 2^+ states have been established in ^{68}Ni. Finally, regarding the 4^+ states, there is only a single instance of a firm 4^+ state assignment in ^{68}Ni at 3147 keV [25], and another, tentative one at 3405 keV. Both of these excitations are slightly higher than the 2610-keV, 4_1^+ and 3166-keV, 4_2^+ levels in ^{64}Ni, which again, is not necessarily atypical for a doubly-magic nucleus.

Lastly, it is important to examine the most neutron-rich Ni isotope for which the low-spin level structure is known: ^{70}Ni. The majority of the data collected on this nucleus has been obtained through β-decay experiments, however, a Coulomb excitation measurement was performed by Perru, et al. in which the transition strength between the ground and the first-excited 1260-keV, 2_1^+ state, was measured to be 172(28) e^2fm^4 [96]. Both the excitation energy and spin of this level, as well as the strength of the transition to the ground state, are similar to those seen in ^{64}Ni. Comparing the energies of the two 2_1^+ levels, one finds that

of ^{64}Ni to be less than 100 keV off, at 1346 keV. The B(E2) values are close as well, with the same transition in ^{64}Ni possessing a strength of 140(20) e^2fm^4. This, of course, mimics closely the values in ^{66}Ni as well. Interestingly, relative to ^{64}Ni, while ^{70}Ni has a smaller excitation energy for the first-excited state and a larger B(E2) strength associated with its decay to the ground state, this is the reverse of the observation in ^{66}Ni which possesses a higher first-excited state and a lower B(E2) value. This is likely related to the shell evolution of nuclei on "opposite sides" of doubly-magic ^{68}Ni. Moving forward, a tentative 0_2^+ state is located in ^{70}Ni at an energy of 1567 keV [20], e.g., at a considerably lower excitation energy than the same state in ^{64}Ni that is located at 2867 keV. Furthermore, a lower limit of 58 e^2fm^4 was determined for the strength of the $0_2^+ \rightarrow 2_1^+$ decay mode [94], which is of the same magnitude as the analogous transition in ^{64}Ni, measured at 48(3) e^2fm^4. Another 2_2^+ state is situated at 1868 keV [18, 20], which again lies below the analogous level in ^{64}Ni at an energy of 2277 keV. Beyond this, a 4_1^+ level was observed at an excitation energy of 2229 keV, again, sufficiently lower than the 2610-keV, 4_1^+ state in the nucleus of interest. Finally, one tentative 4_2^+ level has been seen in ^{70}Ni and is associated with an excitation energy of 2508 keV [18]. If this is, indeed, confirmed to be the 4_2^+ state, it continues the trend of comparably lower excitation energies, as this is located well below the 3166-keV, 4_2^+ level in ^{64}Ni. With ^{70}Ni, the last two neutrons occupy states above the N=40 shell gap and this appears to result, overall, in a more compressed spectrum.

A plot of the B(E2;$2_1^+ \rightarrow 0_1^+$) transition strengths for the even-even Ni isotopes is provided in Figure 5.1, where the data are restricted to the cases where this quantity is known with suitable accuracy; i.e., in the $56 \leq A \leq 70$ range. Data also exist for ^{72}Ni and ^{74}Ni from measurements carried out at the GANIL (France), NSCL (USA) or RIBF (Japan) radioactive beam facilities. In fact, for both isotopes, several values of the strength are available in the literature, but these do not agree, usually differing by factors of 3-5. Hence, further work will be required before a clear picture emerges. Figure 5.1 indicates the presence of the N = 28 and 40 shell closures through the two minima in the B(E2) values as a function of

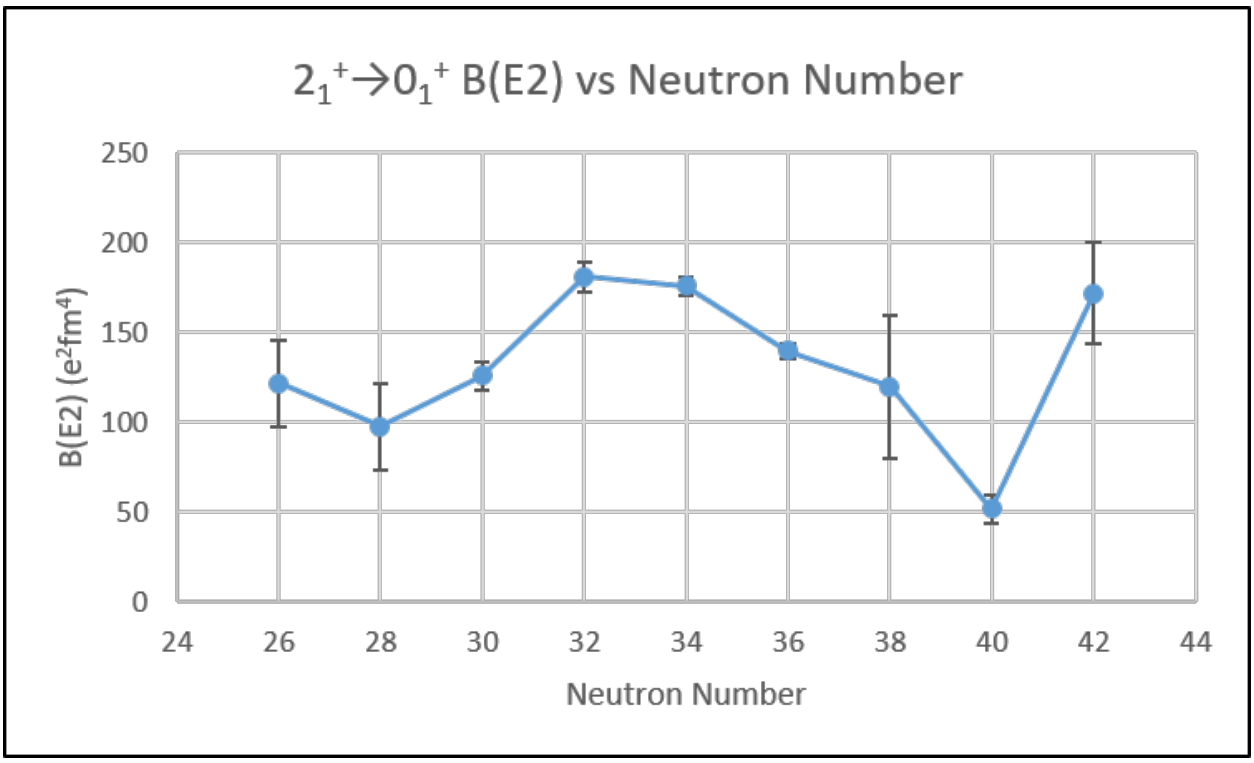

Figure 5.1: B(E2) reduced transition strengths for the $2_1^+ \rightarrow 0_1^+$ decay mode as a function of neutron number in the even-even Ni isotopes.

mass at these neutron numbers. Furthermore, the smooth, almost parabolic, dependence of the strength with mass A between the shell closures, with a maximum around N = 32-34 can be viewed as a signature of the increase in the contributions of the valence neutrons toward midshell. Indeed, the number of neutron particles increases toward midshell while the number of available holes decreases as $N = 40$ is approached. Figure 5.2 presents the excitation energy of the 2_1^+ levels as a function of mass throughout the isotopic chain. In this instance, the figure includes every even isotope up the doubly-magic ^{78}Ni, which has only recently been observed at RIBF, Japan [14]. In this case as well, the presence of the $N = 28$, 40 and 50 shell closures is clearly demonstrated through peaks in the respective 2_1^+ excitation energies. Here as well, the midshell between $N = 28$ and $N = 40$ translates into a minimum in the 2_1^+ excitation energy at neutron number 34.

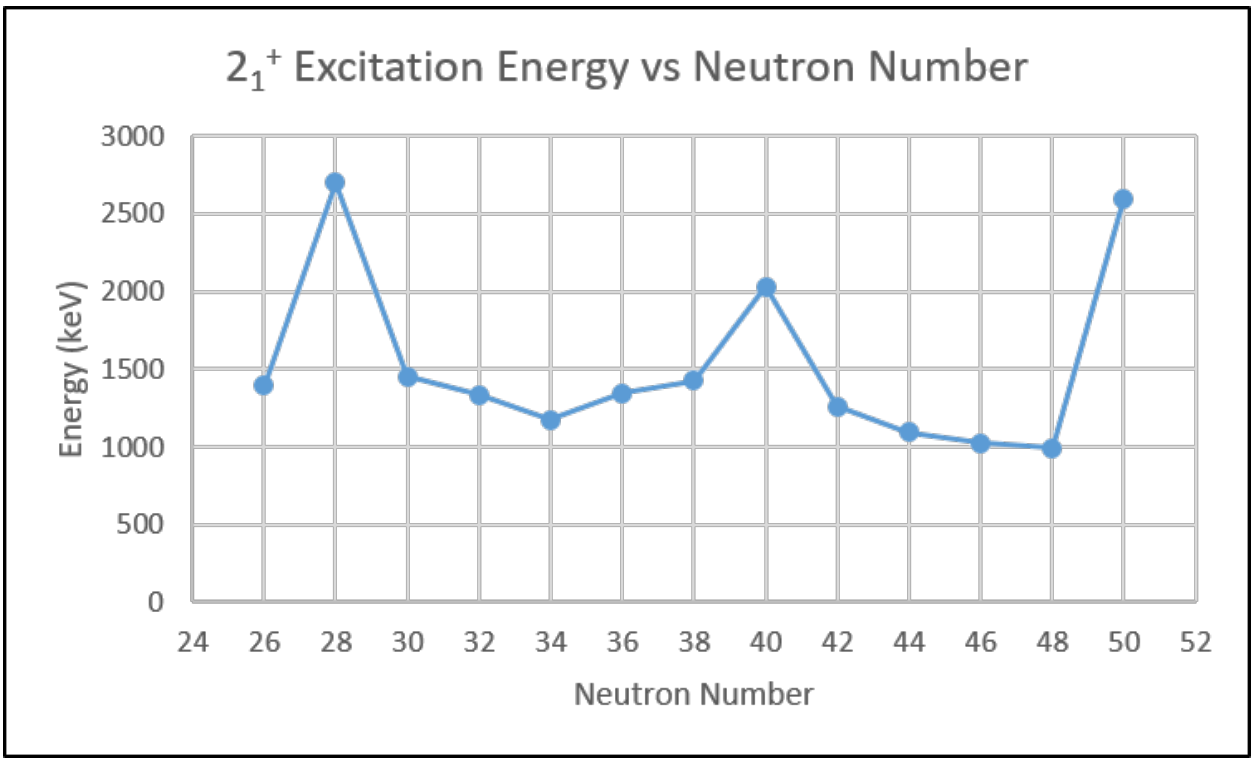

Figure 5.2: Excitation energies for the 2_1^+ states in even Ni isotopes as a function of neutron number.

Section 5.2: Spin, Parity and Energy Comparisions with Shell-Model Calculations and with MCSM

By comparing the spins, level energies, and transition strengths observed experimentally with those produced via shell-model and MCSM calculations, a more comprehensive understanding of the underlying nuclear structure can be gained, and information can be derived about the strengths and weaknesses of the models and the effective interactions these use. Before addressing ^{64}Ni, however, some of the calculations performed on the nearby nuclei, ^{62}Ni, ^{66}Ni, and ^{68}Ni will be explored in order to gain a relative understanding of the accuracy of each approach. Figures 5.3 and 5.4 can be found in Ref. [25], while Figure 5.6 was obtained from Ref. [28]. These figures include calculations using the jj44b and JUN45 effective interactions. While the jj44(b) Hamiltonian has already been discussed in the Theory chapter, the JUN45 effective interaction includes the same $f_{5/2}$, $p_{3/2,1/2}$, $g_{9/2}$ valence space as the jj44 one presented in the same chapter, but was developed by considering data on

levels in nuclei with $Z \approx 32$ and $N \approx 50$. The JUN45 interaction was designed based off the so-called Bonn-C potential and refined utilizing 133 two-body matrix elements and four single-particle energies that were modified empirically to fit 400 experimental energy data in 69 nuclei with mass numbers $A = 63 \sim 96$. As opposed to the jj44 Hamiltonian, the JUN45 one explicitly excludes the Ni and Cu isotopes from the fit due to the perceived "soft" core in ^{56}Ni [41, 97], and, because excitations of nucleons from the $f_{7/2}$ state to other orbitals can be significant in these nuclei [98]. Furthermore, Figure 5.5, gathered from Ref. [24], gives an illustration of MCSM calculations in comparison to the experimental data for ^{66}Ni. These should help to set the stage for comparisons with ^{64}Ni.

It is worth examining first the jj44b and JUN45 calculations for doubly-magic ^{68}Ni. Recall that, in this nucleus, the 0_2^+ state is pushed down in energy below that of the 2_1^+ level due to the effects of Type-II shell evolution, as discussed in the Chapter 2. Both calculations reproduce this effect and the level energies of both the 0_2^+ and 2_1^+ states are reproduced quite well by the JUN45 calculation, both lying within 100 keV of the experimental value. The jj44b interaction also performs relatively well, but with a divergence from the experimental values of about 300 keV. Surprisingly, however, neither the jj44b nor the JUN45 interaction was able to reproduce the 0_3^+ or 2_2^+ levels observed experimentally. As pointed out by Broda et al. [25], while both calculations reproduce the low-spin states rather well, they also indicate that the associated wavefunctions are rather complex and without a large contribution from a single configuration. Beyond these, the experimental 3147-keV, 4_1^+ state is reasonably predicted by the JUN45 calculation, to within 100 keV, and overestimated by the jj44b one by about 350 keV. The ordering of the positive-parity states is matched well by both sets of calculations, except for a tentative 4_2^+ level observed experimentally at 3405 keV, for which there is no analogous state in the computations. Besides this, both calculations predict a 11^+ state that has yet to be seen in an experiment. Now looking at the negative-parity states, the calculations appear to do a good job in reproducing the experimentally observed energies and spins. Aside from the jj44b interaction underpredicting the 3_1^- level by about

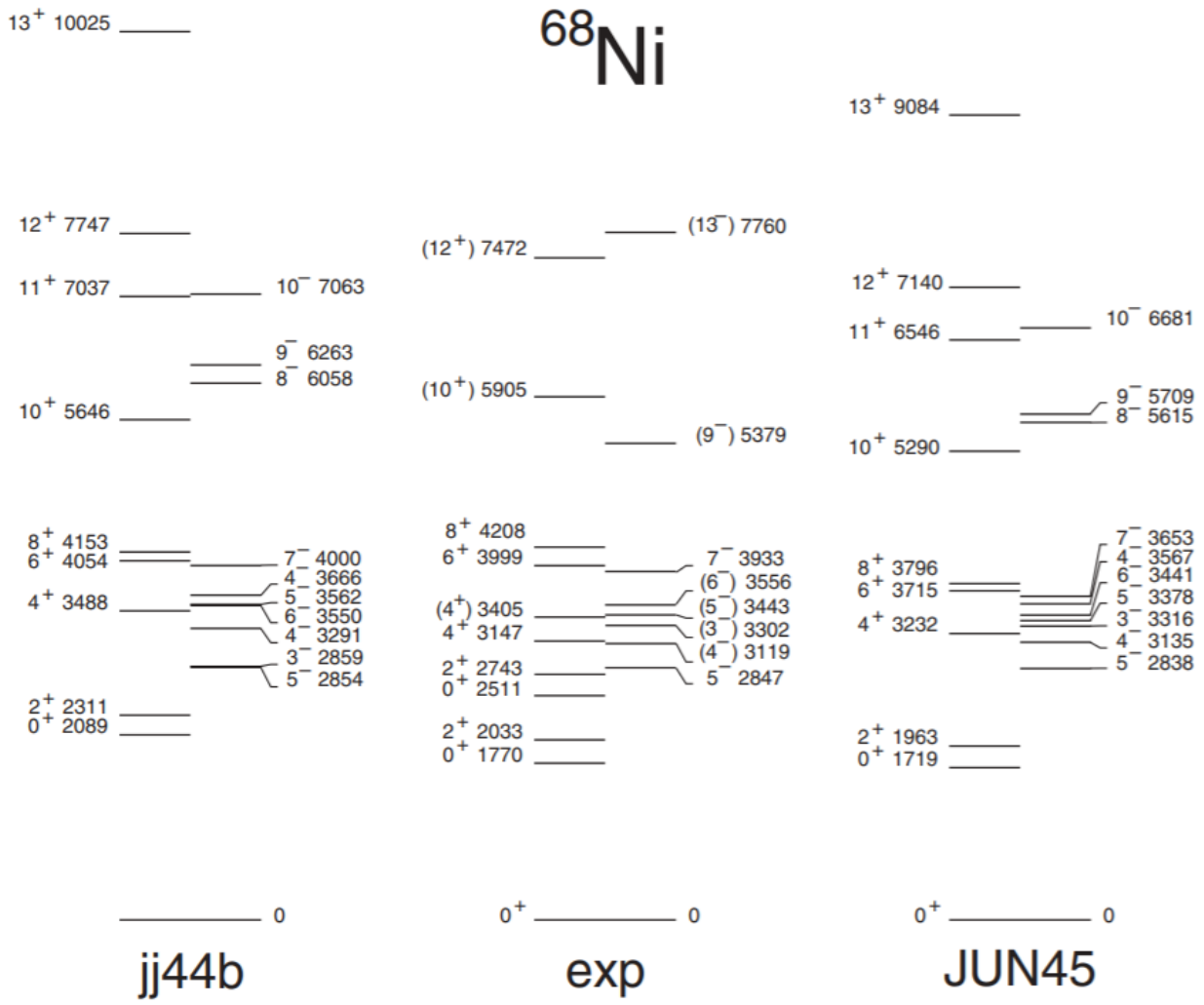

Figure 5.3: Comparison of jj44b and JUN45 calculations with experimentally observed states in ^{68}Ni [25].

450 keV, and altering the order of the 5_2^- and 6_1^- states, the levels are not far off from the experimental values. The JUN45 interaction appears to perform even better, predicting all of the negative-parity states below spin 7 to within 100 keV, and the 7_1^- level to within 300 keV. The ordering of the spin sequences matches that of the experiment, aside from a 4_2^- level that was predicted by both the jj44b and JUN45 Hamiltonians, but was not observed thus far.

Moving onto ^{66}Ni, and its 1425-keV, first-excited state, it is clear from Figure 5.4 that both the jj44b and JUN45 Hamiltonians reproduce this state, with levels located only 100-200 keV off at 1542 and 1624 keV, respectively. In this respect, the jj44b calculations perform slightly better, although the difference is likely within the uncertainties associated with these effective interactions. Looking at the 0_2^+ state at 2443 keV, both models reproduce this state reasonably well, with the jj44b calculations slightly underestimating the excitation energy at 2351 keV, and the JUN45 ones overestimating it somewhat at 2539 keV. Beyond this point, the discrepancies between theory and experiment become more apparent. The 0_3^+ state, located at 2671 keV, is overestimated by both models, with the JUN45 interaction predicting the excitation energy to be 2896 keV, e.g. roughly 200 keV off, while jj44b calculations place the state at 3011 keV, almost 350 keV above the experimental value. Both the 2_2^+ and 4_1^+ levels are reproduced well by both approaches, however, the experimentally observed 2_3^+ state is not accounted for by either of the two calculations. The excited 4_2^+ and 4_3^+ states observed at energies 3614 and 3793 keV, are significantly overestimated with the jj44b interaction, producing values roughly 500 keV higher at energies of 4197 and 4240 keV. In contrast, the JUN45 calculations predict the 4_2^+ state to within 200 keV, however, the calculated 4_3^+ level of 4154 keV, is still computed to be considerably higher than the observed one. The order of the positive-parity states remains relatively consistent between the experimental data and calculations at lower spins, despite the fact that the JUN45 computations switch the order of the 3_1^+ and 4_1^+ levels. Conversely though, the ordering of the negative-parity states is quite inconsistent when comparing all three level diagrams.

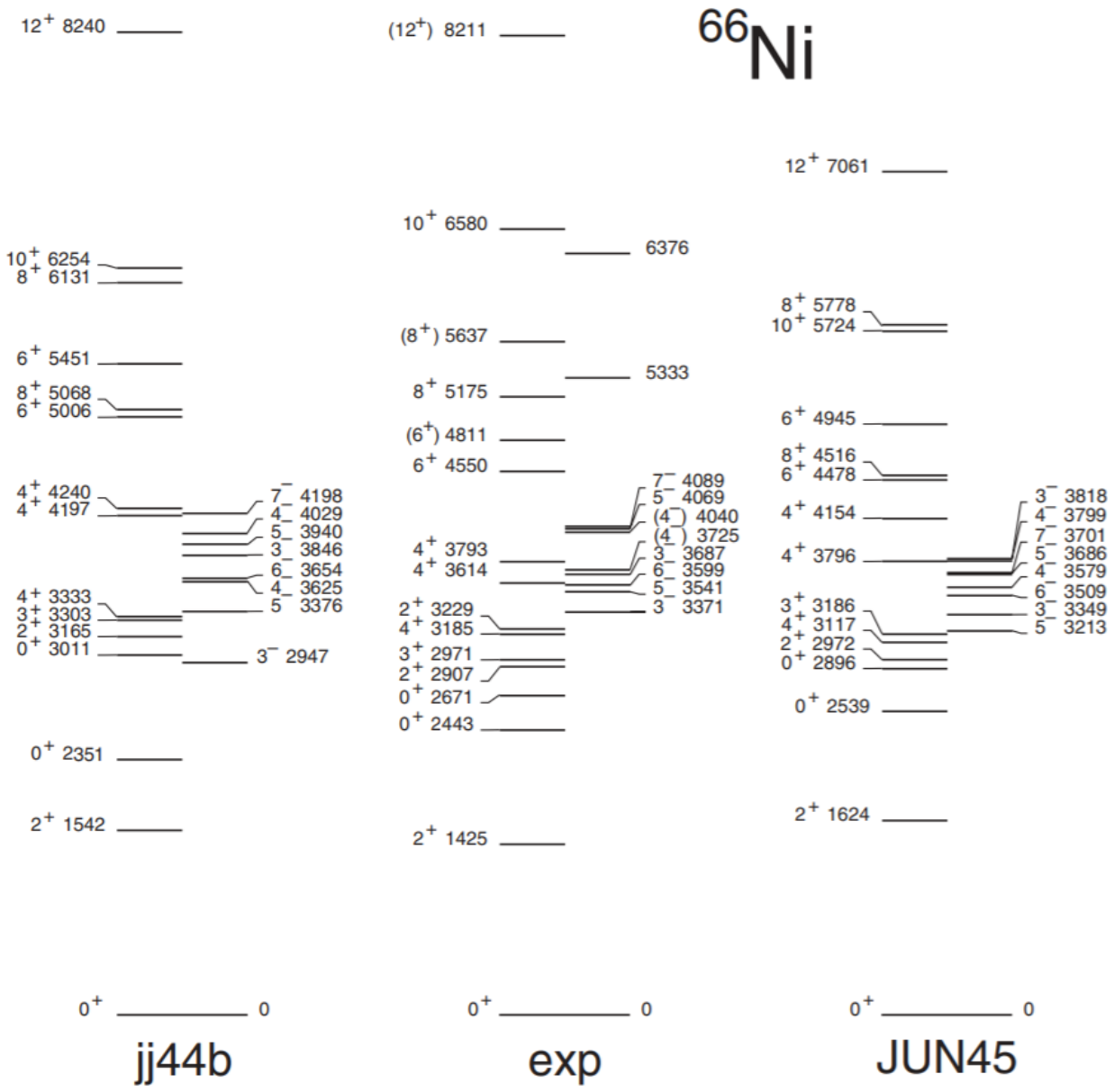

Figure 5.4: Comparison of jj44b and JUN45 calculations with experimentally observed states in ^{66}Ni [25].

The sequence of spins observed experimentally for the negative-parity levels varies notably from the sequences produced by both calculations and, in addition, those with the jj44b Hamiltonian appear to underpredict the 3_1^- state by over 400 keV. In essence, what can be said is that, while both jj44b and JUN45 interactions reproduce the positive-parity states reasonably well, given a few discrepancies, the negative-parity states appear much harder to predict. A priori, negative-parity states would be associated with excitations with one neutron occupying the $p_{3/2}$, $f_{5/2}$, or $p_{1/2}$ negative-parity orbitals near the Fermi surface and the other being in the positive-parity $g_{9/2}$ state. It is possible that, as suggested by Broda et al. [25], both interactions do not account properly for the $g_{9/2}$ single-particle energy. However, as Ref. [25] also indicates, the calculations with both interactions suggest that the states are characterized by complex structures involving typically more than ten configurations with contributions to the wavefunction exceeding a few percent (see Table 5 of Ref. [25]). In conclusion, based on these comparisons, there appears to be no clear advantage of one interaction over the other.

Taking a glance at the MCSM calculations performed for ^{66}Ni (see Figure 5.5) as referenced by Leoni et al. [24], it can initially be seen that the 1425-keV, 2_1^+ state is matched well by the theory. However, above this, the 0_2^+ and 2_2^+ states measured at excitation energies of 2443 and 2907 keV, respectively, seem to differ by a few hundred keV from the values predicted by the MCSM calculations. The accuracy is somewhat difficult to determine because the exact energies of the MCSM levels were not included in Figure 5.5 (the only information available in this case). Nevertheless, it can be estimated that the computed excitation energies for each of the states differ from the data by about 400 keV. The 0_3^+ state then appears to be reproduced reasonably well by the calculations, whereas the 0_4^+ level again seems to be accounted for more poorly. It may be worth reiterating here that the ground and 0_3^+ levels in ^{66}Ni are both interpreted within the calculations as associated with a spherical shape, whereas the 0_2^+ and 0_4^+ ones are understood as being characteristic of weak oblate and strong prolate deformation, respectively. More generally, the ordering of both the positive-

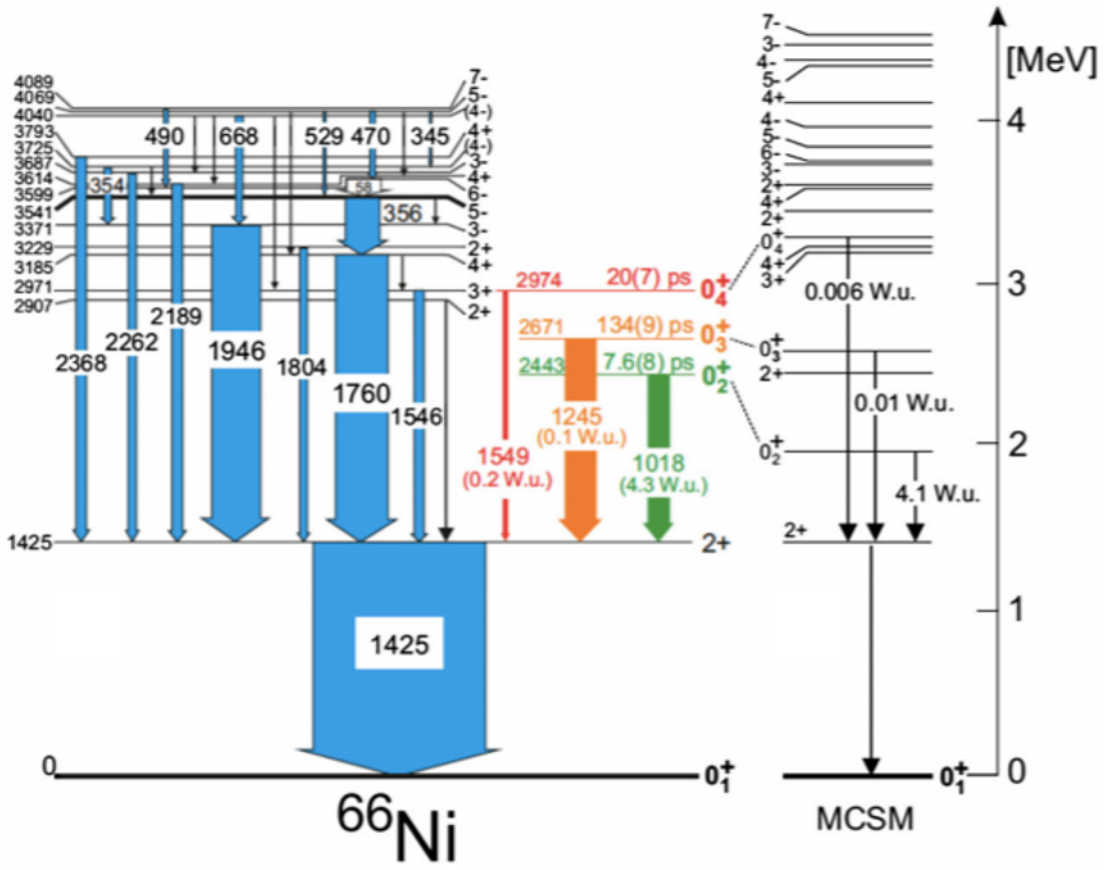

Figure 5.5: Comparison of MCSM calculations with experimentally observed states in ^{66}Ni [24]. Information on the exact level energies from MCSM calculations is not available.

and negative-parity states appears to differ somewhat from that observed. In this case, the MCSM computations do a good job of reproducing the first excited state, as well as the spherical 0_3^+ level, but have difficulty with some of the others. All in all, the agreement between theory and data is comparable with the three calculations.

Looking at the calculations performed for the ^{62}Ni nucleus (Figure 5.6), it should first be noted that the two states identified by red lines in the figure indicate the heads of two deformed bands that were observed in Ref. [28], although this will not be discussed in detail here. From a first, cursory, look at the figure it is immediately clear that the 12^- states predicted by the calculations are located at considerably higher energies than the one observed experimentally. According to Broda et al. [25], this can be viewed as an indication that the calculations are ill-equipped to handle the multi-particle-hole excitations required to generate the highest spins. Moving down to the bottom of the level scheme, and examining the first excited level reveals that the 1172-keV, 2_1^+ state is significantly more difficult for the calculations to reproduce than the first-excited states in the heavier Ni nuclei previously discussed. The jj44b interaction still performs rather well, predicting a level at 1423 keV, only about 250 keV higher than the experimental value, although this is a notable discrepancy in comparison to the accuracy of the predictions for the 2_1^+ states in the heavier isotopes. However, the JUN45 Hamiltonian predicts a 2_1^+ level at 1820 keV, 650 keV higher than the observed value, in stark contrast with similar comparisons above. Interestingly though, the 2336-keV, 4_1^+ level is reproduced more accurately by the JUN45 calculation, with an energy only about 130 keV lower at 2204 keV. In this instance, the jj44b result overestimates the excitation energy, placing the same level at 2689 keV, about 350 keV higher than observed. The 3177-keV, 4_2^+ state is well reproduced by both of the calculations, each being less than 100 keV removed from the data, whereas the 3276-keV, 4_3^+ one is overpredicted by both, with the jj44b calculations only erring by about 200 keV, and the JUN45 ones overestimating by 380 keV. This being said, the ordering of the positive-parity states in both calculations is the same as that observed experimentally. It appears that with regard to the negative-parity

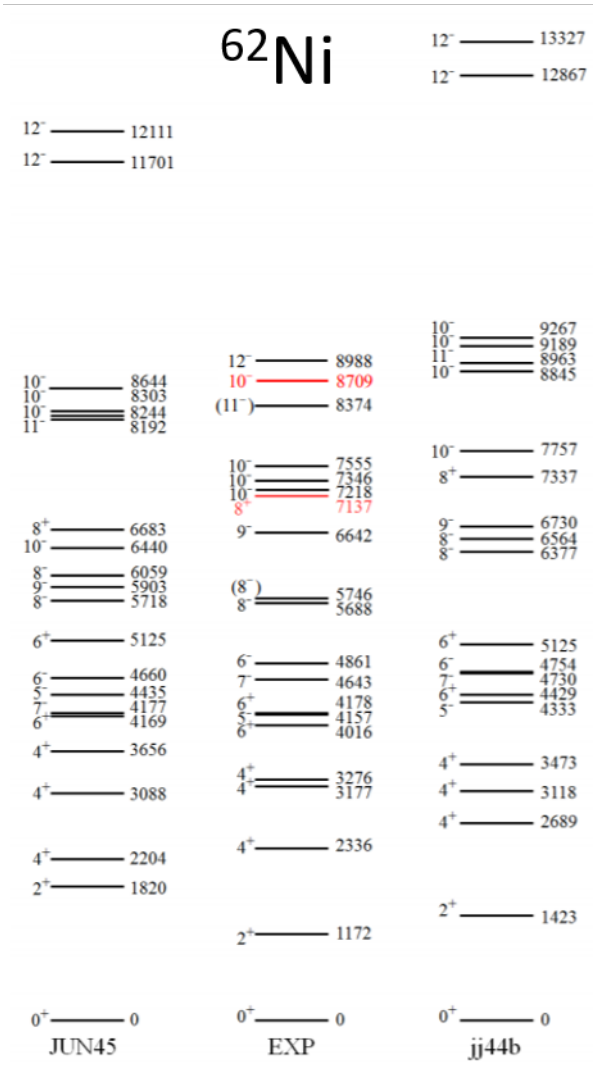

Figure 5.6: Comparison of jj44b and JUN45 calculations with experimentally observed states in ^{62}Ni [28]. The red lines in the figure mark the heads of two deformed bands observed in Ref. [28], following a deep-inelastic reaction.

states, both calculations perform rather well for spin 5_1^-, 6_1^- and 7_1^- states, with the exception of the JUN45 computation reversing the ordering of the states of spin 5_1^- and 7_1^-. The two spin 8^- states at energies of 5688 and 5746 keV are also reproduced well by the JUN45 calculations, whereas the jj44b results predict the same states to be located considerably higher, at energies of 6377 and 6564 keV, respectively. With respect to this ^{62}Ni nucleus, most notable appears to be the difficulty the theory has with reproducing the first excited state. This may reflect the fact that this is a midshell nucleus resulting in wavefunctions where more configurations contribute, which is, then, more sensitive to the lack of knowledge of the single-particle energies and the effective interactions as a result.

Generally speaking, the comparisons presented above for the ^{62,66,68}Ni neighbors of ^{64}Ni indicate that the jj44b and JUN45 Hamiltonians reproduce most of the features present in the low-spin level structures, especially when it comes to the positive-parity states. In every instance, however, the calculations indicate rather complex wavefunctions involving a number of configurations, all with amplitudes of no more than 10-20%. Attention was drawn above to the negative-parity states as these require excitations involving holes in the fp orbitals, with neutrons being promoted across the gap into the $g_{9/2}$ or other nearby, positive-parity neutron orbitals.

Turning to ^{64}Ni, the focus of this thesis, Figure 5.7 depicts the results of the shell-model calculations with the two effective interactions, jj44b and JUN45, and compares these with the ^{64}Ni level scheme obtained in the ^{48}Ca + ^{26}Mg deep-inelastic reaction described in the present work. It should be noted that, in this figure, the observed states are only listed up to the energy of the highest 10^+ level. As stated above, when comparing theory and experiment for the other isotopes, the complexity of the wavefunctions increases with spin with a large number of multi-particle-hole configurations contributing. As a result, the computed states can often not be readily associated with specific observed levels, leaving meaningful comparisons to future work. Note, however, that below spin 10, calculated states that were not observed in the deep-inelastic experiment, such as the excited 0^+ states, are

still depicted in order to present a more comprehensive picture of the theory predictions.

In addition to the calculations used for comparison with the the deep-inelastic experiment, two additional shell-model calculations have been carried out by Alex Brown for comparison with the ^{64}Ni Coulomb excitation data. These calculations use the jj44 and fp model spaces, as referred to in Section 1 of the Theory chapter. In addition, Monte Carlo shell-model (MCSM) calculations performed by the Tokyo group of Takaharu Otsuka are available as well. Comparisons of the experimental results with the jj44, fp, and MCSM calculations are depicted in Figures 5.8, 5.9, and 5.10, respectively.

Examining the comparison between the levels obtained from deep-inelastic reactions with those calculated in Ref. [25], one can see that the jj44b effective interaction accurately reproduces the majority of the states observed in this experiment. The first-excited state, located at 1346 keV, is only about 140 keV lower than that determined by the jj44b interaction, which places the same level at an energy of 1484 keV. The 2277-keV, 2_2^+ state is also predicted well by the jj44b calculations, this time being slightly higher than the theoretically determined value of 2135 keV. Both the 4_1^+ and 4_3^+ states are also reproduced well by the jj44b Hamiltonian, with the first being only 34 keV higher and the second underestimating the experimental value by a little under 200 keV. The 3166-keV, 4_2^+ level is characterized by a slightly larger discrepancy, with the calculated value corresponding to 3494 keV, about 300 keV higher in energy. The 8^+ level also matches up to within 200 keV, however, the 7461-keV, 10^+ state does appear to be overestimated by the jj44b calculations by almost 700 keV, although this is typical when compared to higher-spin states in the previously discussed calculations. On the other hand, the calculated 10^+ state is quite close to the experimentally observed tentative 10_2^+ level at 7440 keV. The positive-parity states are clearly reproduced well by the jj44b interaction both in terms of ordering and excitation energy. With regard to the negative-parity states, the ordering once again matches well with that observed experimentally. Furthermore, aside from the 3^- and 6^- levels, all the calculated negative-parity states match the experimental excitation energies to within 200 keV. The

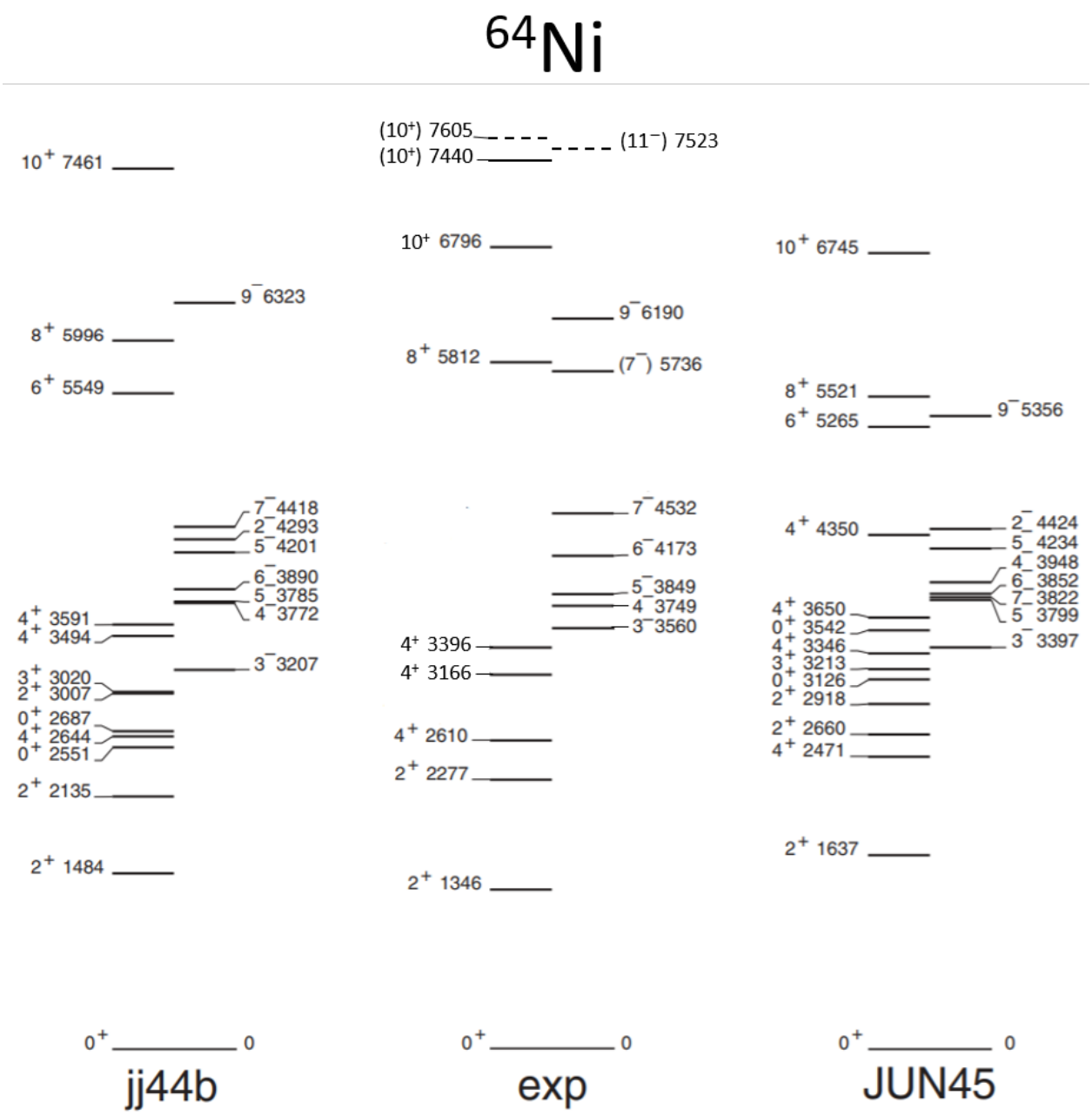

Figure 5.7: Comparison of jj44b and JUN45 calculations (obtained from Ref. [25]) with experimentally observed states in ^{64}Ni for this experiment. Note that the two 10^+ levels located at 7440 and 7605 keV, as well as the 11^- one at 7523 keV have been observed for the first time in the present work.

3^- and 6^- states located at 3560 and 4173 keV, respectively, are both underestimated by the jj44b calculations by around 300 keV, however, even this discrepancy is in line with the deviations seen for other levels. The only state the interaction appears to have difficulty reproducing is the tentative 7_2^- one at 5736 keV. The jj44b calculations only reproduce a single 7^- state located at 4418 keV, which compares well to the 7_1^- level seen experimentally at 4532 keV, but the tentative 7_2^- one has no comparable analogue. Aside from these minor discrepancies, the jj44b results perform well with regard to reproducing the levels of ^{64}Ni observed in deep-inelastic reactions.

The JUN45 interaction, on the other hand, seems to have a harder time reproducing both the majority of the level energies, and the ordering of the states. When examining the first-excited state, one can already see that the JUN45 Hamiltonian produces a value nearly 300 keV higher at 1637 keV. Additionally, the 2_2^+ state in the JUN45 calculations is pushed up above the 4_1^+ level, overshooting the experimental 2_2^+ level by nearly 400 keV. The computed 4_1^+ state, on the other hand, appears to match up well with the experimental value, showing a disparity of only 140 keV. The 4_2^+ and 4_3^+ levels also compare reasonably well, with the calculations overestimating them by about 200 and 250 keV, respectively. The 5812-keV, 8^+ state observed in the experiment is predicted to be nearly 300 keV lower by the JUN45 interaction, although, once again, for a higher-spin state this is not unusual. Interestingly though, the 10_1^+ level is well-reproduced by the calculations, showing a difference of only 50 keV. While it seems apparent that the JUN45 Hamiltonian is outperformed by the jj44b one regarding the positive-parity states, the former still offers a reliable prediction. The greater disparity arises when reproducing the negative-parity levels. Firstly, the experimental ordering of the latter states is quite different from the calculated one. As addressed in Ref. [25], this disorganization is largely due to the role of state mixing, which affects relative positions of levels and is an inherent consequence of the choice of residual interactions. It can be seen that while the 3_1^- state is predicted to within about 160 keV, the 7^- state, in particular, is 700 keV lower in the calculations than the 7_1^- state observed experimentally,

and is situated below both the 4^- and 6^- states, herewith producing a largely different ordering of levels. The energies of the 4^- and 5^- states are predicted well, to within 250 and 50 keV, respectively, however, the 6^- level is underestimated by the JUN45 Hamiltonian by about 320 keV, placing it below the 4^- state. Lastly, the 6190-keV, 9^- level is considerably underpredicted by the calculations, as the 5356-keV computed excitation energy is over 800 keV lower than the data. As previously noted, according to Ref. [25], the negative-parity states of spin 2^- to spin 7^- in the nuclei ^{64,66,68}Ni correspond to the promotion of a single neutron to the $g_{9/2}$ orbital, which then couples with the three lower, natural-parity states. Consequently, the fact that the energies of these states are consistently underpredicted by the JUN45 calculations, not only in ^{64}Ni, but in ^{66}Ni and ^{68}Ni as well, implies that the adopted single-particle energy of the $g_{9/2}$ neutron orbital is too low. This also contributes to the difficulty in reproducing higher-spin states, as these predominantly arise from complex excitations involving two or more $g_{9/2}$ neutrons. Overall, the JUN45 interaction performs reasonably well, but with regard to ^{64}Ni, it is clearly inferior to the jj44b one. This may be expected, due to the fact that the data used to define the JUN45 effective interaction explicitly exclude the Ni and Cu isotopes, whereas the jj44b Hamiltonian is based specifically on data on Ni isotopes with masses A from A=57 to 78, including ^{64}Ni itself, as referenced in Chapter 2.

In summary, it is worth remembering that the deep-inelastic scattering experiment serves as one of the two main focuses of this dissertation. While no new levels were observed above the 0^+ excited states of interest, 12 new higher-spin states were discovered at high excitation energy and these have been placed in the ^{64}Ni level scheme, along with 13 new transitions. Tentative spins were assigned for each of the new levels. Furthermore, the known yrast sequence was extended by a single 873-keV transition, leading to a new (12^+) state at 7669 keV. Comparisons with the jj44b and JUN45 effective interactions reveal the significance of including explicit Ni and Cu data when constructing effective interactions whenever it is necessary to properly account for the "soft" core of such nuclei. Moreover, as addressed

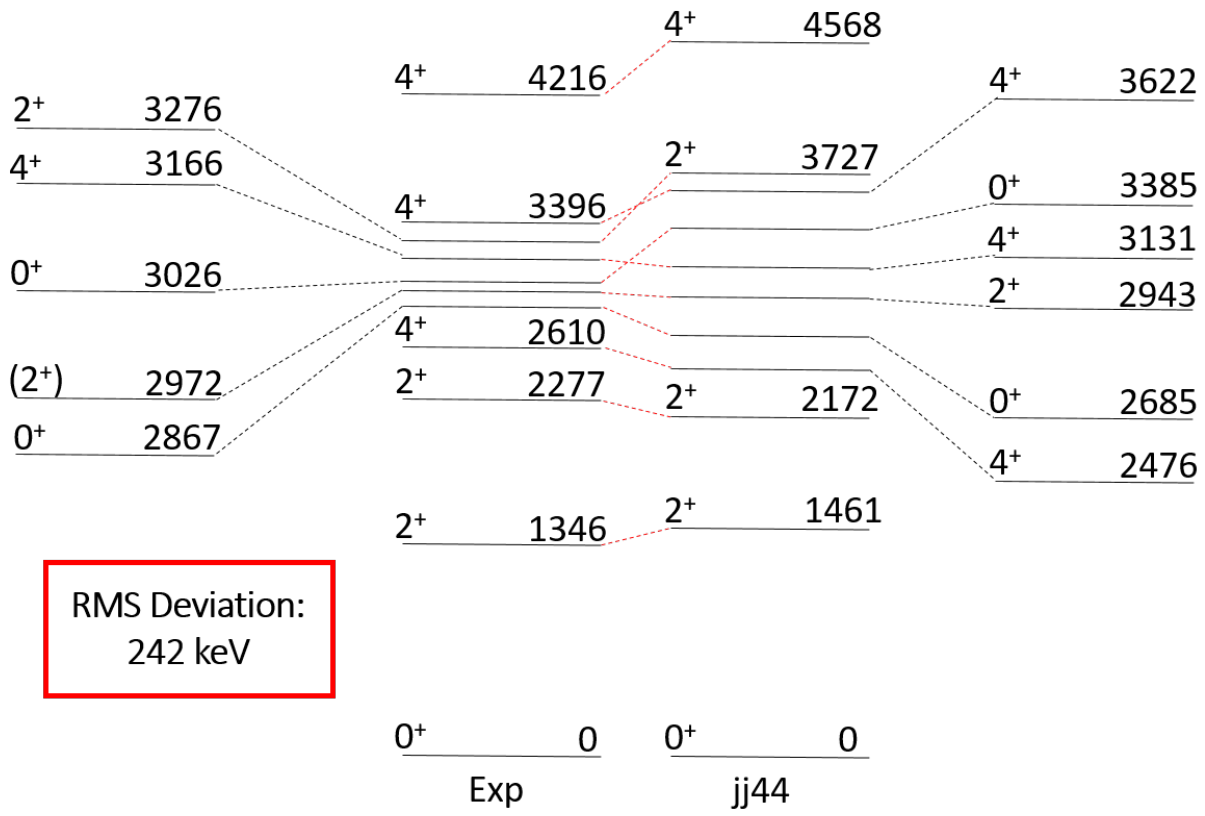

Figure 5.8: Comparison of jj44 calculations performed by Alex Brown with the ^{64}Ni states observed in the present Coulomb excitation experiment.

in Ref. [25], it was reaffirmed that the adopted single-particle energy of the $g_{9/2}$ neutron orbital is likely too low, hampering the ability of the models to reproduce negative-parity and high-spin states. This concludes the deep-inelastic portion of the discussion, with the remainder of the chapter focusing on the states and transitions observed specifically by the Coulomb excitation experiment.

An examination of the Coulomb excitation results begins with a comparison between the observed levels and the new jj44, fp, and MCSM calculations (the first two being carried out by Alex Brown [99], and the third by Takaharu Otsuka and collaborators [100]), which are illustrated in Figures 5.8, 5.9, and 5.10, respectively. Judging by the root mean square (RMS) deviations of the calculated levels from the experimental ones, it can be seen that while all three calculations do a satisfactory job at reproducing the experimentally observed

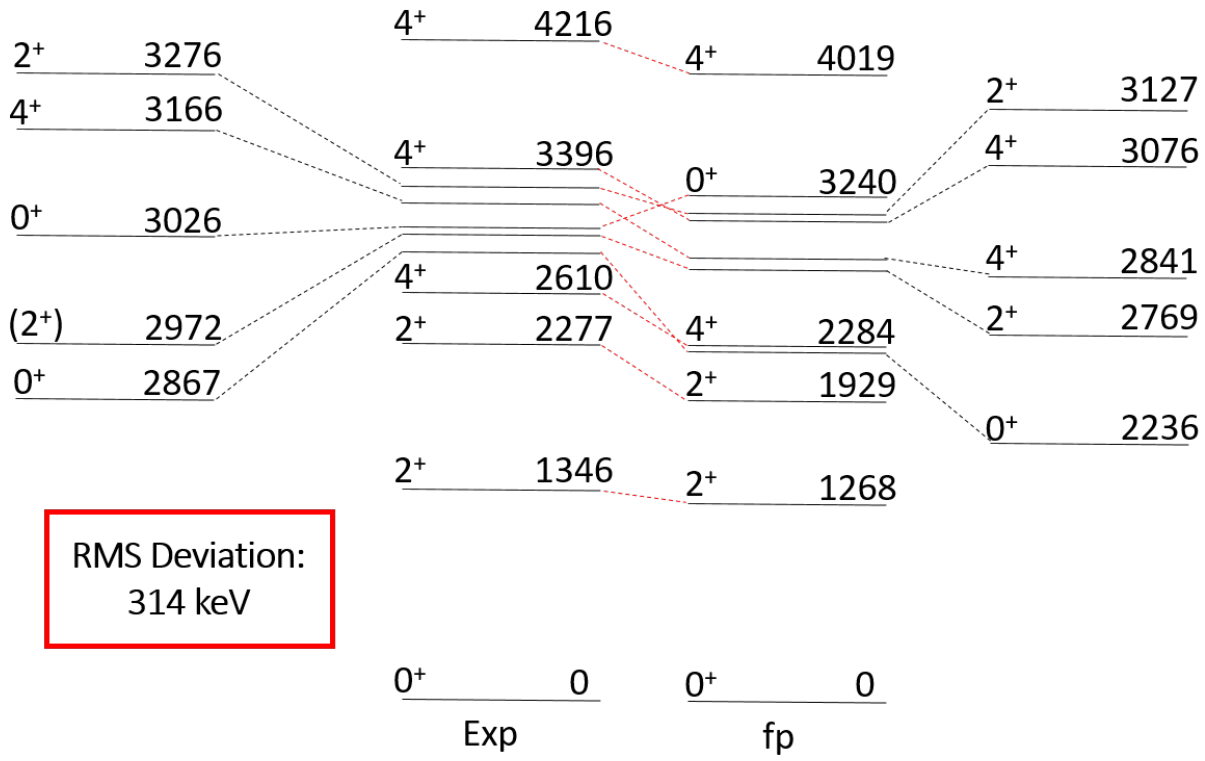

Figure 5.9: Comparison of fp calculations performed by Alex Brown with the ^{64}Ni states observed in the present Coulomb excitation experiment.

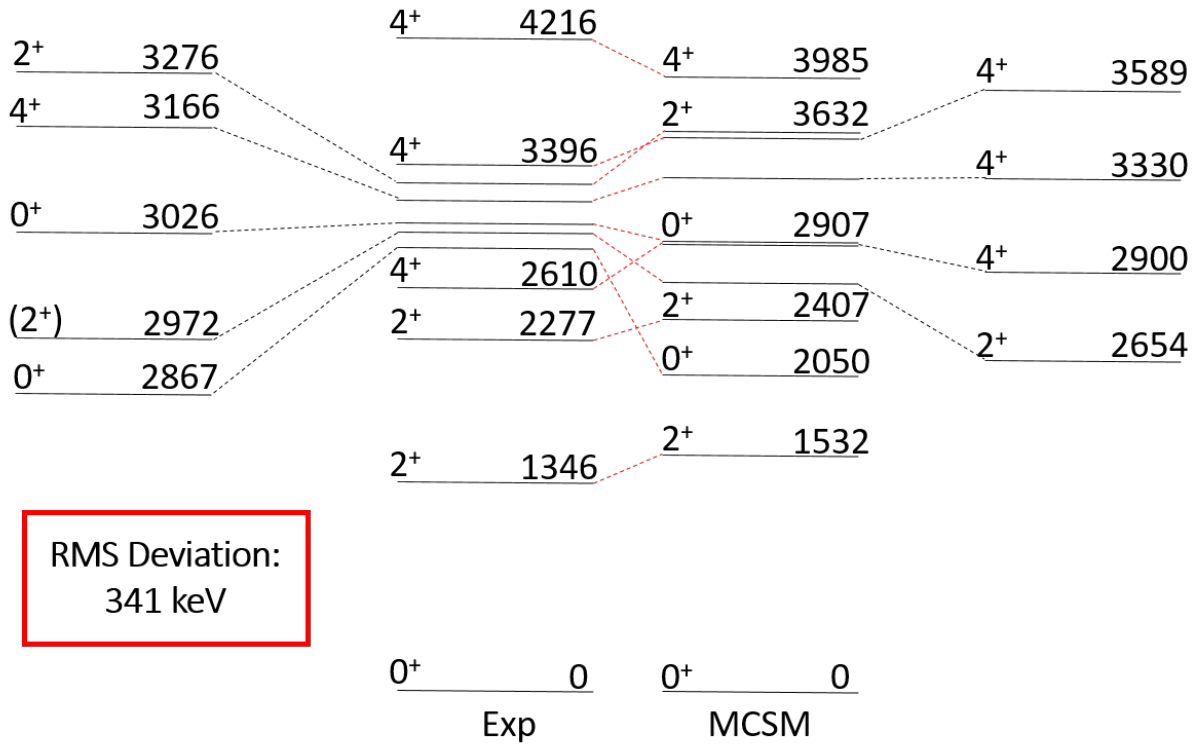

Figure 5.10: Comparison of MCSM calculations performed by the Tokyo group of Takaharu Otsuka with the ^{64}Ni states observed in the present Coulomb excitation experiment.

states, the jj44 results tend to be the most accurate, followed by the fp one, with the MCSM calculations showing the largest deviations. Each of the RMS deviations are in the vicinity of 200-300 keV, which is typically as good as can be expected from such calculations. In addition to the RMS deviations, a glance at the level diagram from the jj44 computations once again highlights the fact that this model space performs comparatively well with regard to reproducing the ordering of the different spin states, showing only two states out of order with respect to those observed experimentally. This result is especially worth noting, due to the fact that the jj44 calculations only consider excitations involving neutrons in the $f_{5/2}$, $p_{3/2,1/2}$, and $g_{9/2}$ orbitals. Since ^{64}Ni possesses a closed major proton shell (magic number Z=28), it was thought a priori that most of the low-energy states would be associated predominantly with neutron excitations, and this is, indeed, supported by the success of the jj44 calculations. However, taking a closer look at the 0_3^+ state, specifically, one can see that this level is in fact reproduced most accurately by the MCSM calculations, followed by the fp ones, and lastly those in the jj44 space. This is noteworthy as it may suggest that the configuration of the 0_3^+ level might involve a combination of both proton and neutron excitations rather than only the neutron excitations, which reproduce the other low-spin states. This conjecture can be explored further through comparisons of the three calculations with the reduced transition strengths.

Section 5.3: Comparisons of Calculated and Observed Reduced Transition Strengths

Table 5.1 lists the measured reduced transition strengths, as determined by the analysis with the GOSIA code, alongside those obtained from the two shell-model calculations within the jj44 and fp model spaces as well as those using the MCSM approach. Transitions for which an experimental value is not listed in the table were not determined via the analysis with GOSIA, but the calculated values are included because of their relevance for the discussion below. Note that decay modes involving the 3560-keV, 3^- level are not listed in this table

$I_i^\pi \to I_f^\pi$	$Mult(\pi\lambda)$	$E_\gamma(keV)$	Exp	$B(\pi\lambda_\downarrow; i \to f)^*$ fp	jj44	MCSM
$2_1^+ \to 0_1^+$	E2	1346	140(20)	139	142.5	151
$2_2^+ \to 0_1^+$	E2		$0.05^{+0.05}_{-0.02}$	2.0	2.2	0.44
$2_2^+ \to 2_1^+$	E2	931	44^{+4}_{-2}	139.6	185.9	132
$2_2^+ \to 2_1^+$	M1	931	$0.1^{+0.6}_{-0.1}$	0.014	0.011	0.010
$4_1^+ \to 2_1^+$	E2	1264	66^{+7}_{-4}	28.9	0.22	124
$4_1^+ \to 2_2^+$	E2		200^{+50}_{-30}	61.5	43.2	25
$0_2^+ \to 2_1^+$	E2	1522	48(3)	70.9	1.8	43
$0_2^+ \to 2_2^+$	E2		700(200)	69.2	21.9	237
$2_3^+ \to 0_1^+$	E2	2972	0.15(5)	7.4	0.25	0.11
$2_3^+ \to 2_1^+$	E2	1626	5^{+5}_{-3}	20.2	6.2	6
$2_3^+ \to 2_1^+$	M1	1626	$0.000002^{+0.000378}_{-0.000002}$	0.026	0.0054	0.0016
$2_3^+ \to 2_2^+$	E2		2^{+20}_{-2}	7.7	1.4	270
$2_3^+ \to 2_2^+$	M1		$0.007^{+0.003}_{-0.005}$	0.028	0.067	0.0057
$2_3^+ \to 4_1^+$	E2		130(50)	0.48	11.5	0.42
$0_3^+ \to 2_1^+$	E2	1680	10(1)	0.21	1.5	5.8
$0_3^+ \to 2_2^+$	E2		600(300)	31.9	2.1	2.6
$4_2^+ \to 2_1^+$	E2	1820	69(2)	133.7	140.1	131
$4_2^+ \to 2_2^+$	E2			2.8	2.1	54
$2_4^+ \to 0_1^+$	E2	3276	1.8(2)	2.4	0.006	5
$2_4^+ \to 2_1^+$	E2	1930	9(1)	11.2	0.2	9
$2_4^+ \to 2_1^+$	M1	1930	$0.00006^{+0.00031}_{-0.00006}$	0.0022	0.000009	0.012
$4_3^+ \to 2_1^+$	E2	2050	2.5(5)	8.2	10.1	3
$4_3^+ \to 2_2^+$	E2			3.9	0.06	213
$4_3^+ \to 4_2^+$	E2			24.6	9.6	127
$4_4^+ \to 2_1^+$	E2		$11.4^{+1.6}_{-1.5}$	3.8	1.9	0.58
$4_4^+ \to 4_1^+$	E2	1606	900^{+2000}_{-200}	1.7	5.4	0.33
$4_4^+ \to 4_1^+$	M1	1606	0.2(2)	0.34	0.018	0.0068

Table 5.1: Comparison of experimental reduced transition strengths with those obtained via fp, jj44, and MCSM calculations.
*Units for reduced transition strengths are μ_n^2 and e^2fm^4 for M1 and E2 transitions, respectively.

as the three calculations have not been extended to the negative-parity states.

The computations of reduced transition probabilities within the shell model require the use of effective charges. All three calculations adopt the conventional value of 1.5 e for the proton effective charge. However, while the MCSM and fp computations also adopt the canonical 0.5 e value for the neutron effective charge, the jj44 ones use 1.2 e. As stated in the theory chapter, the jj44 calculations only consider neutron excitations, including those involving neutrons in the $g_{9/2}$ orbital. As protons are ignored in this case, their contribution to the B(E2) is mimicked by boosting the neutron effective charges to 1.2 e, the value required to reproduce the measured B(E2; $2_1^+ \to 0_1^+$) transition probability.

As was the case throughout this discussion chapter, the calculated reduced transition

				π					ν		
I^π	Calculation	$f_{7/2}$	$p_{3/2}$	$f_{5/2}$	$p_{1/2}$	$g_{9/2}$	$f_{7/2}$	$p_{3/2}$	$f_{5/2}$	$p_{1/2}$	$g_{9/2}$
0_1^+	fp	7.51	0.37	0.1	0.03		7.92	3.22	4.03	0.83	
	jj44							3.04	3.57	0.74	0.65
	MCSM	7.39	0.37	0.1	0.03	0.09	7.84	3.18	3.57	0.82	0.55
2_1^+	fp	7.38	0.48	0.1	0.03		7.92	3.22	4.03	0.83	
	jj44							3.04	3.57	0.74	0.65
	MCSM	7.1	0.6	0.14	0.05	0.09	7.82	3.09	3.33	1.09	0.63
2_2^+	fp	7.41	0.46	0.1	0.03		7.94	3.4	3.83	0.84	
	jj44							3.12	3.57	0.92	0.39
	MCSM	6.7	0.84	0.26	0.1	0.08	7.75	2.86	3.27	1	1.08
2_3^+	fp	7.41	0.44	1	0.03		7.94	3.36	3.62	1.08	
	jj44							2.24	4.88	0.26	0.62
	MCSM	6.65	0.88	0.27	0.1	0.08	7.74	2.8	3.27	1.1	1.05
2_4^+	fp	7.58	0.32	0.09	0.02		7.93	2.12	4.19	0.77	
	jj44							3.24	3.24	1.11	0.41
	MCSM	7.43	0.38	0.07	0.02	0.08	7.88	3.28	3.48	1.04	0.29

Table 5.2: Orbital occupancy values associated with 2^+ states in ^{64}Ni, as predicted by the fp, jj44, and MCSM calculations. The occupancy values of the spin-0, ground state are also included here for reference. All proton occupancy values correspond to zero for the jj44 computation due to the fact that proton excitations were excluded from the model space in this case (see text for details).

				π					ν		
I^π	Calculation	$f_{7/2}$	$p_{3/2}$	$f_{5/2}$	$p_{1/2}$	$g_{9/2}$	$f_{7/2}$	$p_{3/2}$	$f_{5/2}$	$p_{1/2}$	$g_{9/2}$
0_1^+	fp	7.51	0.37	0.1	0.03		7.92	3.22	4.03	0.83	
	jj44							3.04	3.57	0.74	0.65
	MCSM	7.39	0.37	0.1	0.03	0.09	7.84	3.18	3.57	0.82	0.55
2_1^+	fp	7.38	0.48	0.1	0.03		7.92	3.22	4.03	0.83	
	jj44							3.04	3.57	0.74	0.65
	MCSM	7.1	0.6	0.14	0.05	0.09	7.82	3.09	3.33	1.09	0.63
0_2^+	fp	7.38	0.49	0.1	0.04		7.92	3.47	3.33	1.28	
	jj44							3.56	2.58	1.5	0.35
	MCSM	5.94	1.32	0.46	0.19	0.08	7.62	2.38	2.79	1.19	1.97
0_3^+	fp	7.61	0.29	0.09	0.02		7.9	2.67	4.97	0.46	
	jj44							4.88	2.24	0.26	0.62
	MCSM	7.3	0.46	0.1	0.03	0.1	7.82	3.44	3.12	1.21	0.38

Table 5.3: Orbital occupancy values associated with 0^+ states in ^{64}Ni, as predicted by the fp, jj44, and MCSM calculations. The occupancy values of the 2_1^+ state are also included here for reference. All proton occupancy values correspond to zero for the jj44 computation due to the fact that proton excitations were excluded from the model space in this case (see text for details).

strengths are compared hereafter with the data on a case-by-case basis. The strength of the 1346-keV ground state transition is computed satisfactorily as the measured value of 140(20) e^2fm^4 is reproduced within errors by all three calculations. This result is significant only for the fp and MCSM calculations as they are carried out with the standard effective charges. In fact, this agreement can be viewed as reinforcing confidence in the present data. In the case of the jj44 computations, the calculated 142.5 e^2fm^4 value solely reflects the fact that the adjustment of the neutron effective charge seems appropriate. An inspection of the occupancies in the three calculations (see Table 5.2) reveals that the proton $f_{7/2,5/2}$, $p_{3/2,1/2}$ configurations in the fp and MCSM spaces are similar for the 2_1^+ level; e.g. the $\pi g_{9/2}$ and the $\nu g_{9/2}$ and $\nu d_{5/2}$ occupations are found to be negligible in the MCSM approach. It is worth noting that this observation of a small occupation of proton orbitals across the shell gap is valid for all the levels discussed in the present work. Furthermore, the respective neutron occupancies in the MCSM and fp results are similar in the 0_1^+ and in the 2_1^+ levels. Hence, no significant difference between the fp and MCSM strengths should be expected. In addition, the neutron occupancies in the MCSM and jj44 calculations are similar as well, with the $\nu g_{9/2}$ orbital participating in the wavefunction at the 0.63 level only.

The $2_2^+ \rightarrow 0_1^+$ transition is experimentally determined to be quite small (Table 5.1), with a value of $0.05^{+0.05}_{-0.02}$ e^2fm^4. Indeed, all three calculations reproduce this value rather well, with the MCSM one matching it nearly exactly with a strength of 0.44 e^2fm^4. Looking at the $2_2^+ \rightarrow 2_1^+$ transition, the strengths determined by all three computations are calculated to be larger than that to the ground state. Furthermore, they are also larger than that of 44^{+4}_{-2} e^2fm^4 observed experimentally. While the fp, and MCSM strengths are comparable in this case, the jj44 computation overpredicts the value even more, suggesting a strength of 185.9 e^2fm^4. This overprediction is likely due to the artificially large effective charge of the neutrons applied in the jj44 calculations. Hence, the overprediction by the jj44 model in comparison to the other two values also suggests that the majority of the wavefunctions involved in the 2_1^+ and 2_2^+ levels occurs within the fp space. Moreover, all three calculations

also reproduce small M1 values similar to the $0.1^{+0.6}_{-0.1}\ \mu_n^2$ one observed experimentally. Looking at the neutron occupancies for this 2_2^+ level, there is general agreement between all the three computations. The most significant differences between the MCSM calculations and the other ones appear to be slight reductions in the $f_{7/2,5/2}$ and $p_{3/2}$ MCSM occupancies, compensated by larger occupancies of the higher-energy $p_{1/2}$ and $g_{9/2}$ orbitals. In particular, there is, thus, a significant contribution from the three aforementioned orbitals to the $\nu g_{9/2}$ one from across the shell gap. The MCSM value of 1.08 for this $g_{9/2}$ occupation number is considerably larger than the analogous value of 0.39 in the jj44 space, indicating that this increase in occupancy is likely one of the main disparities between the wavefuction associated with the 2_2^+ level and the 0_1^+ one. Additionally, while the occupation values for the proton orbitals remain mostly unchanged between the 2_2^+ level and the ground state in the fp space, and the MCSM values agree for the most part with those of the fp calculations, the MCSM occupancies still indicate some movement of protons from the $f_{7/2}$ orbital to the $p_{3/2}$ one. Hence, the calculations of the $2_2^+ \rightarrow 0_1^+$ transition strength indicate that proton excitations may play a minor role in the 2_2^+ wavefunction. Lastly, the large yield to the 2_1^+ level also appears reasonable due to the similar configurations of the two 2^+ states in terms of occupancies.

Moving onto the 2_3^+ state, a very small strength of 0.15(5) e^2fm^4 was measured for the $2_3^+ \rightarrow 0_1^+$ transition, which both the MCSM and jj44 calculations reflect well (Table 5.1). The fp computation, on the other hand, produces a considerably larger value of 7.4 e^2fm^4, suggesting that this transition is likely dominated by neutron excitations outside the fp model space. The $2_3^+ \rightarrow 2_1^+$ decay mode affirms this interpretation, as it is also calculated well by both the MCSM and jj44 computations and, once again, is overpredicted by the fp one. The small M1 transition strength further emphasizes the prevalence of neutron excitations. The small experimental $2_3^+ \rightarrow 2_2^+$ transition strength ($2^{+20}_{-2}\ e^2fm^4$) is predicted reasonably well by the fp calculations and even more so by the jj44 ones, whereas the MCSM result drastically overshoots, predicting a value of 270 e^2fm^4. Here, not much more is revealed by

the weak B(M1) transition. The final decay mode involving the 2_3^+ level worth noting is the $2_3^+ \rightarrow 4_1^+$ transition. The large experimentally determined strength of 130(50) e^2fm^4 is best reproduced by the jj44 calculations with a significantly smaller value of 11.5 e^2fm^4, whereas the MCSM and fp ones are far too small with values of 0.42 and 0.48 e^2fm^4, respectively. From the patterns exposed by all the transitions de-exciting the 2_3^+ level, it appears that this state is dominated by neutron excitations and may involve the $g_{9/2}$ intruder orbital. Turning to the occupancies, the values for proton ones differ somewhat between the fp and MCSM calculations, with the MCSM results indicating a drop in the $f_{7/2}$ occupation number and a redistribution of protons, predominantly to the $p_{3/2}$ orbital. Moreover, similar to the 2_2^+ level, the MCSM results predict a relatively high contribution from the neutron $g_{9/2}$ orbital (1.05 neutrons). Notably, the jj44 occupancies see a significant drop in both p orbitals and an increase in the $f_{5/2}$ one, in addition to the $g_{9/2}$ occupancy. One important takeaway here is the fact that it is likely the larger neutron occupancy that brings the MCSM calculations in agreement with the observed $2_3^+ \rightarrow 0_1^+$ transition strength. The $2_3^+ \rightarrow 2_2^+$ decay mode, on the other hand, is more challenging to comprehend by following the same line of arguments. It is understandable in the jj44 calculations that the disparity in the $g_{9/2}$ orbital between the two states would lead to a smaller transition strength. However, assuming that this applies for neutrons in the MCSM result as well, it must then be concluded that the rearrangement of the protons in this MCSM case (with respect to the fp one) leads to such a large effect in the transition strength.

Examining the 2_4^+ level, the measured strength of the $2_4^+ \rightarrow 0_1^+$ decay mode (1.8(2) e^2fm^4) is accurately reproduced by both fp and MCSM calculations, while the jj44 one, corresponding to 0.006 e^2fm^4, appears to be too small, thus, arguing for the strength being associated with excitations predominantly within the fp space. Examining the $2_4^+ \rightarrow 2_1^+$ transition leads to the same conclusion, with the fp and MCSM calculations, once again, closely predicting the observed value of 9(1) e^2fm^4, while the jj44 computation provides too small (0.2 e^2fm^4) a value. Unfortunately, the M1 transition strength does not reveal

much in this case either, as each set of calculations predicts it to be quite small. The proton occupancies of the 2_4^+ level with respect to that of the ground state are nearly the same for both the fp and MCSM calculations, suggesting that the difference in wavefunctions between the two levels largely arises from neutron contributions. In terms of neutron occupancies, the fp calculations compute a drop in the $p_{3/2}$ neutron number, while the MCSM ones do not. Instead they indicate a drop in the $g_{9/2}$ orbital occupancy with respect to the ground state. However, the accuracy of the fp value in this case may indicate that $g_{9/2}$ orbital excitations do not play as significant of a role in this state, and that, instead, the redistribution of neutrons to the $p_{3/2}$ orbital may be more relevant. With respect to the 2_1^+ level, both fp and MCSM calculations predict a small reorganization of protons from the $p_{3/2}$ state back to the $f_{7/2}$ orbital, but, for the most part, the proton occupancies remain quite similar between the two states. From the considerations above, it can be concluded that the 2_4^+ level corresponds to an excitation within the fp shell.

Next, the transition strengths of the excited 4^+ states will be explored. The same occupancy trends observed in the excited 2^+ states are manifest in this instance as well and, consequently, the occupancies for the 4^+ states will not be discussed further, concentrating instead solely on comparisons between measured and computed strengths. Beginning with the 4_1^+ level, a value of 66^{+7}_{-4} e^2fm^4 was measured for the $4_1^+ \rightarrow 2_1^+$ transition strength. This is reproduced most accurately by the fp calculations with a value of 28.9 e^2fm^4. The MCSM value of 124 e^2fm^4 is somewhat too large, but within a factor of 2 of the data. However, the jj44 value of 0.22 e^2fm^4 is much too small. This, once more, argues for the predominance of wavefunctions within the fp space as being involved in the description of this level. The $4_1^+ \rightarrow 2_2^+$ transition on the other hand, while not observed experimentally, is determined by GOSIA to have a large strength of 200^{+50}_{-30} e^2fm^4. All three calculations, indeed, predict large transition strengths, albeit, not as large as that calculated by GOSIA, with the fp one being the largest, corresponding to a value of 61.5 e^2fm^4. Furthermore, when previously discussing the 2_2^+ level, it was suggested that the fp space was favored for the description of

this state, a pattern that is confirmed here.

Considering the 4_2^+ state, the $4_2^+ \rightarrow 2_1^+$ transition strength is predicted to be comparably large in all three calculations, with values around 130-140 e^2fm^4. All three computed strengths are roughly double the measured one of 69(2) e^2fm^4, herewith providing no further insight about the configurations involved in the wavefunction. In addition, the $4_2^+ \rightarrow 2_2^+$ transition was not observed experimentally, but was predicted to be small (about 2 e^2fm^4) by both the fp and jj44 calculations, and larger by the MCSM one. Hence, no further guidance on the wavefunctions involved can be gathered.

The only observed decay mode from the 4_3^+ level is the $4_3^+ \rightarrow 2_1^+$ transition, for which a small transition strength of 2.5(5) e^2fm^4 was measured. This is reproduced particularly well by the MCSM calculations (3 e^2fm^4) and reasonably so by the fp and jj44 ones. Furthermore, upon examining the computed values for the $4_3^+ \rightarrow 2_2^+$ transition (not observed), one notes that the MCSM calculations predict a very large transition strength of 213 e^2fm^4, which is clearly inconsistent with the fact that such a transition was not seen. This suggests that the $g_{9/2}$ and $d_{5/2}$ orbitals included in the MCSM computation do not play significant roles in the wavefunction of the 4_3^+ state, thereby favoring a configuration within the fp space. Finally, the calculations for the $4_3^+ \rightarrow 4_2^+$ transition (which was not observed either) may be argued the same way: the jj44 calculations correspond to the smallest strength of 9.6 e^2fm^4; hence supporting the view that the wavefunction may be dominated by a neutron configuration within the fp shell.

No direct transition between the 4_4^+ and 2_1^+ states was observed, however, the data are inferred by GOSIA, which determined an associated strength of $11.4^{+1.6}_{-1.5}$ e^2fm^4 for this transition. This value is best reproduced by the fp calculations (3.8 e^2fm^4), but all three values are comparably small. Regarding the observed $4_4^+ \rightarrow 4_1^+$ decay mode, a very large transition strength of 900^{+2000}_{-200} e^2fm^4 is determined by GOSIA, albeit, with large uncertainties. This measured strength greatly exceeds all those determined by the calculations, and the only conclusion inferred from the comparisons is that the data provide no compelling evidence

for an excitation across the proton and/or neutron shell gaps.

Now that both the 2^+ and 4^+ levels have been discussed, the focus can be placed on the two excited 0^+ states observed in the Coulomb excitation measurements. Starting with the 0_2^+ level, the MCSM and fp interactions provide strong indications about the nature of this state. The measured strength for the $0_2^+ \rightarrow 2_1^+$ transition is relatively large (48(3) e^2fm^4), and is reproduced almost exactly by the MCSM calculations, whereas the fp value of 70.9 overestimates it somewhat, but not even by a factor of two, i.e., a satisfactory result considering the degree of agreement between data and calculations observed above for the 2^+ and 4^+ states. The most striking aspect in this instance is the small jj44 strength of 1.8 e^2fm^4. Furthermore, the data for the $0_2^+ \rightarrow 2_2^+$ decay mode lead to a similar observation: the value determined by GOSIA, 700(200) e^2fm^4, is large, and both the MCSM (237 e^2fm^4) and the fp (69.2 e^2fm^4) computations predict large strengths, while those within the jj44 space produce the smallest value (21.9 e^2fm^4). The two following conclusions may be drawn from these comparisons. First, the wavefunction for the 0_2^+ level must predominantly be dominated by configurations within the fp space, and, secondly, that neutron excitations alone cannot fully account for the description of this state. This is confirmed when exploring the proton and neutron occupancies of Table 5.3. When first comparing those for the 0_2^+ and 2_1^+ levels, it can be seen that the proton occupancies remain the same within the fp calculations, however, the MCSM result indicates a reduction of the $f_{7/2}$ orbital population for the 0_2^+ level, which appears to be redistributed into the $p_{3/2}$ and $f_{5/2}$ orbitals. Looking at the neutrons, the occupancies of these two states are, once again, similar for the fp calculations, with the main difference being a reduction in the $f_{5/2}$ occupation and a slight increase in the $p_{1/2}$ one. With regard to the MCSM computations, there is a significant increase in the $g_{9/2}$ occupation value up to 1.97 neutrons, correlated with a depletion in that of both the $p_{3/2}$ and $f_{5/2}$ orbitals. Lastly, the jj44 calculations confirm a small $g_{9/2}$ neutron occupation. It can, thus, be concluded that the occupancies reinforce the observations drawn from the B(E2) strengths and, as neutrons contribute with the opposite sign to the reduced

transition probability, the MCSM strengths would be expected to be smaller than those of the fp calculations, as the comparison between experiment and theory indicate.

Coming to the 0_3^+ level, once more, the MCSM calculations predict the largest $0_3^+ \rightarrow 2_1^+$ transition strength with a value of 5.8 e^2fm^4, which also comes the closest to the experimental value of 10(1) e^2fm^4. Here, however, the fp calculations perform the worst while the jj44 ones are within an order of magnitude. This difference with the observations for the 0_2^+ level indicates that, in this case, the $g_{9/2}$ orbital plays a larger role, which cannot be accounted for within the fp space. Moreover, it appears that both proton and neutron excitations must be included, based on the subsequent examination of the $0_3^+ \rightarrow 2_2^+$ decay mode. Here, the measured strength is large (600(300) e^2fm^4), and mimicked to a degree by the fp calculations (31.9 e^2fm^4), whereas the jj44 and MCSM computations derive strengths smaller by an order of magnitude. So, from the inspection of these two decay modes, it can be concluded that proton configurations within the fp space, as well as neutron ones, including those from the $g_{9/2}$ orbital, are involved in the 0_3^+ wavefunction. An examination of the predicted orbital occupancies supports this interpretation further. For the protons, the occupancy values are quite similar for both the fp and MCSM model spaces, as concluded above from the transition strengths. For the neutrons, the occupation of the $g_{9/2}$ orbital in the jj44 calculations is nearly the same as that of the 2_1^+ state, which is consistent with the observation that, in this case, the jj44 calculations perform better than the fp ones. However, the $g_{9/2}$ occupancy in the jj44 calculations is larger than that given by the MCSM ones, which could perhaps account for the fact that the MCSM computations come closest to reproducing the experimental value, i.e., a smaller $g_{9/2}$ occupation leads to a larger transition strength. Overall, the patterns observed from the transition strengths and the occupancy values for the 0_2^+ and 0_3^+ states can, thus, be understood in a consistent picture.

The detailed discussion above of transition strengths and orbital occupancies provide an understanding of the states observed in the multi-step Coulomb excitation measurements described in the present work. It is, however, worthwhile at this point to examine more

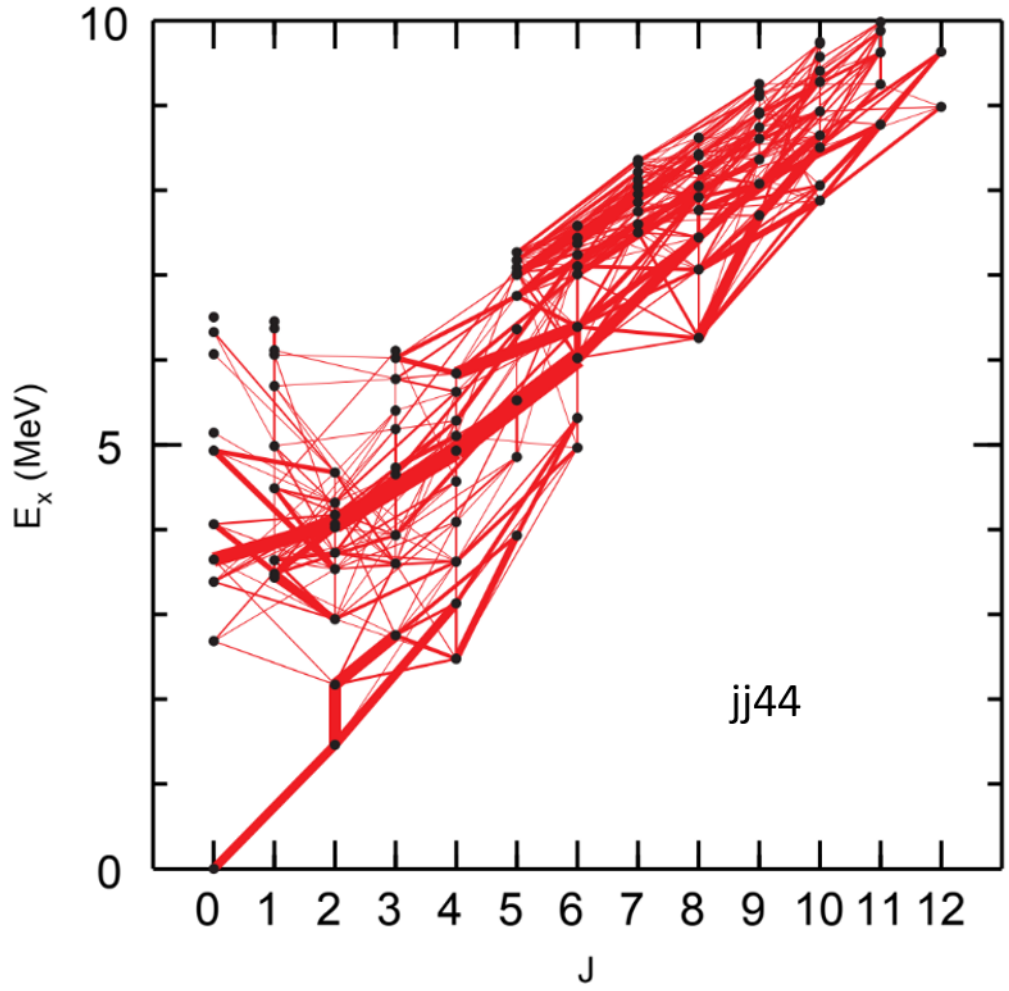

Figure 5.11: Plot of the reduced transition strengths connecting states in ^{64}Ni, as predicted by the jj44 calculations (see text for details).

globally the general trends exhibited by the data and to compare these with the calculations. For this purpose, the so-called transition networks of Figures 5.11 and 5.12 have been generated from the shell-model calculations within the fp and jj44 spaces. The two figures present the locations of the calculated states as dots while the lines connecting them represent the decay paths, considering E2 transitions only. The widths of the various lines are directly proportional to the calculated reduced transition probabilities. Note that, for each spin value, many more states than discussed thus far are presented, i.e., the plots extend up to 6—7 MeV above the yrast line.

Both figures indicate clearly that the ground state and the 2_1^+ level are linked by a strong

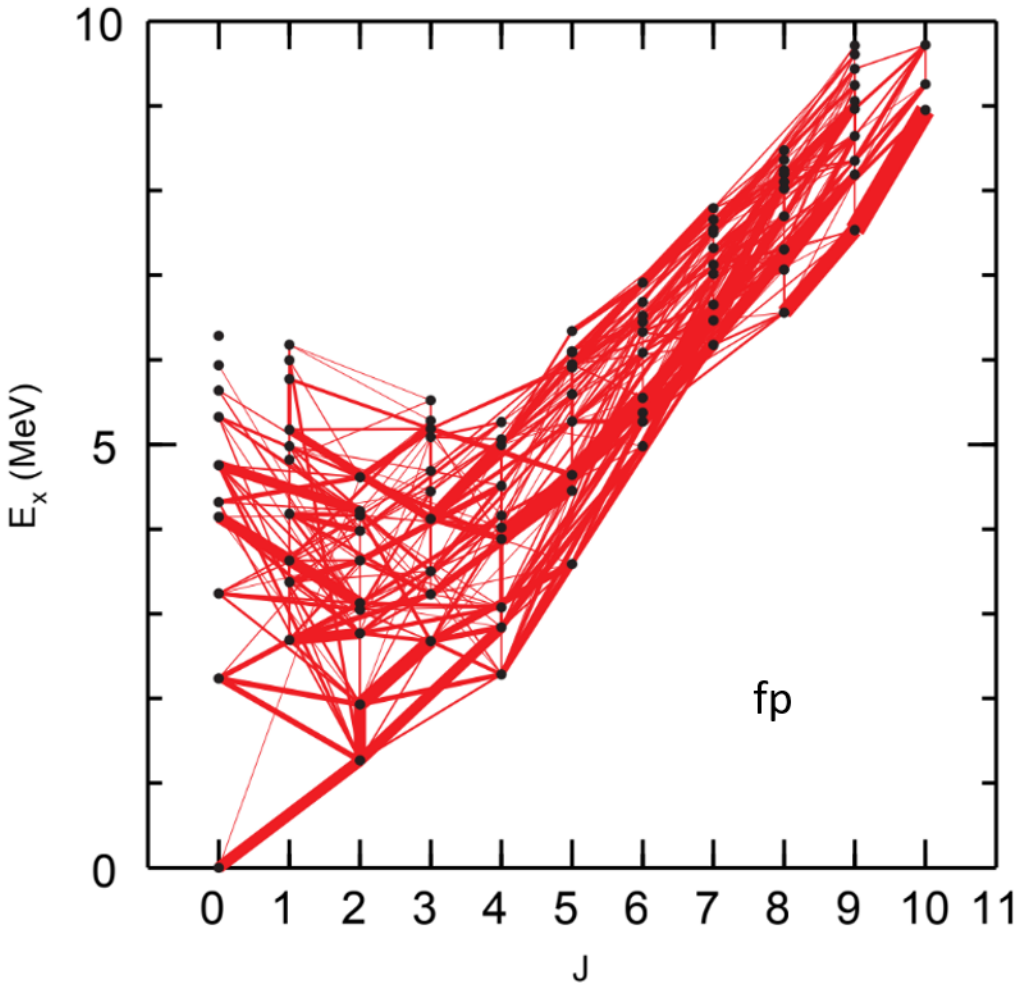

Figure 5.12: Plot of the reduced transition strengths connecting states in ^{64}Ni, as predicted by the fp calculations (see text for details).

transition strength. Hence, the calculations imply that the feeding of higher-spin states will proceed predominantly through multi-step Coulomb excitation from this 2_1^+ level, as seen in the data. Calculations in both model spaces also predict that, beyond the 2_1^+ state, the excitation path splits in two directions with nearly comparable strengths and feeds the 2_2^+ and 4_2^+ states. This predicted trend is seen in the data: the measured strengths of the $2_2^+ \rightarrow 2_1^+$ and $4_2^+ \rightarrow 2_1^+$ transitions are of the same order ($2.9^{+0.3}_{-0.2}$ W.u vs 4.5(2) W.u.) and only slightly lower than the 9(1) W.u probability measured for the ground-state transition as the widths in the two figures suggest. From Figure 5.11, the reader would also infer that the 4_1^+ state should not be observed if the calculations within the jj44 space reflected reality. In this instance, the data favor the fp model space as the $4_1^+ \rightarrow 2_1^+$ strength has been determined experimentally, and found to be smaller than that linking the 4_1^+ and 2_2^+ states, in qualitative agreement with the calculations in this space. In fact, the similarity between the data and the fp calculations extends clearly to the 0_2^+ level, where the computed de-excitation pattern also mirrors that seen in the measurements. Specifically, the noted absence of a $0_2^+ \rightarrow 2_1^+$ transition in the jj44 prediction is not born out by the data. Generally speaking, the fact that all the transitions out of the 0_2^+ state in Figure 5.12 are of comparable width, e.g. of the same order of magnitude, can be viewed as a signature for a small degree of collectivity. This observation can then in turn be related with the results of the MCSM calculations that associate the 0_2^+ state with a small, oblate deformation.

In Figures 5.11 and 5.12, signatures of strong collectivity would manifest themselves through the appearance of bands of transitions with the same strength linking successive states separated by two units of spin. While no such band is present in the plot presenting the shell-model calculations within the fp space, one is clearly visible within the jj44 one (Figure 5.11). Indeed, a rather clear 8^+ - 6^+ - 4^+ - 2^+ - 0^+ sequence appears, terminating in the fourth calculated 0^+ level (i.e., the 0_4^+ state) at an excitation energy of 3.646 MeV. Assuming that the jj44 calculations are a close representation of the data, the question then arises as to why this 0_4^+ state, and by extension, the cascade of collective E2 transitions built

on it was not observed in the two experiments reported here. Figure 5.11 clearly indicates that the strengths of transitions linking the states in the cascade with the lower-lying, near-yrast states are always small. In terms of multi-step Coulomb excitation, this implies that the cross section for feeding the 0_4^+ state must be small as well and that, hence, the associated transitions such as the $0_4^+ \rightarrow 2_2^+$ link would be below the detection limit of the experiment. It is also worth noting that the entire band in Figure 5.11 is not calculated to become yrast, even at spin 10 or above. In the previous chapter, where the results of measurements following deep-inelastic reactions were also reported, it was shown that only states at or near the yrast line were fed with measurable cross sections. Hence, the observation of a sequence that would indicate collectivity would be unlikely via this approach as well. In addition, the fact that the fp calculations provide essentially the same results as the MCSM ones for most of the B(E2) rates (in particular, those discussed regarding Figures 5.11 and 5.12) suggests that a figure for the MCSM results would closely mirror the fp one. The agreement between these two computations also serves to motivate the search for an additional excited 0^+ state (e.g., 0_4^+) in ^{64}Ni.

Section 5.4: Evidence for a 0_4^+ State

From the discussion above and the calculations illustrated in Figures 5.11 and 5.12, it is clear that observing a 0_4^+ state through multi-step Coulomb excitation or deep-inelastic reactions would be very challenging, if not impossible. Nevertheless, the decay patterns delineated in Figure 5.11 as well as the results of similar calculations within the MCSM framework (not shown) stimulated further attempts to identify possible candidates for a 0^+ level associated with a prolate minimum in the potential. Two experimental approaches were considered: a nuclear resonance fluorescence measurement and/or a neutron capture one. A collaboration between groups at the Nuclear Physics Institute in Krakow, Poland (led by B. Fornal), at the University of Milano, Milan, Italy (led by S. Leoni) and at the University of North Carolina at Chapel Hill (led by R. Janssens) proposed to conduct a

^{63}Ni(n,γ) experiment at the high flux reactor of the Institute Laue Langevin, Grenoble, France. The measurement involved a radioactive ^{63}Ni target ($T_{1/2}$ = 101.2 y) available at the institute. The experiment was approved and a nearly one-month measurement took place in the September-October, 2019 period with an array of 18 germanium detectors. While the analysis is still ongoing, preliminary results are already available [101].

Since the ground state of ^{63}Ni has a $\frac{1}{2}^-$ spin and parity, neutron capture into ^{64}Ni is expected to proceed through levels with 0^- or 1^- quantum numbers. Therefore, strong population of 0^+, 1^+ and 2^+ states through fast E1 primary γ rays should be expected. Indeed, the direct feeding of the known 0^+_2 and 0^+_3 states, at 2867 and 3026 keV was observed and the $0^+_{2,3} \rightarrow 2^+_1 \rightarrow 0^+_1$ γ-ray cascades were observed in the coincidence data with an intensity sufficient to confirm through angular correlations the E2 character of the transitions involved. Hence, this experiment provides an unambiguous means to identify 0^+ excitations in ^{64}Ni. The analysis has already revealed the presence of the 3463-keV state decaying in part via a 1187-keV transition to the 2^+_2, 2277-keV level. Angular correlations unambiguously determined this 3463-keV level to have 0^+ spin and parity. It should be noted that this level had been observed in earlier measurements. In particular, it was observed very weakly by Broda et al. [25] and was included in the level scheme presented in this work - see Figure 1.4 in this thesis. However, in Ref. [25] and Fig. 1.4, the level was tentatively assigned as a (2^+, 3^-) state. The neutron capture data rule out these quantum numbers and the 0^+_4 assignment is firm. As expected from the discussion above, the $0^+_4 \rightarrow 2^+_2$, 1187-keV transition was not observed in the present Coulomb excitation data. However, an upper limit to its γ-ray intensity could be determined from the spectra at backward angles. As a result, an upper limit of 1.3 e^2fm^4 or 0.08 W.u. was established for the B(E2; $0^+_4 \rightarrow 2^+_2$) transition strength.

With this new, preliminary result the similarity between the low-spin structures of ^{66}Ni and ^{64}Ni is striking. Indeed, both nuclei reveal the presence of three excited 0^+ states with similar de-excitation patterns (for ^{66}Ni see Fig. 5.5 above). Specifically, looking at the B(E2;

$0_i^+ \rightarrow 2^+$) strengths, the following observations can be made: (a) the two 0_2^+ levels decay toward the respective 2_1^+ states with strengths of 4.3 (^{66}Ni) and 3.2 (^{64}Ni) W.u; (b) for the 0_3^+ states, the corresponding B(E2) probabilities are 0.1 and 0.65 W.u. and (c) the 0.2 W.u value reported for the ^{66}Ni 0_4^+ state can be compared with the 0.08 W.u. upper limit reported here for ^{64}Ni. In view of these observations, a similar interpretation for the nature of these excitations in both nuclei seems warranted. Based on the results of the MCSM calculations it is, thus, proposed that the 0_1^+ and 0_3^+ levels are associated with a spherical shape, the 0_2^+ states with an oblate shape, and the 0_4^+ ones with a prolate shape. As predicted by these calculations, the excitation energy of the three modes increases with decreasing neutron number: the measured 0_2^+ energy increases from 2443 to 2867 keV between ^{66}Ni and ^{64}Ni, that of the 0_3^+ levels increases from 2671 to 3026 keV, and the 0_4^+ states are located at 2974 and 3463 keV, respectively. The analysis of neutron-capture data is still ongoing. However, all the information available thus far validates the results presented in this work. Hence, the interpretation of the structure of ^{64}Ni in terms of shape coexistence is supported by the total of the available experimental evidence.

CHAPTER 6: Conclusions

Section 6.1: Overview

The Ni isotopic chain has long been the subject of extensive nuclear structure studies. With a magic number of protons, the chain includes doubly-magic ^{48}Ni, ^{58}Ni and ^{78}Ni. As discussed in this work, ^{68}Ni can be viewed as doubly-magic as well. However, following the unexpected discovery of shape coexistence in the latter isotope [95], considerable experimental efforts have been devoted to explore neighboring Ni isotopes in search of the same phenomenon. With the observation of a prolate-deformed 0^+ state in ^{70}Ni at 1567 keV [22], and with ^{66}Ni manifesting both oblate- and prolate-deformed 0^+ levels at 2445 and 2965 keV, respectively, alongside a spherical one at 2664 keV [23], it became clear that shape coexistence is rather ubiquitous in this region. Furthermore, studies of high-spin states in ^{62}Ni and ^{63}Ni [28, 29] provided further evidence for collectivity. As a result of these experimental observations, a number of calculations have been carried out with various approaches in an attempt to identify which aspects of the nuclear force are responsible for driving the nuclear shape. Meanwhile, additional experimental work has been initiated to investigate more thoroughly the nature of the excitations involved in the isotopes where shape coexistence is already known to exist, and to explore the Ni chain further. The present work addresses the following question: does the most neutron-rich, stable isotope, ^{64}Ni, also exhibit shape coexistence, and, if so, at which excitation energy?

A two-pronged experimental approach was used in the present work to address these questions. First, Coulomb excitation of ^{64}Ni was carried out at the ATLAS accelerator at Argonne National Laboratory, utilizing the new GRETINA γ-ray tracking array in combination with the CHICO2 particle detector in order to probe the nature of low-lying states in this nucleus

and assess the presence of collectivity. The data were analyzed with the GOSIA Coulomb excitation analysis software, in order to obtain reduced transition strengths, and quadrupole moments and compare these with those predicted by shell-model and Monte Carlo shell-model (MCSM) calculations. Secondly, data from deep-inelastic reactions collected with the Gammasphere detector array and the Fragment Mass Analyzer were examined in order to search for new, higher-energy, higher-spin levels in ^{64}Ni.

No evidence for rotational bands was found in the present data. However, the transition strengths for the de-excitation of the known excited 0^+ states are found to be reproduced well by theory and, in fact, support the view that ^{64}Ni closely resembles its neighbor ^{66}Ni, herewith favoring an interpretation in terms of shape coexistence. Thus, transition strengths and quadrupole moments indicate that the ground and 0^+_3 states are spherical, and the 0^+_2 level is characterized by a small oblate deformation. Moreover, convergence between the B(E2) strengths in experiment and calculations indicates that most excitations observed in Coulomb excitation are confined to the fp shell. Furthermore, the data on excitation energies, spins, and parity indicate that single-particle excitations dominate up to the highest energy. It is worth noting that the strength of the first-excited 2^+_1 state measured in this work agrees with that observed in previous studies, herewith validating these results. Furthermore, thirteen new transitions, along with twelve new states, were discovered so that the level sequences in this nucleus now extend up to an energy of 17930 keV, with a tentative (16 or 17) spin assignment.

Lastly, while not observed in this work, a 3463-keV state was identified by Ref. [25] and unambiguously confirmed to be the 0^+_4 level by the Krakov-Milano-Bucharest-UNC collaboration [101]. This 0^+_4 state fits well within the pattern observed in the adjacent ^{66}Ni. Indeed, if these nuclei closely mirror one another, as suggested by the data, it is reasonable to associate this newly identified 3463-keV, 0^+_4 state with prolate deformation, a conclusion strengthened by an upper limit of 0.08 W.u. for the strength of the $0^+_4 \rightarrow 2^+_2$ transition deduced from the present data. This value can be compared with the strength

of the analogous transition of 0.2 W.u. observed in ^{66}Ni. Figure 6.1 illustrates the nuclear deformation of each of the 0^+ states in ^{64}Ni in terms of their spectroscopic and intrinsic quadrupole moments, as predicted by the MCSM calculations carried out by the Tokyo group of Otsuka et al. [100]. Here, the color scheme indicates the depth of the potential well and dots specify the location in deformation space of the basis states sampled by the calculations. It is clear from these computations that both the ground and 0_3^+ levels are expected to be spherical, whereas it is anticipated that the 0_2^+ and 0_4^+ states are associated with oblate and prolate minima, respectively. Moreover, a comparison of low-spin excitations in terms of excitation energies is depicted in Figure 6.2. Here, the pattern exhibited by the even-even Ni isotopes as a function of mass is apparent, especially with regard to the excited 0^+ levels. Thus, while more study is necessary in order to further assess the nature of such states in ^{64}Ni, the agreement between experiment and theory, alongside the trends seen in the Ni chain, make a strong case for shape coexistence in this nucleus.

Section 6.2: Future Work

Naturally, one might inquire as to whether the patterns exhibited in Figures 6.1 and 6.2 continue to lower-mass Ni isotopes. Indeed, the nucleus ^{62}Ni is the lightest one in the Ni chain proposed to manifest shape coexistence according to the MCSM calculations by the Tokyo group. Thus, moving forward, an exploration of this nucleus via Coulomb excitation and/or deep-inelastic reactions would be an intuitive next step. However, as Figure 6.2 suggests, the 0^+ prolate state would be expected to be located even higher in energy, thereby fostering the need for a neutron-capture or nuclear resonance fluorescence (NRF) measurement to be performed at HIγS, as these two processes are likely to feed every spin 0, 1, and 2 level of a nucleus from the ground state to the nuclear binding energy. Furthermore, by utilizing the clover array currently under construction at HIγS, one may take advantage of coincidence relationships to investigate decay patterns in detail and compare experiment and theory for branching ratios, for example. The polarization of the γ-ray beam can also be exploited to

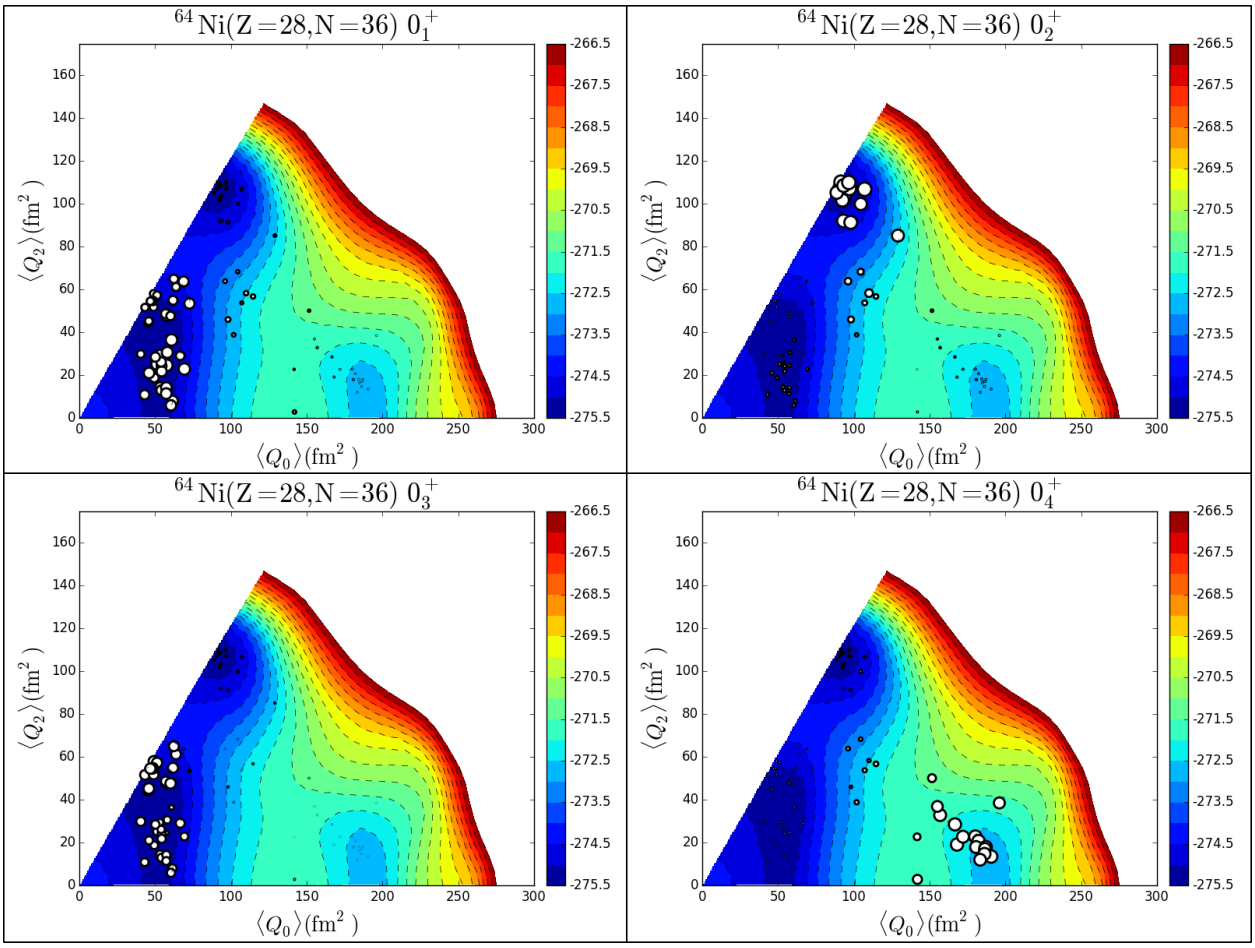

Figure 6.1: Nuclear deformation of each 0^+ state in ^{64}Ni in terms of its spectroscopic, $\langle Q_2 \rangle$, and intrinsic, $\langle Q_0 \rangle$, quadrupole moments, as predicted by the MCSM calculations carried out by the Tokyo group. The color scheme indicates the depth of the potential well and dots specify the location of the basis states sampled for the calculations.

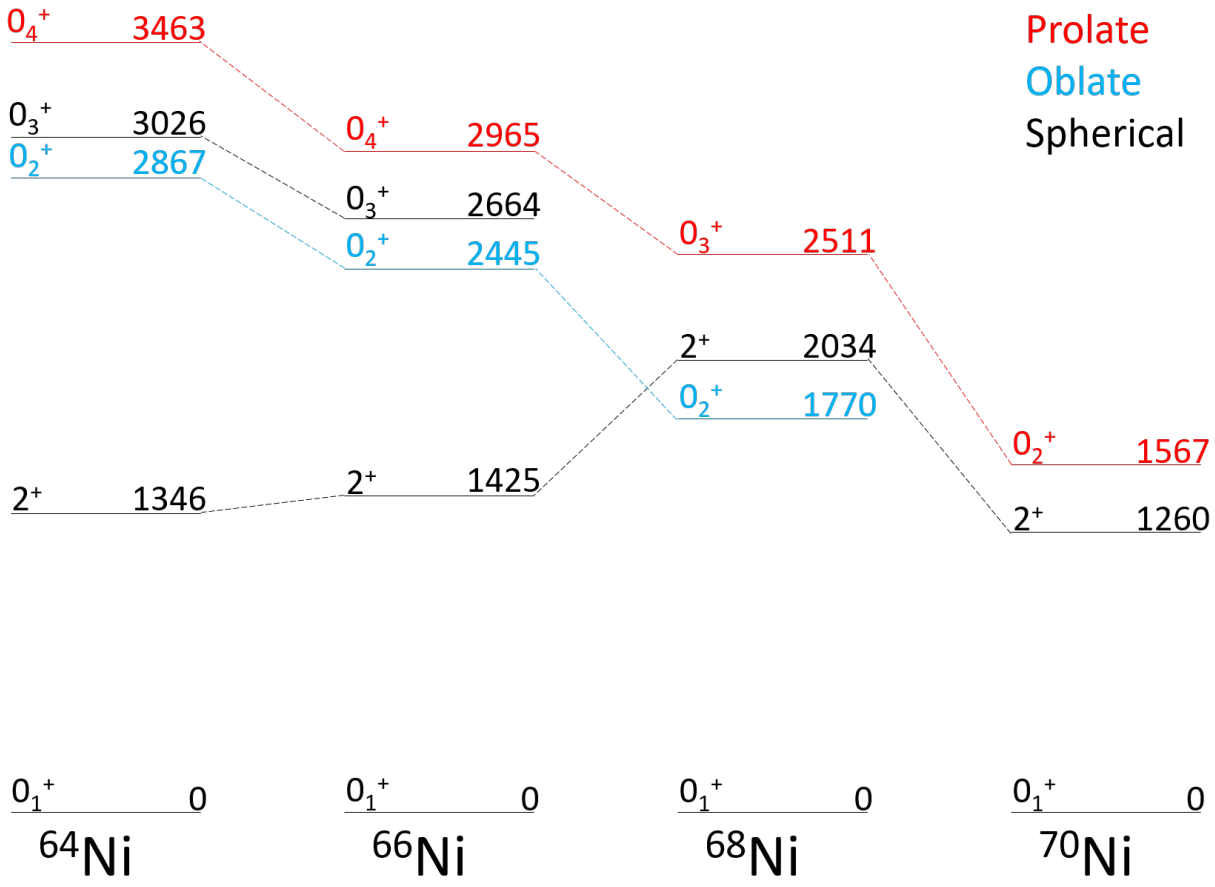

Figure 6.2: Energy level comparison for excited 0^+ states and 2_1^+ levels in even-even Ni isotopes from ^{64}Ni to ^{70}Ni. Black labels indicate spherical states, while blue and red ones identify states interpreted as associated with oblate and prolate deformations, respectively.

obtain direct information on the multipolarity of each transition. Such an experiment has already been approved for ^{62}Ni. Along the same lines, the MCSM calculations also indicate that the 0^+ prolate level is associated with particle-hole excitations involving both protons and neutrons. It is possible to probe the role of proton excitations in the isotones of ^{64,66,68}Ni, i.e. ^{66}Zn, ^{68}Zn, and ^{70}Zn, in order to further assess their significance. One potential course of action would be to begin by attempting to identify excited 0^+ states via NRF and beta decay, leaving Coulomb excitation and deep-inelastic reactions for a second phase, depending on the findings. Lastly, the search for shape coexistence in heavier, unstable Ni isotopes, i.e. ^{72,74}Ni, can be pursued as soon as the new Facility for Rare Isotope Beams (FRIB) becomes operational. Further, once the facility is at full power, this search can be extended to even heavier nuclei, such as ^{76}Ni and doubly-magic ^{78}Ni. Hence, additional data important to test further the theoretical descriptions discussed in the present work should be anticipated in the next decade.

BIBLIOGRAPHY

[1] D. DiJulio, *Probing single-particle and collective states in atomic nuclei with Coulomb excitation*, Ph.D. thesis, Lund University (2013).

[2] Aa. Bohr and B.R. Mottelson, "Nuclear structure, vol. II, App. 6A," (1975).

[3] R.V.F. Janssens, Physica Scripta **2013**, 014005 (2013).

[4] H. Morinaga, Phys. Rev. **101**, 254 (1956).

[5] E.B. Carter, G.E. Mitchell, and R.H. Davis, Phys. Rev. **133**, B1421 (1964).

[6] G.E. Mitchell, E.B. Carter, and R.H. Davis, Phys. Rev. **133**, B1434 (1964).

[7] A.V. Afanasjev, M. Devlin, E. Ideguchi, W. Reviol, and D.G. Sarantites, Phys. Rev. Lett. **87** (2003).

[8] C.J. Chiara, E. Ideguchi, M. Devlin, D.R. LaFosse, F. Lerma, W. Reviol, S.K. Ryu, D.G. Sarantites, C. Baktash, A. Galindo-Uribarri, *et al.*, Phys. Rev. C **67**, 041303 (2003).

[9] A.N. Andreyev, M. Huyse, P. Van Duppen, L. Weissman, D. Ackermann, J. Gerl, F.P. Hessberger, S. Hofmann, A. Kleinböhl, G. Münzenberg, *et al.*, Nature **405**, 430 (2000).

[10] E. Caurier, F. Nowacki, A. Poves, and J. Retamosa, Phys. Rev. C **58**, 2033 (1998).

[11] R.V.F. Janssens, B. Fornal, P.F. Mantica, B.A. Brown, R. Broda, P. Bhattacharyya, M.P. Carpenter, M. Cinausero, P.J. Daly, A.D. Davies, *et al.*, Phys. Lett. B **546** (2002).

[12] A. Gade and S.N. Liddick, Journal of Physics G: Nuclear and Particle Physics **43**, 024001 (2016).

[13] M. Pomorski, M. Pfützner, W. Dominik, R. Grzywacz, A. Stolz, T. Baumann, J.S. Berryman, H. Czyrkowski, R. Dabrowski, A. Fijałkowska, *et al.*, Phys. Rev. C **90**, 014311 (2014).

[14] R. Taniuchi, C. Santamaria, P. Doornenbal, A. Obertelli, K. Yoneda, G. Authelet, H. Baba, D. Calvet, F. Château, A. Corsi, *et al.*, Nature **569** (2019).

[15] M. Bernas, Ph. Dessagne, M. Langevin, J. Payet, F. Pougheon, and P. Roussel, Phys. Lett. B **113** (1982).

[16] F. Recchia, C.J. Chiara, R.V.F. Janssens, D. Weisshaar, A. Gade, W.B. Walters, M. Albers, M. Alcorta, V.M. Bader, T. Baugher, *et al.*, Phys. Rev. C **88**, 041302 (2013).

[17] S.M. Lenzi (IOP Publishing, 2013) p. 012026.

[18] C.J. Chiara, D. Weisshaar, R.V.F. Janssens, Y. Tsunoda, T. Otsuka, J. Harker, W.B. Walters, F. Recchia, M. Albers, M. Alcorta, *et al.*, Phys. Rev. C **91**, 044309 (2015).

[19] B. Elman, A. Gade, R.V.F. Janssens, A.D. Ayangeakaa, D. Bazin, J. Belarge, P. Bender, B. Brown, C. Campbell, M.P. Carpenter, *et al.*, Phys. Rev. C **100**, 034317 (2019).

[20] C. Prokop, B. Crider, S. Liddick, A.D. Ayangeakaa, M.P. Carpenter, J. Carroll, J. Chen, C.J. Chiara, H. David, A. Dombos, *et al.*, Phys. Rev. C **92**, 061302 (2015).

[21] C. Babcock, H. Heylen, J. Billowes, M. Bissell, K. Blaum, P. Campbell, B. Cheal, R. G. Ruiz, C. Geppert, W. Gins, *et al.*, Phys. Lett. B **750**, 176 (2015).

[22] S. Lenzi, F. Nowacki, A. Poves, and K. Sieja, Phys. Rev. C **82**, 054301 (2010).

[23] B. Olaizola, L. Fraile, H. Mach, A. Poves, F. Nowacki, A. Aprahamian, J. Briz, J. Cal-González, D. Ghiţa, U. Köster, *et al.*, Phys. Rev. C **95**, 061303 (2017).

[24] S. Leoni, B. Fornal, N. Mărginean, M. Sferrazza, Y. Tsunoda, T. Otsuka, G. Bocchi, F. C. L. Crespi, A. Bracco, S. Aydin, *et al.*, Phys. Rev. Lett. **118**, 162502 (2017).

[25] R. Broda, T. Pawłat, W. Królas, R.V.F. Janssens, S. Zhu, W.B. Walters, B. Fornal, C.J. Chiara, M.P. Carpenter, N. Hoteling, *et al.*, Phys. Rev. C **86**, 064312 (2012).

[26] O. Kenn, K.-H. Speidel, R. Ernst, J. Gerber, P. Maier-Komor, and F. Nowacki, Phys. Rev. C **63**, 064306 (2001).

[27] A.D. Ayangeakaa, S. Zhu, R.V.F. Janssens, M.P. Carpenter, M. Albers, M. Alcorta, T. Baugher, P. Bertone, C.J. Chiara, P. Chowdhury, *et al.*, Phys. Rev. C **91**, 044327 (2015).

[28] M. Albers, S. Zhu, A.D. Ayangeakaa, R.V.F. Janssens, J. Gellanki, I. Ragnarsson, M. Alcorta, T. Baugher, P. Bertone, M.P. Carpenter, C.J. Chiara, *et al.*, Phys. Rev. C **94**, 034301 (2016).

[29] M. Albers, S. Zhu, R.V.F. Janssens, J. Gellanki, I. Ragnarsson, M. Alcorta, T. Baugher, P. Bertone, M.P. Carpenter, C.J. Chiara, *et al.*, Phys. Rev. C **88**, 054314 (2013).

[30] A. N. Deacon, *Shape changes in neutron-rich fp-shell nuclei* (The University of Manchester (United Kingdom), 2006).

[31] M. Abramowitz and I. A. Stegun, *Handbook of mathematical functions with formulas, graphs, and mathematical tables*, Vol. 55 (US Government printing office, 1948).

[32] M. Goeppert-Mayer, Phys. Rev **78**, 16 (1950).

[33] O. Haxel, J. H. D. Jensen, and H. E. Suess, Zeitschrift für Physik **128**, 295 (1950).

[34] B. T. Feld, Annual Review of Nuclear Science **2**, 239 (1953).

[35] M. Honma, T. Otsuka, B. Brown, and T. Mizusaki, The European Physical Journal A-Hadrons and Nuclei **25**, 499 (2005).

[36] M. Honma, B. Brown, T. Mizusaki, and T. Otsuka, Nucl. Phys. A **704**, 134 (2002).

[37] M. Honma, T. Otsuka, B. A. Brown, and T. Mizusaki, Phys. Rev. C **65**, 061301 (2002).

[38] A. Lisetskiy, B. A. Brown, M. Horoi, and H. Grawe, Phys. Rev. C **70**, 044314 (2004).

[39] M. Honma, T. Mizusaki, and T. Otsuka, Phys. Rev. Lett. **75**, 1284 (1995).

[40] M. Honma, T. Mizusaki, and T. Otsuka, Phys. Rev. Lett. **77**, 3315 (1996).

[41] T. Otsuka, M. Honma, and T. Mizusaki, Phys. Rev. Lett. **81**, 1588 (1998).

[42] T. Otsuka and Y. Tsunoda, Journal of Physics G: Nuclear and Particle Physics **43**, 024009 (2016).

[43] T. Otsuka, A. Gade, O. Sorlin, T. Suzuki, and Y. Utsuno, arXiv preprint arXiv:1805.06501 (2018).

[44] T. Otsuka, T. Suzuki, R. Fujimoto, H. Grawe, and Y. Akaishi, Phys. Rev. Lett. **95**, 232502 (2005).

[45] T. Otsuka, Physica Scripta **2013**, 014007 (2013).

[46] D. Cline, T. Czosnyka, A. Hayes, P. Napiorkowski, N. Warr, and C. Wu, Gosia Steering Committee **18**, 19 (2012).

[47] K. S. Krane, *Introductory nuclear physics* (1987).

[48] D. Weil, R. Wirowski, E. Ott, A. Dewald, P. von Brentano, H. Wolters, and R.M. Lieder, Nucl. Phys. A **567**, 431 (1994).

[49] S. Zhu, M.P. Carpenter, R.V.F. Janssens, S. Frauendorf, I. Ahmad, T. Khoo, F. Kondev, T. Lauritsen, C. Lister, and D. Seweryniak, Phys. Rev. C **81**, 041306 (2010).

[50] T. Lauritsen, M.P. Carpenter, T. Døssing, P. Fallon, B. Herskind, R.V.F. Janssens, D. Jenkins, T. Khoo, F. Kondev, A. Lopez-Martens, *et al.*, Phys. Rev. Lett. **88**, 042501 (2002).

[51] G. Bertsch and R.V.F. Janssens, American Journal of Physics **65**, 668 (1997).

[52] M. Yeh, P. Garrett, C. McGrath, S. Yates, and T. Belgya, Phys. Rev. Lett. **76**, 1208 (1996).

[53] D. Ward, H. Andrews, G. Ball, A. Galindo-Uribarri, V. Janzen, T. Nakatsukasa, D. Radford, T. Drake, J. DeGraaf, S. Pilotte, *et al.*, Nucl. Phys. A **600**, 88 (1996).

[54] T. Glasmacher, Annual Review of Nuclear and Particle Science **48**, 1 (1998).

[55] D. Cline, "Multiple Coulomb excitation techniques," `http://www.pas.rochester.edu/~cline/Research/coultechniques.pdf`.

[56] S. Paschalis, I. Lee, A. Macchiavelli, C. Campbell, M. Cromaz, S. Gros, J. Pavan, J. Qian, R. Clark, H. Crawford, *et al.*, Nucl. Instrum. Methods Phys. Res. A **709**, 44 (2013).

[57] C. Wu, D. Cline, A. Hayes, R. Flight, A. Melchionna, C. Zhou, I. Lee, D. Swan, R. Fox, and J. Anderson, Nucl. Instrum. Methods Phys. Res. A **814**, 6 (2016).

[58] C. Bertulani, arXiv preprint arXiv:0908.4307 (2009).

[59] R. Broda, M. Quader, P. Daly, R.V.F. Janssens, T. Khoo, W. Ma, and M. Drigert, Phys. Lett. B **251**, 245 (1990).

[60] W. Królas, R. Broda, B. Fornal, T. Pawłat, J. Wrzesiński, D. Bazzacco, G. de Angelis, S. Lunardi, R. Menegazzo, D. Napoli, *et al.*, Nucl. Phys. A **832**, 170 (2010).

[61] V. V. Volkov, Physics Reports **44**, 93 (1978).

[62] M. Cromaz (IOP Publishing, 2015) p. 012016.

[63] D. Weisshaar, D. Bazin, P. Bender, C. Campbell, F. Recchia, V. Bader, T. Baugher, J. Belarge, M.P. Carpenter, H. Crawford, *et al.*, Nucl. Instrum. Methods Phys. Res. A **847**, 187 (2017).

[64] A. Korichi and T. Lauritsen, The European Physical Journal A **55**, 121 (2019).

[65] M. Simon, D. Cline, C. Wu, R. Gray, R. Teng, and C. Long, Nucl. Instrum. Methods Phys. Res. A **452**, 205 (2000).

[66] R.V.F. Janssens and F.S. Stephens, Nuclear Physics News **6**, 9 (1996).

[67] A. Baxter, T. Khoo, M. Bleich, M.P. Carpenter, I. Ahmad, R.V.F. Janssens, E. Moore, I. Bearden, J. Beene, and I. Lee, Nucl. Instrum. Methods Phys. Res. A **317**, 101 (1992).

[68] "Gammmasphere efficiency," `https://www.phy.anl.gov/gammasphere/doc/efficiency/index.html`.

[69] "Gammasphere absorbers," `https://www.phy.anl.gov/gammasphere/doc/absorbers/Cu_Cd_Ta_absratios.gif`.

[70] M. Devlin, L. Sobotka, D. Sarantites, and D. LaFosse, Nucl. Instrum. Methods Phys. Res. A **383**, 506 (1996).

[71] C. N. Davids and J. D. Larson, Nucl. Instrum. Methods Phys. Res. B **40**, 1224 (1989).

[72] C. N. Davids, B. Back, K. Bindra, D. Henderson, W. Kutschera, T. Lauritsen, Y. Nagame, P. Sugathan, A. Ramayya, and W.B. Walters, Nucl. Instrum. Methods Phys. Res. B **70**, 358 (1992).

[73] A. Garnsworthy, C. Lister, P. Regan, B. Blank, I. Cullen, S. Gros, D. Henderson, G. Jones, Z. Liu, D. Seweryniak, *et al.*, Nucl. Instrum. Methods Phys. Res. A **594**, 184 (2008).

[74] D.C. Radford, URL http://radware. phy. ornl. gov/gf3/gf3 (2000).

[75] J. M. Allmond, B. Brown, A. E. Stuchbery, A. Galindo-Uribarri, E. Padilla-Rodal, D. C. Radford, J. Batchelder, M. E. Howard, J. F. Liang, B. Manning, *et al.*, Phys. Rev. C **90**, 034309 (2014).

[76] A. Krämer-Flecken, T. Morek, R.M. Lieder, W. Gast, G. Hebbinghaus, H. Jäger, and W. Urban, Nucl. Instrum. Methods Phys. Res. A **275**, 333 (1989).

[77] N. ENSDF, "online data service, ensdf database," (2020).

[78] R. Holzmann, I. Ahmad, R.V.F. Janssens, T. Khoo, D. Radford, M. Drigert, and U. Garg, Nucl. Instrum. Methods Phys. Res. A **260**, 153 (1987).

[79] B. Singh, Nuclear Data Sheets **108**, 197 (2007).

[80] D. Pauwels, D. Radulov, W.B. Walters, I. Darby, H. De Witte, J. Diriken, D. Fedorov, V. Fedosseev, L. Fraile, M. Huyse, *et al.*, Phys. Rev. C **86**, 064318 (2012).

[81] A. Harder, S. Michaelsen, A. Jungclaus, K. Lieb, A. Williams, H. Börner, and M. Trautmannsheimer, Zeitschrift für Physik A Hadrons and Nuclei **343**, 7 (1992).

[82] B. Pritychenko, J. Choquette, M. Horoi, B. Karamy, and B. Singh, Atomic Data and Nuclear Data Tables **98**, 798 (2012).

[83] Y. G. Kosyak, D. Kaipov, and L. Chekushina, Izv. Akad. Nauk SSSR, Ser. Fiz **53**, 2130 (1989).

[84] E. Paul, "Nuclear structure from gamma-ray spectroscopy," `http://ns.ph.liv.ac.uk/~ajb/summerschool/files/ESP-Lecture3.pdf`.

[85] F.G. Kondev, private communication.

[86] A.D. Ayangeakaa, private communication.

[87] P. Lesser, D. Cline, C. Kalbach-Cline, and A. Bahnsen, Nucl. Phys. A **223**, 563 (1974).

[88] O. Sorlin, S. Leenhardt, C. Donzaud, J. Duprat, F. Azaiez, F. Nowacki, H. Grawe, Z. Dombrádi, F. Amorini, A. Astier, *et al.*, Phys. Rev. Lett. **88**, 092501 (2002).

[89] W. Darcey, R. Chapman, and S. Hinds, Nucl. Phys. A **170**, 253 (1971).

[90] R. Singhal, S. Brain, W. Gillespie, A. Johnston, E. Lees, and A. Slight, Nucl. Phys. A **218**, 189 (1974).

[91] J. Lightbody Jr, Phys. Lett. B **38**, 475 (1972).

[92] Y. Torizuka, Y. Kojima, M. Oyamada, K. Nakahara, K. Sugiyama, T. Terasawa, K. Itoh, A. Yamaguchi, and M. Kimura, Phys. Rev. **185**, 1499 (1969).

[93] N. Bree, I. Stefanescu, P. A. Butler, J. Cederkäll, T. Davinson, P. Delahaye, J. Eberth, D. Fedorov, V. N. Fedosseev, L. M. Fraile, *et al.*, Phys. Rev. C **78**, 047301 (2008).

[94] B. Crider, C. Prokop, S. Liddick, M. Al-Shudifat, A.D. Ayangeakaa, M.P. Carpenter, J. Carroll, J. Chen, C.J. Chiara, H. David, *et al.*, Phys. Lett. B **763**, 108 (2016).

[95] S. Suchyta, S. Liddick, Y. Tsunoda, T. Otsuka, M. Bennett, A. Chemey, M. Honma, N. Larson, C. Prokop, S. Quinn, *et al.*, Phys. Rev. C **89**, 021301 (2014).

[96] O. Perru, O. Sorlin, S. Franchoo, F. Azaiez, E. Bouchez, C. Bourgeois, A. Chatillon, J. Daugas, Z. Dlouhy, Z. Dombrádi, *et al.*, Phys. Rev. Lett. **96**, 232501 (2006).

[97] M. Honma, T. Otsuka, B. A. Brown, and T. Mizusaki, Phys. Rev. C **69**, 034335 (2004).

[98] M. Honma, T. Otsuka, T. Mizusaki, and M. Hjorth-Jensen, Phys. Rev. C **80**, 064323 (2009).

[99] A.B. Brown, private communication.

[100] T. Otsuka, private communication.

[101] S. Leoni, B. Fornal, R.V.F. Janssens, D. Little, and the U. Milano, Krakow NP, U. North Carolina, Bucharest, Grenoble collaboration, To be published.